List of used symbols and abbreviations

a	contact radius
$\dot{A}$	cutting rate
A^*	jet structure parameter
A_C	pore cross section
A_H	hydrodemolished area
A_N	nozzle (orifice) cross section
A_P	plunger cross section
a_V	vibration parameter (acceleration)
b	jetting tool geometry parameter
B^*	jet structure parameter
B_M	brittleness
c_F	speed of sound water
c_M	speed of sound target
C_P	constant
C_S	interlock cohesion parameter
c_W	shock wave velocity
D	sand section test parameter
d_D	drop diameter
d_{Dmax}	maximum drop diameter
d_{DS}	Sauter diameter (water drop)
d_F	focus diameter
d_H	hose diameter
d_J	jet diameter
d_M	material grain diameter
d_N	nozzle (orifice) diameter
d_O	pore diameter
d_P	plunger diameter
d_S	particle diameter
d_T	threshold diameter
E_A	kinetic energy hydro-abrasive jet
E_B	basic output
E_D	drop disintegration energy
E_{EL}	elastic strain energy density
E_H	hydrodemolition efficiency

E_J	kinetic energy water jet
E_M	Young's modulus material
E_P	Young's modulus particle
E_S	kinetic energy abrasive particle
E_{SP}	specific energy
E_T	threshold energy
E_V	volumetric efficiency
F_C	contact force
f_d	frequency pulsating liquid jet
F_F	frictional force
f_N	nozzle oscillation frequenvy
F_P	plunger rod force
F_R	reaction force
g	acceleration due to gravity
G_{Ic}	critical crack extension force
G_F	fracture energy
H	geodetic height
h_L	erosion depth
h_M	depth of cut
H_M	micro hardness
h_P	water penetration depth
H_S	stroke
h_T	critical depth of cut
$\dot{I}_j$	jet impulse flow
k	internal roughness
K^*	pressure distribution parameter
K_{Ic}	fracture toughness
k_P	permeability
l_C	crack length
L_C	characteristic length
l_F	focus length
l_H	hose length
L_R	radial crack length
m	fracture toughness power exponent
$\dot{m}_A$	abrasive mass flow rate
m_M	mass loss
$\dot{m}_w$	water mass flow rate
n	velocity power exponent
n_C	crank-shaft speed
N_D	drop number
N_M	machinability number
N_P	plunger number
N_R	number of radial cracks
n_S	erosion/cutting steps
N_S	particle number
Oh	Ohnesorge number

p	pressure
p_A	atmospheric pressure
P_D	power density water jet
P_H	hydraulic power
p_J	cavitation pressure
P_J	jet power
P_M	porosity
p_O	optimum pressure
pR	pressure at crack tip
Pr	pore perimeter
p_S	stagnation pressure
P_T	theoretical hydraulic power
p_T	threshold pressure
p_V	pressure loss
$\dot{Q}_A$	actual volumetric flow rate
$\dot{Q}_L$	loss in volumetric flow rate
$\dot{Q}_N$	nominal volumetric flow rate
$\dot{Q}_P$	theoretical volumetric flow rate
Q_S	penetrating water volume
Q_W	water volume
$\dot{Q}_W$	volumetric flow rate water
r_C	transition radius
Re	Reynolds number
R_E	specific erodability
R_M	mixing ratio
R_O	bubble radius
R_P	pressure ratio
r_T	radial distance nozzle - rotational centre
R_t	roughness depth
S_d	Strouhal number
s_M	sound impedance
S_{VJ}	water jet velocity standard deviation
t_B	working time
t_E	exposure time
t_O	optimum exposure time
t_P	impact duration
T_U	turbulence
V	sand section test parameter
v_O	theoretical jet velocity
v_C	crank-shaft circumferential velocity
v_D	drop velocity
v_E	velocity of entrained water
v_F	flow velocity
V_G	material grain volume
v_H	threshold velocity for crack formation

v_J	jet velocity
$\overline{v}_J$	average water jet velocity
V_M	volume removal
$\dot{V}_M$	volumetric removal rate
v_N	nozzle (orifice) flow velocity
v_P	average plunger speed
v_{PL}	velocity for plastic flow
v_R	elastic threshold velocity
v_S	abrasive particle velocity
v_t	threshold velocity
v_T	traverse rate
w	crack opening displacement
W	water consumption
We	Weber number
W_M	removal width
x	jet length; stand-off distance
x_C	water jet core length
x_L	critical jet length
x_{TR}	water jet transition zone length
y	traverse increment
y_O	optimum traverse increment
Δp	hose pressure loss
ΔP	power loss
α	nozzle (orifice) flow parameter
α_A	abrasive mixing efficiency parameter
α_C	crank-shaft angle
α_G	gas content
α_L	fracture geometry parameter
α_S	dowel parameter
χ	cutting pass parameter
χ_R	reinforcement cutting parameter
ε	efficiency parameter
ϕ	impact angle
Φ	R-curve parameter
γ	jetting tool angle
γ_M	specific surface energy
η_O	pump efficiency
η_C	elastic parameter (compressibility)
η_F	kinematic viscosity water
η_G	volumetric rating parameter
η_h	hydraulic efficiency
η_M	mechanical efficiency
η_T	transmission efficiency
η_V	volumetric efficiency
κ_S	friction parameter

μ	nozzle (orifice) efficiency parameter
ν_F	dynamic viscosity water
ν_M	Poisson's ratio target material
ν_P	Poisson's ratio particle
θ_R	nozzle (orifice) angle
ρ_L	density air
ρ_M	density target
ρ_S	density particle
ρ_W	density liquid
σ_C	compressive strength
σ_D	impact stress (water hammer pressure)
σ_f	flow stress
σ_F	surface tension water
σ_T	tensile strength
σ_Y	yield stress
τ_S	shear stress
ω^*	water penetration parameter
ω_T	rotational speed
ξ_C	compressibility parameter
ξ_F	hose friction number
ξ_L	volume loss parameter

CHAPTER 1

Introduction

1.1 Introductory remarks

The formation and utilisation of water jets are not human discoveries. As with many other engineering discoveries, the principle was already known and utilised in nature. A process that is comparable with water jetting is the "spitting" of some fish species, namely Colisa chuna, Colisa lalia, and Toxotes jaculatrix. The latter species uses some type of discontinuous water jets for spitting for feeding. The other species show spit behaviour in case of nest building, fry tending, and owing to excitement. An example is shown in Fig. 1.1a. Detailed investigations are provided by Lüling (1958, 1969) and Vierke (1973). Another example of how water jets are utilised in nature is provided by the snapping shrimp. Snapping shrimps produce a fast, well focused water jet by rapid closure of their specialised snapper claw (Versluis et al., 2000). One of the effects of the snapping is to stun or kill pray animals. Main water jet velocity was measured to be 6.5 m/s (Herberholz and Schmitz, 1999). Illustrative images from a high-speed video are shown in Fig. 1.1b.

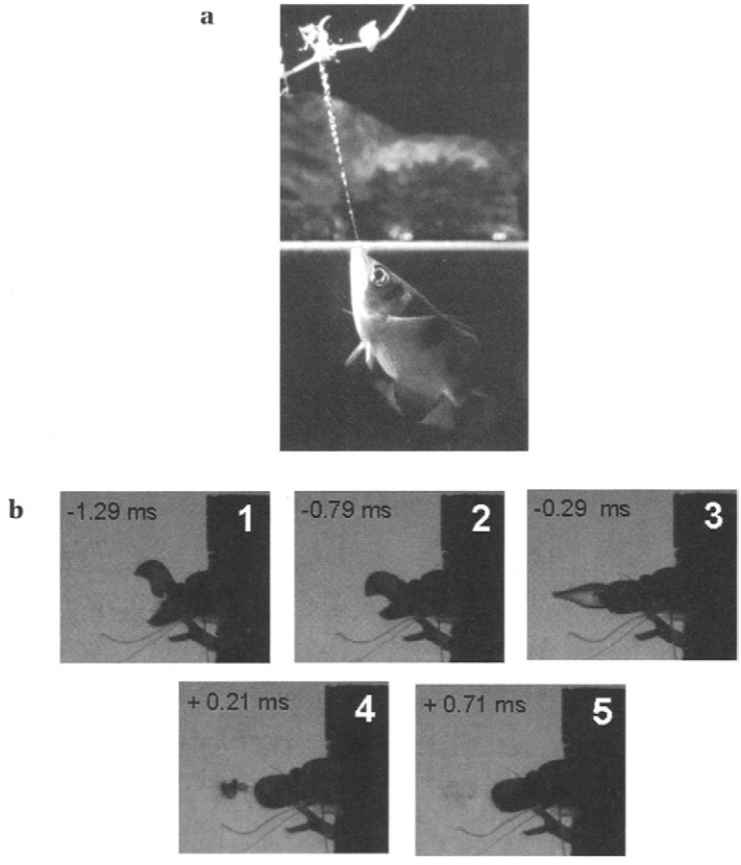

Figure 1.1 Water jet utilisation in nature
(a) Toxotes jaculatrix providing a train of water slugs (photograph: David Stone)
(b) Snapping shrimp producing a high-speed water jet (photographs: Faculty of Appl. Physics, University of Twente)

The purposeful use of waterjets is as old as human engineering. Reviews about early cases of water jet utilisation for material removal, namely for soil removal and hydraulic mining, are provided by Jeremic (1981), Summers (1995) and Wilson (1912). Figure 1.2 shows a so-called hydromonitor as used in the 19th century on mineral mining sites in the USA. In the 1920s, water jet were introduced into the steel producing industry for descaling, and into the foundry industry for cleaning castings. In those times the first systematic investigations into water jet formation and material removal optimisation were performed especially in Germany (see Rodehüser, 1930).

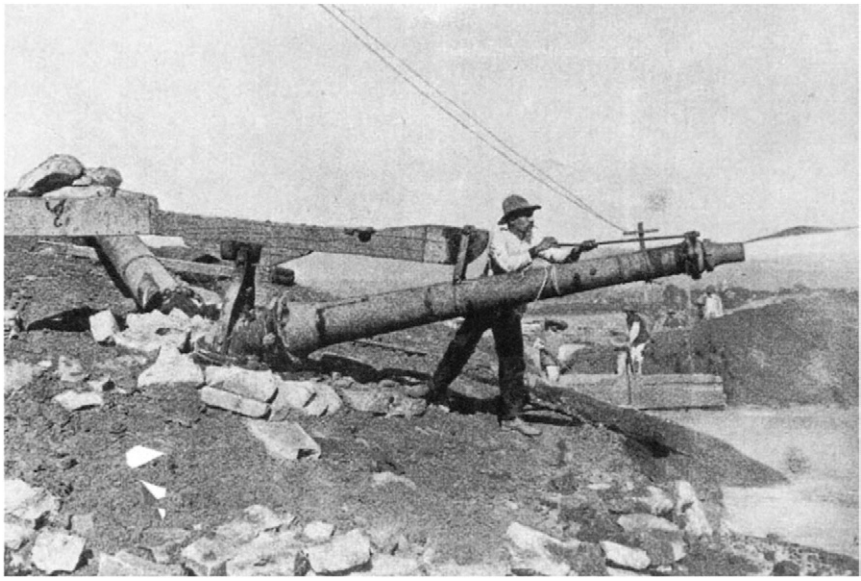

Figure 1.2 Early hydromonitor used for the removal of soil and rock debris from mineral mining sites (photograph: HAB Weimar)

The first serious approach to use water jets for concrete hydrodemolition was probably that of McCurrich and Browne (1972). They found that water jet cutting of concrete featured poor energy utilisation; estimated values varied between 400 and 4,000 GJ/m^3. The pump pressure applied for this study was 70 MPa. The most interesting results of the study were, from the point of view of engineering history, the following:

(i) "The aggregate was impossible to cut at (an operating pressure of) 70 MN/m^2.";

(ii) "A practicable site cutting tool will require pressures of at least 380 MN/m^2."

Today is known that both statements were wrong. The research community at that time did not know enough about material removal modes and the effects of

process parameters. However, the results were that discouraging that it took 10 more years till an industrial institution finally developed and introduced the first commercial hydrodemolition unit. Modern hydrodemolition systems work at operating pressures of about 100 MPa, thus, only about 30% of the threshold suggested by McCurrich and Browne (1972). Since that, the technology was rapidly growing. Already in the 1980s, about 10% of all contractors involved in concrete rehabilitation in Austria, used water jets (Kloner, 1987). At present, this tool is widely used for cleaning, profiling, removal, drilling and demolition of concrete substrates and reinforced concrete structures (Momber, 1998a). Hydrodemolition is state-of-the-art in concrete technology and structural rehabilitation. Major fields of application include the following:

- bridge and parking deck repair;
- construction joint cleaning;
- decommissioning;
- decontamination;
- road maintenance;
- tunnel rehabilitation.

The automatic, remotely controlled hydrodemolition robot shown in Fig. 1.3 probably best illustrates the high standard of the technique.

Figure 1.3 Modern hydrodemolition robot (photograph: Aquajet A.B., Holsbybrunn)

1.2 Industrial applications

1.2.1 Civil and construction engineering

Water jet technology is a state-of-the-art technology not only in the area of surface engineering. It is one of the most flexible techniques available in industrial maintenance. In the industry, water jet technology is frequently used in the following areas:

- building sanitation and rehabilitation;
- concrete removal and cleaning = HYDRODEMOLITION;
- decontamination and demilitarisation;
- demolition of technical structures;
- foundation engineering;
- industrial cleaning;
- jet cutting of ceramics, fibre-reinforced plastics, food, glasses, metals and rocks;
- maintenance of technical structures and equipment;
- mechanical processing of minerals;
- medical applications;
- mining and rock cutting;
- paint and lacquer stripping;
- rock fragmentation;
- sewer channel and pipe cleaning;
- surface preparation for protective coatings.

Several of these applications as well as the corresponding major operational parameters are summarised in Fig. 1.4.

Water jetting is state-of-the-art in civil engineering. A recent review, including an extensive database, is given by Momber (1998a). Several aspects of civil engineering use are also mentioned by Summers (1995). The applications include the following:

- cleaning of concrete joints prior to concreting (Utsumi et al., 1999);
- cleaning of concrete, stone, masonry and brick surfaces (Lee et al., 1999);
- cleaning of soils (Sondermann, 1998);
- cutting of soil (Atmatzidis and Ferrin, 1983);
- cutting and drilling of natural rocks in quarries (Ciccu and Bortolussi, 1998);
- decontamination of industrial floors;
- jet cutting of construction materials, such as tiles, natural rocks and glass (Momber and Kovacevic, 1998);
- preparation of soil samples (Hennies et al., 2002);
- removal of asphalt and bitumen from traffic constructions (Momber, 1993);
- removal of rubber deposits from airport runways (Choo and Teck, 1990a,b);
- removal of traffic marks from roadways;
- selective concrete removal by hydrodemolition (Hilmersson 1998; Momber, 1998b; Momber, 2003b; Momber et al., 1995);

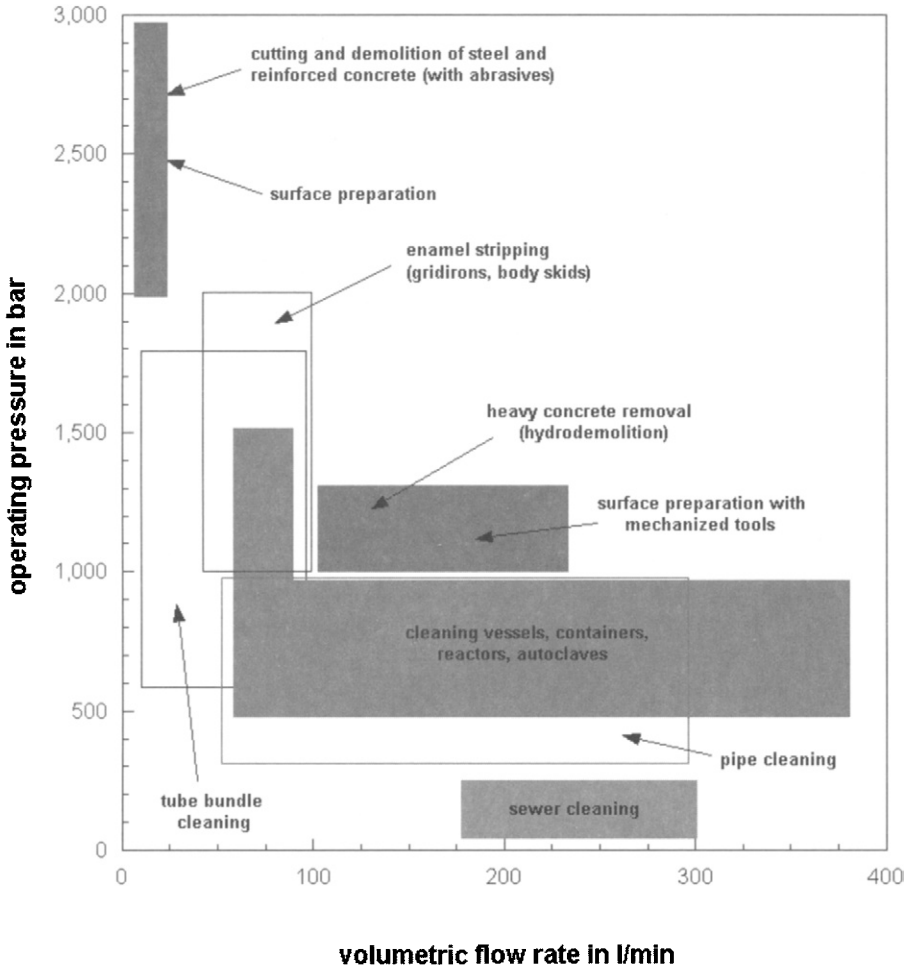

Figure 1.4 Industrial applications of high-speed water jets

- soil stabilisation and improvement by Jet Grouting (Yonekura et al., 1996; Gross and Wiesinger, 1998);
- vibration-free demolition with abrasive water jets (Momber, 1998a; Momber et al., 2002c);
- water jet assisted cable plowing (Reichman et al., 1983);
- water jet assisted gravel winning (Rockwell, 1981);
- water jet assisted pile driving (Horigushi and Kajihara, 1988).

Several of these applications are illustrated in Fig. 1.5.

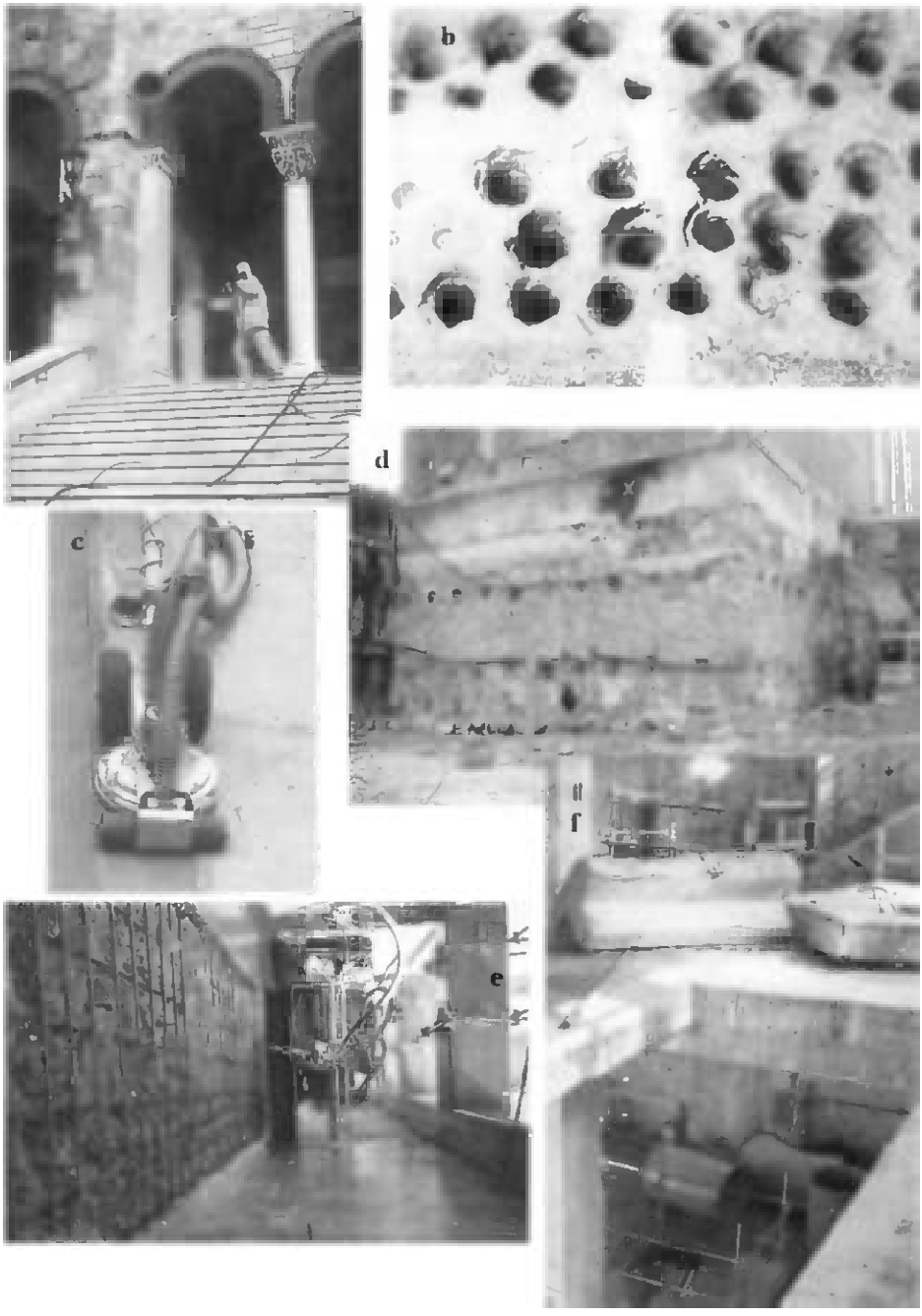

Figure 1.5 Civil and construction engineering applications of water jets
(a) surface cleaning (WOMA GmbH, Duisburg); (b) rock drilling (BMGR, RWTH Aachen, Aachen); (c) floor decontamination (Hammelmann GmbH, Oelde); (d) soil stabilisazion (Keller Grundbau GmbH, Fallingbostel); (e) hydrodemolition (Aquajet Systems AB, Holsbybrunn); (f) building demolition (WOMA GmbH, Duisburg)

1.2.2 Industrial cleaning

Industrial cleaning is the classical industrial application of the water jet technology. It reaches back as far as in the 1920's where it was used for cleaning of moulds and castings (Rodehüser, 1930). Later, in the late 1950s, as reliable high-pressure pumps have been developed, the water jet revolutionised the areas of sewer and pipe cleaning. Today, commercialised water jetting covers the following cleaning applications:

- aircraft cleaning in the aviation industry: removal of paint, grease, dirt (Hofacker, 1993);
- cement kiln and autoclave vessel cleaning in the construction materials industry: removal of cement lips, incrustations, lime, solidified dust (Wood, 1996);
- gridiron and body skid cleaning in the automotive industry: removal of non-hardened, sprayed lacquer (Halbartschlager, 1985);
- pipe cleaning in the municipal and chemical industry: removal of worn protective coatings, incrustations, solidified materials, etc. (Momber, 1997; Momber and Nielsen, 1998);
- reactor, vessel, and container cleaning in the chemistry and oil industry: removal of production leftovers, especially resins, latex, adhesives, oils or plastics (Geskin, 1998);
- roller drum cleaning in the printing industry: removal of ink;
- semiconductor frame cleaning in the electronic industry: removal of excess resin (Yasui et al., 1993);
- sewer cleaning in the municipal industry: removal of deposits (Lenz and Wielenberg, 1998);
- ship cleaning in the maritime industry: removal of marine growth, loosen paint, dirt and rust (Momber, 2003c);
- sieve and filter cleaning in the process engineering industry: removal of production leftovers, especially solidified agglomerates (Jung and Drucks, 1996);
- steel cleaning in steel mills: removal of weld slag, water scale, mill scale and rust (Raudensky et al., 1999);
- tube bundle cleaning in the process engineering and oil industry: removal of incrustations and residues, especially calcium carbonate, from internal and external tube surfaces (Momber, 2000c).

Some of these applications are shown in Fig. 1.6.

1.2.3 Environmental engineering and other applications

The introduction of the water jet technology into environmental engineering is one of the most recent developments in that technique. Water jets, due to their capability to selectively remove materials, and due to their heat-free performance, are ideally suited for separation processes. A review about typical applications is given

Figure 1.6 Industrial cleaning applications of water jets
(a) aircraft cleaning (WOMA GmbH, Duisburg); (b) cement kiln cleaning (WOMA GmbH, Duisburg); (c) pipe cleaning (WOMA GmbH, Duisburg); (d) sewer cleaning (WOMA GmbH, Duisburg); (e) tube bundle cleaning (WOMA GmbH, Duisburg); (f) coating removal with UHPAB for steel surface protection (Mühlhan Equipment Services GmbH, Hamburg)

by Momber (1995a). More recent developments are summarised in Momber's (2000b) book. The technique is, among others, used to solve the following problems:

- aggregate liberation from cement-based composites (Isobe, 2003; Momber, 2004d);
- comminution of concrete (Momber, 2005);
- decoating of compact discs (Witzel, 1998);
- decontamination and decommissioning of nuclear power equipment (Bond and Makai, 1996; Lelaidier and Spitz, 1978);
- decontamination of soils (Sondermann, 1998; Heimhardt, 1998);
- demolition of mercury-contaminated constructions;
- dismantling of nuclear power plants (Alba et al., 1999);
- encapsulation of contaminated ground and hazardous waste sites (Carter, 1998);
- exposure of land mines (Denier et al., 1998);
- preparation of secondary fiber stock (Galecki et al., 1991);
- removal of explosives from shells (Fossey et al., 1997);
- removal of propellants from rocket motors (Foldyna, 1998);
- removal of PCB-contaminants (Crine, 1988);
- repair of oil wells (Flak, 1992);
- selective carpet recycling (Momber et al., 2000; Weiß and Momber, 1998; Weiß et al., 2003, 2004);
- selective separation of automotive interior compounds (Weiß and Momber, 2003).

Some of these applications are shown in Fig. 1.7.

Other industrial applications being either under practical consideration or in the laboratory stage only include the following:

- processing (cutting) of meet (Alitavoli and McGeough, 1998);
- various medical applications (Siegert et al., 2000);
- spunlancing of non-wovens (Watzl, 2001).

1.3 Subdivision of water jets

1.3.1 Definitions and pressure ranges

A subdivision of different types of liquid jets is provided in Table 1.1. The tool of any hydrodemolition process is a high-speed water jet. Although the speed of the jet is its fundamental physical property, the pressure generated by the pump unit that produces the jet is the most important evaluation parameter in practice. Fundamentals of jet generation are provided in Chapter 3.

According to the Water Jet Technology Association, St. Louis, water jet applications can be distinguished according to the level of the applied operational pressure (WJTA, 1994) as follows:

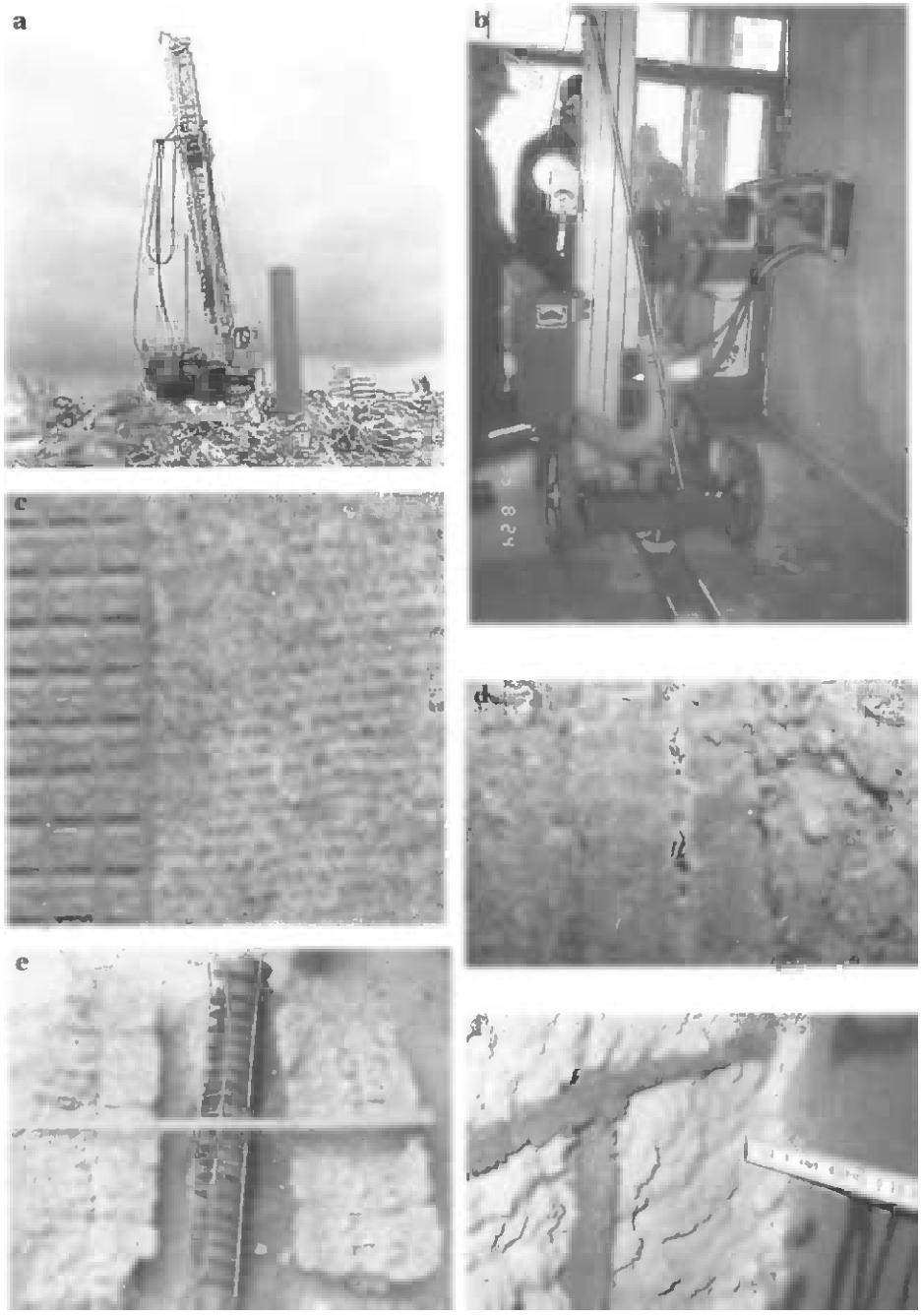

Figure 1.7 Environmental applications of water jets
(a) soil decontamination (Keller Grundbau GmbH); (b) removal of PCB-contaminated plaster (DSW GmbH, Duisburg); (c) carpet separation (Weiß et al., 2003); (d) textile compound separation (Weiß and Momber, 2003); (e) recycling of used oxygen lances (WOMA GmbH, Duisburg); (f) "soft" selective demolition of buildings (Andrea and Partner, Stuttgart)

Table 1.1 Subdivision of liquid jets

Liquid jet		
Pressure range	Loading dynamics	Fluid medium
High pressure	Continuous liquid jets	Plain liquid jets
Ultra-high pressure	Discontinuous liquid jets	Liquid jets with abrasives (not dissolving)
		Liquid jets with additives (dissolving)

- *Pressure* cleaning:
  The use of pressurised water, with or without the addition of other liquids or solid particles, to remove unwanted matter from various surfaces, and where the pump pressure is below 340 bar (34 MPa).
- *High-pressure* water cleaning:
  The use of high-pressure water, with or without the addition of other liquids or solid particles, to remove unwanted matter from various surfaces, and where the pump pressure is between 340 bar (34 MPa) and 2,000 bar (200 MPa).
- *Ultra high-pressure* water cleaning:
  The use of pressurised water, with or without the addition of other liquids or solid particles, to remove unwanted matter from various surfaces, and where the pump pressure exceeds 2,000 bar (200 MPa).

From these definitions, three different modes of hydrodemolition can be distinguished:

- mode (i): heavy mechanised hydrodemolition (see Fig. 1.8a) at the *high-pressure* level;
- mode (ii): surface preparation with hand held tools (see Fig. 1.8b) at the *ultra high-pressure* level;
- mode (iii): abrasive waterjet cutting (see Fig. 1.8c) at the *ultra high-pressure* level.

Applications of these hydrodemolition modes are discussed in Chapters 4 to 6.

1.3.2 Fluid medium and loading regime

According to the fluid medium, there can generally be distinguished between the following modifications:

- plain water jets;
- additive water jets: water jets with soluble additives (Howells, 1998);
- abrasive water jets: water jets with non-soluble additives (Momber and Kovacevic, 1998).

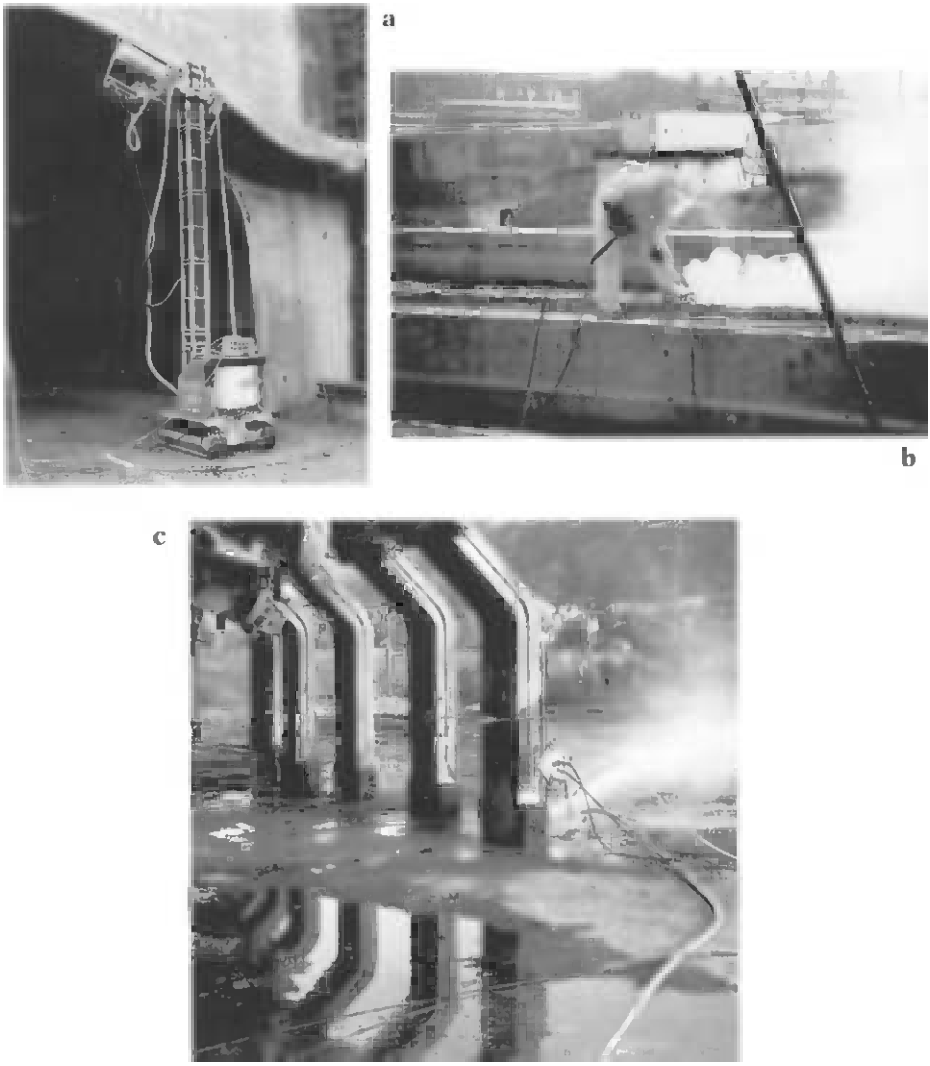

Figure 1.8 Hydrodemolition modes
(a) Heavy hydrodemolition application (photograph: Aquajet Systems AB, Holsbybrunn); (b) Hand-held tool application (photograph: WOMA Aparatebau GmbH, Duisburg); (c) Abrasive water jet application (photograph: WOMA Aparatebau GmbH, Duisburg)

Other liquid media than water were used frequently in the laboratory stage, but could not find their way into site practice. These liquids include, among others, the following:

- liquid metals (Oshina and Yamane, 1988);
- liquefied carbon dioxide (Dunsky and Hashish, 1995; Kolle and Marvin, 2000);

- liquefied nitrogen (Dunsky and Hashish, 1995);
- liquefied ammonia (Hashish and Miller, 2000).

Abrasive water jets divide further according to their generation and phase composition into the following types:

- injection-abrasive water jets;
- suspension-abrasive water jets.

An injection-abrasive water jet consists of water, air, and abrasives, and is considered to be a three-phase jet. In contrast, a suspension-abrasive water jet does not contain air and, therefore, is a two-phase jet. Formation, behaviour and applications of abrasive water jets are in detail discussed by Momber and Kovacevic (1998) and Summers (1995).

Regarding the loading regime, there can be generally distinguished between the two following types:

- continuous jets;
- discontinuous jets (Vijay, 1998a).

Wiedemeier (1981) defined a jet as discontinuous, if it generates a discontinuous load at the impact site. But as Momber (1993) pointed out, every water jet internally contains discontinuous phases resulting from pressure fluctuations, jet vibrations and droplet formation. He suggested that 'discontinuous jets' are formed artificially by external mechanisms, whereas 'continuous jets' are not influenced by external mechanisms. Reviews about the formation, properties, and applications of discontinuous water jets were given by Labus (1991), Momber (1993), and Vijay (1998a).

1.4 Failure behaviour of cementitious materials

1.4.1 Structure and properties of cementitious materials

Concrete can be modelled to consist of cement paste, pore water and inserts. The inserts may include aggregate particles or fillers, and reinforcements. Interfaces between these phases largely affect mechanical properties and the behaviour of concrete under load. Generally, the interface between cement and aggregate is the weak link in concrete. As will be shown in Section 2, these interfaces significantly determine the material response to water jet impingement. Therefore, they are of particular interest. Figure 1.9 is a schematic drawing of the structure of a matrix-aggregate interface. Properties of a typical matrix-aggregate interface are illustrated in Fig. 1.10. Porosity at the interface is relatively high and decreases toward the bulk paste; this is shown in Fig. 1.10a. Attempts have been made to characterise the mechanical properties of the interface. Microhardness tests around interfaces, using the Vickers indentation technique, showed that the

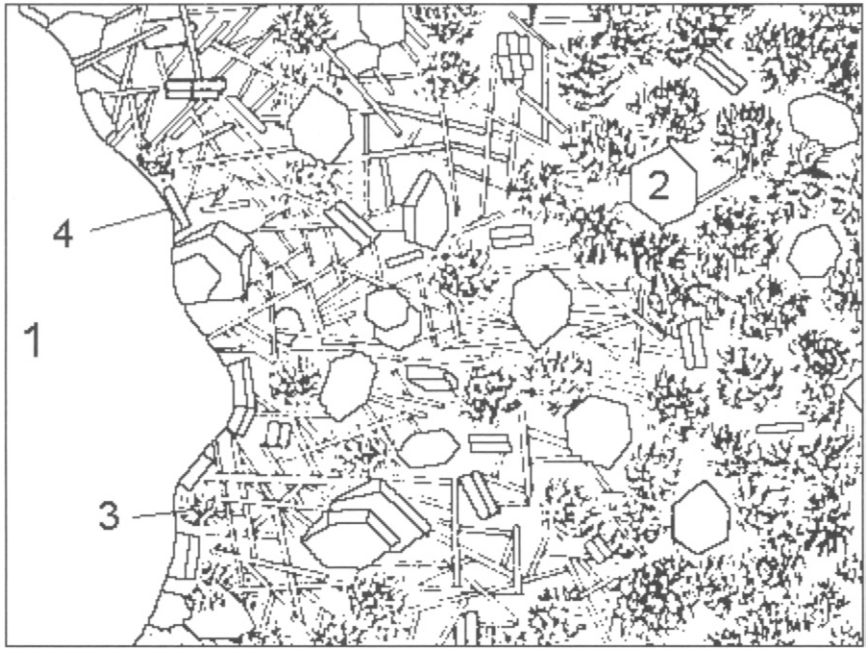

Figure 1.9 Schematic representation of matrix-aggregate interface in concrete (Mehta, 1986)
1 – aggregate, 2 – $Ca(OH)_2$, 3 – C-S-H, 4 – ettringite

hardness of the interfacial zone was lower than that of the bulk matrix; see Fig. 1.10b for an example. These results are of special importance because wear and erosion processes are particularly sensitive to material hardness. More information about paste-aggregate interfaces in cementitious composites are provided by Aquino et al. (1995), Larbi (1993) and Mitsui et al. (1994). Mechanical and fracture parameters of concrete vary for the individual structural components. Typical values for cement pastes, aggregates and interfaces are listed in Tables 1.2 and 1.3. Values for interfaces are low compared to values for bulk cement pastes, and this is one reason that failure in concrete usually occurs in these interfacial zones.

Concrete is a porous and permeable material. The following types of pores can be distinguished:

- closed pores;
- open pores;
- bottleneck pores.

Figure 1.11 shows a typical closed pore in a mortar; this originally closed pore was formed during the concrete casting process, and was then opened during water jet erosion. Hardened cement paste contains mainly gel pores and capillary pores. Their dimensions are listed in Table 1.4. Capillary pores are shown in Fig. 1.12.

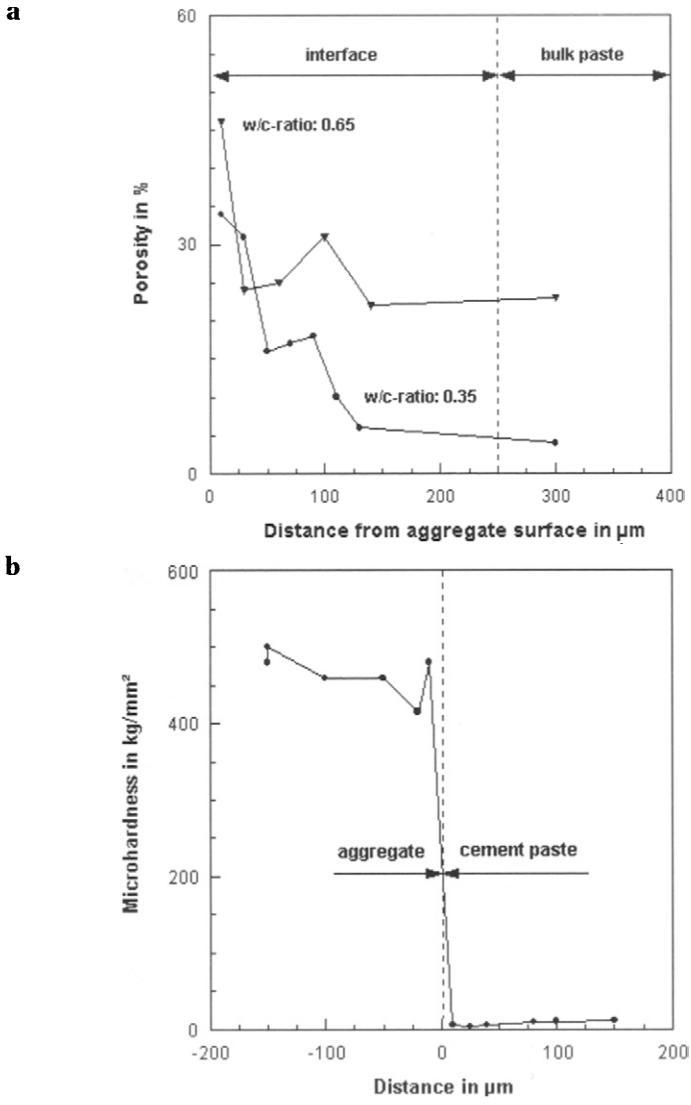

Figure 1.10 Effect of distance from aggregate on paste properties
(a) Porosity as function of distance from interface (Mitsui et al., 1994)
(b) Hardness as function of distance from interface (Lyubimova and Pinus, 1968)

Pores and pore distributions are much often assessed through the mercury intrusion method. A typical pore distribution diagram, based on such a measurement, is plotted Fig. 1.13. The peak appearing at about 50 nm is characteristic for the capillary pore system. Porosity depends largely on the water-cement ratio of the concrete mix, which is illustrated in Fig. 1.14. Permeability is another important physical property because it affects the flow conditions in the structure if entered by a liquid. Permeability is measured by different methods which deliver different physical units;

Table 1.2 Energy values for concrete compounds (Hilsdorf and Ziegeldorf, 1981; Tschegg et al., 1995)

Material	Surface energy in J/m²	Fracture energy in N/m
Interface cement paste – limestone	0.6	6
Interface cement paste – quartz	0.8	–
Cement mortar	21–24	
Cement paste	7	80

Table 1.3 Hardness values of some concrete structural materials

Material	Vickers-hardness in MPa	Reference
Cement paste (W/C=0.4)	370–420	Glinicki and Zielinski (2004)
Cement paste (W/C=0.5)	250	Glinicki and Zielinski (2004)
Calcit	1,200	Grabko et al. (2002)
Feldspar	8,700–9,000	Grabko et al. (2002)
Quartz	11,000	Grabko et al. (2002)

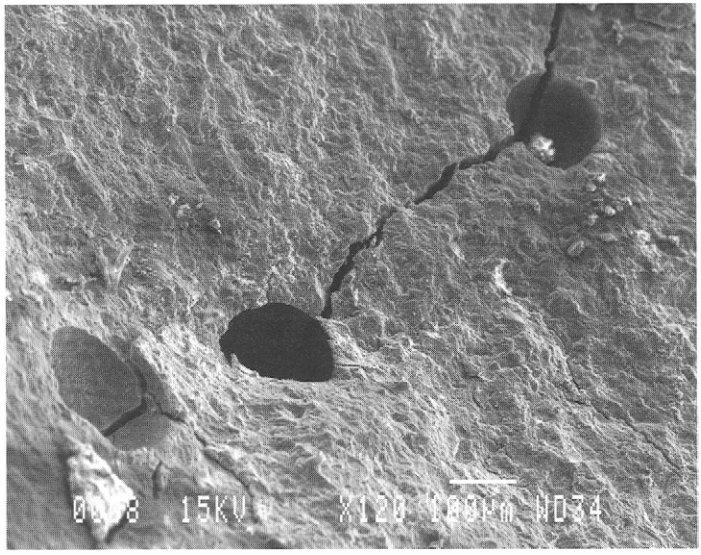

Figure 1.11 Air pore in hardened cement paste, opened after water jet erosion (photograph: author)

Table 1.4 Pore and crack dimensions in cement paste (Schneider and Herbst, 1989)

Pore/crack class	Radius in nm
Gel pores	< 10
Capillary pores	10–100
Microcracks	100–1,000
Cracks	> 1,000

Figure 1.12 Capillary pores in hardened cement paste (photograph: author)

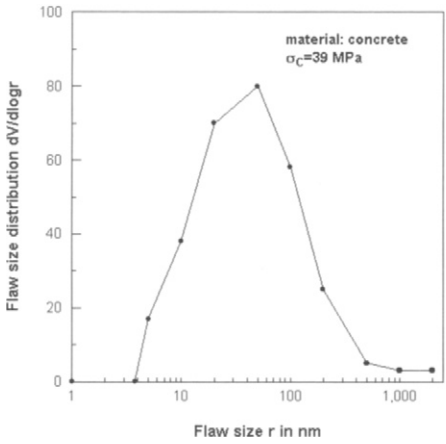

Figure 1.13 Pore distribution in concrete (Momber and Kovacevic, 1994); results from mercury intrusion measurements

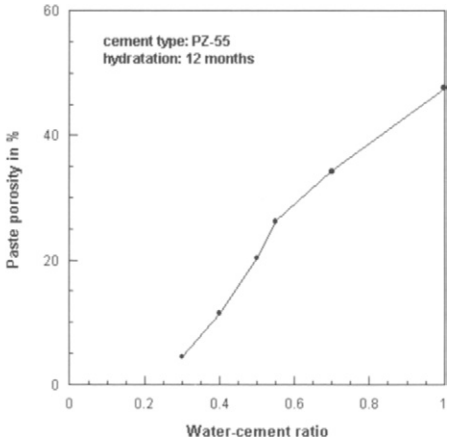

Figure 1.14 Effect of water-cement ratio on porosity of concrete (Odler and Köster, 1983)

e.g. [m/s] and [m^2]. Some typical values are listed in Table 1.5. Structural properties of concrete are different for the core region and the near-surface region. This is shown in Fig. 1.15 – permeability increases in the near-surface region. The same trend applies to porosity (Wilson, 2002). This aspect is of decisive importance because hydrodemolition is essentially a surface preparation method.

Table 1.5 Permeability values for cementitious composites

Material	Permeability in m/s	Reference
Concrete (σ_c=100,3 MPa)	$0.02 \cdot 10^{-11}$	Bamforth (1991)
Concrete (σ_c=39,4 MPa, fly ash)	$12.68 \cdot 10^{-11}$	Bamforth (1991)
Concrete (σ_c=51,5 MPa)	$9.87 \cdot 10^{-11}$	Bamforth (1991)
Concrete (σ_c=60,6 MPa)	$1.91 \cdot 10^{-11}$	Bamforth (1991)
Cement paste (W/C =0.3)	$3.56 \cdot 10^{-15}$	Odler und Köster (1983)
Cement paste (W/C =0.4)	$3.60 \cdot 10^{-14}$	Odler und Köster (1983)
Cement paste (W/C =0.5)	$7.64 \cdot 10^{-13}$	Odler und Köster (1983)
Cement paste (W/C =0.6)	$2.30 \cdot 10^{-12}$	Mehta und Manmohan (1980)
Cement paste (W/C =0.7)	$2.58 \cdot 10^{-11}$	Odler und Köster (1983)

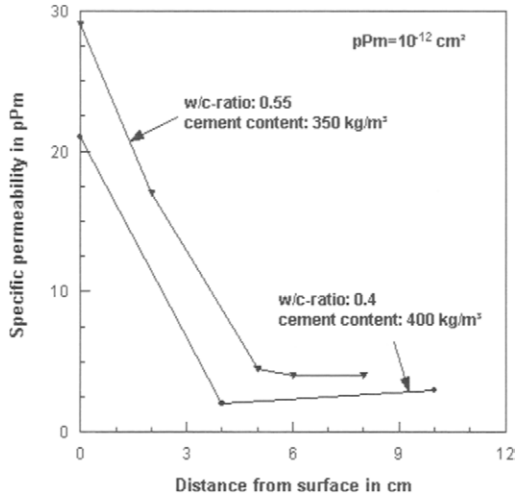

Figure 1.15 Effect of distance from concrete surface on permeability in concrete (Calogovic and Bjegovic, 1996)

1.4.2 Fracture behaviour of cementitious materials

Cementitious composites are characterised by a fracture process zone. The fracture process zone is a zone characterised by progressive softening, for which the stress decreases at increasing deformation. It is surrounded by a non-softening zone. Together, these two zones form a non-linear zone. Depending on the relative size of these zones and of the structure, three basic types of fracture can be distinguished as illustrated in Fig. 1.16. In the first fracture type, the non-linear zone is small compared to the structural size, and the entire fracture process takes place almost at the crack tip. This type of fracture approximates materials that usually are called *brittle,* like glass, brittle ceramics, and hardened cement paste. In the second fracture type, most of the non-linear zone consists of elasto-plastic hardening, or yielding. The actual softening zone (process zone) is comparatively small compared

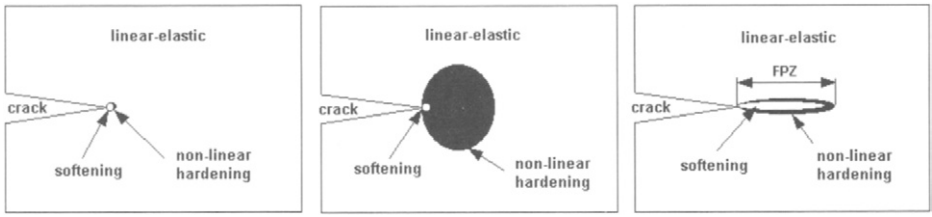

Figure 1.16 Basic types of fracture (Bazant and Planas, 1998)

with the zones occupied by hardening or yielding. Materials that are usually called *ductile*, such as many metals, fall into this category. The third fracture type – considered in this book – is characterised by a comparatively large fracture process zone, or softening. A typical fracture process zone for a brittle, tension-softening material is illustrated in Fig. 1.17. Reasons for the establishment of a fracture process zone may be microcrack shielding, inclusion bridging, crack rim friction, transgranular fracture, crack branching, etc. (Shah and Ouyang, 1993). Basic mechanisms are illustrated in Fig. 1.18. In contrast to the so-called ductile fracture, hardening or yielding can usually be neglected. This type of fracture, called *quasi-brittle*, covers materials such as concrete, mortar, rocks, fibre-reinforced composites, or refractory ceramics. For more brittle-behaving materials, such as cement paste, the fracture process zone is short. This is illustrated by the values listed in Table 1.6. The major mechanisms responsible for the formation of a fracture process zone are

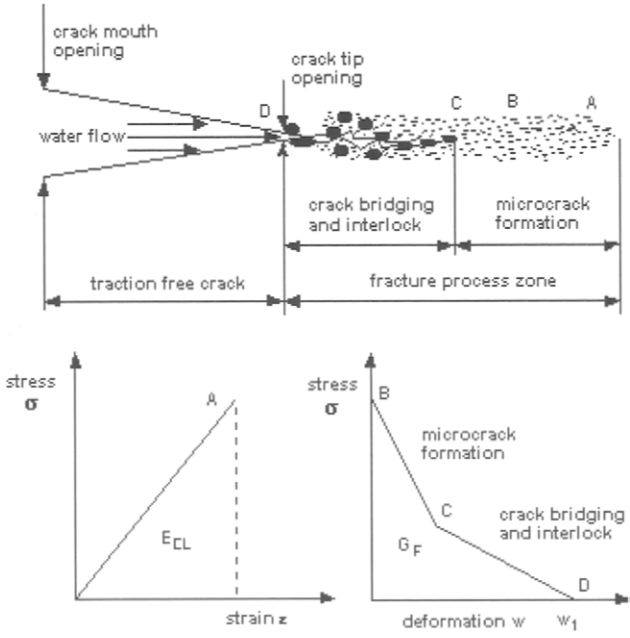

Figure 1.17 Fracture process zone for a brittle, tension-softening material

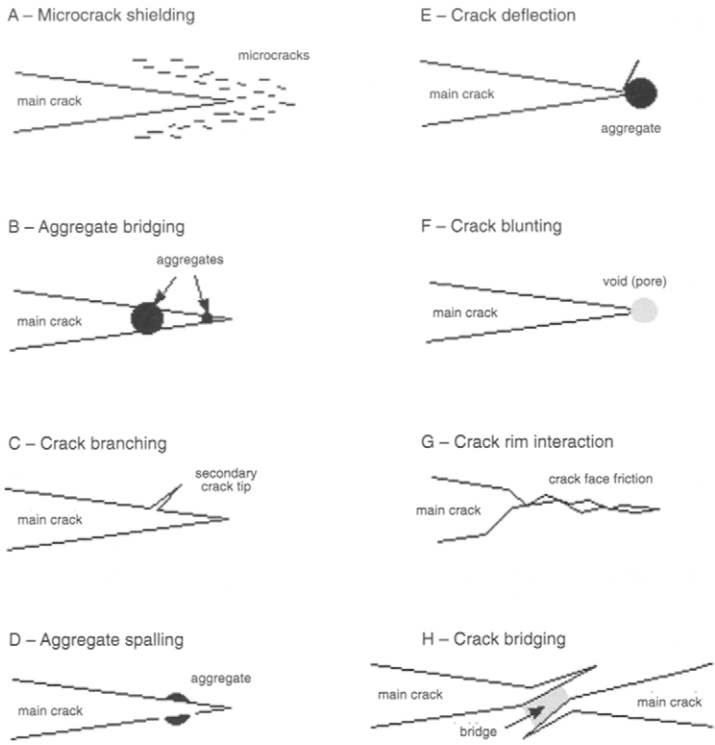

Figure 1.18 Basic energy dissipative processes in the fracture process zone

Table 1.6 Quasi-brittle fracture properties of cementitious materials

Material	Characteristic length in mm	Brittleness in mm^{-1}	Fracture energy in J/m^2	Reference
Asphalt concrete	113–1,290	0.004–0.0004	744–1,158	Tschegg et al. (1995)
Mass concrete	1,413	0.00035	201	Brühwiler and Saouma (1995)
Micro-concrete	531	0.0009	108	Bache (1989)
Cement paste	10	0.05	20	Bache (1989)
Mortar + steel fibres	600	0.0008	16,000	Bache (1989)
Concrete (normal)	200	0.0025	–	Bache (1989)

grain bridging and crack-rim friction behind the actual crack tip, and microcracking in front of the crack tip. This is illustrated in Fig. 1.17. Another parameter that judges fracture behaviour is the characteristic length which is linearly related to the fracture process zone and which can be measured by special arrangements. Values for the characteristic lengths of relevant materials are listed in Table 1.6. Characteristic

length is small for rather brittle-responding materials, such as hardened cement paste, and long for reinforced materials. Certain approaches for modelling the non-linear behaviour of brittle materials are known, namely the fictitious crack model, the crack-band model, the two-parameter model, and the size-effect model. Detailed information about these models is provided by Karihaloo (1995). The characteristic length can be estimated (Hillerborg et al. 1976):

$$L_C = \frac{E_M \cdot G_F}{\sigma_T^2} \tag{1.1}$$

Here, E_M is Young's modulus, G_F is the fracture energy, and σ_T is the tensile strength. Physically, the characteristic length can be interpreted as the brittleness of a material. The standard equation for the elastic strain energy absorbed during the tensile test is (see Fig. 1.17):

$$E_{EL} = \frac{\sigma_T^2}{2 \cdot E_M} \tag{1.2}$$

If the elastic strain energy is related to the energy absorbed in the fracture process zone, the following relationship for the brittleness results from Eqs. (1.1) and (1.2):

$$\frac{E_{EL}}{G_F} = B_M = \frac{1}{2 \cdot L_C} \tag{1.3}$$

For materials with a very high amount of elastically absorbed energy: $E_{EL} \rightarrow \infty$, $B_M \rightarrow \infty$. In contrast, for materials with a very high amount of tension softening: $G_F \rightarrow \infty$, $B_M \rightarrow 0$. Typical brittleness-values for several brittle materials showing a tension-softening behaviour are listed in Table 1.6. Brittleness is high for brittle behaving materials, such as hardened cement paste, and low for toughened materials, such as the fibre reinforced concrete. The fracture energy, G_F, which is usually considered to be the energy absorbed in the fracture process zone during fracture is given from the load-displacement-curve shown in Fig. 1.17 (Hillerborg et al. 1976):

$$G_F = \int_0^{w_1} \sigma(w)\, dw \tag{1.4}$$

Methods how to experimentally estimate the fracture energy are recommended in RILEM (1985). An alternative method that allows the use of drilling core testing, which is important for the evaluation of concrete structures to be refurbished, is suggested by Linsbauer (1991).

CHAPTER 2

Fundamentals of Hydrodemolition

2.1 Properties and structure of high-speed water jets

2.1.1 Kinematics of high-speed water jets

Properties of water are listed in Table 2.1. Numerous properties, namely density, viscosity or compressibility depend on pressure and temperature. Other properties, such as speed of sound, are dependent of the conditions on the contact between water and solid. The acceleration of a given volume of pressurised water in a nozzle generates a high-speed water jet. For that case, Bernoulli's law delivers:

$$p_A + \frac{\rho_W}{2} \cdot v_0^2 + \rho_W \cdot g \cdot H_1 = p + \frac{\rho_W}{2} \cdot v_N^2 + \rho_W \cdot g \cdot H_2 \tag{2.1}$$

With $H_1=H_2$, $p_A<<p$, and $v_0>>v_N$, the approximate theoretical jet exit velocity is:

$$v_0 = \left(\frac{2 \cdot p}{\rho_W} \right)^{1/2} \tag{2.2}$$

Considering friction losses in the nozzle, the real water jet velocity is:

$$v_J = \left(\frac{2 \cdot (p - p_V)}{\rho_W} \right)^{1/2} = \left(\frac{2 \cdot p \cdot (1 - p_V / p)}{\rho_W} \right)^{1/2} \tag{2.3}$$

With $[1 - (p_v/p)]^{1/2} = \mu$, neglecting the compressibility of the water, and applying p in MPa, one obtains:

Table 2.1 Typical water properties (temperature: 20°C)

Property	Unit	Value
Dynamic viscosity	Pa·s	0.001
Kinematic viscosity	10^{-6} m²/s	1.004
Density	kg/m³	997.3
Speed of sound	m/s	1,460 (15°C)
Coefficient of extension	1/K	0.00018
Specific heat	cal/g·K	1.0
Melting temperature	°C	0
Specific melting heat	kcal/kg	79.7
Vaporization heat	kcal/kg	539.1
Surface tension	N/m	0,071
Prandtl-number	–	13.31
Heat conductivity	W/m·K	5.68
Vapour pressure	kPa	2.4
Temperature of ebullation	°C	99.63
Young's modulus	MPa	4,070

$$v_J = \mu \cdot \left(\frac{2 \cdot p}{\rho_W}\right)^{1/2} \approx \mu \cdot 44.71 \cdot p^{1/2} \tag{2.4}$$

Table 2.2 Values for the nozzle efficiency parameter μ

Reference	Pump pressure	μ-value
Neusen et al. (1992)	69–241 MPa	0.92
Himmelreich and Riess (1991)	100 MPa	0.92
Chen and Geskin (1991)	90–350 MPa	0.85–0.90
Neusen et al. (1994)	69–310 MPa	0.93–0.98

In that equation, v_j is in m/s. For p_V=0, μ=1: the theoretical velocity will be reached. For p_V=p, μ=0: the entire pump pressure is absorbed, which delivers v_j=0. The certain value of the parameter μ depends on nozzle design, pump pressure and nozzle diameter. Typical values for commercial sapphire nozzles are between 0.9<μ<0.95 (Momber and Kovacevic, 1998). Some results obtained from direct velocity measurements are listed in Table 2.2. The exit velocity of a water jet generated at a pressure of p=140 MPa in a typical sapphire nozzle (μ=0.95) is v_j=503 m/s. Results of Eq. (2.4) are plotted in Fig. 2.1. It is important to note that the jet velocity does not depend on nozzle diameter. As the water jet exits the nozzle, its kinetic energy is:

$$E_J = 1/2 \cdot \dot{m}_W \cdot v_J^2 \cdot t_E \tag{2.5}$$

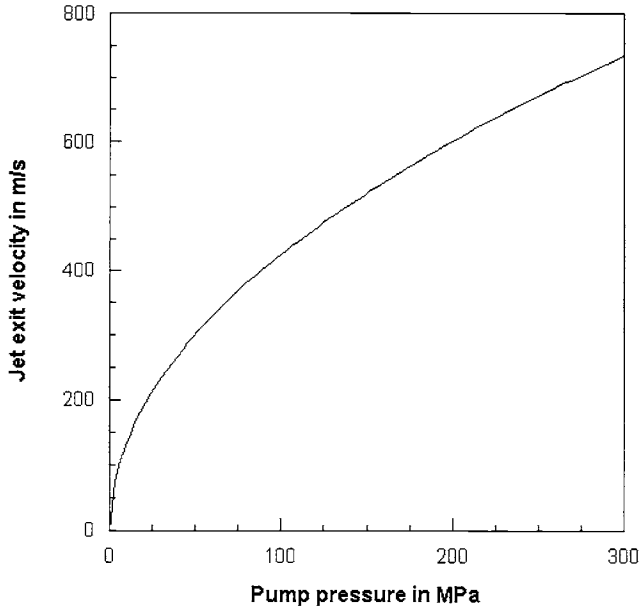

Figure 2.1 Relationship between pump pressure and water jet velocity

The actual water mass flow rate is:

$$\dot{m}_W = \dot{Q}_A \cdot \rho_W = A_N \cdot v_J \cdot \rho_W = \alpha \cdot (\pi/4) \cdot d_N^2 \cdot v_J \cdot \rho_W \qquad (2.6)$$

In that equation, α is a nozzle discharge parameter that considers the reduction in the volumetric flow rate due to the sudden changes in the fluid conditions in a nozzle with a sharp orifice. The parameter depends on nozzle geometry and nozzle diameter; some relationships are shown in Fig. 2.2. The relationship to the pump pressure is very weak and can be neglected (Wulf, 1986). For diamond orifices, values of $0.65<\alpha<0.75$ (Momber, 2001; Momber and Kovacevic, 1998) can be assumed, and for steady nozzles a value of $\alpha=0.9$ (Werner, 1991a; Wulf, 1986) can be assumed.

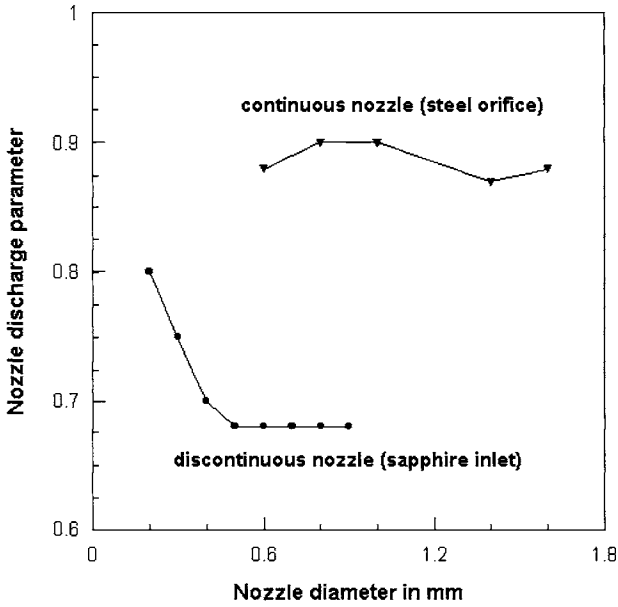

Figure 2.2 Parameter effects on nozzle discharge parameter

For a nozzle diameter of $d_N=3.0$ mm, a pump pressure of p=140 MPa and $\alpha=0.8$, Eq. (2.6) delivers a mass flow rate of =2.27 kg/s. With Eqs. (2.4), (2.6) and an exposure time of $t_E=d_N/v_T$, the kinetic jet energy is:

$$E_J = \frac{\alpha \cdot \pi \cdot \mu^3 \cdot p^{3/2} \cdot d_N^3}{2^{3/2} \cdot \rho_W^{1/2} \cdot v_T} \qquad (2.7)$$

Here, v_T is the traverse speed of the nozzle. If the nozzle is fixed at a rotating nozzle carrier (see Fig. 3.17), the traverse speed is:

$$v_T = \omega_T \cdot r_T \qquad (2.8)$$

Here, ω_T is the rotational speed, and r_T is the distance between nozzle and rotational centre. For the water jet mentioned with r_T=120 mm and ω_T=150 min^{-1} (these two values are from a hydrodemolition tool 'Orbiter', WOMA Apparatebau GmbH, Duisburg), the traverse speed is 0.3 m/s, and the exposure time is t_E=0.01 s. All these conditions are typical for a hydrodemolition application. The kinetic energy of this water jet is $E_J=2.87 \cdot 10^3$ Nm (Ws). The power density, which is the power acting over a certain time increment on a certain circular cross section, is

$$P_D = \frac{4 \cdot P_J}{\pi \cdot d_J^2} \tag{2.9}$$

Note that the power density at the nozzle exit is independent on nozzle diameter. Any increase in nozzle diameter will rise impinged cross section as well as volumetric flow rate in a quadratic relationship. For the assumed conditions, the power density is P_D=5.1 MW/cm^2. For comparison, a typical value for a laser used to efficiently strip paint from airplanes is about 5 MW/cm^2 (US Air Force, 1999). Equations (2.7) and (2.9) are valid only for the conditions immediately after the nozzle exit. For the specific conditions in a high-speed water jet, some values, such as pressure and water density, must be varied. Also, d_N must be replaced by d_J. Specific power (or energy) is not evenly distributed over the surface; its distribution depends on nozzle configuration and nozzle carrier movement. This is shown in Fig. 2.3. The energy distribution can be smooth down if a high overlap ratio between the individual cleaning steps is realised. Models how to estimate power distributions of rotating hydrodemolition tools are provided by Blades (1994) and Küfer (1999).

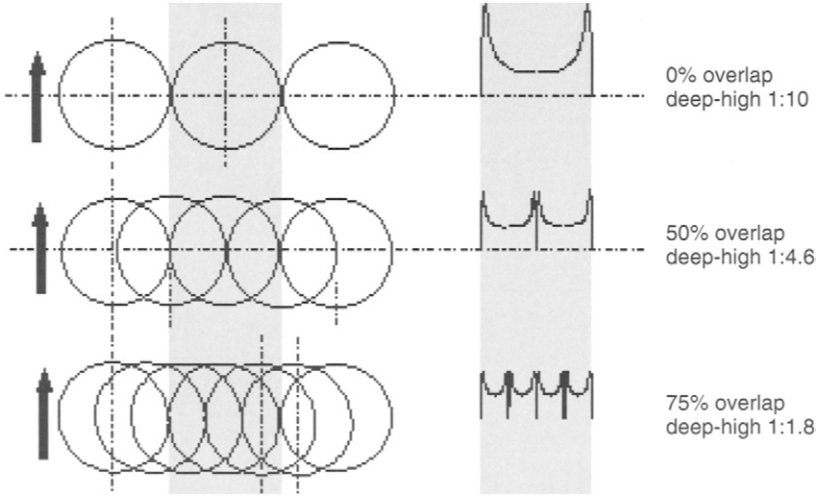

Figure 2.3 Energy distribution for a rotating nozzle carrier (Momber et al., 2000)

2.1.2 Structure of high-speed water jets

The structure of high-speed water jets escaping into air is described by Thikomirov et al. (1992) and Momber and Kovacevic (1998). However, a few relationships may be mentioned here. The general structure of a water jet is shown in Fig. 2.4. In the axial (x-) direction, the jet typically divides into three zones: A core zone, a transition zone, and a final zone. In the cone-shaped core zone, the flow properties, such as stagnation pressure and flow velocity, are constant along the jet axis. Usually, the length of this zone, x_C, is related to the nozzle diameter. For low Reynolds numbers ($Re<4 \cdot 10^5$) the following relationship applies (Nikonov, 1971):

$$\frac{x_C}{d_N} = A^* - B^* \cdot Re \tag{2.10}$$

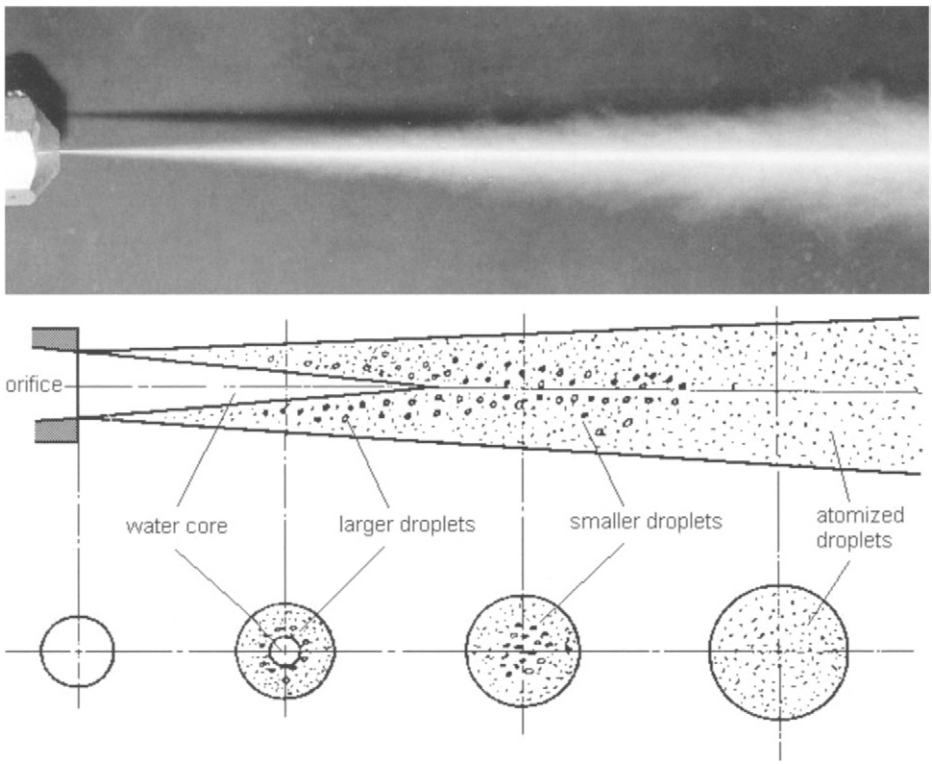

Figure 2.4 Structure of a high-speed water jet; photograph: BGMR, RWTH Aachen (for scaling: nozzle exit diameter: 0.8 mm); jet scheme: Zou et al. (1985)

The parameters A* and B* depend on the Reynolds number of the jet flow, and on nozzle geometry and quality. For larger Reynolds numbers ($Re>4 \cdot 10^5$), the ratio x_C/d_N is a constant value that depends on nozzle finish quality. More detailed information is provided in Table 2.3. An average from values published in the

Table 2.3 Water jet structural parameters (Nikonov, 1971)

Reynolds number	Parameter	Nozzle finish	
		Poor	Good
$< 4 \cdot 10^5$	A*	84	112
$< 4 \cdot 10^5$	B*	$68 \cdot 10^6$	$68 \cdot 10^6$
$> 4 \cdot 10^5$	x_C/d_N	50–60	85–90

literature is $x_C/d_N=100$ (see Momber and Kovacevic, 1998). An approximation for the core-zone length as a function of the pump pressure can be established based on measurements from Neusen et al. (1994). Their results fit very well into a negative power relation

$$\frac{x_C}{d_N} = 1958 \cdot p^{-0.65} \tag{2.11}$$

In that equation, p is given in MPa. For the above assumed pressure of p=140 MPa and the nozzle diameter of $d_N=3$ mm, the length of the core zone is $x_C=236$ mm. As illustrated in Table 2.3, the ratio x_C/d_N can be utilised to evaluate nozzle quality; it is high for 'good' orifices, and low for rather 'bad' orifices. Thus, jet quality can characterise nozzle condition as well, and it can be used to monitor the condition of nozzles. In the transition zone, the flow velocity is a function of the jet radius, $v_J=f(r_J)$. This radial velocity profile has a typical bell shape that can mathematically be described by exponential functions. Several examples are published by Momber and Kovacevic (1998). Additionally, the axial flow velocity drops in that region. The length of the transition zone, x_{TR}, relates to the core zone as follows:

$$\frac{x_{TR}}{x_C} = B \tag{2.12}$$

A typical value for the constant is B=5.33 (Yanaida, 1974). Figure 2.4 shows a notable increase in jet diameter with increasing jet length. A quantitative relationship is shown in Fig. 2.5. A mathematical relationship is (Yanaida, 1974):

$$\frac{d_J}{d_N} = 0.42 \cdot x^{1/2} \tag{2.13}$$

Himmelreich (1992), Himmelreich and Rieß (1991a,b), and Neusen et al. (1991) performed investigations of the structure of plain high-speed water jets. Figure 2.6a shows some results from measurements of the velocity distribution of the water in a jet. It can be seen that the velocity has high values at the centre of the jet and decreases as it approximates the rim of the jet. Figure 2.6b illustrates the turbulence of a water jet, which is defined as:

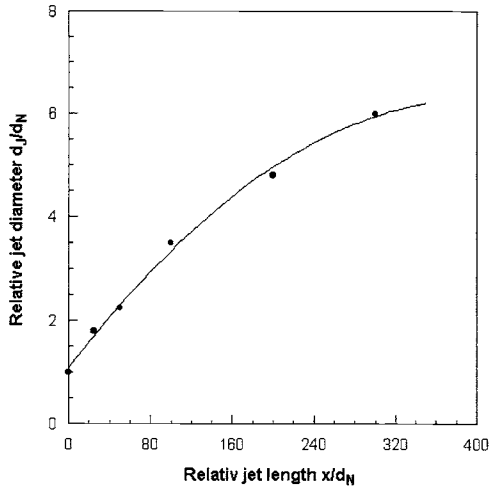

Figure 2.5 Jet diameter as function of jet length; measurements: Yanaida and Ohashi (1980)

$$T_U = (S_{V_J} / \overline{v}_J) \cdot 100 \qquad (2.14)$$

The turbulence is about 6% with higher values in radial direction. Therefore, water jets have a notable radial velocity component which causes jet disintegration, liquid slug formation and air entrainment. It is evident from Fig. 2.6 that turbulence is also the reason for the decrease in the axial velocity of the fluid particles at the rim of the jet.

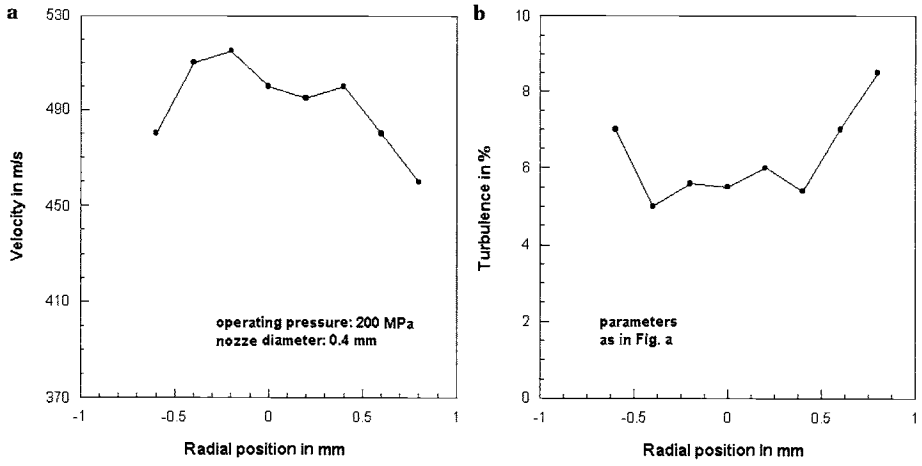

Figure 2.6 Distributions of velocity and turbulence in a water jet (Himmelreich and Rieß, 1991a)
a – velocity
b – turbulence

2.1.3 Water drop formation

In the transition zone, water drop formation occurs in the jet due to external friction, air entrainment and internal turbulence. These drops add a highly dynamic component to the jet. The average drop diameter can be approximated by the following equation known from liquid atomisation (Schmidt and Walzel, 1984):

$$d_{DS} = \frac{1+3.3\cdot Oh}{We^{1/2}} \cdot \left(\frac{\rho_L}{\rho_F}\right)^{-1/4} \cdot d_N \tag{2.15}$$

The diameter d_{DS} is the 'sauter mean diameter'; this is the diameter of a drop that has the same ratio of volume to surface area as the ratio of total volume to total surface area in a distribution of drops. In Eq. (2.15), Oh is the Ohnesorge number (in Ohnesorge's (1936) original work notated 'Z'); it balances viscous force and surface tension force and inertia force:

$$Oh = f(Re) = We^{1/2} / Re \tag{2.16}$$

For friction less fluids: Oh=0. The parameter We is the Weber number:

$$We = \frac{\rho_F \cdot d_N \cdot v_D^2}{\sigma_F} \tag{2.17}$$

and Re is the Reynolds number:

$$Re = \frac{v_D \cdot d_N}{\nu_F} \tag{2.18}$$

From Eqs. (2.15) to (2.18) follows:

$$d_D \propto v_J^{-1} \tag{2.19}$$

The higher jet velocity, the smaller the average drop diameter. The maximum (stable) drop diameter in a disintegrated liquid jet can be approximated according to a relationship derived by Troesch (1954):

$$\frac{\sigma_F}{\rho_F \cdot v_D^2 \cdot d_{D\max}} \cdot \left(1+10^6 \cdot \frac{\eta_F^2}{\sigma_F \cdot \rho_F \cdot d_{D\max}}\right)^{1/12} \cdot \left(1-0.5\cdot\frac{\rho_L}{\rho_F}\right) = 4.8\cdot 10^{-5} \tag{2.20}$$

The maximum drop diameter can be calculated by an iterative calculation procedure. Fig. 2.7 shows some results from Eq. (2.15) for typical pressure and nozzle diameter ranges. For rather high pump pressures, average and maximum drop diameter are equal. Liquid atomisation consumes a certain amount of energy

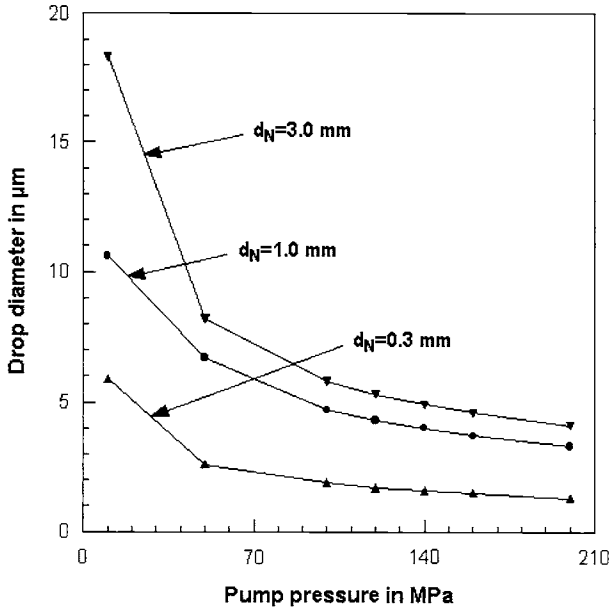

Figure 2.7 Drop diameter as function of pump pressure and orifice diameter

that is not available for the hydrodemolition process. This energy loss can be approximated:

$$E_D = N_D \cdot \sigma_F \cdot \pi \cdot d_D^2 \tag{2.21}$$

If the sauter mean diameter is used for d_D (see Fig. 2.7), the energy consumed by drop formation in a water jet with the conditions mentioned above is about $E_D = 2.23 \cdot 10^{-6}$ Nm.

2.2 Material loading due to stationary jets

2.2.1 General loading modes

If the jet hits a solid surface, a stagnation pressure profile forms at that surface. The profile shape was measured by several authors, and approximate equations were derived (Momber and Kovacevic, 1998). Such profiles are shown in Fig. 2.8 as functions of relative jet length. In the centre (r=0) the pressure equals the stagnation pressure:

$$p_S = \frac{\rho_F}{2} \cdot v_J^2 \tag{2.22}$$

The stagnation pressure depends on jet length (stand-off distance, respectively) according to the following function (Nikonov, 1971; Shavlovsky, 1972):

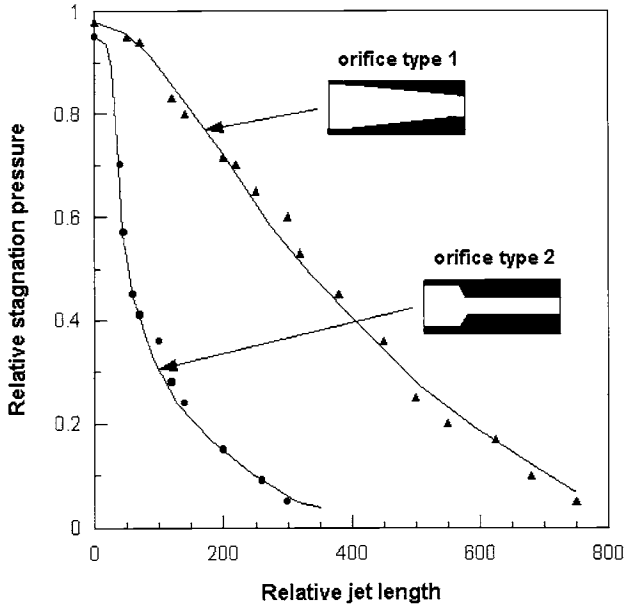

Figure 2.8 Orifice type effects on stagnation pressure profiles (Leach and Walker, 1966)

$$\frac{p_S(x)}{p_S(0)} = \left(\frac{x_C}{x}\right)^{K^*} \tag{2.23}$$

for $x<3\cdot x_C$: $K^*=0.27+0.075\cdot(x/x_C)^2$.
for $x>3\cdot x_C$: $K^*=0.3$.

The loading duration is given through the exposure time which is for a moving jet:

$$t_E = \frac{d_N}{v_T} \tag{2.24}$$

The difference between the stagnation pressure at the surface and the pressure inside the target material forces a certain volume of water to penetrate the structure. This volume is

$$Q_S = \varpi^* \cdot \dot{Q}_A \cdot t_E \tag{2.25}$$

where $\omega^*=0$ is the limiting case for a completely non-permeable material, and $\omega^*=1$ is the limiting case when the whole volume delivered by the nozzle penetrates into the material. For $\omega^*>0$, the following three cases can be distinguished:

(i) the water flows into a crack and creates a corresponding stress at the crack tip;
(ii) the water flows into a capillary which results in pressure amplification;
(iii) the water flows through an open pore system and creates friction forces to the structural elements (e.g. grains).

Case (i) was experimentally investigated by Mazurkiewicz et al. (1986) whose results are illustrated in Fig. 2.9. Although the experiments were restricted to comparatively low water pressures, a linear relationship between pump pressure and pressure developed at the crack tip could be noted. If jet velocity is considered instead of pump pressure, the following relationship is valid:

$$p_R = C_1 \cdot v_J^2 \tag{2.26}$$

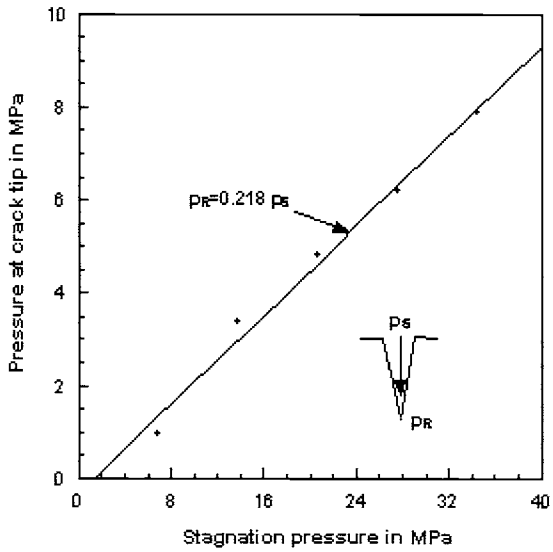

Figure 2.9 Water flow into a crack (Mazurkiewicz et al., 1986)

The constant was found to be C_1=0.22 which corresponded closely to values estimated by Momber and Kovacevic (1995) who found $0.19<C_1<0.21$ based on an LEFM-model. Lin et al. (1996) used a finite element code to investigate the influence of the water jet velocity on principal stresses as well as stress intensity at the crack tip. Some of their results are shown in Fig. 2.10. The calculated points (filled circles) can be approximated by a square-root relationships which verifies Eq. (2.25). The open circles in Fig. 2.10 are experimental points estimated by Witzel (1998) on rocks. However, the calculated points in Fig. 2.10 can be approximated by an almost linear function in the range of low jet velocities up to 300 m/s. A

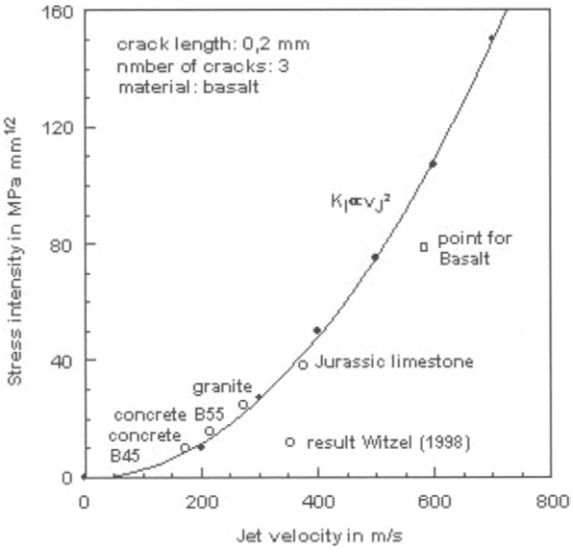

Figure 2.10 Relationship between jet velocity and stress intensity (Lin et al., 1996)

mercury intrusion study performed by Momber (1992) on cementitious composites showed clearly that the fracture started in the interfacial zone between cement matrix and aggregate which is known to be the weakest link in conventional concrete. Moreover, fracture propagation was mainly affected by aggregate size and distribution. A detailed microscopic study on crack-aggregate interactions in concrete samples eroded by water jets were made by Momber (2003b) who found clear evidence of crack deflection, crack stopping, crack tip bluntness, but also of crack bridging and crack face friction. Some of these features are illustrated in Fig. 2.11.

Case (ii) corresponds to capillary-like micropores. A model for pressure intensification in "blind", air filled tubes was developed by Evers et al. (1982). A

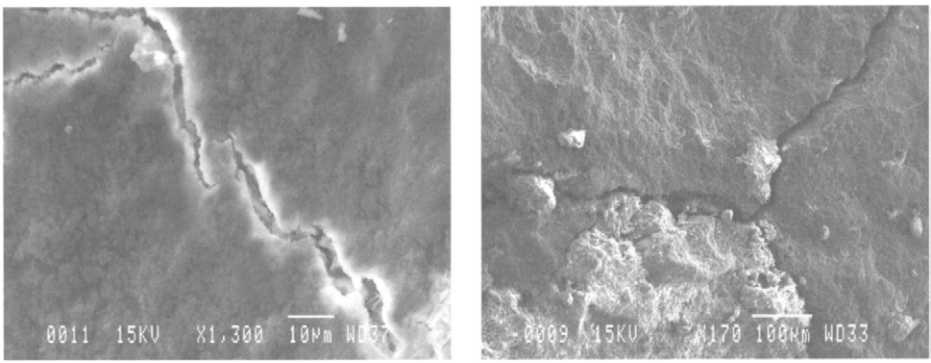

Figure 2.11 Microscopic features of concrete eroded by high-speed water jets (Momber, 2003b)

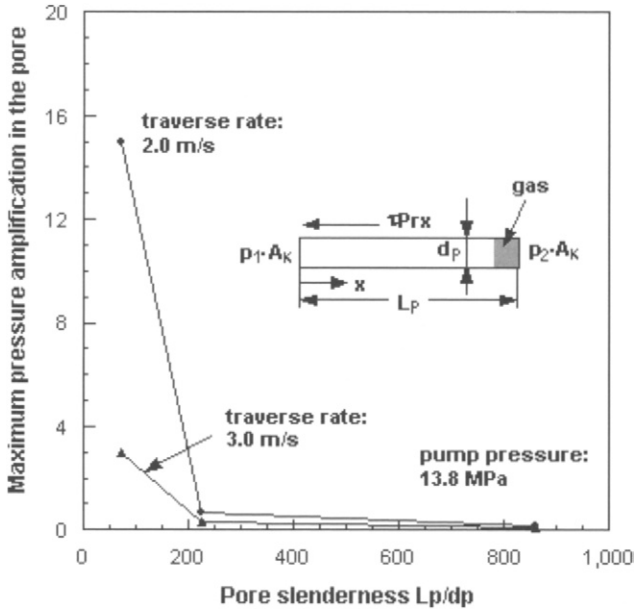

Figure 2.12 Pressure amplification in a pore subjected by a water jet (Evers et al., 1982)

liquid jet, that strikes a pore opening, transports liquid into this capillary and displaces the air. A force balance as shown in Fig. 2.12 delivers the following:

$$p_1 \cdot A_C = \tau_S \cdot Pr \cdot x + p_2 \cdot A_C \tag{2.27}$$

Thus, pressure intensification depends on shear stress, pore geometry and perimeter of the liquid column. The approach was later modified by Evers and Eddingfield (1984) by considering compressibility effects. The capillary model was verified experimentally for rather large pores and low pressures. For a pore with a diameter of 0.2 mm and a length of 38 mm where a water jet with a velocity of 71 m/s traversed over with a speed of 6.0 m/s (corresponding exposure time would be $3.3 \cdot 10^{-5}$ s), a pressure intensification of 3.5 was estimated.

Case (iii) was in detail investigated by Rehbinder (1977) for porous solids. Based on a known pressure gradient, the speed, the liquid penetrates the pore system at, can be estimated with Darcy's Law:

$$v_F = -\frac{k_P}{\mu_W} \cdot \text{grad}\, p_S \tag{2.28}$$

The frictional force acting on an individual grain due to the liquid flow can be approximated for low Reynolds numbers and spherical particles as follows:

$$F_F = C \cdot d_M \cdot \mu_W \cdot v_F \tag{2.29}$$

Further treatment – especially the replacement of the constant C – delivers the following relationship (Rehbinder, 1977):

$$F_F = \frac{V_M}{1 - P_M} \cdot \text{grad}\, p_S \tag{2.30}$$

If this frictional force exceeds the cohesion force to neighbouring grains, the grain in question will be removed.

2.2.2 Material response

Important information about the response of concrete to water jet loading is stored in the structure of fracture faces. Depending on loading regime and material structure, two general types of macroscopic failure can be distinguished:

- type I: sections without brittle fracture features;
- type II: sections with dominant brittle fracture features.

Both types, that were probably first distinguished by Nikonov (1971) for coal cutting with water jets, are illustrated in Fig. 2.13. It can be noted that type-II failure occurred always near larger aggregate particles. Investigations on rock materials have shown that the transition from type-I to type-II failure depended on jet velocity and exposure time. The transition jet velocity was a function of the

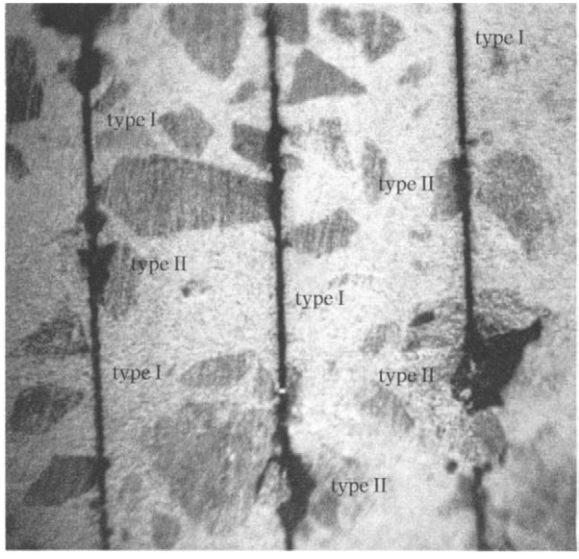

Figure 2.13 Failure types in concrete during hydrodemolition (Momber, 2004a)

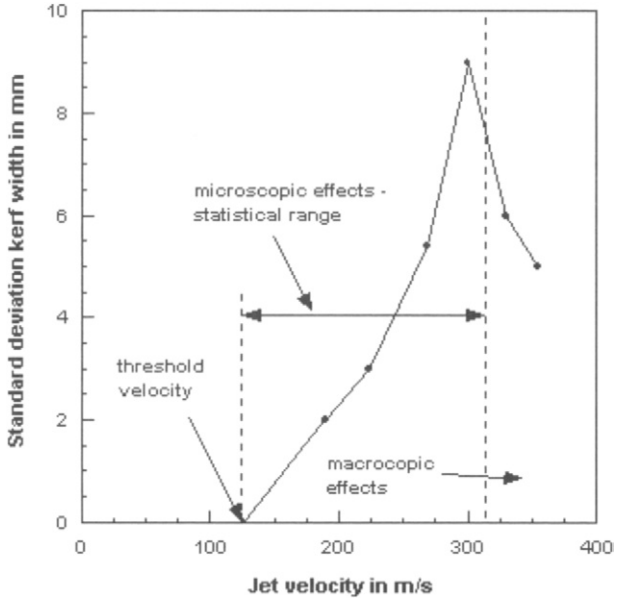

Figure 2.14 Effect of jet velocity on kerf width variation in concrete (Momber and Kovacevic, 1995)

Figure 2.15 Fracture surface of a cement sample cut with a high-speed water jet (Momber and Kovacevic, 1994)

tensile strength, whereas the transition exposure time followed a more complex relationship (Sugawara et al., 1998). Momber and Kovacevic (1995) have investigated the influence of jet velocity on the fracture statistics of concrete surfaces. The results illustrated in Fig. 2.14 show that the standard deviation of the kerf width started to drop at a certain jet velocity (at about 300 m/s). If this velocity was exceeded the failure process was more homogeneous. Effects due to the microstructure (e.g. microcrack distribution) were eliminated, and a macroscopic material property, lets say tensile strength, determined the material response. The average kerf width was always larger for a plain matrix material (cement matrix) than for a composite (mortar or concrete) due to the rather unrestrained fracture propagation in the matrix. This is illustrated in Fig. 2.15 showing the very smooth fracture face in a cement matrix. It may, however, be noted that the roughness of the surface increased as the fracture propagated (from top to bottom). Such effects are known from other brittle material as well (Hull, 1999; Schönert, 1972) and is considered to be a result of crack acceleration. If two concrete materials were compared, a water jet formed wider kerfs in the material with the coarser aggregates (Momber, 1998b; Werner, 1991a).

2.2.3 Material resistance parameters

Conventional properties of concrete, namely strength parameters, can not characterise the resistance against water jet erosion. This was found in very detailed studies performed by Kauw (1996) and Werner (1991a); an illustrative example is shown in Fig. 2.16. Figure 2.17 shows the situation if the compressive strength in Fig. 2.16 is replaced by the characteristic length. The characteristic length is a fracture parameter originating from a fracture model introduced for concrete by Hillerborg et al. (1976); see Section 1.4.2. The relationship between volumetric erosion rate and characteristic length is:

$$\dot{V}_M \propto L_{ch} = C_M \cdot \frac{d_A}{\sigma_C^{0.3}} \tag{2.31}$$

whereby the very right term expresses an empirical relationship between aggregate size, compressive strength, and characteristic length (Hilsdorf and Brameshuber, 1991). It was shown that Eq. (2.31) also holds for other impact situations, namely for the comminution of concrete in a jaw breaker (Momber, 2002b). The supporting effect of coarse aggregates on concrete hydrodemolition, as expressed in Eq. (2.31), was verified by Werner (1991a). The proportionality coefficient C_M is considered to be a machine parameter.

Rehbinder (1978) defined a so-called 'specific erodability' to evaluate the resistance of porous solids against water jet erosion. This parameter is defined as follows:

$$R_E = \frac{k_P}{\mu_W \cdot d_M} = \frac{\Delta h_M}{\Delta p} \cdot \frac{1}{t_E} \tag{2.32}$$

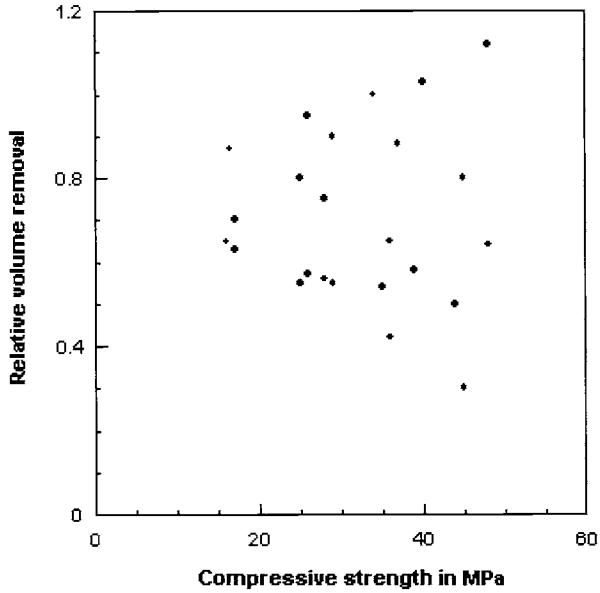

Figure 2.16 Relationship between removal rate in concrete and compressive strength (Werner, 1991)

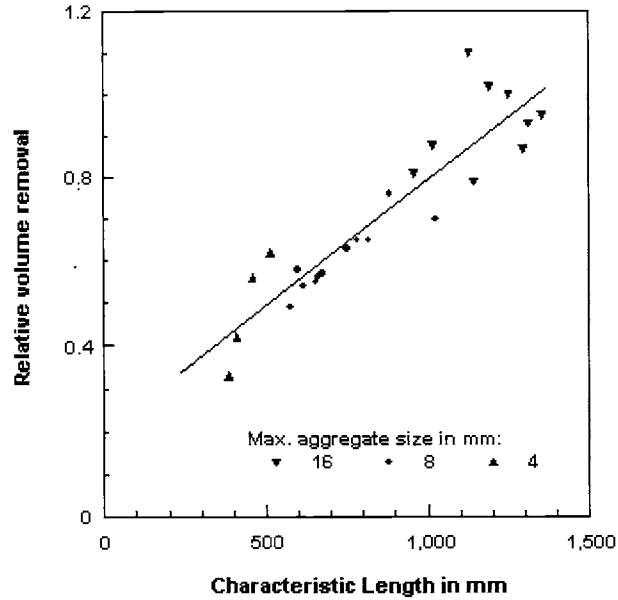

Figure 2.17 Relationship between removal rate in concrete and characteristic length (Momber, 2003c); values correspond to Fig. 2.16

The higher specific erodability, the lower the resistance. The physical unit of this parameter is [$m^3/N{\cdot}s$]. The right term of Eq. (2.32) allows the experimental estimation of R_E, whereby $\Delta h_M/\Delta p$ is simply the progress of an erosion depth-pressure function. Specific erodability increases as grain size or viscosity decreases, and as permeability increases. It was in fact shown by Kolle and Marvin (2000) that the resistance of rock materials was higher for water as a liquid compared to liquefied carbon dioxide (having a lower viscosity). If, however, viscosity is a constant value, erosion resistance depend only on pore structure (Rehbinder, 1980):

$$R_E \propto \frac{1}{d_M} \cdot \left(\frac{d_M}{d_O} \right)^2 \tag{2.33}$$

Thus, resistance is proportional to pore slenderness and it decreases if – for a given pore slenderness – grain size decreases. These results are partly in agreement with experimental results obtained by Evers et al. (1982) on rocks.

2.3 Process parameter effects on material removal

2.3.1 Parameter definitions

Basic target parameters include thickness of removed layers (h_M), volume removal (V_M), volumetric removal rate ($\dot{V}_M$), and removal width (w_M). They are illustrated in Fig. 2.18. For the erosion with a stationary water jet, these parameters are related through the following approximation:

$$V_M = \frac{\pi \cdot w_M^2 \cdot h_M}{4} \tag{2.34}$$

For a given removal width, a certain concrete volume must be removed to completely erode a layer of given thickness. A maximum volume removal is desired. The energy efficiency of the demolition process is given by the specific energy:

$$E_S = \frac{E_J}{V_M} \tag{2.35}$$

This parameter should be as low as possible; its physical unit is [kJ/m^3]. The volumetric removal rate is the mass removed in a given period of time:

$$\dot{V}_M = \frac{V_M}{t_E} \tag{2.36}$$

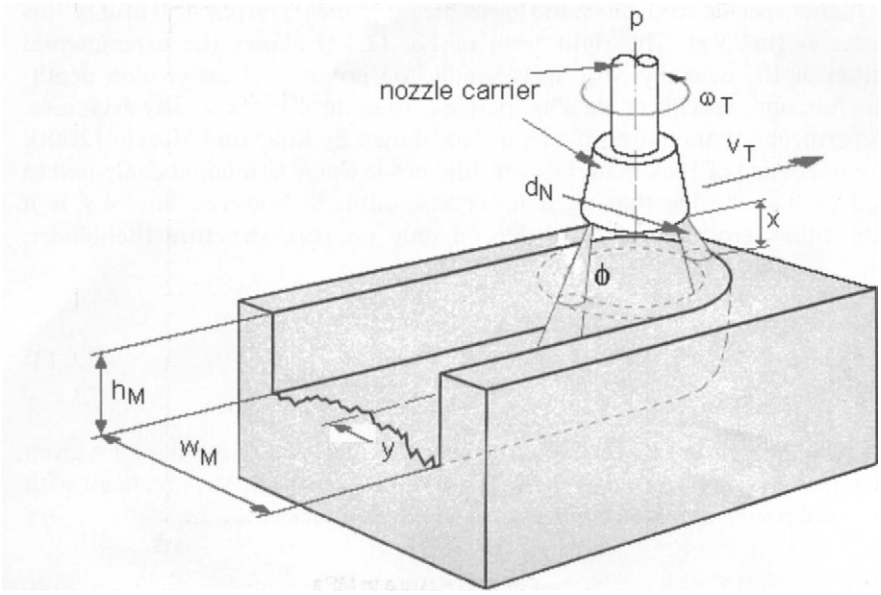

Figure 2.18 Target and process parameters for hydrodemolition

Volumetric removal rate should also be maximum; its physical unit is [m^3/h]. Other target parameters that may focus on the surface quality, such as roughness or cleanliness, are not considered in this paragraph. Hydrodemolition process parameters are summarised in Fig. 2.18. They can be subdivided into hydraulic parameters and performance parameters. Hydraulic parameters characterise the pump-nozzle-system; they include the following:

- operating pressure (p);
- volumetric flow rate ($\dot{Q}_A$);
- nozzle diameter (d_N).

Typical relationships between these parameters are described in Chapter 3. Performance parameters are more related to the process and include the following:

- stand-off distance (x);
- traverse rate (v_T);
- traverse increment (y);
- impact angle (ϕ);
- nozzle guidance.

The traverse rate covers additional parameters, such as the number of cleaning steps, n_S, and the exposure time t_E.

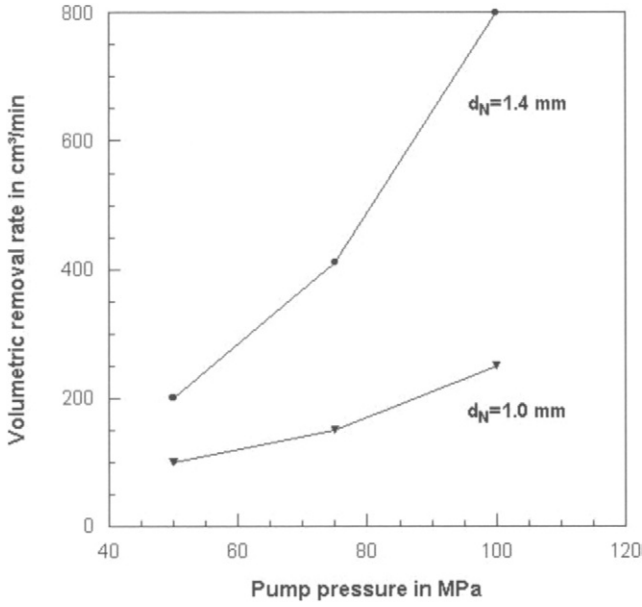

Figure 2.19 Effect of pump pressure on material removal rate (Werner, 1991a)

2.3.2 Pump pressure effects

Figure 2.19 shows the relationship between pump pressure and concrete mass loss which can be described mathematically as follows:

$$\begin{aligned} p \le p_T: &\qquad \dot{V}_M = 0 \\ p > p_T: &\qquad \dot{V}_M = A_1 \cdot (p - p_T)^{B_1}. \end{aligned} \tag{2.37}$$

This function features three parameters: A threshold pressure p_T, a progress parameter A_1, and a power exponent B_1. The threshold pressure appeared in several experimental studies (Momber, 1992; Werner, 1991a). The meaning of this parameter is illustrated in Figs. 2.20 and 2.21. Figure 2.20 shows high-speed camera images taken during the removal of a latex-coating from a fibrous substrate. Note from the left image the complete reflection of the impinging jet from the coating surface; no material was removed. This situation counts for $p<p_T$. In the right image material erosion occurred; the jet completely removed the coating and penetrated the fibrous substrate. This situation counts for $p>p_T$. Figure 2.21 illustrates the situation for concrete. It can be seen that part of the concrete structure, denoted "U", remains undamaged; this situation counts for $p<p_T$. Other parts of the structure are removed due to water jet erosion; this corresponds to the case $p>p_T$. According to Eq. (2.2), the critical pressure actually characterises a

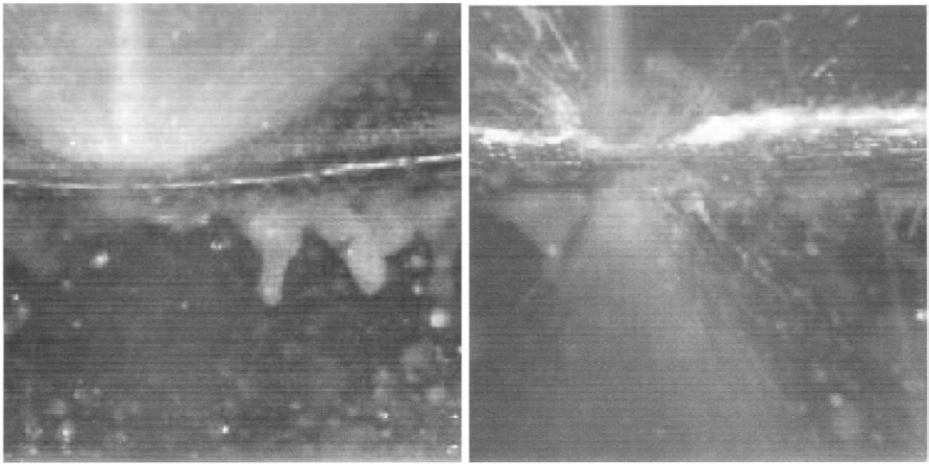

Figure 2.20 Threshold conditions for a latex layer (Weiß and Momber, 2003) left: $p<p_T$; right: $p>p_T$; scale: 5 mm; fibrous substrate

Figure 2.21 Threshold situation in a hydrodemolished concrete substrate (photograph: Aquajet Systems AB, Holsbybrunn)

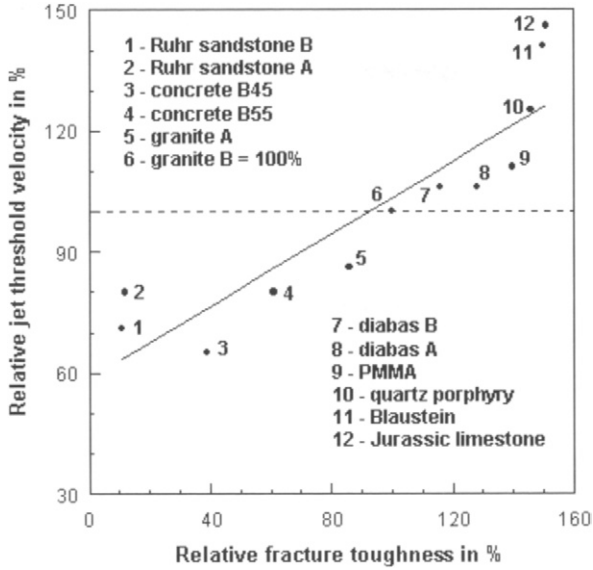

Figure 2.22 Effect of fracture toughness on threshold velocity; values taken from Wiedemeier (1981) and Witzel (1998)

critical velocity of the impinging jet. Wiedemeier (1981) and Witzel (1998) performed measurements on rock materials in order to install relationships between threshold velocity and material properties. Their results are summarised in Fig. 2.22, and the following relationship can be noted:

$$v_T = C_T \cdot K_{Ic} \tag{2.38}$$

These experimental results agree with a statistical fracture model developed by Momber and Kovacvic (1995) for multiphase materials. Calculation results based on this model are shown in Fig. 2.23. The material phase owing the lowest fracture toughness (interfacial zone between matrix and aggregate) shows the highest failure probability and, therefore, the lowest threshold value. The power exponent B_1 in Eq. (2.37) depends mainly on nozzle diameter and on target material. It can be seen from Fig. 2.19 that B_1 increases if nozzle diameter increases. For nozzle sizes applied in hydrodemolition, B_1 may always be larger than unity; for d_N=1.4 mm: B_1=2. Therefore, a very high pump pressure leads to an extraordinarily high volumetric removal rate. If B_1 is between 1 and 2, the pressure for minimum energy consumption ($dE_J/d\dot{V}_M$ =Min) delivers p=∞. For B_1=1, however, which was found by Werner (1991a) for small nozzle diameters (between 0.2 and 0.6 mm), the solution for minimum energy consumption delivers $p=3 \cdot p_T$. Therefore, optimum operating pressure depends on nozzle configuration. If small nozzles are used, pressures less than 100 MPa are more efficient from the point of view of energy exploitation.

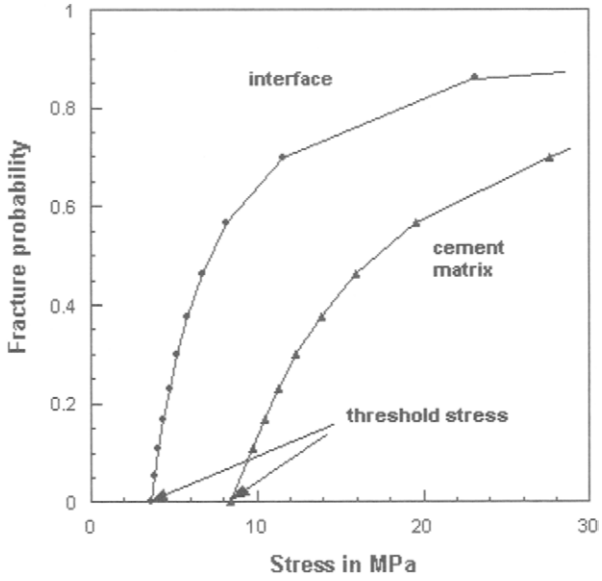

Figure 2.23 Effect of structural elements in concrete on erosion probability (Momber and Kovacevic, 1995)

2.3.3 Nozzle diameter effects

The relation between nozzle diameter and mass loss is shown in Fig. 2.24a. A good approximation to the experimental results is a quadratic function:

$$\dot{V}_M = A_2 \cdot (d_N - d_T)^2 \tag{2.39}$$

which again features a threshold parameter. This threshold diameter is usually less then d_N=0.1 mm. Energy considerations deliver an optimum nozzle diameter for dE_J/dV_M=0 at d_N=1.5·d_T; this relationship is shown in Fig. 2.24b. It can be seen that any nozzle diameter in excess of 1.5·d_T is associated with low specific energy values, whereas nozzle diameters smaller than 1.5·d_T are very inefficient in terms of specific energy. Considering Rehbinder's (1977) theory, a critical nozzle diameter could be related to material properties as follows:

$$d_T >> \frac{\nu_F}{2 \cdot k_P \cdot (p \cdot \rho_F)^{1/2}} \tag{2.40}$$

Thus, threshold diameter depends on target material permeability and on pump pressure. Werner (1991a) found a tendency, that lower pump pressures require higher values for the threshold nozzle diameter. The quadratic relationship for the nozzle diameter points to a linear effect of the volumetric flow rate on the volumetric removal rate [see Eq.(3.25)]. This suggestion is verified in Fig. 2.25

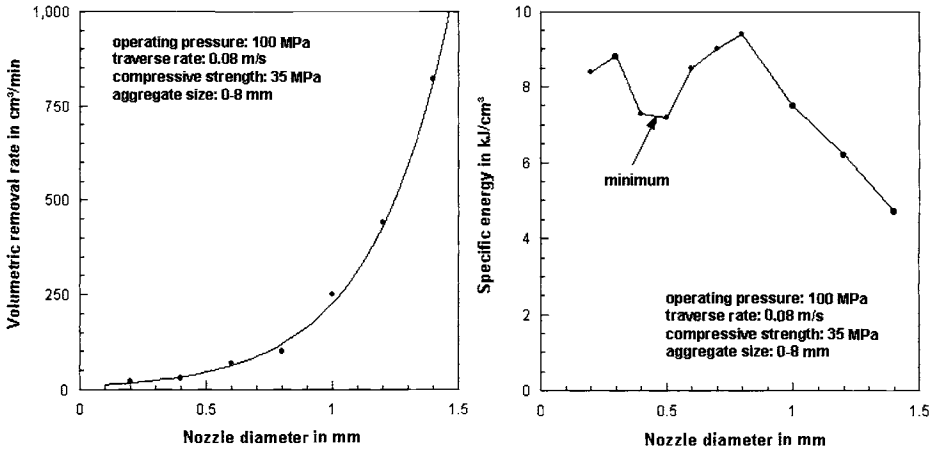

Figure 2.24 Effect of nozzle diameter on concrete removal (Werner, 1991a)
a – removal rate
b – specific removal energy

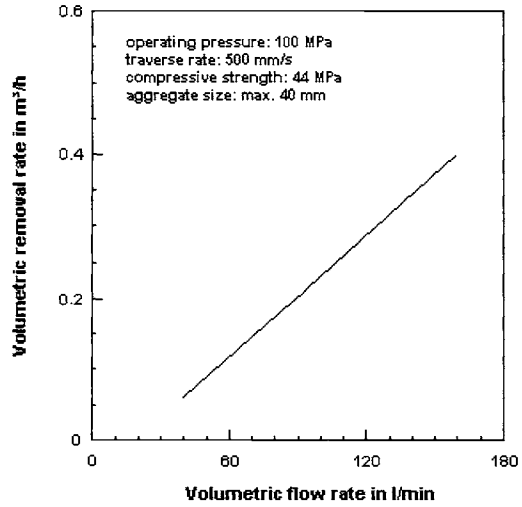

Figure 2.25 Effect of volumetric flow rate on removal rate in concrete (Osanai et al., 1998)

showing such a linear relationship as well as the presence of a threshold volumetric flow rate. Thus, a minimum water volume must be available during the erosion in order to remove material. Interestingly, an equal observation was made if concrete samples were subjected to pulsating water jets. It was shown by Yie et al. (1978) that a certain pulse length (which characterises water volume) was required to visibly damage concrete panels. If the pulse length was shorter than this critical value, no material removal occurred. If, for a given operating pressure, volumetric

flow rate increases up to a certain value, the removal rate could be expected to drop. The reason is that only a certain water volume can penetrate the structure of a concrete in a given period of time. Values for such a critical volumetric flow rate have not been estimated yet, and it seems that they are beyond 100 l/min. This aspect, however, leads to the conclusion that volumetric flow rate and traverse rate (exposure time, respectively) should be related to each other in order to optimise hydrodemolition processes. It may also be mentioned that kerf width and surface roughness of eroded concrete both linearly increase if nozzle diameter increases (Werner, 1991a).

2.3.4 Stand-off distance effects

The effects of stand-off distance on hydrodemolition is investigated by numerous authors, namely Hamada et al. (1974), Labus (1984), Momber (1992), Norsworthy et al. (1974), and Werner (1991a). The results of these investigations can be summarised by the following approximation:

$$h_M = A_3 \cdot x^{B_3} \cdot \exp(C_3 \cdot x) \tag{2.41}$$

with $C_3<0$. As shown in Table 2.4, the exponent B_3 depends on the operating pressure; it has positive values for rather low pressures, and negative values for high pressures. One consequence of $B_3>0$ is that an optimum exists for Eq. (2.41) at $x_0=-B_3/C_3$; this is shown in Fig. 2.26. This trend can be explained with arguments delivered in the previous sections. It was mentioned that a liquid jet disintegrates at a certain length, loading the target material in a mixed mode consisting of a static component, given by Eq. (2.22), and a dynamic component, given by Eq. (7.1). The dynamic component is in particular required if the stagnation pressure is rather low. More information about this issue is given by Momber (2000d). If high operating pressures (p>200 MPa) are applied, stand-off distance should be as short as possible. This is especially recommended if small nozzle diameters are applied. An increase in stand-off distance of 200% for a 0.3-mm nozzle deteriorates efficiency down to 70%, and an increase in stand-off distance of 500% deteriorates efficiency down to 50% (Werner, 1991a).

Table 2.4 Effect of pump pressure on stand-off distance parameters (values from Momber, 1993)

Pump pressure in MPa	Constant B_3 in Eq. (2.42)	Ratio x_0/d_N
40	> 0	19–34
50	> 0	17–23
50	> 0	20
207–483	< 0	→ 0
551	< 0	→ 0
274	< 0	→ 0
300	< 0	→ 0
200	< 0	→ 0

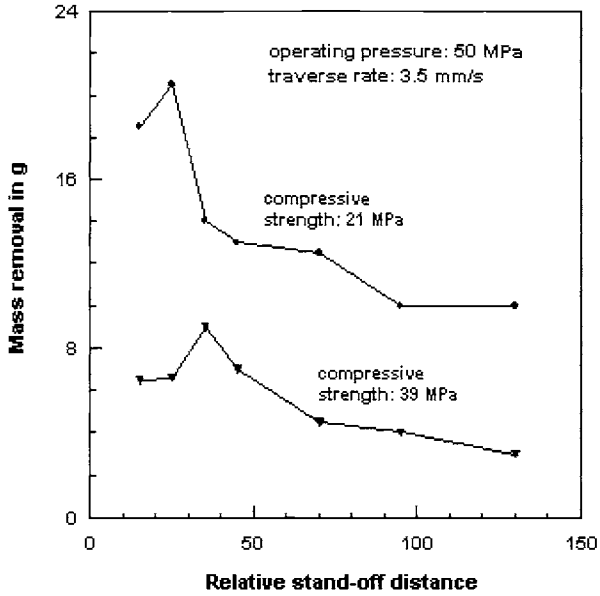

Figure 2.26 Effect of stand-off distance on mass removal for low pump pressures (Momber, 1992)

Unfortunately, there is a gap in the literature for typical hydrodemolition pressures (between 90 and 140 MPa), but it can be assumed that optimum stand-off distances exist in this pressure range. These optimum values are in the order of $x_O/d_N=20$.

2.3.5 Traverse rate effects

A typical relationship between volumetric removal rate and traverse rate is shown in Fig. 2.27. Removal rate increases as traverse rate increases. Therefore, a high traverse rate should be aspired. The relation follows a simple power law:

$$\dot{V}_M = A_4 \cdot v_T^{B_4} \tag{2.42}$$

with $0<B_4<1$. It is, however, one requirement for any hydrodemolition process that mass removal approaches zero at an extremely high traverse rate. Traverse rate actually expresses the local exposure time. A plot of local exposure time versus mass loss is shown in Fig. 2.28; the results were recalculated with Eq. (2.24). Mass loss increases dramatically at low exposure time; if the local exposure time increases further, efficiency (in terms of the slope of the curve) drops. From this point of view, short local exposure times (high traverse rates) are recommended, and this is the explanation for the trend visible in Fig. 2.27. A threshold exposure time can also be noted – it is about 0.01 s for the given operational conditions. After a time of about 0.01 s, a further increase in the exposure time reduces the progress

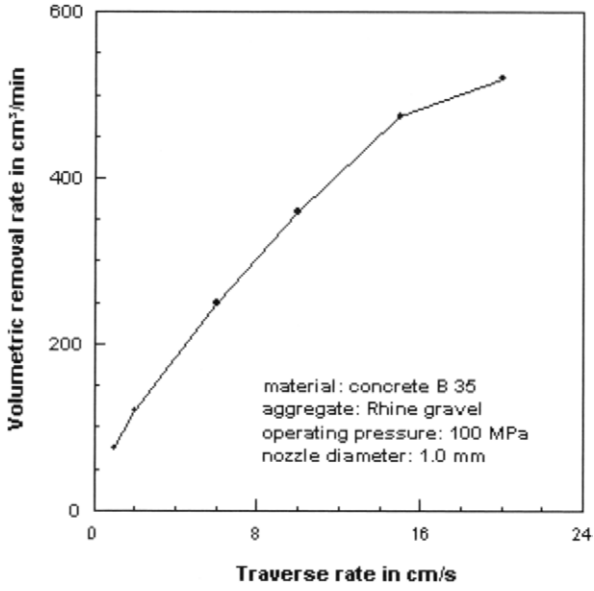

Figure 2.27 Effect of traverse rate on volumetric removal rate (Werner, 1991a)

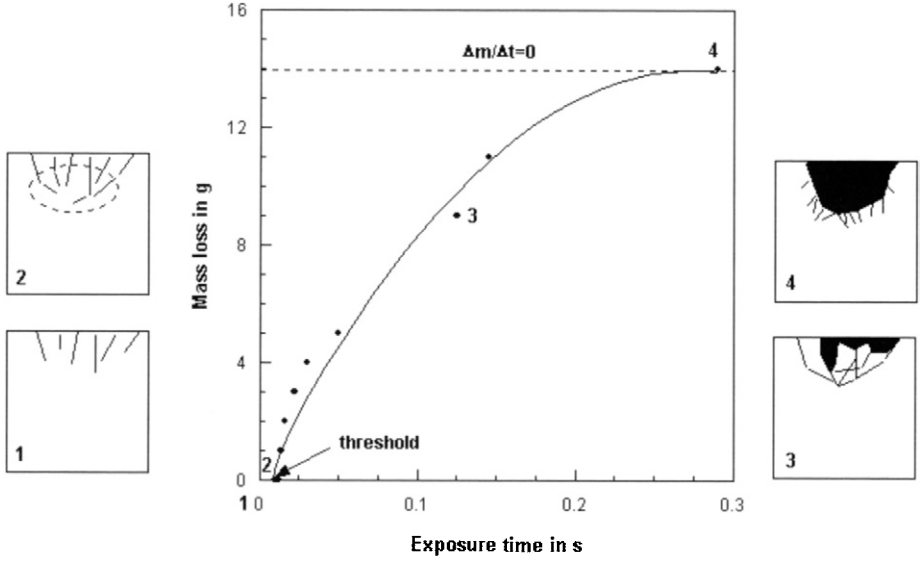

Figure 2.28 Effect of exposure time on mass loss in concrete

of the mass loss function. If this optimum exposure time, t_0, is known, a strategy for multi-pass hydrodemolition can be developed. This strategy simply introduces the optimum exposure time several times into the duration that corresponds to the desired mass loss rate. Thus:

$$t = n_S \cdot t_O \tag{2.43}$$

or, respectively,

$$n_S = \frac{t}{t_O} = \frac{m_M}{m_{M(t=t_O)}}; \quad n_S = 1,2,3 \tag{2.44}$$

An example may be calculated based on Fig. 2.28. If a mass loss of m_C=5,000 mg is required, a local exposure time of t_E=0.05 s is requested. The optimum exposure time for dm_M/dt_E=max is t_O=0.015 s which gives $m_{C(t=to)}$=1,000 mg. The theoretical step number calculated from Eq. (2.44) is n_S=3.33 In practice, n_S=3. The entire exposure time required to remove the desired mass is thus t_E=0.045 s which is about 90% of the time for a one-step-removal. The gain in efficiency is, therefore, 10%.

2.3.6 Traverse increment effects

The effect of the traverse increment is illustrated in Fig. 2.29. It is shown that an optimum increment exists for maximum efficiency. If the increment is too wide, unbroken ribs remain between the eroded kerfs as shown in Fig. 2.30a. These ribs must be broken away by additional jackhammering (Fehlemann, 1986). Is, on the contrary, the increment too narrow, surface regions are treated twice – a process that absorbs unnecessary energy. An empirical relationship for a rough approximation is:

$$y_O \cong 10 \cdot d_N \tag{2.45}$$

It is, however, demonstrated by Momber (1998b) that optimum values depend on the concrete structure. It is rather narrow for fine-grained concrete with high water-cement ratio (low structural homogeneity), and wide for concrete with low water-cement ratio containing coarse broken aggregate (high structural homogeneity). These relationships are shown in Fig. 2.30. Experimental results obtained by Kauw (1996) and Werner (1991a) verify these trends. A fracture mechanics model developed by Momber (1995c) delivers the following solution to an optimum increment:

$$y_O = A_5 \cdot \left[B_5 + C_5 \cdot \ln\left(\frac{p}{5}\right) \right] \tag{2.46}$$

Here, the constants depend on material properties. They have rather lower values for soft and fine-grained concrete (see Fig. 2.30).

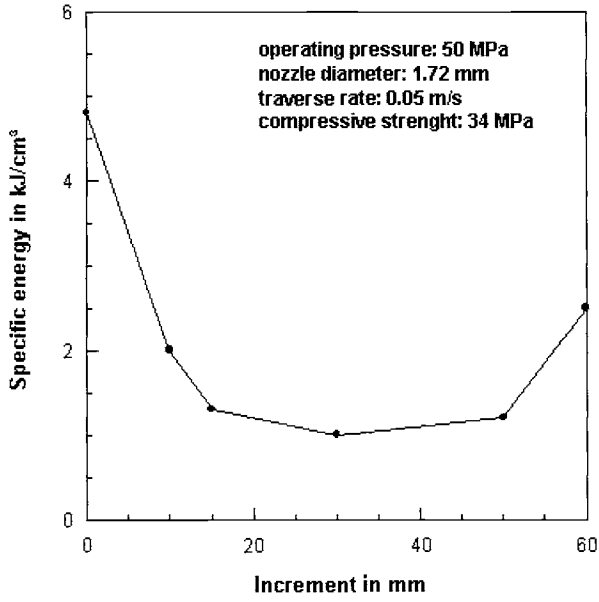

Figure 2.29 Effect of traverse increment on specific energy (Hamada et al., 1974)

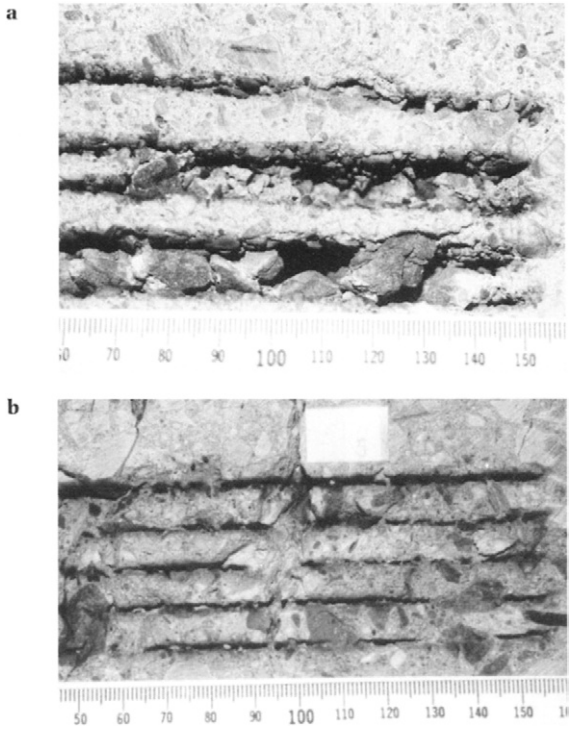

Figure 2.30 Effect of concrete structure on traverse increment optimisation (Momber, 1998b)
(a) – fine-grained concrete mixture; (b) – coarse concrete mixture

2.3.7 Impact angle effects

The relationship between impact angle and volumetric removal rate is illustrated in Fig. 2.31. In that graph, percentage changes in the removal rate are plotted against the impact angle. It can be seen that the intensity of angle effects depends on nozzle diameter. If rather large nozzles are applied, changes in impact angle affect removal rate notably. A jet, inclined in traverse direction, improves hydrodemolition processes. The gain in efficiency is up to 8% at an angle of 30° which would be the optimum angle. If, however, the jet is directed against the traverse direction, efficiency drops. This drop (down to 25%) is much more intense than the gain in efficiency. A jet directed into traverse direction closes the kerf behind the erosion site thus preventing the water from leaving the kerf. The water is partly trapped in the eroded cavity and creates additional stresses at the surrounding walls. This effect may lead to a more intense material stressing. Different results are reported by Kauw (1996) who found positive effects either the water jet was inclined into or against traverse direction. This author could also prove that reinforcement has an additional effect on impact angle variations (see Section 2.4.6).

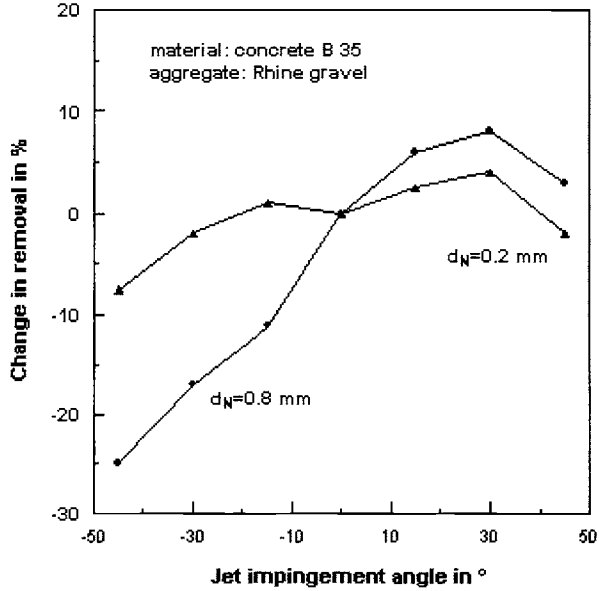

Figure 2.31 Effect of impact angle on removal rate (Werner, 1991a)

2.3.8 Nozzle movement effects

Hydrodemolition nozzles are mounted to nozzle carriers; see Section 3.5 for further information. Nozzle carriers allow to move the nozzles in different ways as illustrated in Fig. 2.32; the most common are: traversal, rotation, oscillation. Comparative investigations about these types of movements are performed by Kauw (1996) and Werner (1991a). These authors could demonstrate that

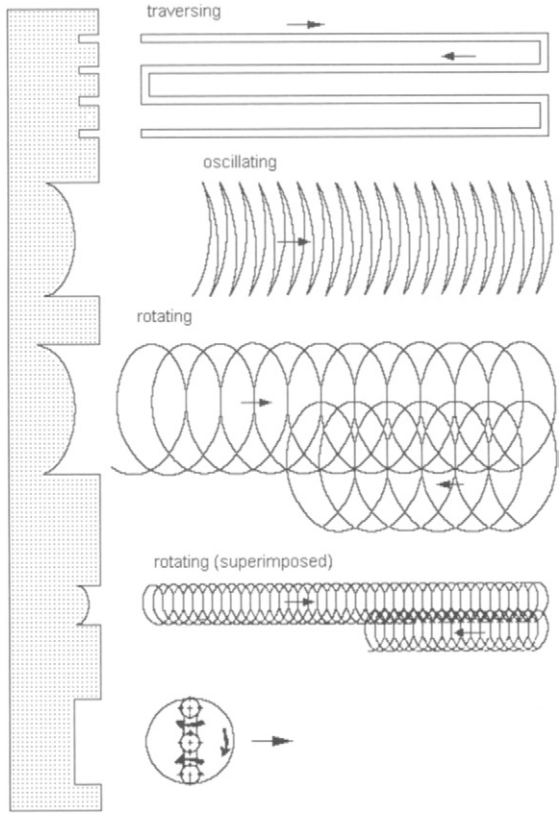

Figure 2.32 Types of nozzle movement (Werner, 1991a)

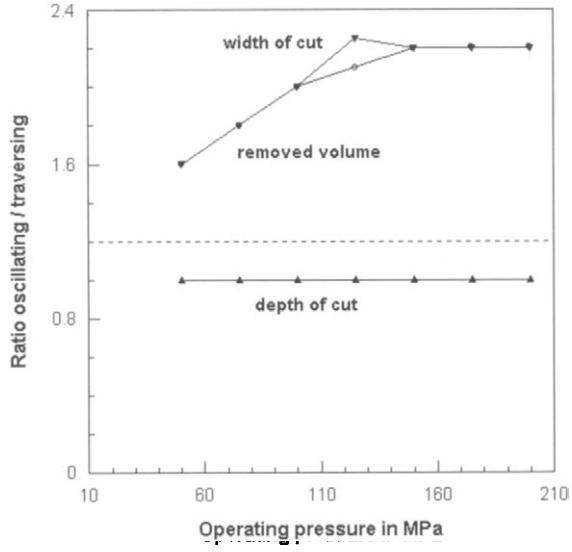

Figure 2.33 Effect of nozzle oscillation on removal rate (Werner, 1991a)

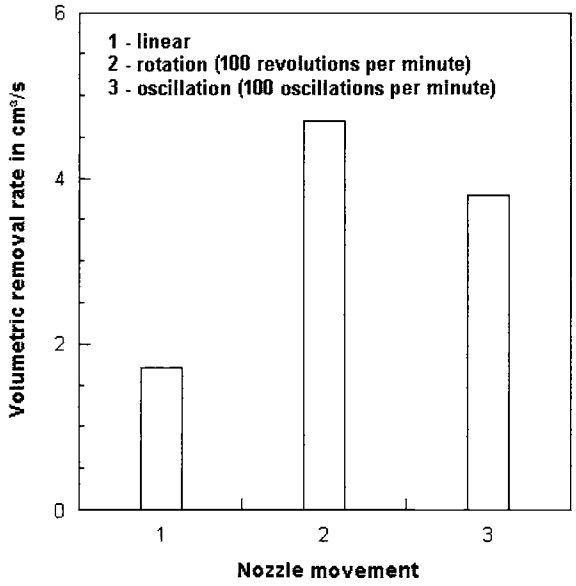

Figure 2.34 Effect of nozzle movement on removal rate (Kauw, 1996)

oscillating and rotating nozzle carriers work more effective than simple traverse mechanisms. Some results of tests with oscillating jets are summarised in Fig. 2.33. For a typical hydrodemolition pump pressure of 125 MPa, the removal rate can be doubled by oscillating the jet perpendicular to the traverse direction. It can be seen that the gain in efficiency is due to the increase in kerf width, whereas removal depth is unaffected. Also, oscillation is more effective for high operating pressures. Figure 2.34 contains results from comparative tests with traversing, oscillating and rotating nozzle carriers. It can be noted that a rotating device is the most effective configuration for hydrodemolition processes; volumetric removal rate increases up to 300% compared to a traversing carrier, and up to 120% compared to an oscillating carrier. In contrast to an oscillating movement, a rotation of the nozzle carrier increases both removal depth and kerf width, and that may be the reason for the higher efficiency. The effects described in this section can be explained further by extending Eq. (2.24):

$$f_N = n_S \cdot \frac{v_T}{d_N} \tag{2.47}$$

Here, f_N is the nozzle oscillation frequency. If, as outlined in Section 2.3.5, an optimum number of traverse steps exists, this number can be transferred into a corresponding oscillation frequency.

2.4 Concrete parameter effects on material removal

2.4.1 Material failure types

Compressive strength is the standard strength parameter of concrete that can be evaluated under site conditions as well. The most common method is to use cylinder cores drilled off the structure. Momber (1998b) was probably the first to suggest to use the way how a cylinder fails during the compression test as a criterion of the material behaviour during hydrodemolition. The studies showed that two general types of failure, type I and type II as listed in Table 2.5, can be distinguished during the compression testing (see Momber (2000f) for more information about the testing of testing of concrete cores). If the failure type I is observed, the following features can be expected for the hydrodemolition process (compare Fig. 2.30a):

- the predominant material removal mode is intergranular erosion of the cement matrix; the aggregates are completely exposed;
- the eroded surface is cleaved and uneven;
- a comparatively large number of small, regular debris is generated;
- the generated kerfs are deep but small;

Table 2.5 Failure types during cylinder core compression testing of concrete (Momber, 1998b, 2000f)

Feature	Type I	Type II
Failure mode	Slow crumbling	Rapid crushing
Primary debris	Two; symmetric	More than two; asymmetric
Secondary debris	Many small debris; round	Several larger debris; irregular
Debris surface	Aggregates exposed, undamaged	Aggregates fractured

If the failure type II is observed, the following features can be expected for the hydrodemolition process (compare Fig. 2.30b):

- the predominant material removal mode is transgranular spalling of the concrete structure;
- the eroded surface is even; just a few gaps appear;
- the eroded surface preferably contains broken aggregate grains;
- a comparatively low number of large, irregular debris is generated;
- the generated kerfs are shallow but wide.

Type II-response could be observed usually with concrete mixtures containing large, irregular (broken) aggregate. It is assumed that the transition criterion, derived in Section 7.1.2 is partly responsible for this behaviour. Rather hard materials, such as many aggregates, respond elastic, whereas softer materials, such as cement matrix, show plastic response (see Table 1.3 for typical hardness values).

2.4.2 Compressive strength effects

The influence of the compressive strength on the relative erosion rate is already illustrated in Fig. 2.16. There is no general trend between both parameters and it seems that standard compressive strength is not a useful parameter to evaluate concrete resistance. An equal trend was reported by Kauw (1996). However, the figure changes if maximum aggregate diameter is considered as done in the graph in Fig. 2.35. Under this circumstances compressive strength can characterise the efficiency of hydrodemolition processes. For large aggregate diameters (16 mm) removal rate increases if compressive strength increases, whereas the opposite trend can be observed for small aggregate diameters (4 mm). For a given compressive strength, removal rate is always higher for a concrete made with coarse aggregates. The reasons for this behaviour are already outlined in Section 2.2.2. A strong and coarse concrete enables the formation of rather large radial fractures in the structure. Based on fracture mechanics arguments, Momber (2003b) introduced the following semi-empirical relationship:

$$\dot{V}_M \propto \frac{d_A}{\sigma_C^{0.3}} \tag{2.48}$$

Note the agreement with the trends in Fig. 2.35 at least for the medium-grained and fine-grained concrete mixtures.

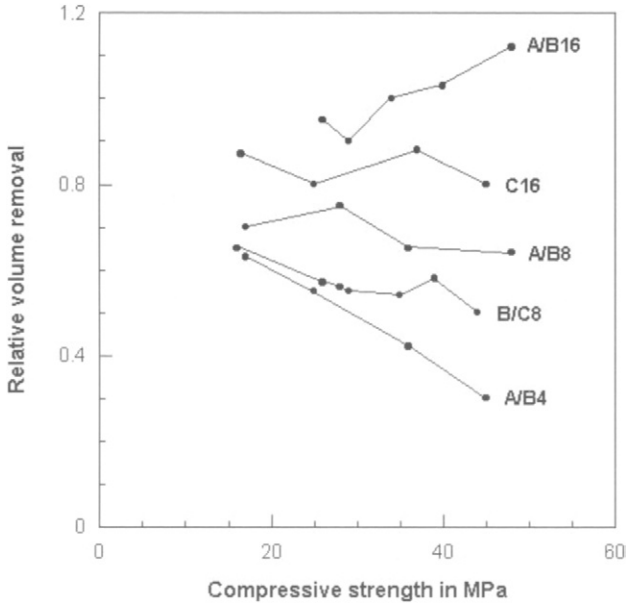

Figure 2.35 Effects of compressive strength and aggregate size on removal rate (Werner, 1991a)

2.4.3 Aggregate fineness effects

Aspects of aggregate fineness are already illustrated in Fig. 2.35 showing that concrete mixtures with fine aggregates are more resistant against water jet erosion. A design parameter that characterises aggregate fineness is the k-number (graining number). The larger the k-number the higher the amount of coarse particles. In Fig. 2.36, the relative removal rate is plotted against the k-numbers for certain sieve lines. A linear relationship, that proves the results obtained in Section 2.4.2, can be noted between both parameters. The coarser the mixture the higher the hydrodemolition efficiency. Another design parameter for concrete manufacture is the flour particle content which is the sum of cement and very fine aggregate particles. It was proven by Werner (1991a) that this parameter did not affect removal rate notably.

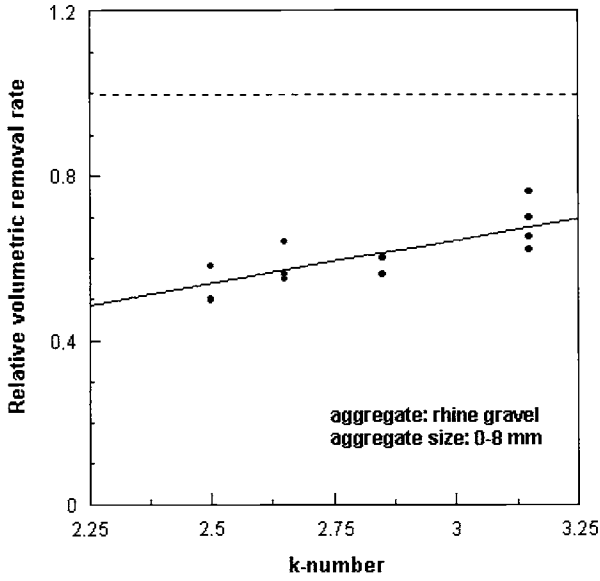

Figure 2.36 Effect of aggregate fineness on removal rate (Werner, 1991a)

2.4.4 Aggregate sort effects

Two basic types of aggregates can be distinguished in concrete. The first type is fine aggregate which is often referred to as 'sand' only. In fact, fine aggregate consists usually of rounded river (quartz) sand. The second type is coarse aggregate which is often referred to as 'gravel'. Coarse aggregate material include in fact gravel (rounded river gravel), but also broken rocks, namely basalt or limestone. It is known that the sort of coarse aggregate affects the response of concrete to hydrodemolition. This includes not only the resistance of the material but also its failure behaviour. Figure 2.37 shows the effects of coarse aggregate sort and sieve

line on the relative removal rate. Notably effects can be noted. The difference between maximum and minimum removal rate is about 470%. Removal rate is maximum for a limestone-based concrete under all circumstances, followed by the gravel-based concrete. The basalt-based concrete has the highest hydrodemolition resistance. It also seems that the effects of aggregate sort become more important for the coarser mixtures. The corresponding eroded surfaces are rather even and characterised by always broken aggregates in case of limestone, whereas they are very uneven and characterised by mainly (but not exclusively) broken aggregates in case of basalt. In case of river gravel the amount of broken aggregate was less than 30% (Werner, 1991a). Numerous aspects cause the different behaviours of the materials, among them morphology and surface energy of the aggregates and the compositions and properties of the aggregate-matrix interfaces.

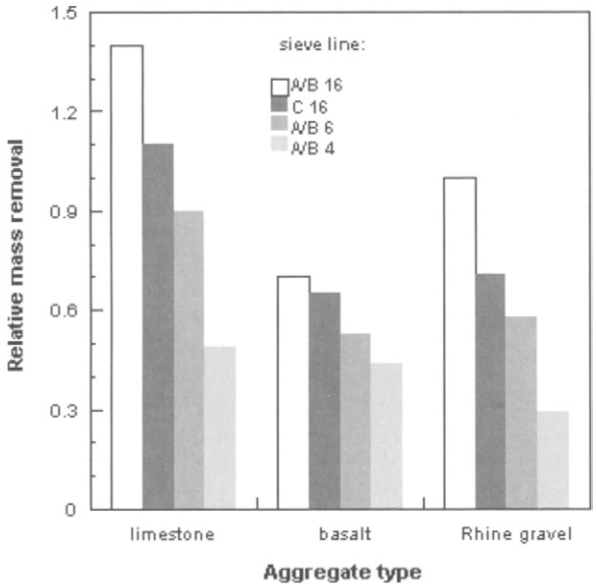

Figure 2.37 Effect of aggregate type on removal rate (Werner, 1991a)

2.4.5 Porosity effects

The influence of cement paste porosity on the relative removal rate are illustrated in Fig. 2.38. The tendencies visible in that graph also apply to the relationship between capillary porosity and removal rate (Werner, 1991a). Porosity parameters alone can not characterise the response of concrete but only if they are combined with another parameter, namely the aggregate size. For coarser concrete mixtures removal rates decrease slightly if porosity increases. The opposite trend is valid for fine concrete mixtures. However, the effects of aggregate size are much more pronounced than those of porosity.

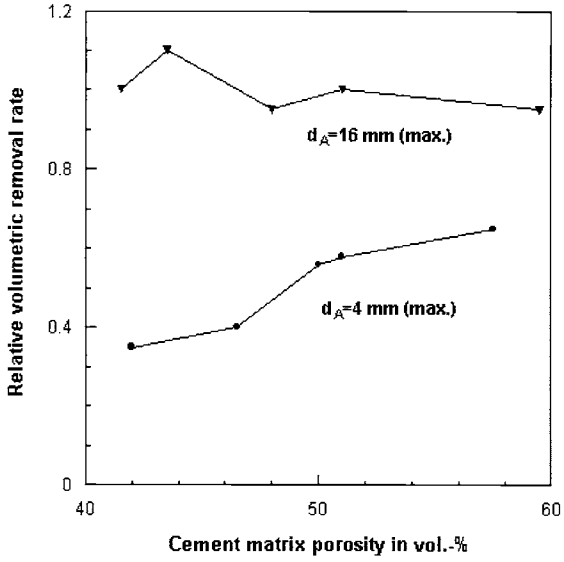

Figure 2.38 Effect of cement paste porosity on removal rate (Werner, 1991a)

2.4.6 Steel bar reinforcement effects

Many practical hydrodemolition applications include reinforced concrete structures. Effects of steel bar reinforcement on volumetric removal rate are shown in Fig. 2.39a where the influence of the depth of reinforcement is illustrated as well. A distinct drop in efficiency can be noted if the depth of reinforcement exceeds a value of 100 mm, which applies to a plain non-reinforced concrete. Thus, reinforcement supports the removal process. The thickness of the concrete layer that covers the reinforcement does, however, not play any role. The same relationship is valid for the removal depth (Kauw, 1996). The reason for the increase in hydrodemolition efficiency due to reinforcement is the installation of weak zones in the interface between concrete and reinforcement bars (Balaguru and Shah, 1992). If a single steel bar is replaced by a bar bundle, as shown in Fig. 2.39b, removal rate drops slightly. However, if a dense reinforcement bar net exists, the concrete removal process is disturbed and 'shadows zones' form at the lower surface of the steel bars. A typical practical example is shown in Fig. 2.40. These 'shadow zones' can be avoided by using complex nozzle guiding systems that include angled jets. The effect of reinforcement becomes stronger if the structure is damaged through chlorides. In that case rust grows at the corroded steel and the stresses generated due to volume expansion form cracks in the surrounding concrete. These cracks are exploited by the water jet. An increase in efficiency of about 15% was estimated if chloride-corroded reinforced concrete was treated instead of non-corroded reinforced concrete (Kauw, 1996).

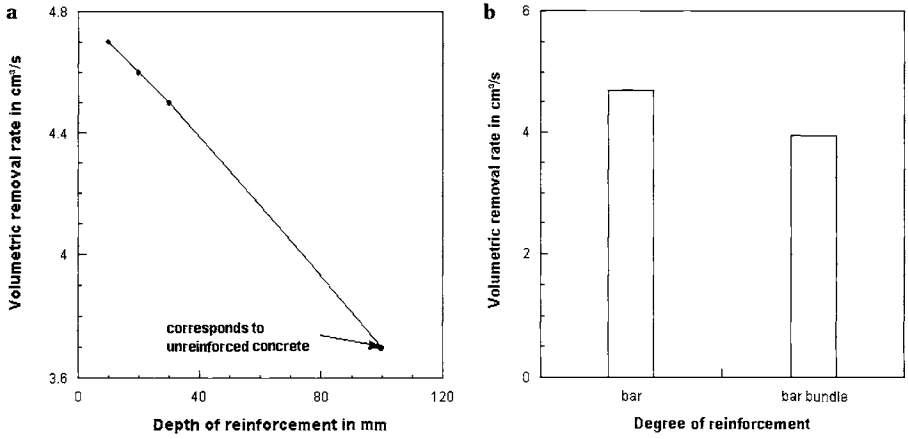

Figure 2.39 Effect of steel bar reinforcement on removal rate (Kauw, 1996)
a – single reinforcement bar
b – bar bundle

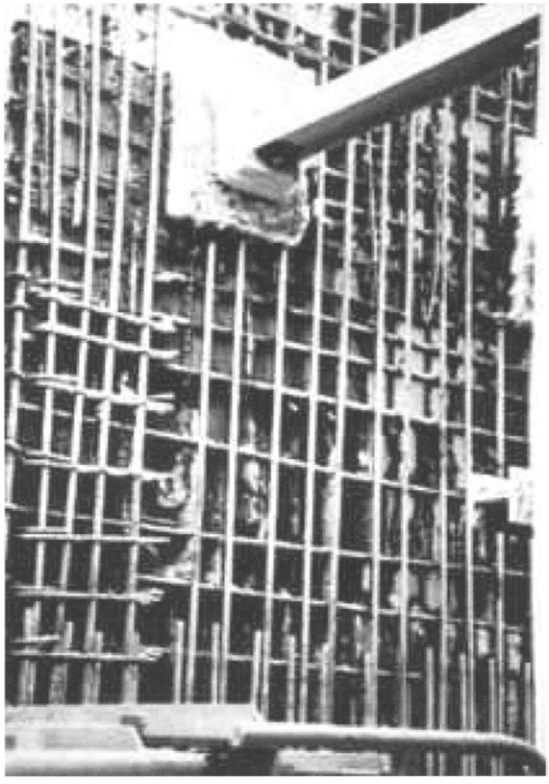

Figure 2.40 Shadow zones, formed under reinforcement bars during hydrodemolition (Rosa, 1991)

2.4.7 Steel fibre reinforcement effects

Hydrodemolition of steel fibre reinforced concrete plays a role if industrial floors or, respectively, hydraulic structures are maintained. Effects of steel fibre reinforcement on hydrodemolition processes are investigated by Hu et al. (2004) who pointed out that impact angle determines the influence of reinforcing fibres. At low impact angles (15°) the fibres form 'shadow zones', as illustrated in Fig. 2.41, that prevent the concrete behind the fibres from being eroded. For this reason, removal rate drops. However, the addition of fibres to a concrete also adds weak interfacial zones between matrix and fibres (Balaguru and Shah, 1992). The pressurised water penetrates these zones and causes a separation of the fibres. Therefore, these zones deteriorate the erosion resistance especially if the material is impinged by jets at vertical angles. Under such conditions, a steel fibre reinforced concrete can even more efficiently be removed by water jets than a corresponding plain concrete; this conclusion is proven in Fig. 2.42.

Figure 2.41 Shadow zones, formed behind reinforcement fibres during water jet erosion (Hu et al., 2004)

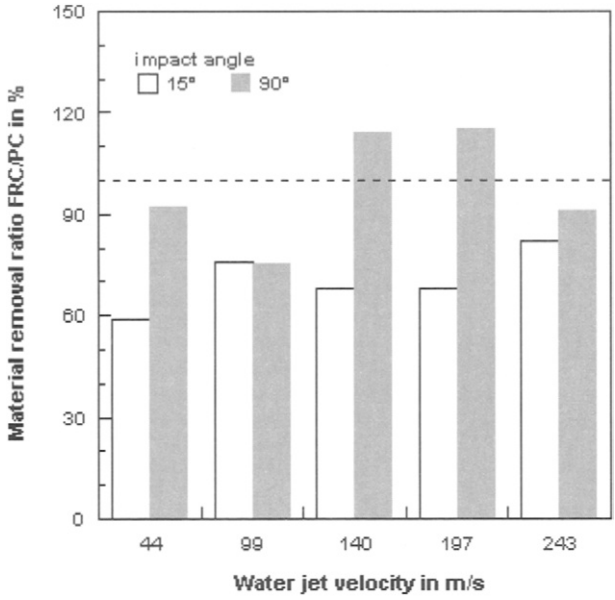

Figure 2.42 Effect of steel fibre reinforcement on mass removal (Hu et al., 2004)

2.5 Hydrodemolition model

Labus (1984) developed models for estimating depth of cut as well as material removal rate for hydrodemolition applications. The model for calculating depth of cut is based on non-dimensional terms; it has the following structure:

$$\frac{h_M}{d_N} = K_0 \cdot \left[\left(\frac{p}{\sigma_C} \right) \cdot \left(\frac{d_N}{x} \right) \cdot \left(\frac{v_J}{v_T} \right)^{0.5} \right]^{K_1} \tag{2.49}$$

Figure 2.43 shows a plot of this relationship as applied to experimentally estimated data. The correlation fits the data quite well with a correlation coefficient of 0.88, and the constants in Eq. (2.49) can be estimated to K_0=9.515, and K_1=0.355. The model was expanded to a rotating nozzle carrier; structure and geometry are illustrated in Fig. 2.44. The final model reads as follows:

$$\dot{V}_M = 2 \cdot v_T \cdot K_0 \cdot \cos\gamma \cdot (b + s \cdot \tan\gamma) \cdot \left[\left(\frac{p}{\sigma_C} \right) \cdot \left(\frac{d_N \cdot \cos\gamma}{s} \right) \cdot \left(\frac{v_J}{[(v_T - \omega_T \cdot b_1 \cdot \sin\omega_T t_E)^2 + (\omega_T \cdot b_1 \cdot \cos\omega_T t_E)^2]^{0.5}} \right)^{0.5} \right]^{K_1} \tag{2.50}$$

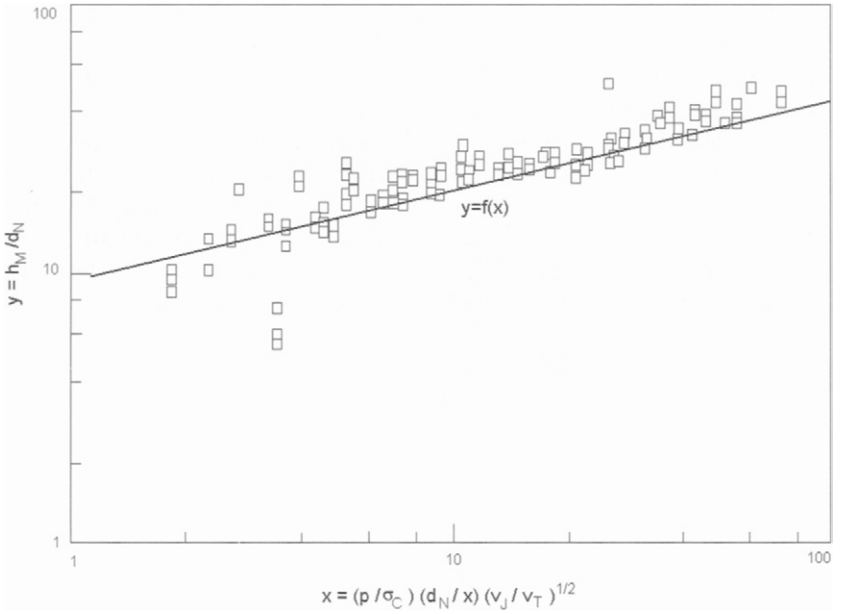

Figure 2.43 Verification of Labus' (1984) hydrodemolition model

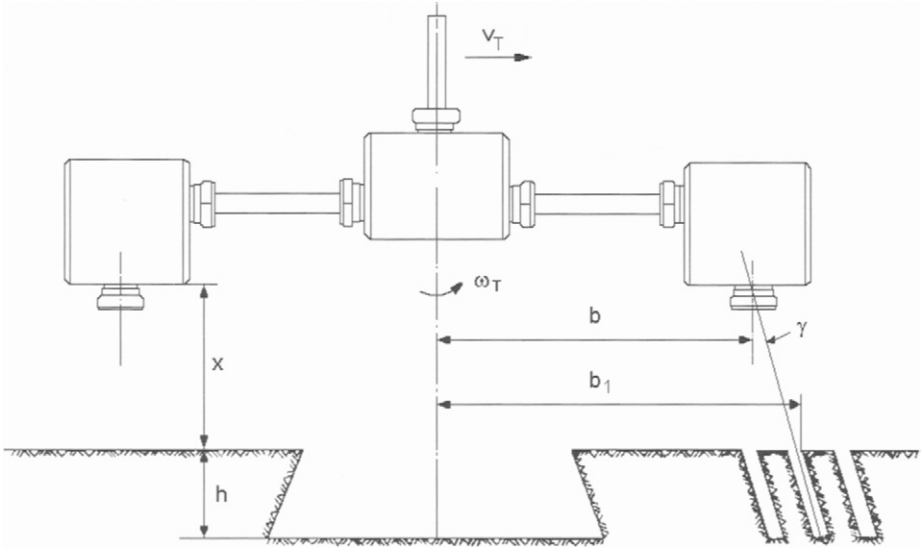

Figure 2.44 Parameters used in Eq. (2.50)

In contrast to the depth of cut, volumetric material removal rate is a function of time, since the relationship is an instantaneous rate. By integrating over the time, it takes for one revolution of the nozzle carrier head, the average volumetric material removal rate can be estimated. Calculations based on the model showed some good agreements with trends from experimental results; this applies in particular to nozzle diameter, pump pressure, and stand-off distance. However, from the results discussed in the previous Sections, it is clear that the model simplifies the effects of material parameters. Compressive strength alone can not determine the resistance of concrete to hydrodemolition. Aggregate type and size are more important, and at least one of these parameters must be included into Eq. (2.50).

CHAPTER 3

Hydrodemolition Equipment

3.1 High-pressure water jet machines

3.1.1 General structure

For on-site applications, high-pressure water jet machines are established. According to the DIN EN 1829 (2004), high-pressure water jet machines are defined correctly as follows: "Machines with nozzles or other speed-increasing openings which allow water – also with admixtures – to emerge as a free jet." High-pressure water jet machines consist of the following major parts:

- drive;
- pressure generator;
- hose lines;
- spraying devices;
- safety mechanisms;
- control and measurement devices.

Mobile high-pressure water jet machines are mobile-readily transportable machines which are designed to be used at various sites, and for this purpose are generally fitted with their own undergear or are vehicle mounted. All necessary supply lines being flexible and readily disconnectable. Stationary high-pressure water jet machines are machines designed to be used at one site for a certain period of time but capable of being moved to another site with suitable equipment. They are generally skid or base frame mounted with supply lines capable of being disconnected. Major parts of a high-pressure water jet machine utilised for hydrodemolition applications are shown in Fig. 3.1a. They include base frame, fuel tank, driving engine, couplings, high-pressure plunger pump, filter, header tank, booster pump, valves. Figure 3.1b shows a containerised hydrodemolition device.

The type of drive depends on the conditions of use. For hydrodemolition applications, drives are basically combustion engines. Under outdoor conditions, diesel combustion engines are most commonly used. Typical power ratings are between 250 kW and 500 kW. These engines drive the high-pressure pumps as well as any auxiliary energy consumers, such as required centrifugal pumps, compressors or high-pressure tools. Many of the engines connected to plunger pumps will run at a fixed speed. However, gear boxes, placed between drive and pump drive shaft, vary the speed of the crank-shaft.

3.1.2 Water supply

For running high-pressure plunger pumps reliably and for achieving a maximum service life, pump manufacturers recommend potable water quality. More detailed requirements are listed in Table 3.1. But if suitable filter and cleaning arrangements are applied, even river water or sea water could be used. The use of sea water may require mobile desalination plants; an example is shown in Fig. 3.2. Recommended filter size depends on sealing system as well as on operating pressure. Typical sizes are listed in Table 3.2. All water filter arrangements are dependent upon the supply water conditions, and they shall be checked at regular intervals,

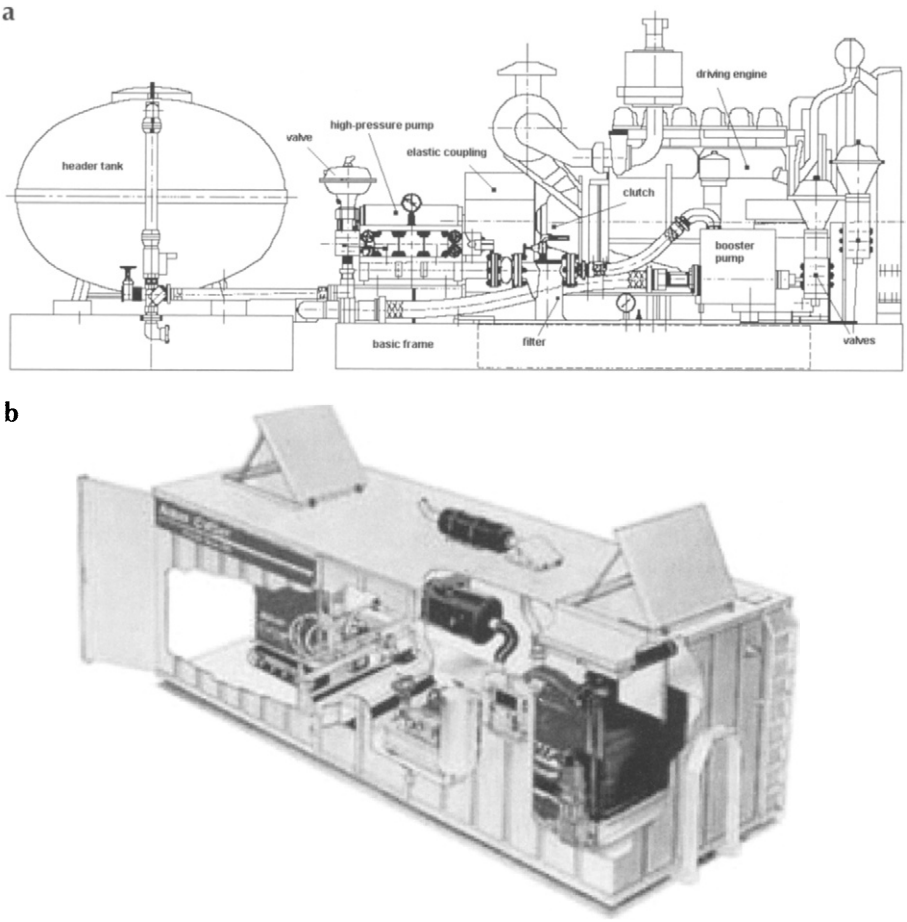

Figure 3.1 High-pressure unit for hydrodemolition applications
a – general structure (WOMA Apparatebau GmbH, Duisburg)
b – containerised unit (photograph: Aquajet Systems AB, Holsbybrunn)

usually not exceeding 8 hours. For high-power pumps as used for hydrodemolition applications, the inlet water must enter the pump under a certain required inlet pressure. Typical values for the inlet pressure are between 0.3 MPa and 0.5 MPa. The inlet pressure is usually generated by centrifugal booster pumps that are part of commercial systems (see Fig. 3.1a).

3.2 High-pressure plunger pumps

3.2.1 Structure of high-pressure plunger pumps

High-pressure pumps generate the operating pressure and supply water to the spraying device. Generally, they can be divided into positive displacement pumps

Table 3.1 Recommended water quality for plunger pumps and drinking water quality (WOMA Apparatebau GmbH, Duisburg)

Parameter / element	Permissible value	Drinking water analysis*
Temperature	35 °C	10–14 °C
pH-value	Depends on carbon hardness	7.45–7.7
Hardness	3° to 30° D.H.**	22.5°–27.5° D.H.**
Fe	0.2 mg/l	0.2 mg/l
Mn	0.05 mg/l	0.02 mg/l
Cl	100 mg/l	48–58 mg/l
$KMnO_4$	12 mg/l	–
SO_4	100 mg/l	140–205 mg/l
Cl_2	0.5 mg/l	–
Dissolved oxygen	min. 5 mg/l	–
Abrasive particles	5 mg/l	–
Conductivity	1,000 µS/cm	700–900 µS/cm

* Water works Duisburg; ** D.H. = German hardness

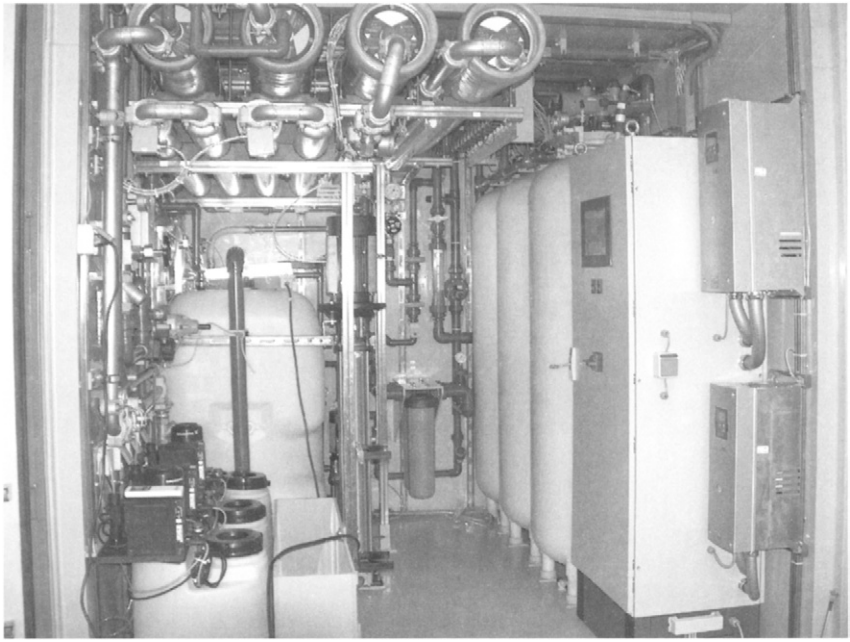

Figure 3.2 Mobile water treatment unit for jetting applications (photograph: Mühlhan Surface Protection International GmbH, Hamburg)

Table 3.2 Recommended water filter sizes (Kauw, 1992)

Operating pressure	Recommended filter size
< 100 MPa	100 µm
100 to 200 MPa	10 µm
> 200 MPa	manufacturer recommendation

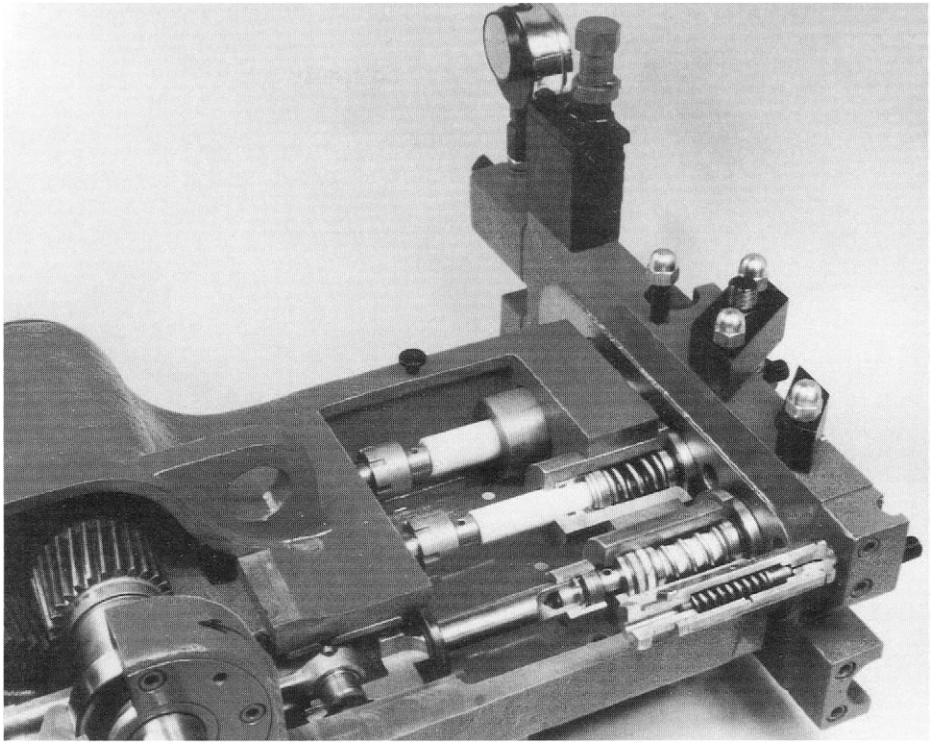

Table 3.3 Typical life time values for plunger pump components (Xue et al., 1996)

Pressure in MPa	< 30	20 ~ 31.5	31.5–50	50–70	70–100
Component	Life time in hours				
Plunger	2500	2000	1500	1000	800
Seal	1500	1000	750	600	520
Valve	3000	2500	2000	1500	1000

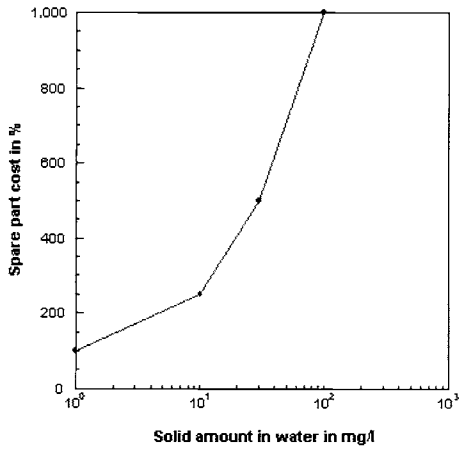

Figure 3.4 Solid content in water and maintenance cost for plunger pumps (source: Reliance Hydrotec Ltd., UK)

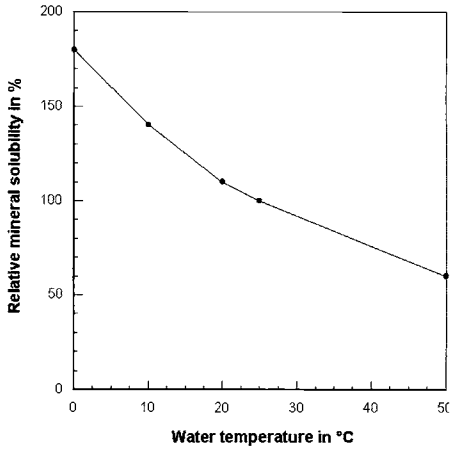

Figure 3.5 Relationship between water temperature and mineral precipitation (Zentrale für Unterrichtsmedien, Tübingen)

increases the probability of mineral precipitation as well as of cavitation. The first aspect is illustrated in Fig. 3.5; a pump part eroded due to cavitation is shown in Fig. 3.6. Both processes are highly erosive to pump components, and temperature control devices, coupled to shut-off mechanisms, should be part of any pump unit.

The pump head hosts the water inlet and water outlet valve arrangements. It consists regularly of corrosive-resistant forged steel, partly also of coated spheriodal graphite cast iron. Typical plunger diameters for on-site high-pressure plunger pumps utilised for hydrodemolition applications are between 25 mm and

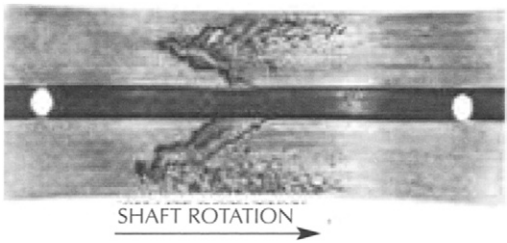

Figure 3.6 Damage to a bearing due to cavitation erosion (photograph: Neale Cons. Engr., Ltd., Dogmersfield)

40 mm. The plungers are made from coated steel alloys, hard metals or ceramics (the latter material is limited to rather low operating pressures).

Safety and control devices include safety devices and pressure-measuring devices. Safety devices prevent the permissible pressure from being exceeded by more than 2.0 MPa, or 15%. These devices include pressure relief valves or burst disks, respectively. Automatic pressure regulating valves limit the pressure at which the pump operates by releasing a present proportion of the generated volumetric flow rate back to the pump suction chamber or to waste. It should be used to regulate the water pressure from the pump and is individually set for each operator. Pressure-measuring devices directly measure and display the actual operating pressure.

3.2.2 Performance charts and efficiency

Plunger pumps can be characterised by performance charts. Pump manufacturers publish performance tables for any commercial pump type. Table 3.4 is a typical performance table. The corresponding chart is plotted in Fig. 3.7. In such charts, the most important technical parameters of the pumps, such as power rating, operation pressure, volumetric flow rate, plunger diameter, and crank-shaft speed, are related to each other. The theoretical hydraulic power consumed by a plunger pump is:

$$P_T = 0.0166 \cdot \dot{Q}_N \cdot p \tag{3.1}$$

Here, p is the operating pressure in MPa, and $\dot{Q}_N$ is the nominal volumetric flow rate in l/min; the power P_T is given in kW. For a given hydraulic power, Eq. (3.1) is a hyperbolic function (y=a/x), and each hyperbola can be considered as a line of constant power. This is shown in Fig. 3.7 for different crank-shaft speeds. For a plunger diameter of d_P=35 mm, a pressure of p=130 MPa, and a crank-shaft speed of n_C=456 min^{-1}, the hydraulic power of the pump would be P_T=371 kW. In practice, however, the consumed power exceeds this theoretical value because of losses due to leakage, pulsation, water compression, and other mechanisms. Thus, the hydraulic efficiency is introduced to assess the efficiency of plunger pumps. This hydraulic efficiency is:

$$\eta_H = P_T / P_H \tag{3.2}$$

Values for η_H depend on pump type and operating pressure: they increase if operating pressure increases. Typically, values between η_H=0.8 and η_H=0.95 can be considered for the pressure range between 200 MPa and 380 MPa. The overall efficiency of a high-pressure plunger pump can be estimated as follows:

$$\eta_O = \eta_H \cdot \eta_M \cdot \eta_T \tag{3.3}$$

where η_M is the mechanical efficiency (internal frictional losses) and η_T is the

Table 3.4 Performance table of a commercial high-pressure plunger pump utilised for hydrodemolition (WOMA Apparatebau GmbH, Duisburg)

Plunger diameter in mm	Gear ratio — Drive speed in min^{-1}			Crank-shaft speed in min^{-1}	Required drive in kW	Volumetric flow rate in l/min	Permissible pressure in MPa
	1,500	1,800	2,100				
30			4.60	456	319	126	140
		3.96		454	318	125	
		4.60		391	273	108	
	3.30			454	318	125	
	3.96			378	265	104	
	4.60			326	228	90	
35			4.60	456	405	172	130
		3.96		454	403	171	
		4.60		391	347	147	
	3.30			454	403	171	
	3.96			378	337	143	
	4.60			326	289	123	
40			4.60	456	415	228	100
		3.96		454	412	227	
		4.60		391	355	196	
	3.30			454	412	227	
	3.96			378	344	190	
	4.60			326	296	163	
45			4.60	456	426	292	80
		3.96		454	424	291	
		4.60		391	365	250	
	3.30			454	424	291	
	3.96			378	353	242	
	4.60			326	304	209	
50			4.60	456	429	364	65
		3.96		454	427	362	
		4.60		391	368	312	
	3.30			454	427	362	
	3.96			378	356	302	
	4.60			326	306	260	

efficiency of energy transmission between drive and pump. Results of measurements are shown in Fig. 3.8. The overall efficiency ranges from 60% to about 85% and increases if operating pressure increases. Compared to overall efficiency values of 60% to 70% for hydraulically driven intensifier pumps, these values are higher.

State-of-the-art high-pressure plunger pumps are capable of generating operating pressures up to p=300 MPa. The maximum permissible operating pressure of a certain pump type depends on the permitted rod force as follows:

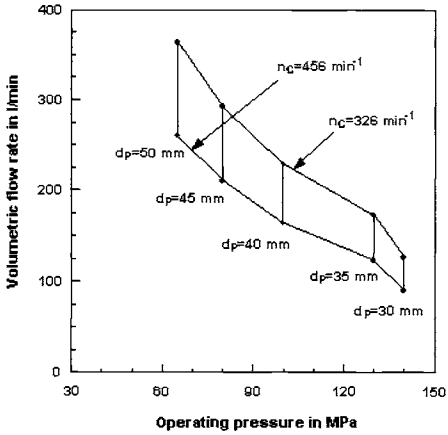

Figure 3.7 Flow chart of a high-pressure plunger pump (based on Table 3.4; H_P=95 mm, n_P=3)

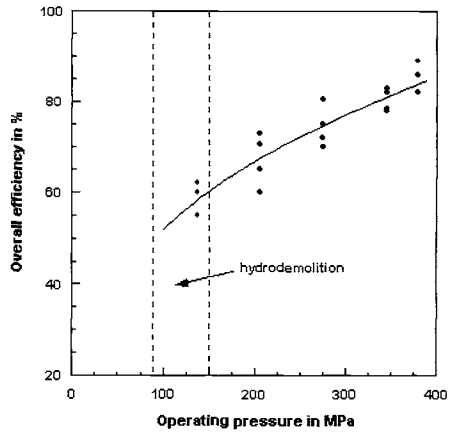

Figure 3.8 Overall efficiency of high-pressure plunger pumps (Veenhuizen, 2000)

$$F_P = (\pi / 4) \cdot d_P^2 \cdot p \tag{3.4}$$

with F_P being the rod force. Plunger diameter that enters the equation in a quadratic relationship, is the critical parameter. The rod force for a plunger diameter of d_P=35 mm operated at a pressure of p=130 MPa would be F_P=125 kN. An increase in the plunger diameter to d_P=40 mm (14% increase) would generate a rod force of F_P=163 kN (30% increase).

3.2.3 Nominal volumetric flow rate

The nominal volumetric flow rate delivered by a plunger pump can be approximated as follows:

$$\dot{Q}_N = \eta_V \cdot \dot{Q}_P \tag{3.5}$$

The loss-free volumetric flow rate is given from geometry assumptions:

$$\dot{Q}_P = n_C \cdot \frac{d_P^2 \cdot \pi}{4} \cdot H_S \cdot N_P \tag{3.6}$$

Here, n_C is the crank-shaft speed, d_P is the plunger diameter, H_S is the stroke, and N_P is the number of plungers. Typical values for these parameters are listed in Table 3.5. Assuming typical values for a hydrodemolition unit (n_C=456 min^{-1}, d_P=35 mm, H_S=140 mm, N_P=3) the corresponding nominal volumetric flow rate is $\dot{Q}_P$ =184 l/min. The crank-shaft speed of a pump drive depends on the stroke. The acceleration of the plunger (of the liquid volume, respectively) should not exceed a critical value. For most pumps, the following criterion holds (Vauck and Müller, 1994):

Table 3.5 Values for typical pump parameters for hydrodemolition applications

Parameter	Unit	Range
Crank-shaft speed	min^{-1}	300–500
Plunger diameter	mm	30–40
Number of plungers	–	3–5
Stroke	mm	100–140

$$n_C^2 \cdot H_S = 1...2\,m/s^2 \tag{3.7}$$

Eq. (3.6) is partly graphically illustrated in Fig. 3.7. State-of-the-art plunger pumps are capable of generating nominal volumetric flow rates up to about 1,000 l/min. However, typical volumetric flow rates for hydrodemolition applications are between 100 l/min and 280 l/min. The volumetric efficiency parameter in Eq. (3.5) can be subdivided into two parts:

$$\eta_V = \eta_C \cdot \eta_G \tag{3.8}$$

whereby η_C is considered to be an elasticity parameter which mainly involves compressibility effects (Fritsch, 1991). An approximation is:

$$\eta_C \cong 1 - \xi_C \tag{3.9}$$

The parameter ξ_C is the water compressibility which becomes important if operating pressure increases. Compressibility can be assessed by applying the volume-elasticity model:

$$\Delta p = -E_W \cdot \frac{\Delta Q}{Q_0} \tag{3.10}$$

whereby the modulus of elasticity of water is E_W=1,962 MPa (Oertel, 2001). For an operating pressure of p=130 MPa, the compressibility factor would be 6.6% (ξ_C=0.066). It can be seen in Fig. 3.9 that Eq. (3.10) can be applied to consider compressibility effects in the pressure range between 80 and 150 MPa that is usually utilised for hydrodemolition. The parameter η_G is a volumetric rating factor considering losses due to leakage. For oscillating plunger pumps, this parameter is often be neglected, and values close to unity can be assumed (Fritsch, 1991). Therefore:

$$\dot{Q}_N \cong (1 - \xi_C) \cdot n_C \cdot \frac{d_P^2 \cdot \pi}{4} \cdot H_S \cdot N_P \tag{3.11}$$

Generally, the volumetric flow rate of a plunger pump is not a constant value. It rather oscillates according to a sinus-function:

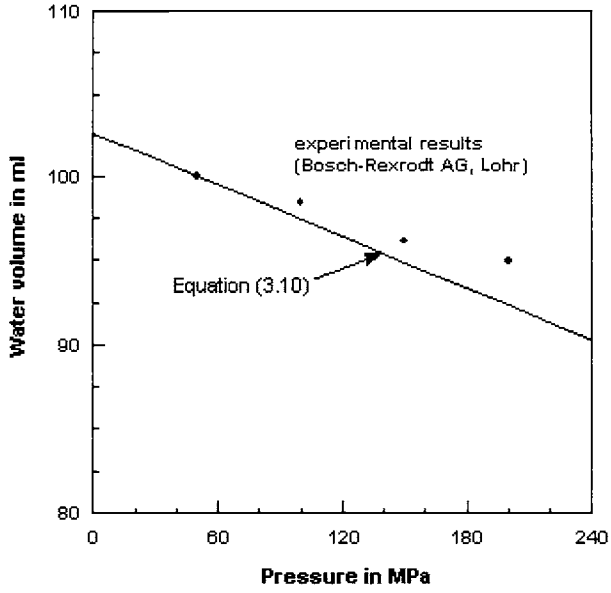

Figure 3.9 Compressibility of water (measurements: Bosch-Rexroth AG, Lohr)

$$\dot{Q}_N = A_P \cdot v_C \cdot \sin \alpha_C \tag{3.12}$$

Here, A_P is the plunger cross section, v_C is the circumferential velocity and α_C is the angle of the crack-shaft. This relationship is illustrated in Fig. 3.10. The water volume is first accelerated an then decelerated. It can be seen from Eq. (3.12) that

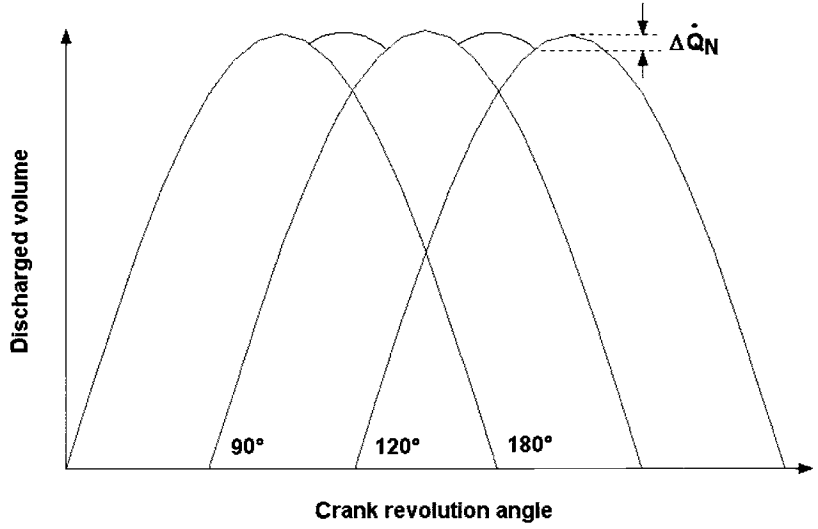

Figure 3.10 Volumetric flow rate oscillation in a triplex plunger pump (adapted from De Santis, 1985)

the unsteady volumetric flow rate is basically a result of the unsteady circumferential velocity of the crank-shaft. The average plunger speed (which is about the average liquid flow velocity in the pump) is simply given as follows:

$$v_P = 2 \cdot H_S \cdot n_C \tag{3.13}$$

See De Santis (1995), Nakaya et al. (1983) and Summers (1995) for further details.

3.3 High-pressure hoses and fittings

3.3.1 Performance parameters of hoses and fittings

The transport of the high-pressure water to the spraying devices occurs through high-pressure lines. For on-site applications, these are flexible hose-lines. Hose lines are actually flexible hoses operationally connected by suitable hose fittings (see Fig. 3.11). Hose fittings are component parts or sub-assemblies of a hose line to functionally connect hoses with a line system or with each other (see Fig. 3.12). High-pressure hoses are flexible, tubular semi-finished products designed of one or several layers and inserts. They consist of an outer cover (polyamide, nylon), a pressure support (specially treated high-tensile steel wire), and an inner core (POM, polyamide, nylon). Any hose must be tested for bursting; the permissible operating pressure of hoses should not exceed 40% of the estimated burst pressure. Hoses

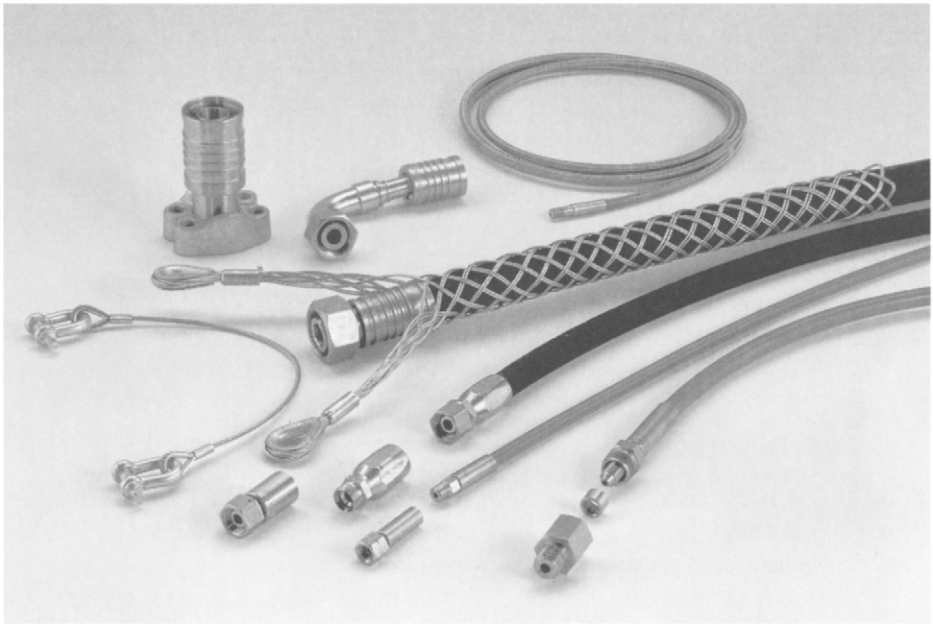

Figure 3.11 High-pressure hoses, fittings and armatures (photograph: WOMA Apparatebau GmbH, Duisburg)

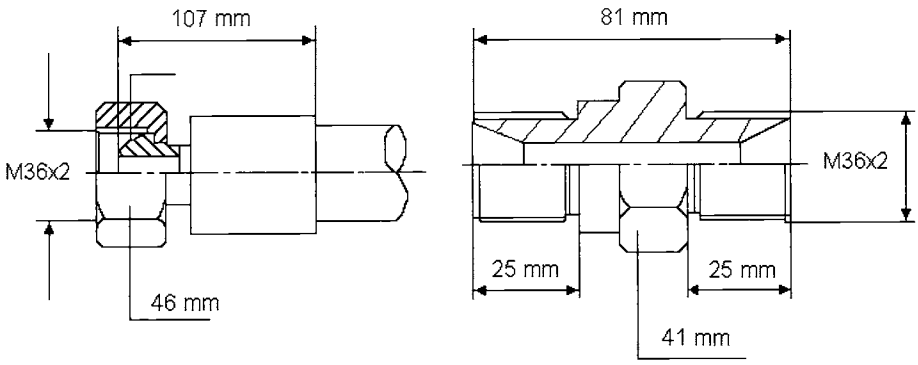

Figure 3.12 High-pressure hose fitting (WOMA Apparatebau GmbH, Duisburg)

capable of use for pressures equal to or higher than the maximum operating pressure of the pressure generating unit must be selected. Typical nominal lengths of high-pressure hoses are between l_H=3 m and l_H=120 m. Table 3.6 contains typical technical parameters for hoses used in hydrodemolition operations.

Table 3.6 Technical data of high-pressure hoses for hydrodemolition operations

Nominal diameter in mm	Maximum operating pressure in MPa	Maximum delivery length in m	Specific weight in kg/m	Minimum bend radius in mm
12	110	40*	1.22	200
12	140	40*	1.71	200
20	90	40*	1.64	280
20	100	40*	2.10	280

* Delivery length above 40 m up to 100 m upon request

3.3.2 Pressure losses in hose lines

A permanent problem with high-pressure hoses is the pressure loss in the hose-lines. An approach for estimating the pressure loss is:

$$\Delta p = \xi_F \cdot \frac{\rho_F}{2} \cdot v_F^2 \cdot \frac{l_H}{d_H} \tag{3.14}$$

Here, ξ_F is a friction number, ρ_F is the water density, v_F is the flow velocity, l_H is the hose length, and d_H is the hose diameter. The flow velocity of the water inside a hose can be estimated from flow rate conservation conditions:

$$v_F = \frac{4 \cdot \dot{Q}_N}{\pi \cdot d_H^2} \tag{3.15}$$

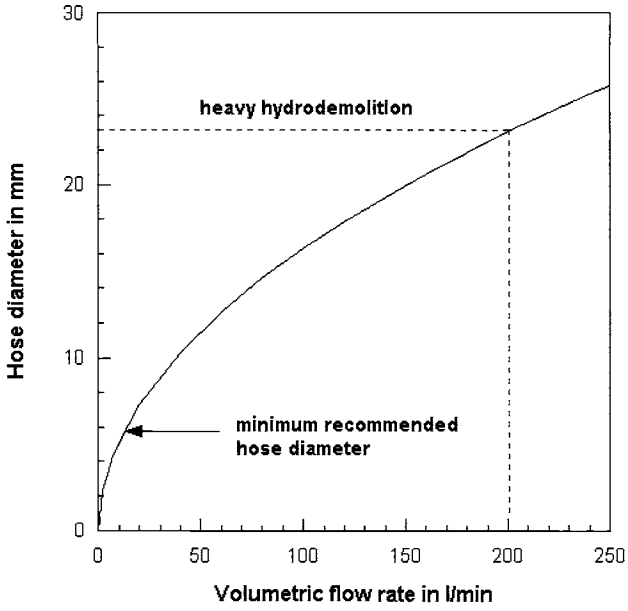

Figure 3.13 Selection of suitable hose diameters

For a hose diameter of d_H=20 mm and a volumetric flow rate of $\dot{Q}_N$=180 l/min, the corresponding flow velocity in the hose would be v_F=9.5 m/s. Recommendations for suitable hose diameters are given in Fig. 3.13. The friction number depends on the Reynolds-Number, Re, and on the ratio between hose diameter and relative internal wall roughness, k:

$$\xi_F = f(Re, k) \tag{3.16a}$$

This number can be estimated from the so-called Nikuradse-Chart which can be found in standard books on fluid mechanics (e.g. Oertel, 2001). An empirical relationship is:

$$\frac{1}{\xi_F^{1/2}} = 1.74 - 2 \cdot \lg\left(\frac{18.7}{Re \cdot \xi_F^{1/2}} + \frac{2 \cdot k}{d_H}\right) \tag{3.16b}$$

The Reynolds-number of the flow through a hose is given as follows:

$$Re = \frac{v_F \cdot d_H}{\nu_F} \tag{3.17a}$$

With Eq. (3.15) and ν_F=10^{-6} m^2/s (Table 2.1), Eq. (3.17a) reduces to:

$$Re = 2.12 \cdot 10^4 \cdot \frac{\dot{Q}_N}{d_H} \tag{3.17b}$$

Here, $\dot{Q}_N$ is given in l/min, and d_H is given in mm. For a typical combination $\dot{Q}_N$=180 l/min and d_H=20 mm, the Reynolds number is Re=1.91·10^5. For a Reynold number range between 1·10^5 and 2·10^5, a friction number of ξ_F=0.038 can be assumed. Eqs. (3.14) to (3.17) deliver:

$$\Delta p \propto d_H^{-5} \tag{3.18}$$

This equation illuminates the overwhelming influence of the hose diameter on the pressure loss. To substitute these pressure losses, a certain amount of additional power

$$\Delta P = \Delta p \cdot \dot{Q}_N \tag{3.19}$$

must be generated by the high-pressure pump. Considering Eqs. (3.18) and (3.19), additional power consumption has a reverse 5th-power relationship to the hose diameter. Manufacturers of hydrodemolition equipment publish pressure-loss charts or pressure-loss tables which can be used for estimating real pressure losses in hoses (see Fig. 3.14 for an example). An empirical rule for selecting the proper hose diameter is: the flow velocity in the hose should not exceed the value of v_F=8 m/s. Based on Eq. (3.15), the corresponding minimum hose diameter is:

$$d_H = 1.63 \cdot \dot{Q}_N^{1/2} \tag{3.20}$$

In that equation, the volumetric flow rate is in l/min, and the hose diameter is in mm. If no standard diameter is available for the calculated value, the next larger

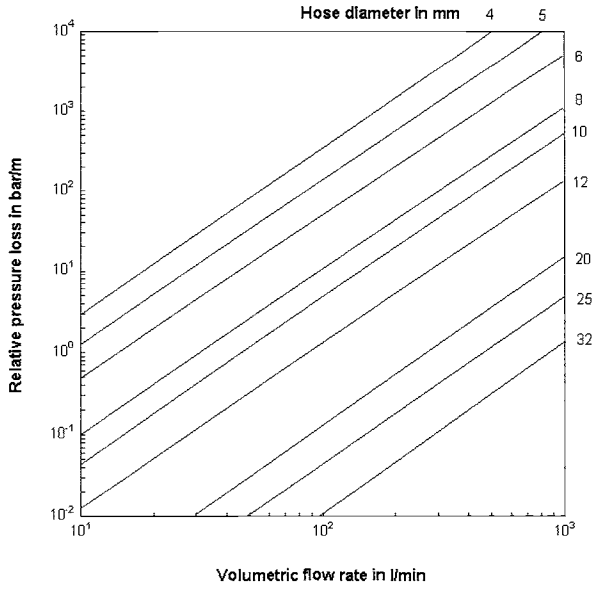

Figure 3.14 Pressure losses in high-pressure hoses (WOMA Apparatebau GmbH, Duisburg)

diameter should be selected. As an example: for a volumetric flow rate of 180 l/min, Eq. (3.20) delivers 21.9 mm; the recommended internal hose diameter is d_H=25 mm. Equation (3.20) is graphically illustrated in Fig. 3.13; this graph allows a quick assessment of suitable hose diameters.

The correct pressure losses in hose fittings should be measured for any individual fitting. However, such values are not available in most cases. The following empirical approximation can be performed: the pressure loss in a single fitting is equal to the pressure loss in a hose of equal diameter with a length of 3 m. If, for example, a volumetric flow rate of 180 l/min and a hose diameter of 25 mm are used, the relative pressure loss estimated from Fig. 3.14 is p_V=0.5 bar/m. Thus, the absolute pressure loss in the fitting is p_V=0.15 MPa. This corresponds to a power loss of E_L=0.153 kW. For hydrodemolition tools and valves, special pressure loss-diagrams are available.

3.3.3 Service life of high-pressure hoses

Factors that affect service life of high-pressure hoses include the following (Webster and Johns, 2003):

- hose fitting stress;
- abrasion;
- kinks and crushes;
- impulse and flex fatigue;
- flex lance damage.

Life time of high-pressure hoses depends on the operating pressure; this is shown in Fig. 3.15. The most common type of damage is at the fittings because this is the weakest point of the hose assembly. To reduce damage, stiffeners can be installed on the hose assembly that reduce the bending moment directly behind the fitting. A general rule of thumb is to keep the hose supported and straight directly behind the fitting for a minimum length of three times the hose diameter. Abrasion occurs to the outer cover and underlying reinforcement. It is caused by rubbing of the hoses against rough surfaces. When the outer cover is abraded to an extent that the reinforcement is visible, the environment causes further degradation. Kinks and crushes are due to mishandling and improper installation. Dragging the hose around a sharp corner or pulling the hose when it is in a coil state and not letting the hose naturally un-twist may cause the hose to kink. Crushes may occur if heavy equipment is dropped on the hose assembly. Both kinks and crushes will significantly reduce service life, or may even lead to immediate failure when pressurised. The main reasons that cause hose fatigue are pressure cycling and, to a lesser extend, hose flexing. Results of some corresponding tests are listed in Table 3.7. Practical experience, however, has shown that service life mainly depends on hose handling. Proper hose handling, even if it is sometimes time consuming, increases service live and reduces cost for repair and replacement.

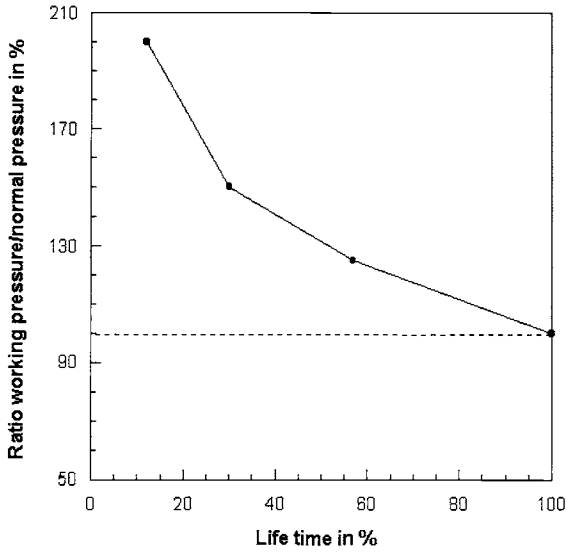

Figure 3.15 Operating pressure and hose life time (JISHA, 1992)

Table 3.7 Results of high-pressure hose tests (Webster and Johns, 2003)

Test	Test results
Torsion test	10% reduction in impulse life with 10-degree twist.
Bent fitting test	63% reduction in impulse life when bent at minumum bend radius without keeping hose straight behind fitting.
Compressive/tensile test	52% reduction in impulse life with 60 lb. continuous axial compressive or tensile load.

3.4 Hydrodemolition tools

3.4.1 General structure and subdivision

Hydrodemolition tools can be subdivided according to Fig. 3.16. Hand-held tools can be used as far as the jet reaction force does not exceed a value of F_R=250 N. For reaction force levels 150 N<F_R<250 N, hand-held guns can only be used with additional body support. The classical tool for manual applications is the high-pressure gun as illustrated in Fig. 3.17. It consists of hand grip, pressure housing, trigger, control units, and nozzle pipe. The guns can be equipped with different nozzle carriers. Any tool can be run with mechanic (valve), electric or pneumatic control, respectively. According to the valve-type, hand-held tools can further be subdivided into dry shut-off safety valve, and dump safety control valve. Dry shut-

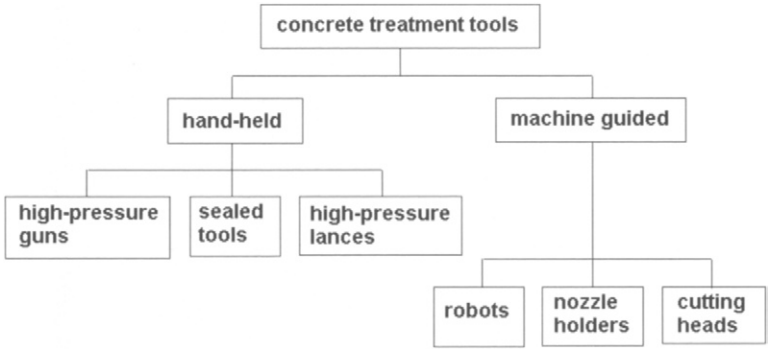

Figure 3.16 Subdivision of hydrodemolition tools

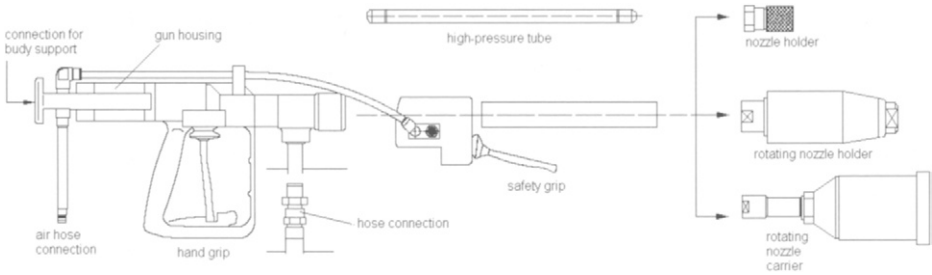

Figure 3.17 High-pressure gun (WOMA Apparatebau GmbH, Duisburg)

off valves, normally hand-controlled, automatically shut off flow to the gun when released by the operator, but retain the operating pressure within the supply line when so shut off. Damp safety control valves automatically terminate significant water flow to the gun when released by the operator, thus relieving the operating pressure within the whole system by diverting the flow rate produced by the pump to atmosphere through an orifice and dump line, which must be of sufficient size. A special hand-held tool for emission-free surface preparation applications is shown in Fig. 3.18. These tools are equipped with sealing systems consisting of brushes or, in case of very high sealing demands, of sealing lips. Typical technical parameters for two tool types – for floor cleaning and for wall cleaning – are listed in Table 3.8.

A basic part of any rotating nozzle carrier is a lead-through. An example is shown in Fig. 3.19a. This construction enables the flow of high-pressure water through rotating parts. The permissible rotational speed can be as high as several thousands revolutions per minute. An operational problem with rotating nozzle carriers is the water volume loss as the high-pressure water passes the lead-through. This loss depends on the operating pressure and can be approximated with the following equation:

Figure 3.18 Emission-free performing hydroblasting tool (WOMA Apparatebau GmbH, Duisburg)

Table 3.8 Technical parameters of emission-free performing concrete cleaning tools

Parameter	Water jetting tool		
	ETRC*[1)]	Vacujet*	Lizard*
max. operating pressure	210 MPa	250 MPa	200 MPa
max. volumetric flow rate	20 l/min	20 l/min	40 l/min
max. rotational speed	2,500 min^{-1}	2,500 min^{-1}	2,500 min^{-1}
weight	9.2 kg	ca. 36 kg	ca. 55 kg
working width	180 mm	ca. 225 mm	ca. 380 mm
number of nozzles	up to 4	up to 8	up to 10

* trade names WOMA Apparatebau GmbH, Duisburg [1)] see Fig. 3.18

$$\dot{Q}_L = \xi_L \cdot p^{1/2} \tag{3.21}$$

Here, the volumetric flow rate is in l/min, and the operating pressure is in MPa. The constant has an approximate value of ξ_L=0.47 for operating pressures up to 120 MPa. The loss in volumetric flow rate for a rotating tool operating at a pressure of p=120 MPa and a volumetric flow rate of $\dot{Q}_N$=180 l/min would be $\dot{Q}_L$=5 l/min, or about 3%. The rate the water jet traverses at over the surface is a function of the rotational speed of the nozzle carrier:

$$v_T = \omega_T \cdot r_T \tag{3.22}$$

Here, ω_N is the rotational speed, and r_T is the radial distance between rotational centre and nozzle location. Typical values for rotational speeds are listed in Table 3.8.

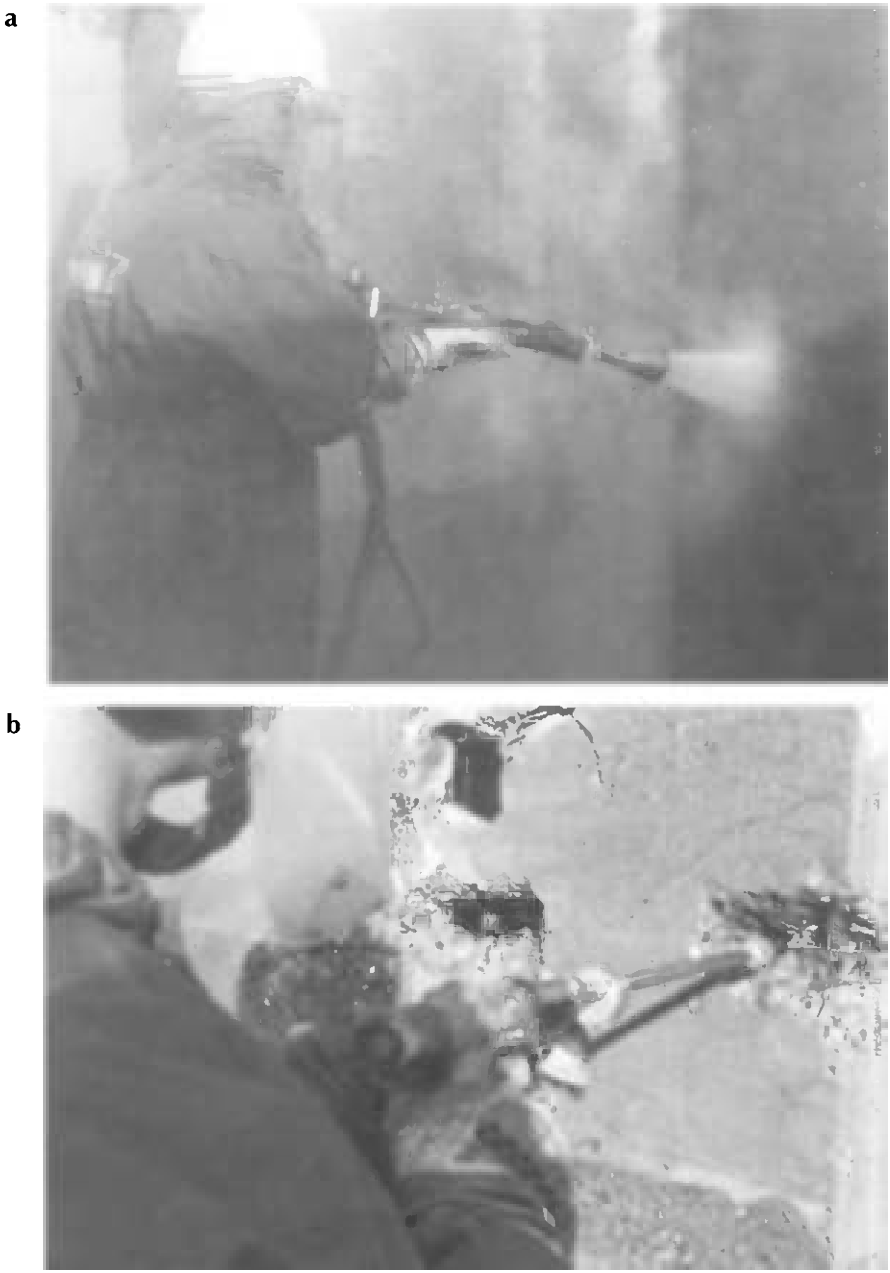

Figure 3.19 High-pressure gun with different nozzle carriers (photographs: WOMA Apparatebau GmbH, Duisburg)
a – pneumatically driven multiple nozzle head with rotating lead-trough
b – single nozzle

Self-propelling rotating nozzle carrier heads (Fig. 3.17) are usually applied for hand-held jetting guns. The driving force is supplied by a radial component of the jet reaction force.

$$F_R^* = \cos\theta_R \cdot F_R \tag{3.23}$$

According to Eq. (3.24) the driving force – and thus the rotational speed – is related linearly to the volumetric flow rate, and has a square-root relationship to the operating pressure. Eq. (3.24) shows also that rotational speed – and thus the exposure time of the exiting water jet – can not be varied independently on volumetric flow rate (nozzle diameter, respectively) and operational pressure. Therefore, the performance of self-propelling rotating nozzle carrier heads can hardly be optimised. On the other hand, no additional energy and no additional lines or hoses are required for driving them. Self-propelling carriers can be utilised for a selective coating removal from concrete surface. Their performance is often more gentle than that of externally driven carriers.

Externally driven rotating nozzle carrier heads are driven by separate mechanisms. Hydraulic and mechanic drives can be found usually in mechanised tools or in stationary systems fed by plunger pumps with comparatively high values of hydraulic power. They are very efficient for driving hydrodemolition robots. Pneumatic drives are used for hand-held cleaning tools as well as for on-site abrasive water jet cutting systems. A typical pneumatic drive device is shown in Fig. 3.19a. For externally driven nozzle carrier heads, rotational speed, operational pressure and volumetric flow rate can be varied independently from each other. Additional power is required to drive external nozzle carriers; a typical value for a pneumatically driven carrier is 0.09 kW which is a negligible part of the complete hydraulic power. Externally driven carriers usually perform more powerful than self-propelling carriers. They can be utilised for the roughening and profiling of concrete surfaces, and for the removal of resistant coatings.

The flow of the high-pressure water through the gun causes pressure losses. These losses can be estimated from pressure loss graphs provided by manufacturers.

3.4.2 Hydrodemolition robots

Mechanised tools are applied for large-scale applications, namely for bridges, parking decks, and tunnels. Most of these tools are also equipped with sealing systems and perform emission-free. Mechanised tools are very flexible. The structure of a commercial hydrodemolition robot is illustrated in Fig. 3.20. Figure 3.21 shows how such a robot can be utilised for various jobs, namely floor decontamination, overhead demolition, and vertical concrete removal. Table 3.9 lists typical performance parameters.

3.4.3 Jet reaction force

The border between hand-held and mechanized tools is set by the permissible reaction force generated by a water jet. At least in Europe exist regulations that

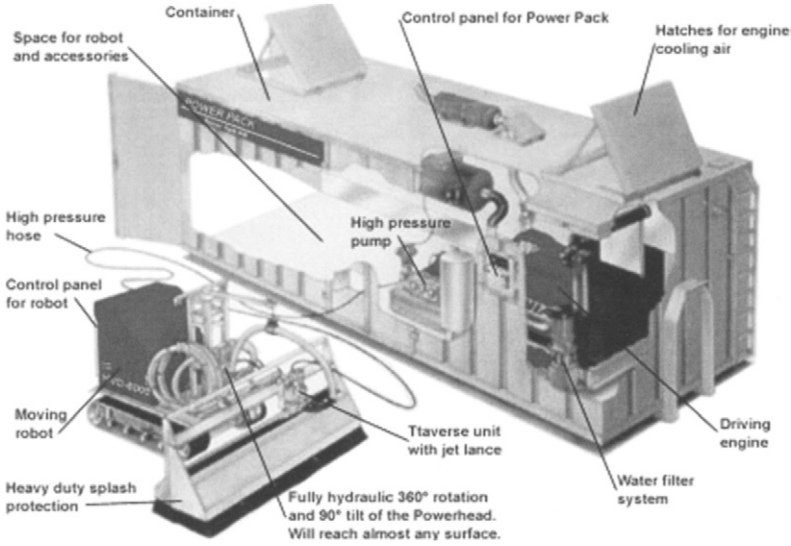

Figure 3.20 Structure of a hydrodemolition robot (photograph: Aquajet Systems AB, Holsbybrunn)

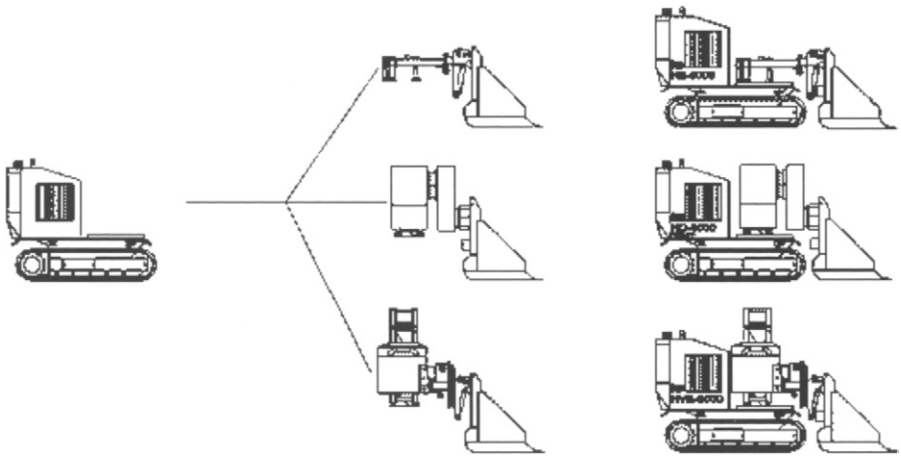

Figure 3.21 Utilisation of a hydrodemolition robot (Aquajet Systems AB, Holsbybrunn)

forbid the application of hand-held devices if the axial component of the reaction force exceeds the critical value of F_R=250 N (corresponding to a weight of 25 kg). In the range between F_R=150 N and F_R=250 N, hand-held guns are allowed, but they need to be reinforced by body support or by a second hand grip. These relationships are illustrated in Fig. 3.22 which also shows critical combinations of operating pressure and volumetric flow rate. An average rule says that an operator may be capable of holding about one-third of his body weight (Summers, 1991). For example: an operator with a body weight of 75 kg could resist a reaction force

Table 3.9 Performance parameters of concrete hydrodemolition robots

Parameter	Type (Manufacturer)	
	Robot 432D (Conjet AB)	HD 6000 (Aquajet AB)
Length in mm	3,500	2,480–2,730
Width in mm	2,660	2,000
Cutting/working width in mm	2,200	up to 2,000
Height in mm	1,500	1,250
Weight in kg	2,500	1,600
Power source	Diesel engine	Diesel engine

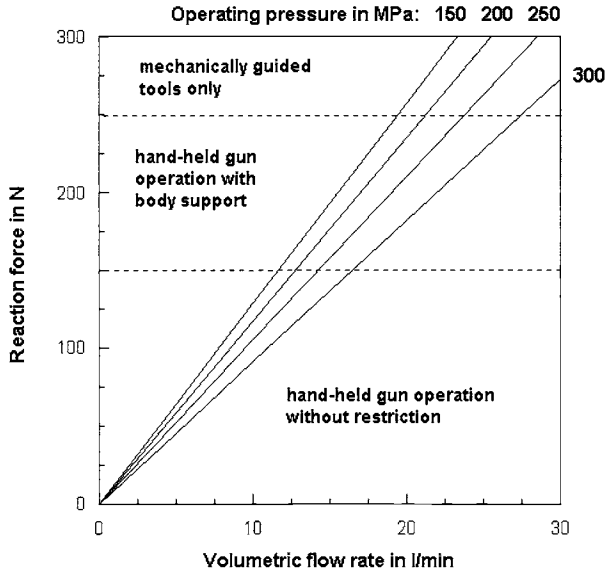

Figure 3.22 Critical conditions for hand-held gun operation; see Eq. (3.24)

of F_R=250 N. The reaction force of a water jet can be estimated through impulse flow conservation:

$$\dot{I}_J = \dot{m}_W \cdot v_J = 0.743 \cdot \dot{Q}_N \cdot p^{1/2} = F_R \qquad (3.24)$$

Here, $\dot{I}_J$ is the jet impulse flow, $\dot{m}_w$ is the water mass flow rate, and v_j is the jet velocity. In the right term of Eq. (3.24), p is in MPa, $\dot{Q}_N$ is in l/min, and F_R is in N. It can be seen that the reaction force is critically related to the volumetric flow rate (and thus to the nozzle orifice cross section). A robot working at an operating pressure of p=130 MPa and a volumetric flow rate of Q_N=180 l/min generates a reaction force of F_R=1.51 kN, a value much too high for any hand-held application. It is partly for this reason that efficient hydrodemolition can be performed with robotic units only. More results from Eq. (3.24) are plotted in Fig. 3.22.

3.5 Nozzles and orifices

3.5.1 Nozzle types and nozzle wear

The fluid jet nozzle (sometimes called orifice) is an extremely important component of any hydrodemolition machine. In the nozzle, the potential energy of the incoming pressurized water is transformed into the kinetic energy of the exiting high-speed water jet. Various nozzle types are known, usually designed for certain applications; this includes the following types:

- pipe cleaning nozzles for operating pressures up to 250 MPa with several orifices, directed sidewards or backwards, for tube bundle cleaning;
- pipe cleaning nozzles for operating pressures up to 140 MPa for cleaning large-diameter pipes;
- whirl jet nozzles for operating pressures up to 75 MPa for cleaning partially or fully blocked tube bundles;
- round jet nozzles with continuous flow channel for operating pressures up to 200 MPa;
- round jet nozzles with sapphire inserts for operating pressures up to 350 MPa;
- fan jet nozzles for operating pressures up to 200 MPa;
- injection nozzles for operating pressures up to 400 bar for the formation of hydro-abrasive water jets.

According to the nozzle design, there can be distinguished between continuous nozzles and discontinuous nozzles. In the operational pressure range up to p=100 MPa, continuous nozzles are most commonly used. They are conically designed and made from hardened steel. For ultra-high pressure applications, because of the comparatively low volumetric flow rates, the discontinuous nozzles become increasingly used. They are characterised by a sapphire-made insert. Typical examples for each type are shown in Fig. 3.23. Nozzle performance strongly depends on upstream conditions. This is illustrated in Fig. 3.24. Depending on the volumetric flow rate supplied by the pump, efficiency decreases down to 50% if poor upstream conditions apply. Table 3.10 lists recommendations for the selection of nozzle materials as functions of the operation conditions.

Nozzle wear may be divided into the following two cases:

- breakage of nozzle body (see Fig. 3.25a);
- steady decrease in nozzle exit diameter (see Fig. 3.25b).

The wear of the nozzles depends on several parameters, among others operating pressure, water quality, nozzle design and material. As Fig. 3.26 shows, three stages can be distinguished during the performance of a discontinuous nozzle: (i) an introduction stage, (ii) a continuous stage, and (iii) a wear stage. It is interesting to note that the flow conditions improve in the introduction state. The reason is that sharp corners inside the nozzle are worn away by the high-speed water flow. The

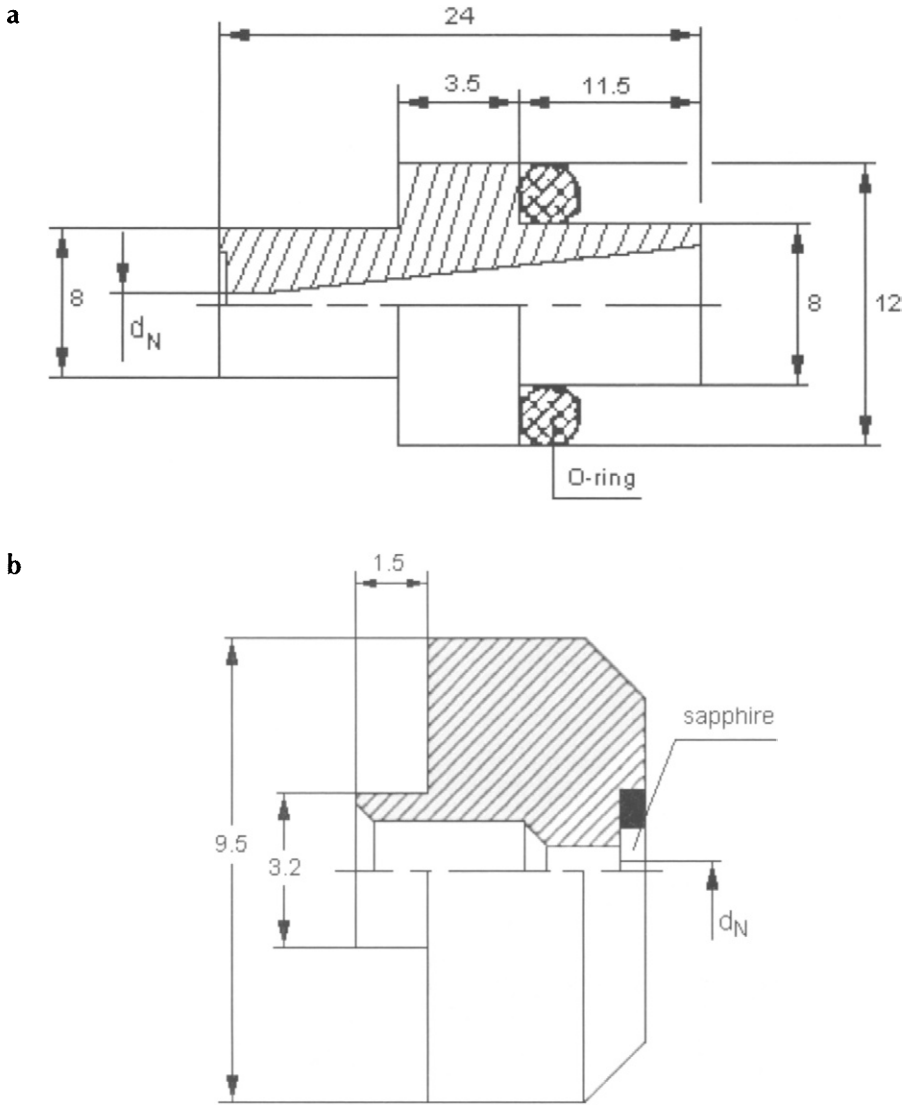

Figure 3.23 Nozzle types (WOMA Apparatebau GmbH, Duisburg)
a – continuous nozzle
b – discontinuous nozzle with sapphire insert

improved flow conditions lead to the increasing material removal capability of the jet as illustrated in Fig. 3.26. General statements about nozzle lifetime can not be made as the wear characteristics of a nozzle depends too much on the operational conditions. It was however, shown that binder content is the most important influence parameter for carbide nozzles; the higher binder content, the less is nozzle wear (Wright et al., 2003). The strong effect of water quality on nozzle wear is highlighted in Tables 3.11 and 3.12.

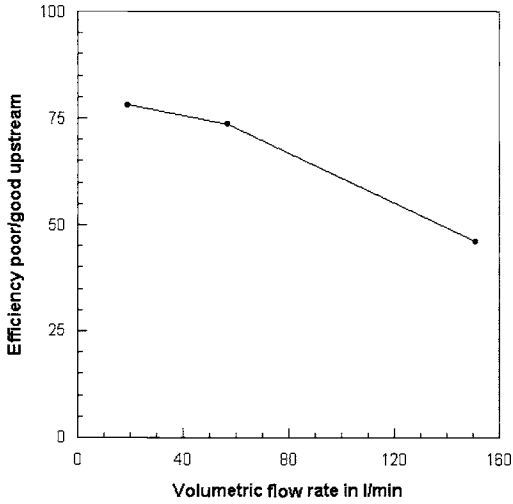

Figure 3.24 Influence of upstream conditions on nozzle performance (measurements: Wright et al., 1999)

Table 3.10 Recommended nozzle materials depending on operation conditions (Wright et al., 2003)

Recommended material	Operation conditions
Carbide	Dirty, unfiltered water; pressures below 140 MPa
Steel	Water filtered to 65 µm or better; pressures below 140 MPa
Sapphire	Water filtered to 25 µm; pressures above 140 MPa

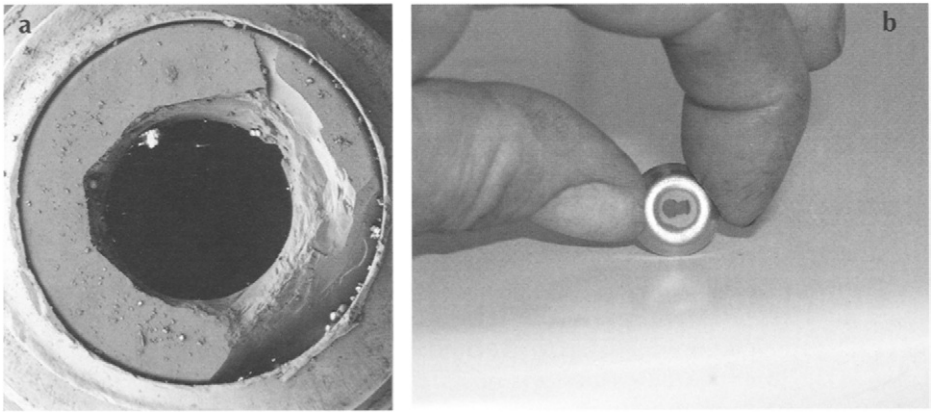

Figure 3.25 Damages to water jet orifices
a – broken nozzle (photograph: BGMR, RWTA Aachen)
b – eroded nozzle (photograph: Mühlhan Equipment Services GmbH, Hamburg)

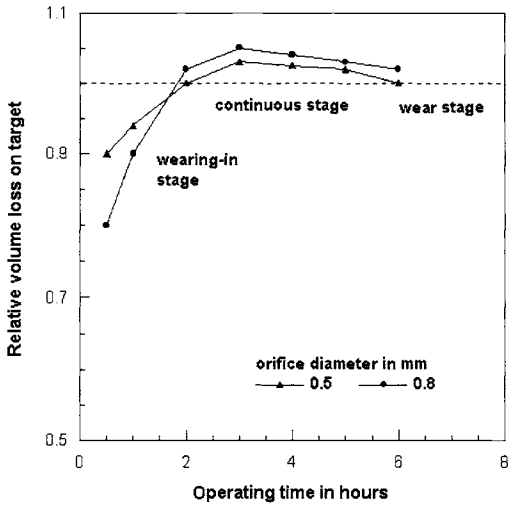

Figure 3.26 Wear stages in a typical sapphire nozzle (measurements: Werner, 1991a)

Table 3.11 Water quality effects on nozzle lifetime (Flow Europe GmbH, Darmstadt)

Water treatment	Nozzle lifetime in h
Tap water	34
Ion exchange (softened water)	78
Reverse osmosis	200
Mixed bed deionised water	> 200

Table 3.12 Water filter size effects on nozzle lifetime (Wright et al., 2003)

Filter size in µm	Nozzle lifetime in h
10	80
50	50
100	20

3.5.2 Optimisation of nozzle arrangements

The velocity of the water jet as it leaves the nozzle can be approximated with Eq. (2.4). The nozzle diameter (exactly spoken: the cross section of the nozzle arrangement) determines the actual volumetric flow rate as well as the actual reaction force of a jet. The actual volumetric flow rate is approximately:

$$\dot{Q}_A = N_N \cdot \alpha \cdot \frac{\pi}{4} \cdot d_N^2 \cdot \mu \cdot \left(\frac{2 \cdot p}{\rho_F}\right)^{1/2} = \varepsilon \cdot \dot{Q}_N \qquad (3.25)$$

Here, N_N is the number of nozzles. The parameter α is often called the discharge coefficient considering losses due to nozzle flow. A very typical value is α=0.7 for discontinuous sapphire nozzles (see Fig. 2.2). Graphs for typically applied nozzle diameters in hydrodemolition are contained in Fig. 3.27.

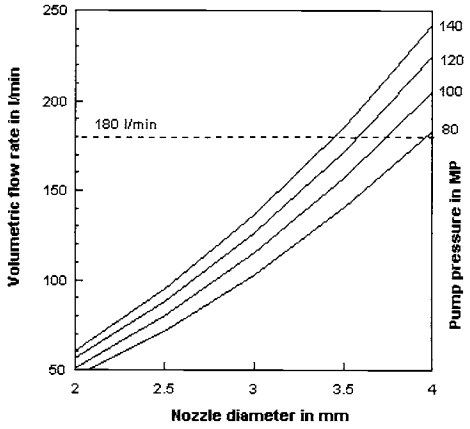

Figure 3.27 Nozzle arrangements for hydrodemolition applications

The parameter ε is the ratio between real volumetric flow rate and nominal volumetric flow rate:

$$\varepsilon = \underbrace{\frac{\dot{Q}_A}{\dot{Q}_N}}_{\text{flow rate-ratio}} = \underbrace{\alpha \cdot \frac{N_N}{N_P} \cdot \left(\frac{d_N}{d_P}\right)^2}_{\text{cross section-ratio}} \cdot \underbrace{\frac{\mu \cdot (2 \cdot p)^{1/2} \cdot \rho_F^{-1/2}}{n_C \cdot H_S}}_{\text{velocity-ratio}} \qquad (3.26)$$

The product $n_C \cdot H_S$ is half the plunger velocity given by Eq. (3.13). Compressibility effects are neglected. For a given pump configuration, Equation (3.26) links operating pressure and nominal volumetric flow rate to the nozzle arrangement. The use of ε for system optimisation is in detail discussed by Momber (2000a). The following relationship can be derived from Eq. (3.26):

$$d_N \propto p^{-1/4} \qquad (3.27)$$

This relationship can be used to control nozzle wear. If nozzle diameter increases due to wear, operating pressure in the pump drops. This is shown in Fig. 3.28, whereby nozzle wear is replaced by exposure time. Because operating pressure can be measured easily on-line, it is a suitable control parameter. If losses in pump, hose line and tool are neglected and the entire cross section is optimally distributed over several orifices or nozzles, the ideal case ε=1 occurs. The optimum cross section is then:

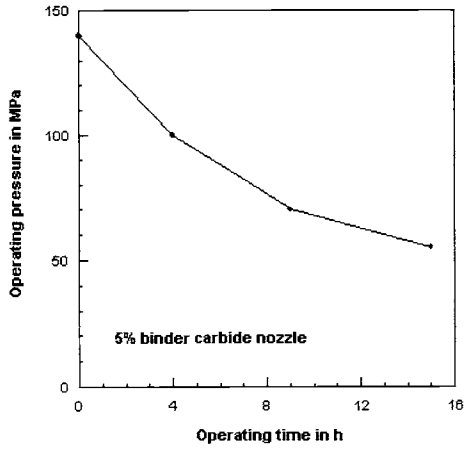

Figure 3.28 Pressure drop due to nozzle wear (measurements: Wright et al., 1999)

$$A_N = N_N \cdot \frac{\pi \cdot d_N^2}{4} = 0.265 \cdot \frac{\dot{Q}_N}{p^{1/2}} \tag{3.28a}$$

In that equation, $\dot{Q}_N$ is in l/min, p is in MPa, and A_N is in mm^2. The optimum nozzle diameter is:

$$d_N^* = \left(\frac{4 \cdot A_N}{\pi \cdot N_N} \right)^{1/2} \tag{3.28b}$$

Here, d^*_N is in mm. However, the case $\varepsilon=1$ is rather unusual in practice. The following, more realistic cases can be distinguished:

(i) $\varepsilon>1$; $d_N>d^*_N$, this case could happen for a broken (see Fig. 3.25a) or worn nozzle (Fig. 3.25b). In a system without response, operating pressure drops according to:

$$\Delta p = p \cdot \left(\frac{1}{\varepsilon^2} - 1 \right) \tag{3.29}$$

(ii) $\varepsilon<1$, $d_N<d^*_N$; this case could happen due to nozzle clogging. In a system without response, a safety valve opens and bypasses a certain amount of the volumetric flow rate given by:

$$\Delta\dot{Q}_N = (1-\varepsilon) \cdot \dot{Q}_N \tag{3.30}$$

(iii) $\varepsilon\neq1$; this is due to the restriction of commercially available nozzle diameters.

Many operators are practicing the case (ii) because they assume that the initial wear of the nozzle, that increases the nozzle diameter step-by-step, will later guarantee optimum performance conditions ($\varepsilon=1$). Table 3.13 lists results of comparative calculations for a typical hydrodemolition system. Note the increase in hydraulic efficiency if an equipment with response is used. The situation improves further if systems with direct on-line control of the crank-shaft speed are used. These systems vary the crank-shaft speed according to the following equation:

$$n_C^* = \varepsilon \cdot n_C \tag{3.31}$$

Table 3.13 Optimisation of a hydrodemolition system (see Momber, 2000a) n_C=398 min^{-1}, H_S=95 mm, N_P=3, d_P=16 mm, p=200 MPa

Parameter	$\varepsilon<1$		$\varepsilon>1$	
	without response	with response	without response	with response
ε	0.785	0.943	1.129	1.055
Δp in MPa	+124.5	+25	–43.1	–20
$\Delta\dot{Q}$ in l/min	4.3	1.2	–	–
ΔP_H in %	21.5	6.0	21.5	10

An example of how a decrease in volumetric flow rate is compensated by variable crack-shaft speeds is shown in Fig. 3.29. The gain in power rating is particularly high in the range between 20% and 50%, and it can be more than 20 kW in that certain case. The control parameter is usually the operating pressure measured with pressure gauges directly at the pump [see Eq. (3.27)]. If Eq. (3.26) is set to $\varepsilon=1$, any change in the operating pressure can be compensated through Eq. (3.31).

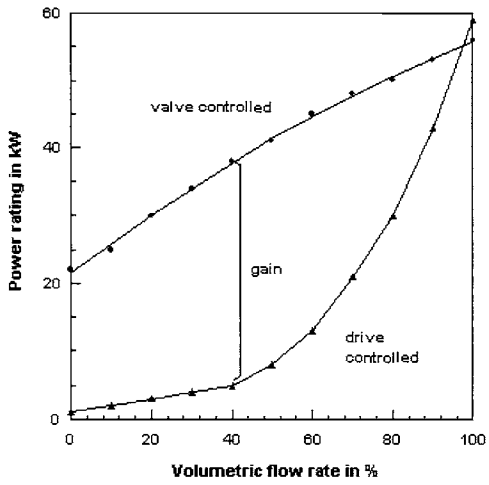

Figure 3.29 Power savings due to on-line crank-shaft control (Köhler et al., 2000)

3.5.3 Performance ranges

Equation (3.25) suggests a hyperbolic relationship between orifice diameter and orifice number. In a diagram for a hand-held gun, each hyperbola is a line of constant orifice cross section (or constant volumetric flow rate, or constant hydraulic power, respectively). The resulting performance ranges are of great practical importance. If a typical job performed with a hand-held gun with p=200 MPa and $\dot{Q}_N$=20 l/min is considered, the following situation appears. In the case N_N=1 (which gives d_N=0.85 mm), the entire hydraulic power delivered by the pump is focused in one jet that owns a high power of P_N=42 kW (if nozzle losses are considered). This case, shown in Fig. 3.19b, is very favourable for performing heavy material removal work, such as exposing reinforcement bars. However, this variant is not suitable for selective paint stripping as there is a risk that the underlying material layer will be damaged. Therefore, the hydraulic power can be divided into several portions by using various nozzles or orifices. In the case N_N=6 (d_N=0.34 mm), six jets having a notably lower power of P_N=7 kW each, are formed that work very gently and do not damage any underlying material. Examples are shown in Figs. 3.19a and 3.19b.

3.6 Waste water treatment systems

Vacuuming and water treatment systems will soon become a standard requirement for an ecologically successful application of hydrodemolition systems. However, commercial systems are already developed. Figure 3.30 shows a vacuuming unit

Figure 3.30 Vacuuming device for concrete cleaning applications (Hammelman GmbH, Oelde)

designed for waterjet tools that perform at an operating pressure up to 200 MPa and volumetric flow rates between 10 and 40 l/min. A typical unit consists of a drive (usually electric), a vacuum pump (liquid-ring-pump) and a 2 m^3-vessel with level control for contaminated water. At a pressure of 5 bar, the maximum vacuum is about 50%. The unit requires a drive of 29 kW. It is containerised and can directly be connected to water treatment systems. A general waste material treatment cycle for hydrodemolition applications is shown in Fig. 4.8, whereas Fig. 3.31 shows a technical solution for the site treatment of process water from hydrodemolition jobs with rather low volumetric flow rates.

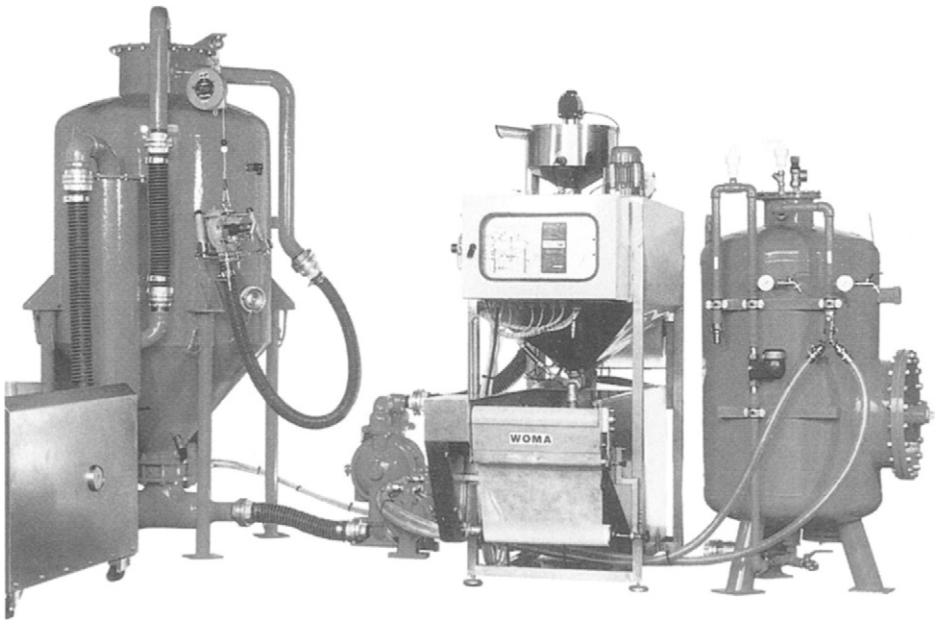

Figure 3.31 Modular water treatment system (photograph: WOMA Apparatebau GmbH, Duisburg)

3.7 Abrasive water jet cutting equipment

3.7.1 Abrasive water jet cutting devices

Major parts of a typical on-site abrasive water jet cutting system are shown in Fig. 3.32. These parts include in particular the following:

- driving device;
- guiding device;
- abrasive hopper;
- abrasive line;
- mixing and acceleration head.

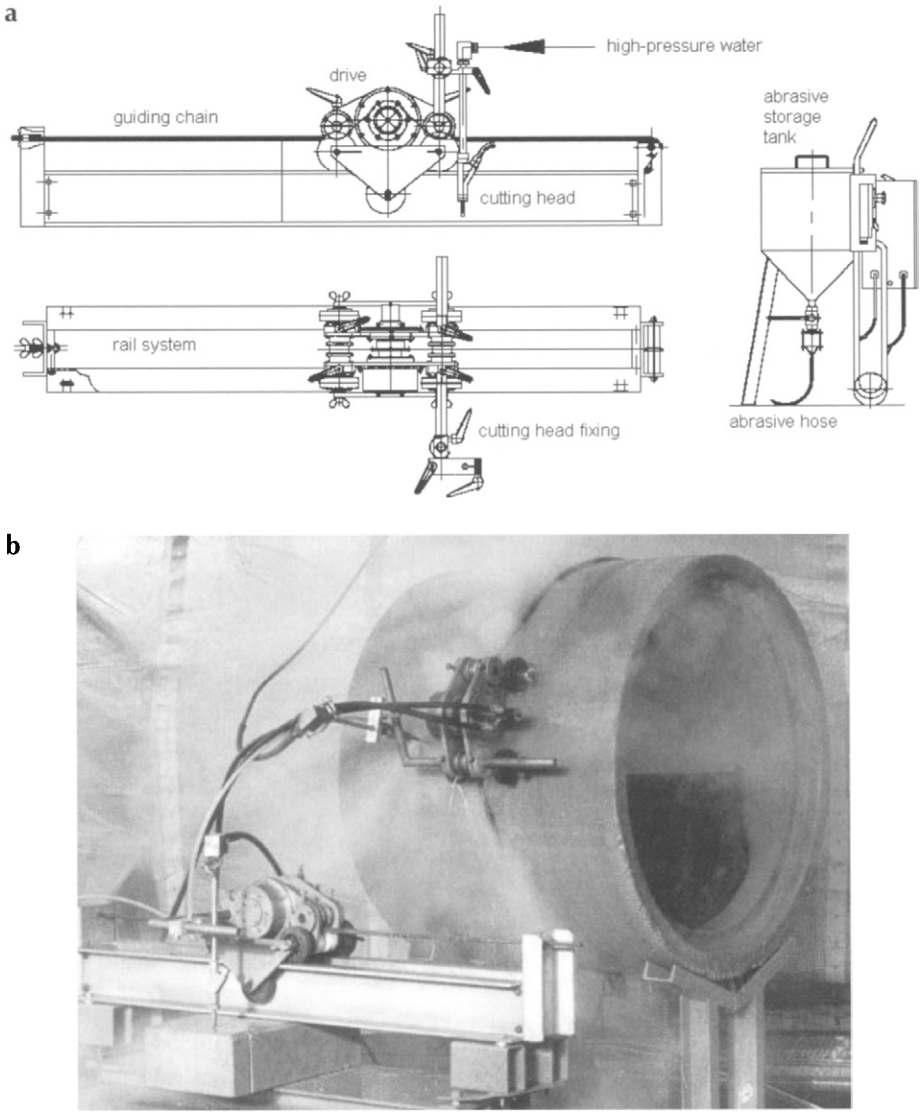

Figure 3.32 On-site abrasive water jet cutting system (WOMA Apparatebau GmbH, Duisburg)
a – principal structure of a linear cutting system
b – cutting systems for concrete floor and, respectively, concrete pipe cutting

Driving devices are usually pneumatic air motors. Traverse speed can be fixed with a high accuracy due to the adjustment of air flow rate or, respectively, air pressure. In contrast to mechanical or hydraulic drives, pneumatic motors are small and lightweight. Guiding devices may feature rails and chains. Rails are usually utilised for straight cutting (see Fig. 3.32a), whereas chains are more appropriate for curved cutting (e.g. cutting of pipes). The abrasive hopper stores the

abrasive material. However, most hoppers are not only storage devices, but contain control and metering mechanisms for abrasive mass flow rate and traverse speed. Abrasive lines serve to transport the abrasive materials from the hopper to the cutting head. They are often made from abrasion resistant plastics, and they are usually transparent so that the feeding process can be observed on-line.

3.7.2 Abrasive water jet cutting heads

The majority of on-site cutting heads works according to the injection principle. A typical on-line abrasive water jet cutting head is shown in Fig. 3.33. It consists of a water inlet, an abrasive inlet, a mixing chamber, and an acceleration focus. The quickly flowing water jet forms a vacuum in the mixing chamber and the resulting pressure difference allows for the flow of an air stream that in turn transports the abrasive particles to the mixing chamber. The processes of mixing and acceleration are in detail described by Momber (2001) and Momber and Kovacevic (1998). Table 3.14 lists performance parameters of the cutting head shown in Fig. 3.32. More information is provided in Chapter 6.

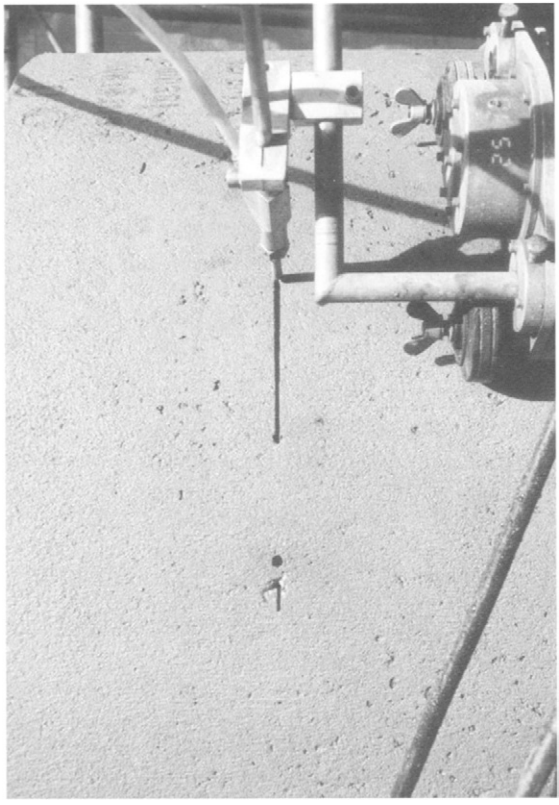

Figure 3.33 Abrasive water jet cutting head (photograph: WOMA Apparatebau GmbH, Duisburg)

Table 3.14 Performance parameters of the on-site abrasive water jet cutting system shown in Fig. 3.32

Parameter	Value
Maximum operating pressure	300 MPa
Volumetric water flow rate	18 to 20 l/min
Maximum air consumption	400 l/min (at 0.6 MPa)
Weight cutting head	1.2 kg
Weight chain	2.5 kg
Total weight	123 kg
Driving speed	25 to 100 mm/min
Length rail system	approx. 1,650 mm
Recommended abrasive material	garnet; size 0.5 to 1.0 mm

Figure 3.34 shows the drawing of a nozzle type developed to accelerate explosive pellets by high-speed water jets (Becker et al., 1999). The pellets are being accelerated to a high speed and are brought to detonation if they hit the material to be cut. The principle of mixing is comparable to that used for the formation of hydro-abrasive water jets.

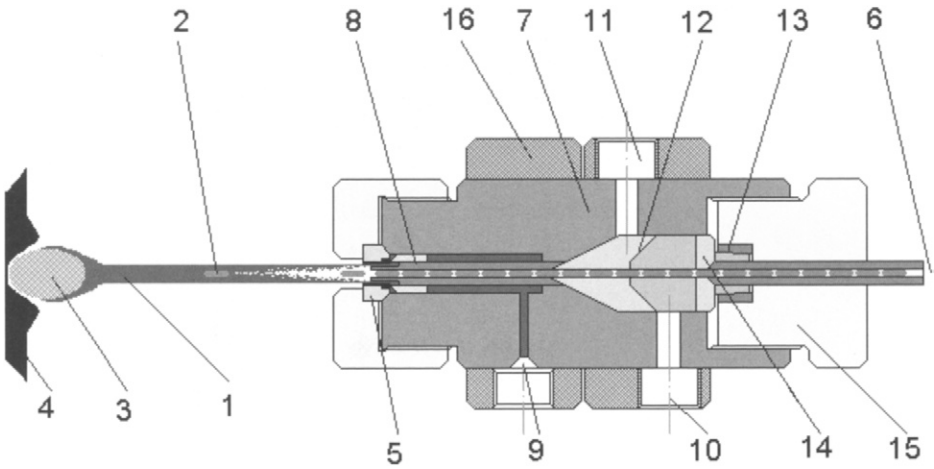

Figure 3.34 Nozzle arrangement for accelerating explosive pellets with a high speed water jet (Becker et al., 1999)

1 – annular water jet
2 – explosive pellets
3 – area exposed to explosion
4 – concrete surface
5 – high-pressure nozzle
6 – pellet feeding inlet
7 – housing
8 – centering segment
9 – liquid medium (water)
10 – second medium (optional)
11 – third medium (optional)
12 – distribution segments
13 – clemp fitting
14 – sealing
15 – thread joint (rear side)
16 – flange

Abrasive particles are the actual cutting tool in abrasive water jet cutting. Basically, metallic and non-metallic abrasive materials can be distinguished. They

are defined and described in ISO 11118 and 1119. However, for on-site concrete cutting jobs, non-metallic abrasive materials, such as garnet or aluminium oxide, are preferred. Important abrasive properties include the following:

- hardness;
- density;
- average grain size;
- grain size distribution;
- grain shape.

A typical abrasive material utilised for on-site concrete cutting jobs is shown in Fig. 3.35. Table 3.15 lists the corresponding physical, chemical and mechanical properties.

Figure 3.35 Abrasive material (photograph: Barton Mines Corp., North Creek)

Table 3.15 Physical properties of a typical abrasive material (Medenec Mine, Czech Republic)

Property	Value
Melting point	1,320 °C
Specific gravity	4,114 kg/m^3
Solubility in water	not soluble
Moisture absorption	less than 0.2% by weight
Volatile	0
Evaporation rate	solid matter
Appearance and odor	odorless
Susceptibility to acids	non, very stable
Crystal system	cubic
Cell parameters	11.547 Å
Granularity characteristics	anisometric grains
Mohs' hardness	7.5
Microhardness (VHN)	13,045–15,053 N/mm^2
Fracture	irregular, sub-conchoidal
Cleavage	none
Durability	very good
Colour	red
Luster	vitreous
Optical character	isotropic
Young's modulus	241 GPa

CHAPTER 4

Concrete Surface Preparation by Hydrodemolition

4.1 Surface preparation methods

Surface preparation processes affect performance and life time of coating systems and of concrete replacement systems significantly. Surface preparation is defined in RILI (2001) as "the generation of a suitable surface of a concrete substrate for concrete replacement or, respectively, surface protection." Surface preparation is an important part of any concrete corrosion protection and rehabilitation strategy. Basically, the following eight principal surface preparation methods can be distinguished (RILI, 2001):

1. chipping (hammer and chisel, electric or pneumatic hammer, needle gun);
2. brushing (rotating steel brush);
3. milling (milling machines);
4. grinding (grinder);
5. Flame cleaning (thermally operating devices);
6. Low-dust blasting (vacuum blasting, shot blasting);
7. Blasting (air pressure blasting, wet blasting, *high-pressure waterjetting* > 60 MPa);
8. Cleaning (suction devices, steam jetting, hot-water jetting).

Typical operations performed with these methods are listed in Table 4.1. Hydrodemolition is designated high-pressure waterjetting in that table. It can be applied to horizontal and vertical surfaces for the following processes:

- removal of deteriorated coatings as well as of near-surface contaminants;
- removal of cement lime and low-strength layers;
- removal of damaged (deteriorated) concrete/concrete replacement as well as reinforcement exposure;
- removal of rust from exposed reinforcement and from other metal parts;
- removal of water, dust and loosely adhering particles from the substrate.

4.2 Efficiency of hydrodemolition processes

4.2.1 Cleaning and roughening of concrete substrates

Cleaning of concrete substrates include decontamination, laitance removal, construction joint cleaning, and the removal of deteriorated coatings. These applications are illustrated in Fig. 4.1. Materials to be removed include oil, soot, organic growth, road markings, paint and linings. Water jets are state-of-the-art tools for these applications. The subdivision of a typical rehabilitation project that contains a certain amount of cleaning is listed in Tables 4.2 and 4.3. The amount of cleaning work is surprisingly high in both cases. For the situation listed in Table 4.3, the amount of cleaning is about 90% in terms of the total area to be treated. It is standard to use hand-held tools driven by very high pressures and rather low

Table 4.1 Methods of concrete surface treatment (RILI, 2001)

Method	Tool / Material	Application					Application range
		1	2	3	4	5	
Chiseling	Hammer and chisel	x	x	x			Local; for smaller areas a)
	Chisel (electric, pneumatic)			x a)			Local; for smaller areas a)
	Needle gun	x	x		(x) g)		Local; for smaller areas a)
Brushing	Rotating steel brush	x	x		(x) g)		Depends on tool being used
Milling	Milling machine	x	x i)	x i) j)			Large-scale removal on horizontal areas
	Large-scale removal to desired depth	x	x i)	x i) j)			Large-scale removal on horizontal areas
Grinding	Grinder	x	x				Local; for smaller areas
Flame cleaning	Device for thermal and mechanical treatment b)	x	x				Horizontal and vertical surfaces
Low-dust blasting	Blasting with abrasives with simultaneous vacuuming; shot blasting	x	x	(x) c)	x		Depending on device; on horizontal and/or vertical surfaces
Blasting	Blasting with abrasives	x	x	(x) c)	x		Horizontal and vertical surfaces
	Fog blasting; Wet blasting with abrasives	x	x	(x) c)	(x) h)		Horizontal and vertical surfaces
	High-pressure water jetting >60 MPa	x	x	(x) e)	(x) h)		Horizontal and vertical surfaces
Cleaning	Blow-off with compressed air					x	Preferably for non-horizontal surfaces a)
	Vacuuming with industrial vacuum cleaners					x	Basic method for large, horizontal surfaces
	Water blasting; Steam jetting; Hot-water jetting					x	Removal of atmospheric contaminants from concrete substares

Applications:
1 removal of deteriorated coatings as well as of near-surface contaminants;
2 removal of cement lime and low-strength layers;
3 removal of damaged (deteriorated) concrete/concrete replacement as well as reinforcement exposure;
4 removal of rust from exposed reinforcement and from other metal parts;
5 removal of water, dust and loosely adhering particles from the substrate.

continued

Table 4.1 *continued*

Legend:

a) In-depth damage to concrete possible.
b) Thermally damaged zones in concrete need to be removed.
c) Degree of concrete removal depends upon pressure and abrasive mass flow rate.
d) Oil-free: Compressor to be used must feature an oil separator with an efficiency of ≤0.01 ppm residual oil.
e) Degree of concrete removal depends upon pressure.
f) Remaining coatings can not always be removed.
g) Not for reinforcement to be coated and other metallic parts.
h) Dry grit blasting if necessary.
i) Maximum removal depth of ≤5 mm must not be exceeded. For deeper removal. an in-depth damage to the concrete is probable.
j) Not for reinforcement exposure.

Table 4.2 Jobs performed at the rehabilitation projects Litti-bridge and Lissibach-bridge, Baar, Switzerland (Walser, 1999)

Task	Tool	Area / volume
Cleaning with 75 MPa	–	6,200 m^2
Cleaning with 240 MPa	hand-held	300 m^2
Concrete removal; horizontal	robot	20 m^3
Concrete removal; removal depth 540 mm	robot	23 m^3
Concrete removal of consoles	robot	100 m^3
Concrete removal	hand-held	25 m^3

Table 4.3 Jobs performed at the rehabilitation project avalanche gallery Willerplangen, Switzerland (Schweizerischer Fachverband für Hydrodynamik am Bau, 1997)

Task	Tool	Area / volume
Laitance removal	hand-held	25,000 m^2
Removal of contaminants	hand-held	8,000 m^2
Concrete removal; depth: 0–50 mm; no exposure of reinforcement	robot	900 m^2
Concrete removal; depth: 20–80 mm; exposure of reinforcement	robot	1,100 m^3

volumetric flow rates for cleaning operations. The problems associated with these applications are in detail discussed by Momber (2003c).

A widely used application is the removal of rubber from airport runways. The problem is illustrated in Fig. 4.2 showing the formation of a smooth rubber layer on concrete substrates within the course of a few weeks due to rubber particles pushed into the concrete surface during the take-off and landing of airplanes. To clean the concrete, mobile water jet machines, usually consisting of a truck based chassis and a rotating nozzle carrier device, are utilised. An example is shown in Fig. 4.3. Acceptance criteria for a successful rubber removal from runway concrete substrates are the following (Choo and Tek, 1990a):

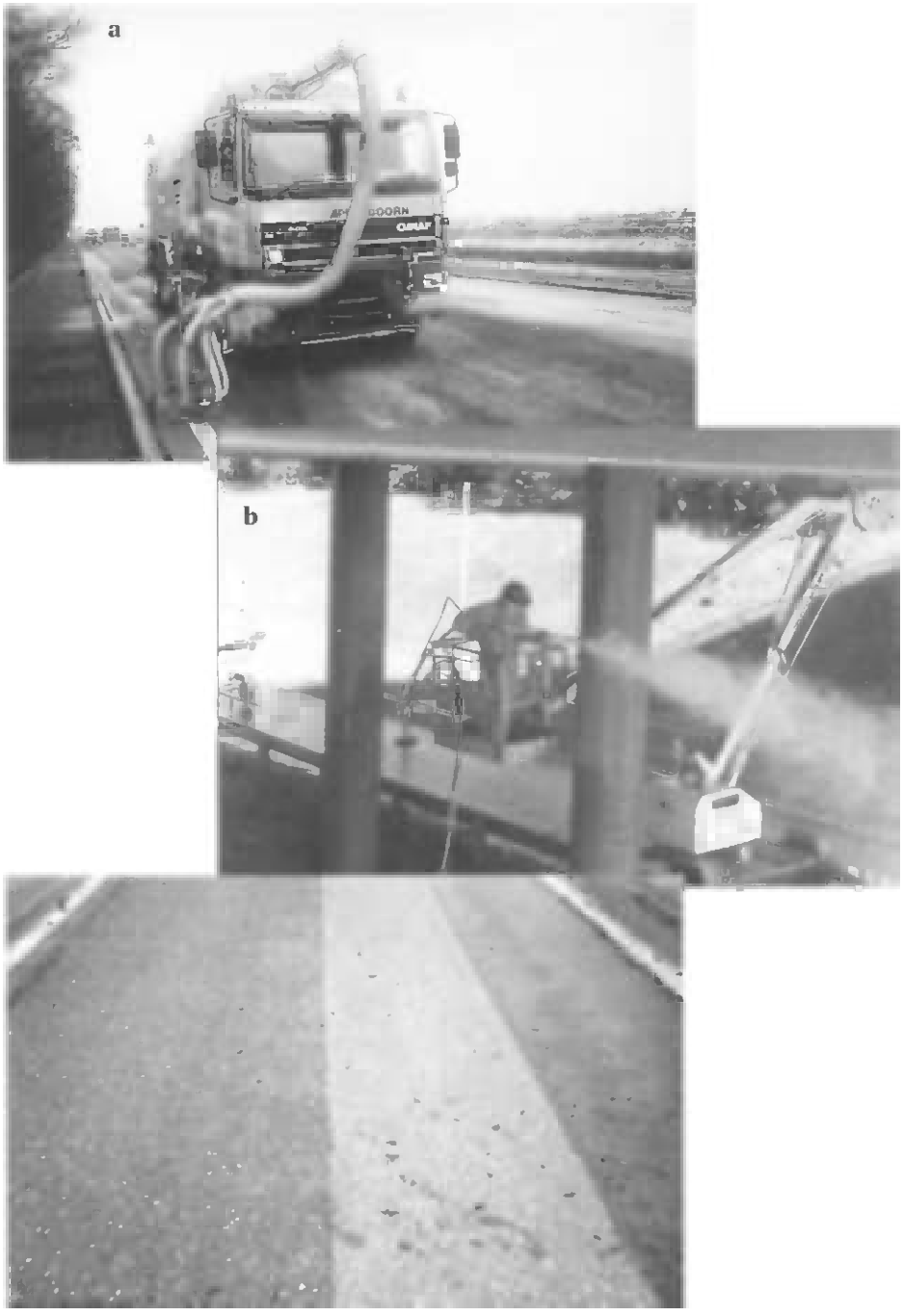

Figure 4.1 Applications of water jets to concrete substrates (photographs: WOMA Apparatebau GmbH, Duisburg)
a – removal of paint b – removal of coatings c – roughening

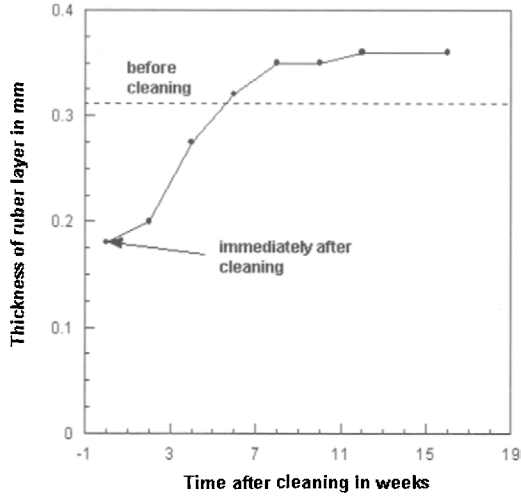

Figure 4.2 Rubber formation on airport runways and cleaning results (Choo and Teck, 1990b)

Figure 4.3 Unit for runway cleaning (photograph: WOMA Apparatebau GmbH, Duisburg)

- friction value at any point along the cleaned area must be less than 0.5;
- removal rate must be between 150 to 300 m^2/h;
- proportion of aggregates (fines) and bitumen being removed must not exceed 40% of the residues collected;
- macro-textural depth of cleaned areas must not be less than 0.25 mm.

The effect of water jet cleaning on friction values is shown in Fig. 4.4. Friction notably increases after the cleaning. Efficiency of the process varies notably, depending on rubber thickness, operating parameters, and on site organisation. However, efficiency values up to 1,500 m^2/h are reported (WOMA Aparatebau GmbH, Duisburg). Table 4.4 lists the composition of residues collected during a cleaning of a runway with water jets. It can be seen that the total of fine aggregates and bitumen is less than 40%. Further results of glue removal tests on runways are provided in Table 4.5.

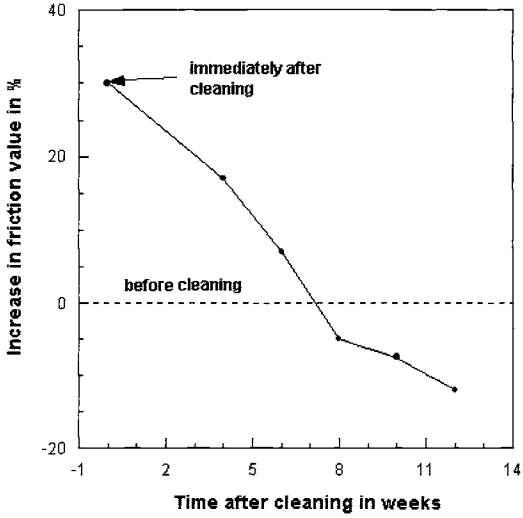

Figure 4.4 Effect of cleaning on friction values of runway substrates (Choo and Teck, 1990b)

Table 4.4 Composition of residues after rubber removal from a runway (Choo and Teck, 1990a)

Part	Material	Percentage
External deposit	Rubber	65.5
Pavement	Fine aggregates	22.7
	Bitumen	11.8
Total		100

Roughening of concrete substrates basically includes the removal of a top laintance layer in order to expose aggregate surfaces. This is shown in Fig. 4.5. It was shown by Schulz (1984) that adhesion to concrete substrates increases if the amount of aggregates visible at the surface increases. Results of a large dam project realised with an automatic removal system are reported by Ohta et al. (1991). Some results are listed in Table 4.6. Efficiency values are rather high and vary between 121 and 155 m^2/h. Further examples are listed in Table 4.7.

Table 4.5 Results of runway glue removal tests (Xue et al., 2001); rotational speed nozzle carrier: 800 min^{-1}

Runway type	Pump pressure in MPa	Cleaner speed in m/min	Cleaning effect
Concrete runway	20	3.0	Not clean.
	30	3.0	Basically clean. Thick glue can not be removed.
	40	3.5	All cleaned.
	40	5.0	Basically clean. Thick glue can only be cleaned partially.
	45	5.0	All cleaned.
	> 45	5.0	Damage appears.
Bitumen runway	45	5.0	Partly cleaned. No damage to runway surface.
	50	3.0	Better than above. No damage to runway surface.
	65	3.0	Most glue layer removed. Little damage to runway surface. Sand and aggregate can be seen.
	65	1.0	Nearly all glue removed. Obvious sand and aggregate can be seen. Medium degree damage to runway surface.

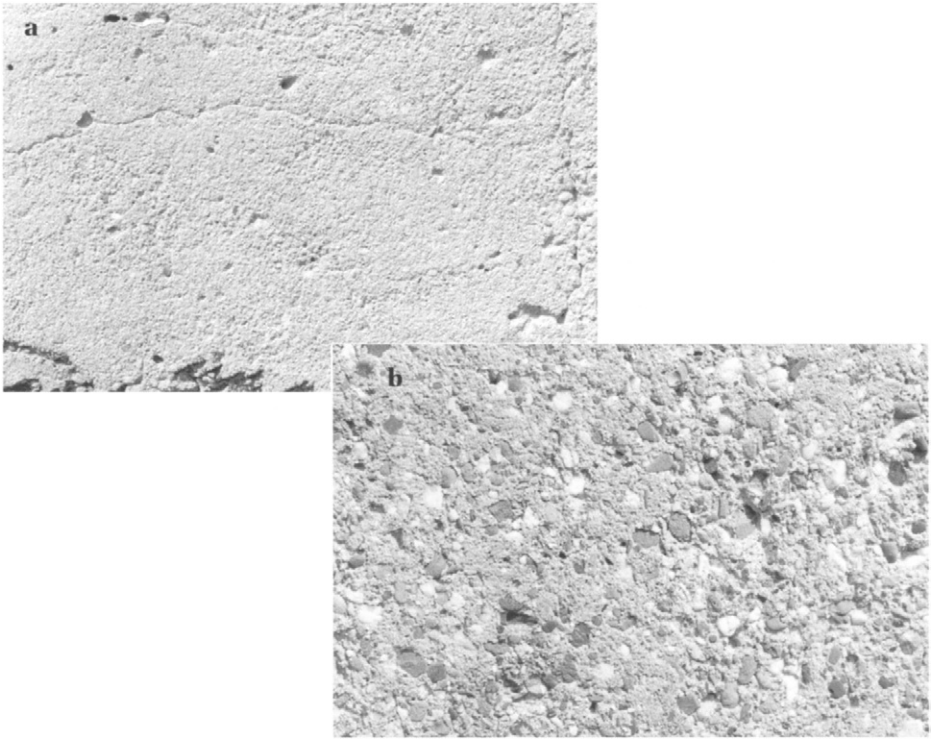

Figure 4.5 Laitance removal with water jets (photographs: WOMA Apparatebau GmbH, Duisburg); pressure: 200 MPa
a – before cleaning b – after cleaning

Table 4.6 Results of laintance removal from green concrete (Ohta et al., 1991)

Compressive strength in MPa	Pump pressure in MPa	Traverse rate in m/min	Efficiency in m^2/h
2.8	40–80	14	155
6.4	60–80	13	144
7.5	70–90	12	132
9.4	80–100	11	121
10.5	80–100	11	121
11.3	80–100	11	121

Table 4.7 Efficiency values for concrete substrate profiling (Momber, 1993)

Problem	Tool	Pump pressure in MPa	Area in m^2	Efficiency in m^2/h
Wall area	Robot	80	2,500	125
Cooling tower internal area	Robot	35	17,000	62
Profiling depth: 2–3 mm	Hand-held gun	70	–	30
Profiling depth: 1–3 mm	Robot	45	–	44
Reinforced concrete wall	Abrasive-gun	75	–	240

4.2.2 Efficiency of hydrodemolition

Table 4.8 lists examples for typical quantities (area, volume) of hydrodemolition jobs. Efficiency values listed in Table 4.9 illustrate that efficiency of hydrodemolition processes varies depending upon location, concrete quality, site organisation, equipment and process parameters. A more rigid subdivision of affecting parameters is shown in Fig. 4.6. A measure of hydrodemolition efficiency is either the area efficiency, defined as:

$$E_H = \frac{A_H}{t_B} \tag{4.1}$$

which is usually applied to cleaning or roughening jobs, or the volumetric efficiency, defined as:

$$E_V = \frac{V_M}{t_B} = E_H \cdot h_M \tag{4.2}$$

which is usually applied to heavy demolition jobs. Both equations are coupled via the removal depth. Area efficiency depends strongly on the size of the area to be treated and on removal depth. These relationships are illustrated in Fig. 4.7.

Dinglinger (1998) distinguished between three typical efficiency rates or, respectively, performance rates:

- basic output, E_B;

Table 4.8 Quantities of typical hydrodemolition jobs (Reference list: Wannenwetsch GmbH, Meiningen)

Total area in m^2	Total volume in m^3	Removal depth in mm
Parking decks		
10,000	900	150
25,000	–	–
–	145	600
5,000	–	30
1,400	60	Various depths
300	–	40
–	30	150
–	160	150
600	–	150
–	70	70
1,000	–	70
3,500	250	70
2,600	–	Various depths
15,000	–	200
2,000	–	50
Tunnels		
–	1,500	300
2,000	–	35
2,400	–	35
600	–	30
–	1,700	250
Bridges		
10,000	100	250
13,000	1,150	90
6,000	–	40
2,000	400	150
–	–	120
800	–	500
–	–	400
–	360	350
–	42	1,100
–	40	100
1,700	–	30
–	60	250
–	–	200
–	20	450
–	100	250
1,000	–	250
1,000	–	270
–	–	1,200
1,000 lfm	–	350

Table 4.8 ***continued***

Special constructions		
–	600	800
600,000	–	–
2,500	–	–
–	30	150
–	50	520
–	40	1,100
–	80	200
–	500	Various depths
–	–	1,000
3,500	–	–
–	40	450
–	20	200
–	15	1,000

Table 4.9 Concrete hydrodemolition efficiency values (Hilmersson, 1998)
Operating pressure: 100 MPa, volumetric water flow rate: 193 l/min, robot type: HVD–6000

Object	Completed area in m^2	Removal depth in mm	Efficiency in m^2/h	Efficiency in m^3/h
Bridge	210	30	14	0.42
Bridge	45	30	13	0.39
Bridge	40	30	15	0.45
Harbour structure	1,550	30	20	0.60
Harbour structure	210	30	15	0.45
Harbour structure	85	200	2	0.40
Bridge	140	60	12	0.72
Bridge	700	120	8	0.96
Floor	300	80	6	0.48
Facade	100	80	5	0.40
Bridge	75	30–60	11	0.33–0.66
Pillar (round)	185	50–80	2	0.10–0.16
Power station	85	30	10	0.30
Bridge (overhead)	80	30	8	0.24
Bridge	12,000	10	40	0.40
Tunnel (overhead)	200	30	11	0.33
Bridge	1,500	60–90	9	0.54–0.81

- maximum effective output, E_{EM};
- average effective output, E_{EA}.

The basic output, E_B, is obtained during the removal of a specific concrete quality by a specific hydrodemolition equipment. Site and equipment status, organisational structure and site organisation as well as climate conditions are not taken into account. The maximum effective output is obtained over a rather short period of time. As for the average effective output, site and equipment status, organisational structure and site organisation as well as climate conditions are not taken into account. The average effective output is defined to be the average

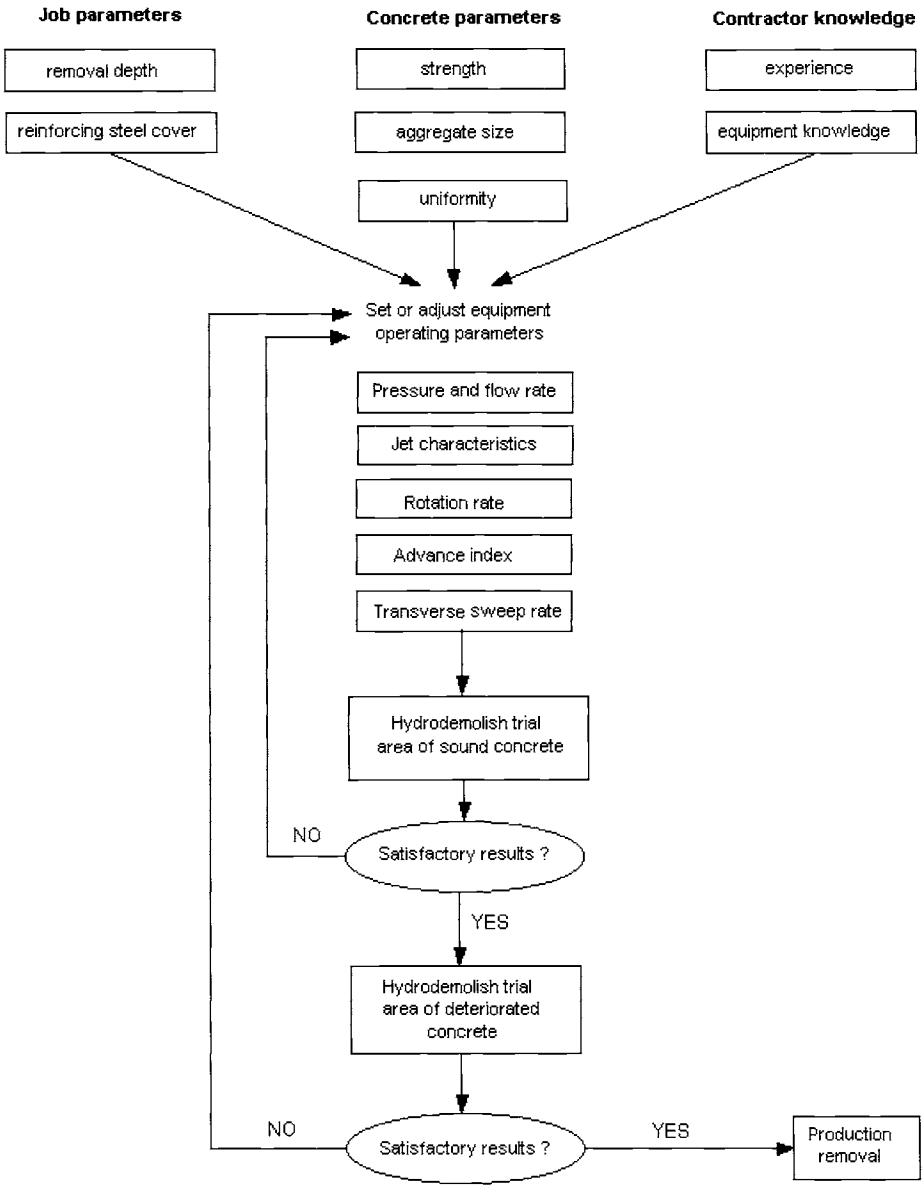

Figure 4.6 Parameters affecting hydrodemolition efficiency (Vorster et al., 1992)

performance continuously obtained over a prolonged period of time. Start-up times, allowances and recovery times are taken into account. The average effective output is of basic interest for efficiency and cost calculations. It is given as follows:

$$E_{AM} = E_B \cdot f_E = E_B \cdot \prod_{i=1}^{5} f_i \tag{4.3}$$

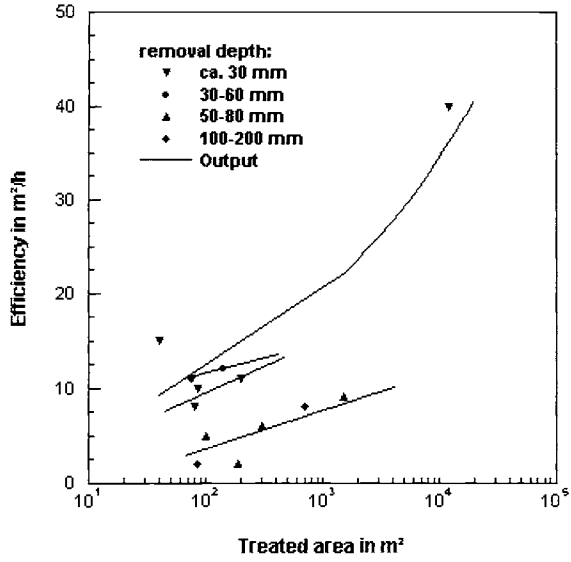

Figure 4.7 Area efficiency for hydrodemolition (based on Table 4.9)

The degradation parameters are defined as follows:

- f_1 – plant employment factor, which includes:
  - $f_{1\text{-}1}$: relocation times,
  - $f_{1\text{-}2}$: operational idle times;
- f_2 – machine factor, which includes:
  - $f_{2\text{-}1}$: maintenance time,
  - $f_{2\text{-}2}$: repair time;
- f_3 – human performance factor;
- f_4 – removal factor;
- f_5 – weather factor.

The maximum efficiency output is reduced down to the average effective output by considering a time influence factor, which delivers the following relationship:

$$E_{EA} = E_{EM} \cdot f_T = E_{EB} \cdot f_E \cdot f_T \tag{4.4}$$

The time influence factor takes into account the following time consuming processes:

- relocation times;
- operational breaks for mechanical reasons;
- performance losses due to start-up and phasing-out times;
- idle times caused by operating personnel.

Table 4.10 lists typical values obtained from practice hydrodemolition jobs. If the basic efficiency is divided by the theoretical efficiency, a factor of influence f* can be obtained. This factor is directly related to the changes in concrete quality parameters (e.g. compressive strength). Values for f* are listed in Table 4.11.

Table 4.10 Efficiency reduction factors for hydrodemolition sites (Dinglinger, 1998)

Factor	Hydrodemolition site					
	1	2	3	4	5	6
f_{1-1}	0.86	0.57	0.84	0.86	0.49	0.83
f_{1-2}	0.97	1.00	0.76	0.88	0.80	0.97
f_{2-1}	0.94	0.54	0.91	0.85	0.87	0.97
f_{2-2}	0.73	1.00	0.98	0.69	1.00	0.92

Table 4.11 Basic output parameters for different hydrodemolition sites (Dinglinger, 1998)

Parameter	Hydrodemolition site					
	1	2	3	4	5	6
A_H in m^2	420.0	59.3	55.7	31.1	71.5	304.0
E_{AG} in m^2/h	47.5	67.1	63.8	58.2	31.2	25.5
E_{VG} in m^3/h	3.7	5.3	5.3	5.6	2.6	2.1
h_M in mm	79	80	84	80	84	81
f*	0.77	1.10	1.05	0.96	0.51	0.42

4.3 Disposal of solid and liquid waste

4.3.1 General disposal problems

Waste can result from a variety of activities related to concrete refurbishment. Hydrodemolition, in particular, can produce a considerable amount of waste, mainly eroded concrete material and removed coatings. A flow chart of how to deal with this residue is shown in Fig. 4.8. Especially older paint systems contain hazardous materials, such as heavy metals, dioxine, PCBs, etc. Typical examples for hazardous substances contained in paint systems are listed in Table 4.12. Most of these substances are not degradable; their health (and disposal) risk is essential. A major problem with the removal of these paint types is the contamination of air and soil.

A duty of care that addresses waste generation, control and disposal, which is a statutory duty that applies to producers, holders, carriers of waste, and those who treat waste, has four major aims (Abrams, 1999):

- to prevent any other person from depositing, disposing of, or recovering controlled waste (residential, commercial, industrial) without a waste management license or in a manner likely to cause environmental pollution or harm to health;

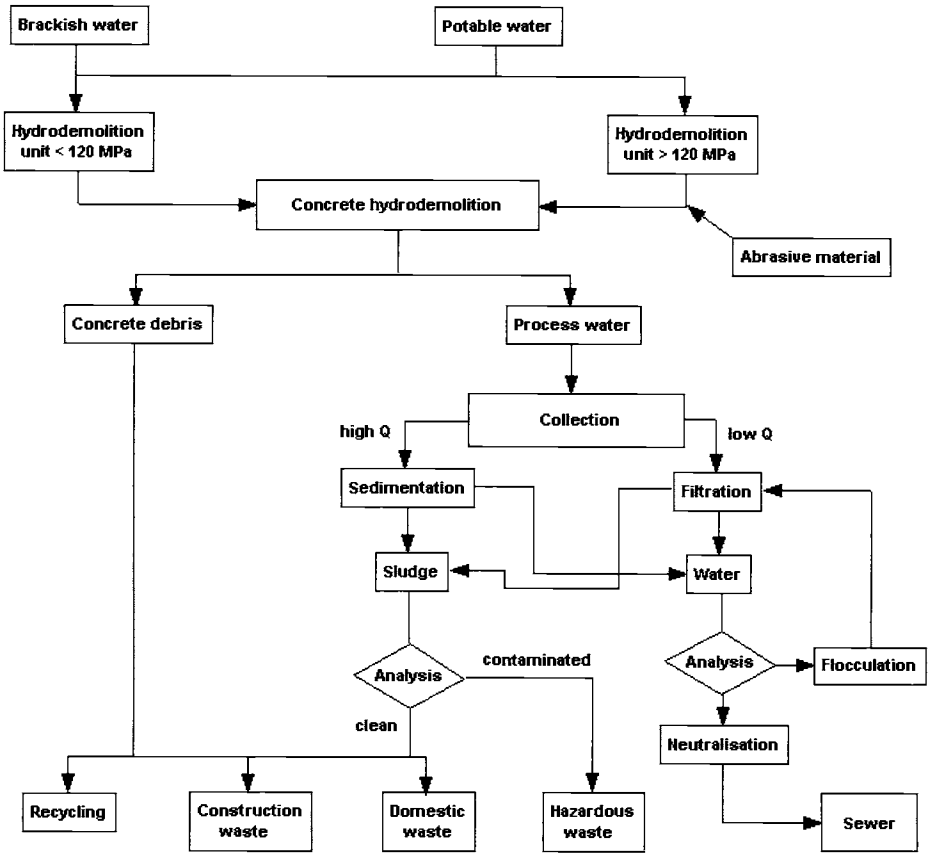

Figure 4.8 Flow chart for hydrodemolition waste treatment (Kauw, 1992)

- to ensure that waste is safely and securely contained, both in storage and in transport, in such a way that it cannot escape;
- to ensure that if waste is transferred that it only goes to an authorised person;
- to ensure that when waste is transferred there is a clear, written description of it so the person receiving the waste can handle it properly and safely without committing any offence.

The following steps are helpful to meet the obligations mentioned above:

- Identification of all types of activity involved in the project (e.g. paint removal; storage of chemicals, fuels, and paints; application of paint).
- Identification of all sources of waste in terms of 'waste streams' (e.g. dry removed paint, blasting water, abrasive and its packaging, dust, chemicals and their packaging, wet paints, fuel), and the estimation of the quantities of waste from each process step prior to the job start.

Table 4.12 Hazardous substance analysis of paint systems

Substance	Content in paint (%)	Reference
Cadmium	0.014*	Dupuy et al. (2001)
Cadmium	0.003–0.01	Marshall (2001)
Chromium	0.86*	Dupuy et al. (2001)
Chromium	1.65	Holle (2000)
Chromium	2.99	Holle (2000)
Chromium	0.093–0.21	Marshall (2001)
Lead	0.31–13.5	Dupuy et al. (2001)
Lead	0.132–0.710	Marshall (2001)
Lead	6.14	Holle (2000)
Lead	11.11	Holle (2000)
Lead	14–20	Mickelsen and Johnston (1995)
PCB	0.12	Holle (2000)
PCB	0.16	Holle (2000)
Zinc **	80–85	Tinklenberg and Doezema (1998)

* Maximum values; ** Zinc rich paint

- Determination of a means of handling and storing waste in order to control and minimise pollution risks. This could include the following:
  - minimising the amount of abrasives or contaminated water which can be done by some type of containment with extraction if necessary;
  - storage of contaminated waste in a properly bunded area;
  - examination of transfer methods from the storage area to the waste contractor to minimise risk of spillage.

4.3.2 Waste water treatment

The water consumption during hydrodemolition basically equals the volumetric flow rate generated by the pump. Typical volumetric flow rates for heavy hydrodemolition jobs are between 150 and 250 l/min. This is a conservative approach because it is the actual volumetric flow rate of the nozzle system that must be considered. It is important to know that operating pressure and volumetric flow rate can not be varied independently if a certain pump power is given (see Fig. 3.7). A rule of thumb is: the higher the pressure for a given pump power, the lower the volumetric flow rate. Dorner (1996) performed a study into the amount and composition of waste water collected during hydrodemolition jobs. Table 4.13 lists values of corresponding absolute volumetric waste water flow rates. It can be seen that values range from 0.75 m^3/h to 15 m^3/h which is a deviation factor of 20. Sometimes, if different jobs are being compared, the relative water consumption which relates the volumetric flow rate to hydrodemolition efficiency, is a more appropriate parameter. Relative water consumption is given as follows:

$$W = \dot{Q}_A / E_H \tag{4.5}$$

Table 4.13 Typical waste water streams from hydrodemolition sites (Dorner, 1996)

Construction	Area (m^2)	Operating pressure (MPa)	Waste water flow rate (m^3/h)
Façade	ca. 2,800	100	0.75
Bridge	ca. 300	100–200	9
Parking deck	ca. 1,50	200	1
Tunnel ceiling	ca. 1,500	100	15
Façade	2,500	55	5
Parking deck	2,500	50	1

This parameter is given in l/m^2 for cleaning processes, and in l/m^3 for heavy hydrodemolition. Table 4.14 lists typical values for hydrodemolition. Specific water consumption depends on type and condition of the material being removed, on site conditions, on performance parameters of the jetting system, and on the tools being used. Basically, automated equipment will consume less water per square meter than hand-held equipment. It must, however, be taken into account that about 30% of the water evaporates (Anonymus, 1997), mainly due to heat generation during the blasting process.

Table 4.14 Specific water consumption of heavy hydrodemolition jobs (based on Table 4.9)

Object	Completed area in m^2	Water consumption in l/m^2	Water consumption in l/m^3
Bridge	210	827	27,570
Bridge	45	890	29,690
Bridge	40	772	25,730
Harbour structure	1,550	580	19,300
Harbour structure	210	772	25,730
Harbour structure	85	5,790	28,950
Bridge	140	965	16,080
Bridge	700	1,447	12,060
Floor	300	1,930	24,125
Facade	100	2,316	28,950
Bridge	75	1,503	17,540–23,100
Pillar (round)	185	5,790	72,370–115,800
Power station	85	1,158	38,600
Bridge (overhead)	80	1,447	48,250
Bridge	12,000	290	28,950
Tunnel (overhead)	200	1,053	35,090
Bridge	1,500	1,287	14,300–21,440

There are regulatory limits of waste water pollutants. These limits may differ from country to country. Table 4.15 lists regulatory limits for the acceptance by a municipal sewer system of two German cities. Therefore, any waste water from hydrodemolition jobs must be treated appropriately in order to meet these and other regulatory limits. Dorner (1996) performed an extensive study into the chemical compositions of waste water collected from hydrodemolition sites. Some results are listed in Table 4.16 for plain concrete removal jobs, and in Table 4.17 for

the cleaning of dirty concrete surfaces. Neither grease nor oil fractions could be detected. Detergents, fluorides and nitrides could also not been found. The result for sulphides points to concrete structures manufactured from Portland cement. Comparisons between Tables 4.15 to 4.17 show that, with the exceptions of the pH-values of two sites, all measured values are below the regulatory limits for the discharge of sewage. The rather low pH-value for the bridge site in Table 4.16 is a result of neutralisation with diluted hydrochloric acid. A unit for the neutralisation of waste water as used on-site is shown in Fig. 4.9. Heavy metal contamination of the waste water was mainly due to chromium, copper, lead, nickel and zinc. The composition of sludge after hydrodemolition is provided in Table 4.18.

Table 4.15 Regulatory limits for water inlet in municipal sewers

Parameter	Limit	
	City of Frankfurt	City of Munich
Temperature	35 °C	–
pH–value	6.0–9.5	–
Element	Limit in mg/l	
Arsenic (Ar)	0.1	0.1
Cadmium (Cd)	0.5	0.2
Chromium (Cr)	2.0	0.5
Copper (Cu)	2.0	0.5
Cyanide (CN)	5.0	–
Iron (Fe)	20.0	–
Lead (Pb)	2.0	0.5
Mercury (Hg)	0.05	0.05
Mineral oil and grease	20.0	
Nickel (Ni)	3.0	0.5
Organic oil and grease	50.0	–
Phenols	20.0	–
Selenium (Se)	1.0	–
Silver (Ag)	2.0	1.0
Solvents, halogenated hydrocarbons	5.0	–
Solvents, organic	10.0	–
Sulfates (SO_4)	400	400
Tin (Sn)	3.0	2.0
Zinc (Zn)	5.0	2.0

Table 4.16 Composition of waste water from hydrodemolition sites (Dorner, 1996)

Parameter	Site			
	Facade	Bridge	Parking deck	Tunnel ceiling
pH-value	12	9	12	12
	Salts (mg/l)			
Chloride	57	265	85	8
Sulphate	190	18	172	14
	Elements (µg/l)			
Arsenic	< 50	< 50	< 5	< 5
Cadmium	< 10	< 10	< 10	< 2
Chromium	23	14	45	22
Cobalt	< 10	< 10	< 10	< 2
Copper	26	< 10	< 10	< 1
Lead	< 50	< 50	< 50	14
Mercury	< 10	< 10	< 10	< 5
Nickel	52	< 50	< 10	< 10
Silver	< 10	< 10	< 10	< 2
Tin	< 50	< 10	< 10	< 10
Zinc	< 10	< 10	< 50	< 4

Table 4.17 Composition of waste water from water jet cleaning sites (Dorner, 1996); only an external dirt layer was removed

Parameter	Facade	Parking deck	Limits municipal sewer system Munich
pH-value	8	8	6–11
	Salts in mg/l		
Chloride	75	36	No limit
Sulphate	270	119	400
	Elements in µg/l		
Arsenic	< 2	< 2	100
Cadmium	< 2	< 2	200
Chromate	–	–	100
Chromium	16	8	500
Cobalt	< 10	< 10	1,000
Copper	15	< 2	500
Lead	< 20	< 20	500
Mercury	< 0.5	< 0.5	50
Nickel	13	< 10	500
Silver	< 10	< 10	1,000
Tin	< 10	< 10	2,000
Zinc	< 10	42	2,000

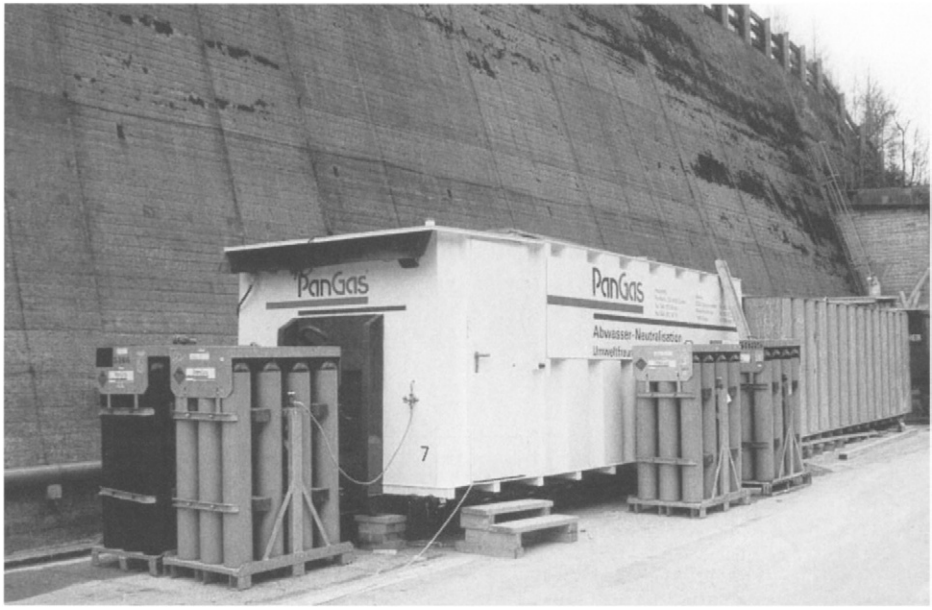

Figure 4.9 On-site neutralisation unit of hydrodemolition waste water (photograph: WOMA Apparatebau GmbH, Duisburg)

Table 4.18 Composition of sludge after hydrodemolition (Werner et al., 1995)

	Unit	Sedimented substances	Excess water
Dry substance	%	38	
Loss due to burning	%	10.0 of dry substance	
pH-value	–		12.4
Electric conductivity	µS/cm		3,310
Cadmium	ppm	0.8	< 0.01
Chloride	ppm		70
Chromium (total)	ppm	20.2	< 0.02
Chromium VI	ppm		< 0.02
Copper	ppm	36.4	< 0.03
CSB	ppm		37
EOX without POX	ppm	1.25	
Hydrocarbons	ppm		2.74
Lead	ppm	42.5	< 0.02
Nickel	ppm	23.7	< 0.02
Sulphate	ppm		< 10
Zinc	ppm	195	< 0.02

4.4 Submerged hydrodemolition

Hydrodemolition can be used to efficiently remove concrete from submerged structures or to clean submerged concrete constructions even in great depths. An example is shown in Fig. 4.10. At water depths between 150 m and 300 m, a

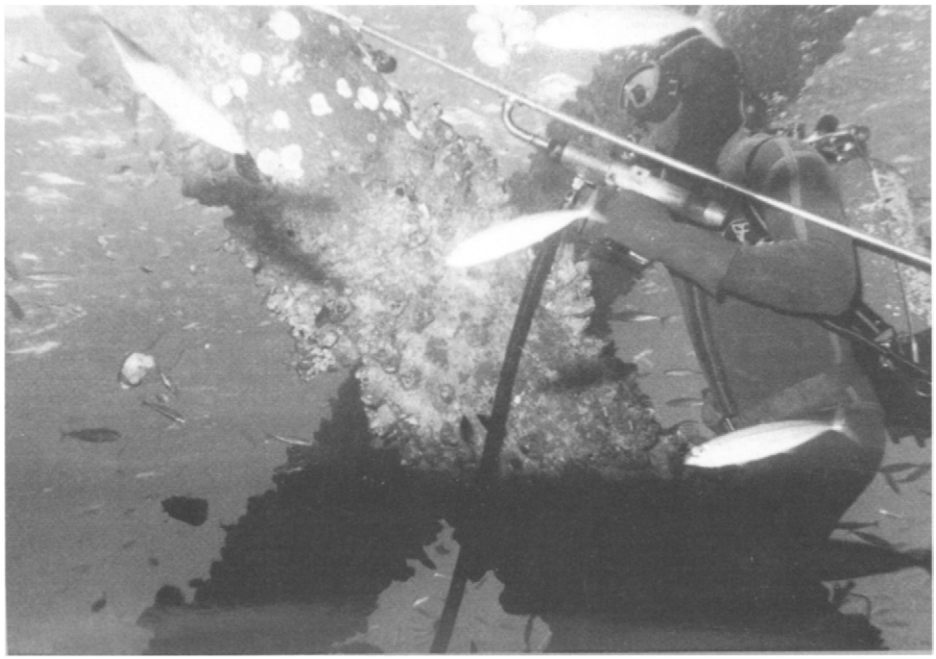

Figure 4.10 Submerged cleaning of a concrete column (photograph: WOMA Apparatebau GmbH, Duisburg)

concrete layer with a thickness of 100 mm could be removed with efficiencies at about 1.2 m/h. If water depth increases, efficiency decreases. For depths greater than 300 m, for example, efficiency dropped down to 0.7 m/h. In all cases, reinforcement bars were completely exposed (Conjet, 1999). Submerged waterjets perform equal to waterjets on air as far as a certain length is not exceeded. This critical length is given as follows (Cheung and Hurlburt, 1976):

$$x_L = \frac{v_J \cdot d_N}{4 \cdot v_E} \cdot \ln\left(0.113 \cdot \frac{v_J}{v_E}\right) \tag{4.6}$$

The parameter v_E is the velocity of entrained water; a typical value may be v_E=15 m/s (Cheung and Hurlburt, 1976). For standard hydrodemolition parameters (v_J=500 m/s; d_N=2 mm), Eq. (4.6) provides x_C=22 mm. This distance may be considered an optimum stand-off distance for submerged concrete removal. For very large nozzles (several mm in diameter), Kondo et al. (1974) developed a method that allows for the estimation of a maximum compressive strength where mortar can still be cut under water by water jets. These threshold conditions depend on Poisson's ratio of the mortar specimens, as shown in Fig. 4.11.

Parameter studies about the effects of process parameters, namely pump pressure, impinging angle, exposure time, stand-off distance, and traverse rate, are performed by Cheung and Hurlburt (1976), Hocheng and Weng (2002) and Klich and Kalukiewicz (1991). Results of these studies are provided in Fig. 4.12.

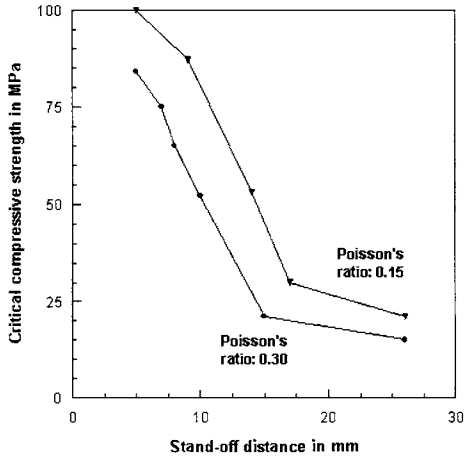

Figure 4.11 Critical stand-off distances for submerged cutting of mineral materials (Kondo et al., 1974)

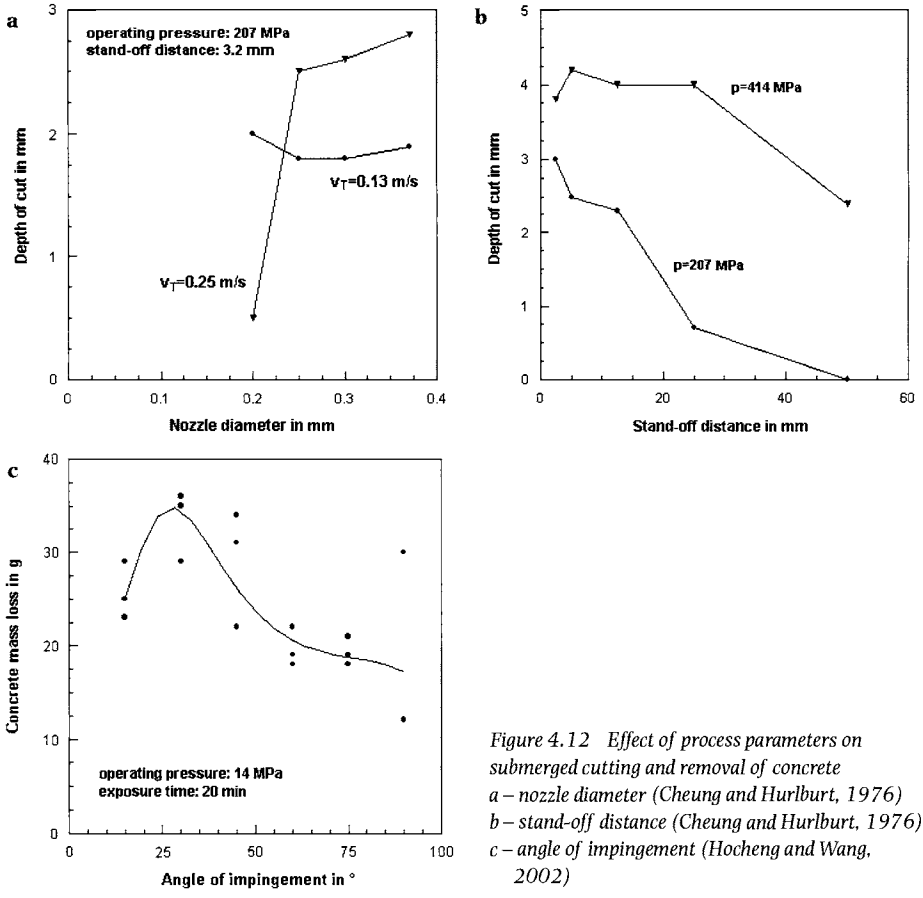

Figure 4.12 Effect of process parameters on submerged cutting and removal of concrete
a – nozzle diameter (Cheung and Hurlburt, 1976)
b – stand-off distance (Cheung and Hurlburt, 1976)
c – angle of impingement (Hocheng and Wang, 2002)

4.5 Health and safety features of hydrodemolition

4.5.1 General safety aspects

High-speed water jets can damage skin, tissue, and – if abrasives are involved – even bones (see, e.g., Axmann et al., 1998). Moreover, a notable amount of energy is stored in the high pressure parts of hydrodemolition equipment; this is illustrated in Fig. 4.13. Endangering due to hydrodemolition technique includes the following (DIN/EN 1329, 2003):

- mechanical hazards;
- hazards during transport and machine movement;
- electric hazards;
- thermal hazards;
- hazards due to noise;
- hazards with program-controlled machines;
- hazards due to sudden start;
- hazards during shut-off.

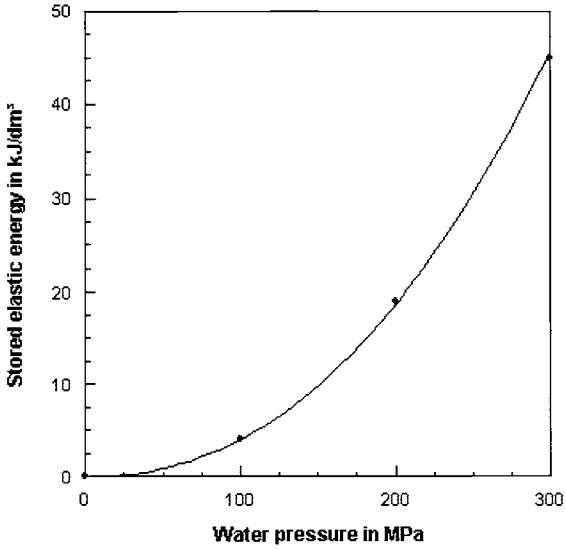

Figure 4.13 Specific energy stored in high-pressure parts of hydrodemolition equipment (Krüner et al., 1982)

General sources of danger to operators include the following (BGV, 1999):

- reactive forces generated by the exiting water jets (see 3.4.3);
- cutting capability of the high-speed jets;
- hose movements (especially during switch on of the pump);

- working in areas of electric devices;
- uncontrolled escape of pressurised water;
- damaged parts being under pressure;
- dust and aerosol formation;
- sound emitted from equipment and water jet;
- impact from rebounding debris from the jet impact point.

To protect operators and those not directly engaged in the blasting operation, the area around a work site that will be required for the hydrodemolition operation must be defined. The boundary of this area shall be clearly marked by the operating team, providing both a visible and a physical barrier to entry by unauthorised personnel. A typical example is shown in Fig. 4.14. The immediate removal site, where the actual tool is in operation, should be encapsulated for several reasons; mainly in order to hold back flying debris and to reduce noise. An example how this problem can be solved under site conditions is provided in Fig. 4.15.

Figure 4.14 Warning sign for a hydrodemolition site

A pre-service and operational check list for hydrodemolition operations is recommended. This list should answer the following questions (WJTA, 1999):

Date: ...
Location: ...
Unit being cleaned ...

- Is the area, including the other end of the unit being cleaned, adequately barricaded, with proper warning signs posted (see Fig. 4.14 for an example)?

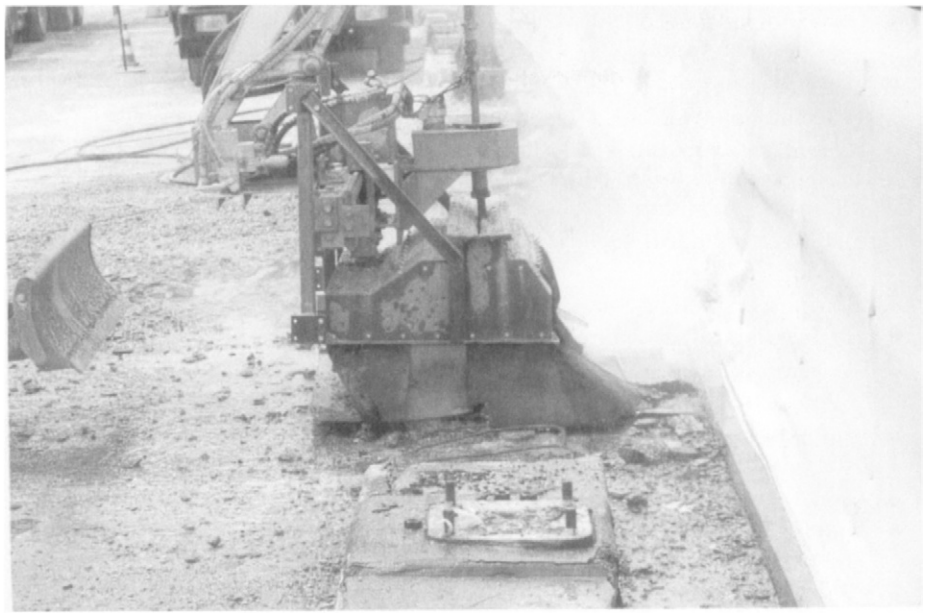

Figure 4.15 Encapsulation of the operating water jet tool (photograph: Aquajet AB, Holsbybrunn)

- Have precautions been taken to protect all electrical equipment?
- Is there any hazard to personnel from possible damage to equipment, such as release of corrosive chemicals, flammable liquids, or gases?
- Are all fittings of the correct pressure rating in accordance with regulations?
- Are all hoses of the correct pressure rating in accordance with regulations?
- Are all hoses in good operating condition?
- Are all fittings in good operating condition?
- Are all nozzles free from plugging and in good operating condition?
- Is the filter on the pump suction clean and in good operating condition?
- Is there an adequate water supply?
- Have precautions been taken against freezing?
- Do all personnel have the proper equipment for this job?
- Do all the personnel have the proper training for this job?
- Are all personnel qualified to perform this work?
- Has the complete hook-up been flushed and air removed from the system before installing the nozzle?
- Has hook-up, including pipes, hoses, and connections, been pressure tested with water at the maximum operating pressure?
- Is the dump system operating properly (will it dump when released)?
- Are all control systems operational?
- Is the location of first aid equipment and an emergency medical centre known?

- Has the job site been examined to determine if confined space entry requirements apply?
- Has the job been examined for environmental considerations, with action as appropriate?

It is also recommended to carry out a risk assessment of the actual environment where a hydrodemolition job will be done before starting the job. This risk assessment may include the following questions (French, 1998):

- How access is to be gained?
- Is there a need for scaffolding?
- Is there confined space?
- What is the surface like where the operators will have to stand?
- the availability of day light or artificial light;
- the presence of electrical supplies / equipment;
- water source and drainage of it;
- nature of contaminate: Is it toxic? Is it a pathogen? Is it asbestos based? Is it harmful or corrosive?
- general layout that will allow visual contact between of the working team;
- permit requirements;
- safety of access (e.g. working on motorways or hazardous areas such as refinery where flameproof equipment and earthing to avoid static electricity may be required);
- Who or what will be affected by flying debris?
- Is noise a problem?
- Will containment be necessary?
- Where will the effluent go?

Statistics of incidents has shown that the average experience of operators affected their involvement in incidents. These relationships are presented in Fig. 4.16. It can be seen that the risk of incidents reduces if average experience increases. Operators who have worked with hydrodemolition equipment less than 12 months, were involved in 55% of all incidents. In that context, ISO 12944-4 (1999) states the following: "Personnel carrying out surface preparation work shall have suitable equipment and sufficient technical knowledge of the processes involved."

Hand-held tools require special attention (see DIN/EN, 1829, 2004). The reaction forces acting on the operator along the jet axis must not exceed the value 250 N. If reaction forces are larger than 150 N, an additional body support must be used (see Fig. 4.27a for an example). Reaction forces cane be calculated with Eq. (3.24). The length of a hand-held gun must exceed the value of 75 cm. If the gun is shorter than this critical length, the gun must be equipped with a two-hand control as shown in Figs 3.17 and, respectively, Fig. 4.27a. The tool must work only if both parts of the control system are activated simultaneously. If the hand grip of a hand-held water jet tool is released, one of the following arrangements must act (DIN 1219, 2003):

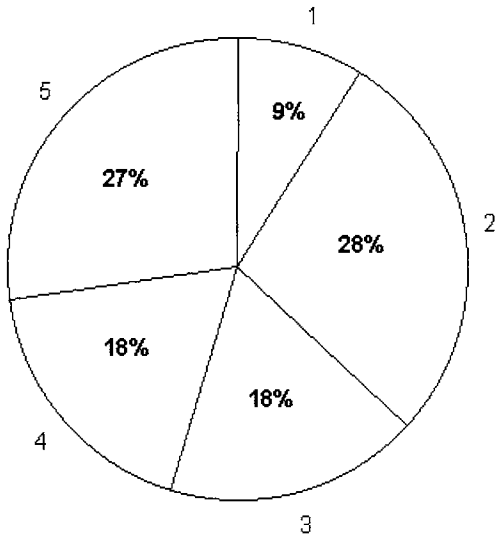

Figure 4.16 Percentage of operators involved in incidents (reference: AUSJET News, August 2000)

Operator's experience:
1 – 60 months
2 – 3 months
3 – 24 to 60 months
4 – 12 to 24 months
5 – 12 months

- no liquid must exit the nozzle;
- if liquid exits the nozzle, the reaction force generated by the liquid must not be larger than the weight force of the tool (for electrically, pneumatically or hydraulically controlled devices);
- pressure generator (pump) must be shut-off. This must occur also in case of damage to, or short-circuits in, electric signal lines.

4.5.2 Emission of air noise

There are four major sources of air sound generated during hydrodemolition operations:

- sound emitted from the pressure generating unit (pump, engine, power transmission);
- sound emitted from the high-speed water jet travelling through the air;
- sound emitted from the erosion site;
- sound emitted from companying trades.

State-of-the-art high-pressure plunger systems are regularly equipped with sound insolating hoods or even placed in containers. Thus, the air sound emission is limited up to 70-75 dB(A). More critical is the air sound emitted by the water jet. This noise is generated due to friction between the high-speed jet and the surrounding air as well as due to turbulences. Thus, the sound level depends on the relative velocity between jet and air, and on the surface exposed to friction. Consequently, air sound level increases as pump pressure, nozzle diameter, and standoff distance increase. Some results of direct measurements shown in Fig. 4.17 and in Fig. 4.18 verify these general trends. However, as shown in Fig. 4.19, the

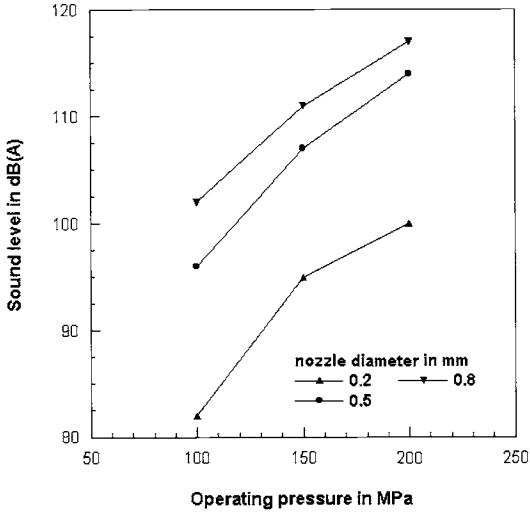

Figure 4.17 Relationships between operating pressure, nozzle diameter and sound level (Werner, 1991b)

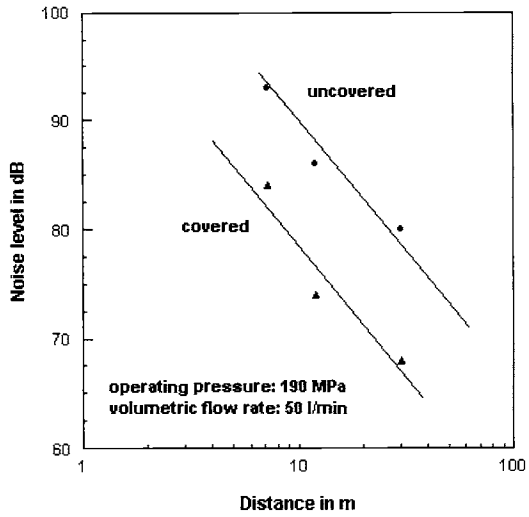

Figure 4.18 Effect of distance from noise source on noise level during hydrodemolition (Katakura, 2000)

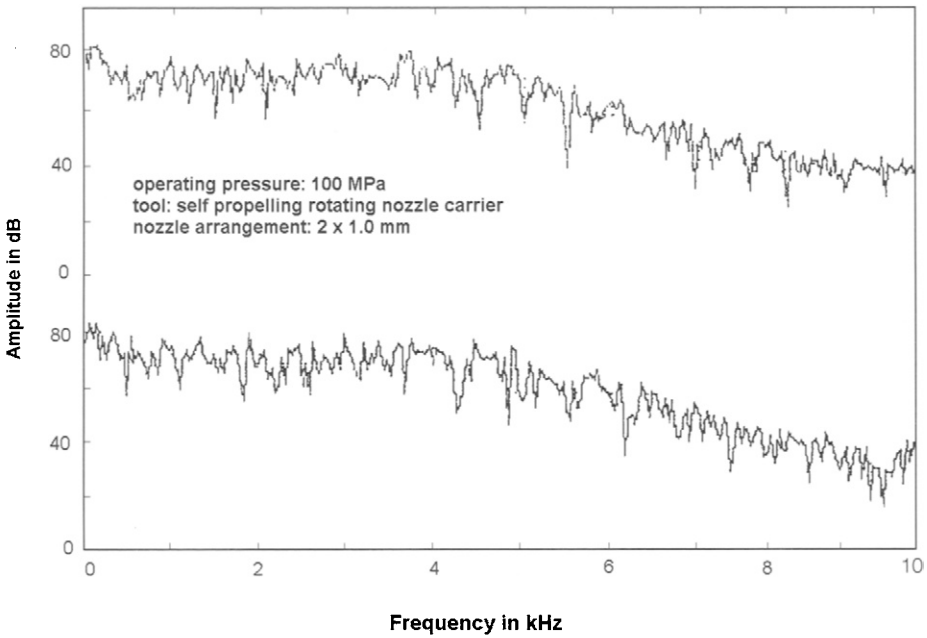

Figure 4.19 Plot of noise measurements during concrete roughening with rotating hand-held tools (Freitag, 1991)

frequency of the sound generated plays an additional role. For rotating nozzle carriers, the very quick radial movement generates turbulences and flow interruptions further contributing to the noise. If a nozzle carrier comprises several small-diameter nozzles instead of one large-diameter nozzle, the total jet area increases and so the noise level does. That is why rotating devices usually generate rather high noise levels. It was reported (Barker et al., 1982) that high amplitudes occurred in the frequency range between f_L=1-8 kHz, and at rather low impact angles (<30°). However, this seemed to be true for small stand-off distances only.

Fig. 4.20 contains results of measurements performed at different rehabilitation sites. Examples for jackhammering, wet blasting and waterjetting are shown. The actual surface treatment processes generate the highest noise levels among all trades. Jackhammering and wet blasting are comparatively silent. Noise generated during waterjetting can notably be reduced if shrouded or sealed tools are used. Such a construction is shown in Fig. 4,21. Commercial hydrodemolition robots work with covered nozzles and their noise levels are, therefore, lower than those from open hand-held tools. The permissible air noise level depends on the exposure time. This is illustrated in Fig. 4.22 based on regulatory limits stated in BGV B3 (2001). It can actually be concluded from that graph that ear protection equipment must be worn by any personally involved operator (see Section 4.5.6).

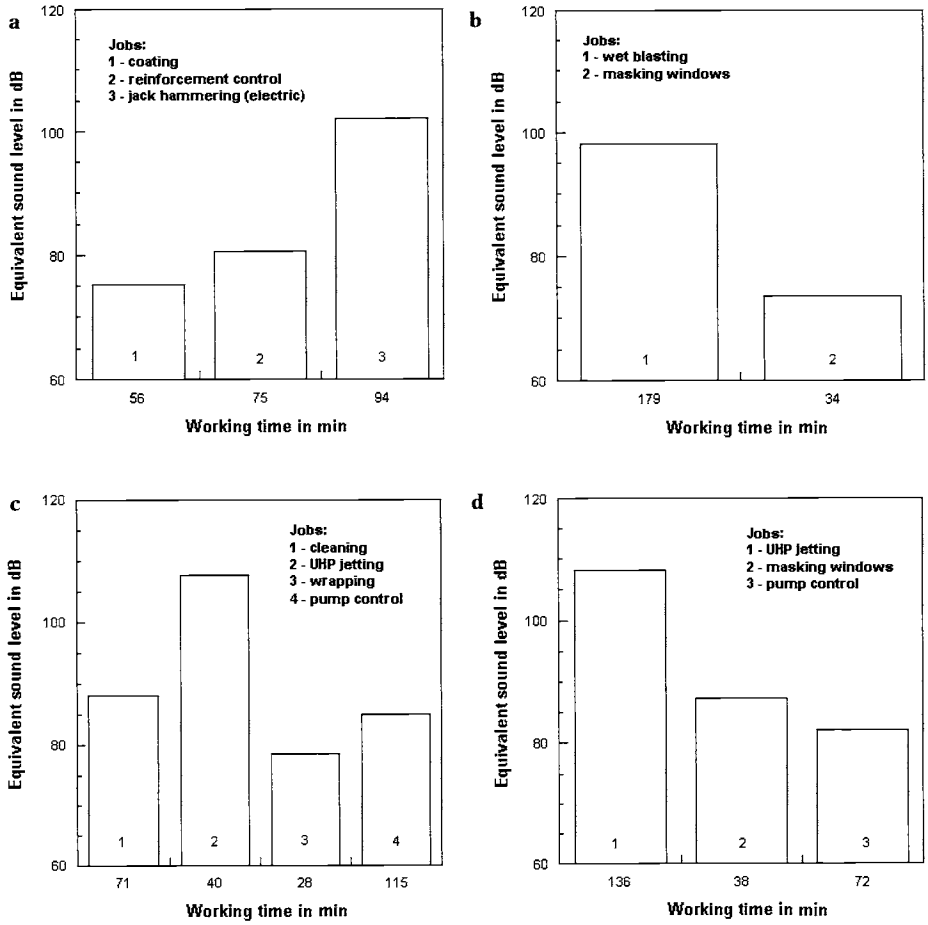

Figure 4.20 Noise measurements from concrete rehabilitation sites (Knipfer and Funke, 1997)
a – jackhammering b – wet blasting c – waterjeting d –waterjeting

4.5.3 Body sound and vibrations

Body sound characterizes waves carrying noise and travelling through solid materials. Therefore, even if windows, doors etc. are properly closed to lock out airborne noise, persons may anyway experience certain noise levels. This noise is generated due to small vibrations; they occur during the tool impact and depend on the acoustic properties, especially on the sound velocity and the acoustic impedance, of both the material to be subjected and the preparation tool. The evaluation parameters of the sound waves are their amplitude and velocity (frequency).

There are some measurements available from concrete facades treated with different preparation tools. Examples are plotted in Fig. 4.23a. It clearly illustrates

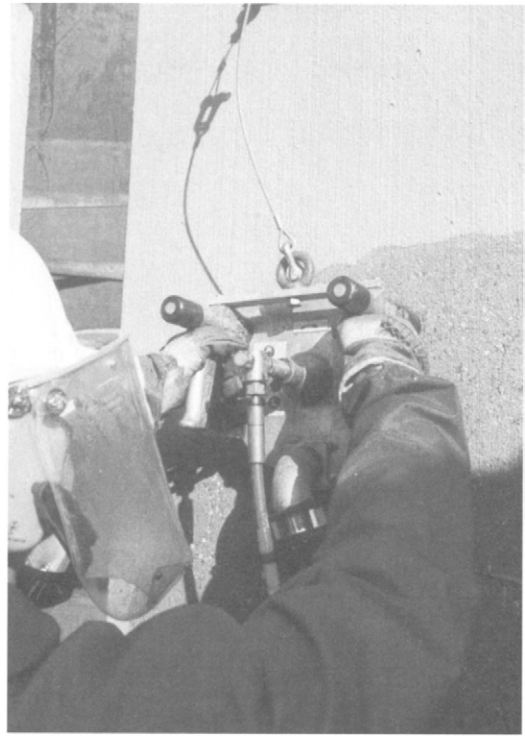

Figure 4.21 Sealed water jet tool for emission-free concrete treatment (photograph: WOMA Apparatebau GmbH, Duisburg)

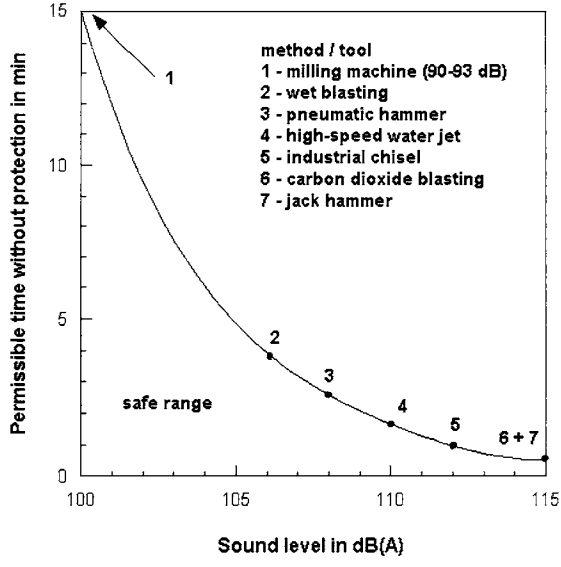

Figure 4.22 Critical exposure times for different preparation tools (solid line according to BGV B3; points from different sources)

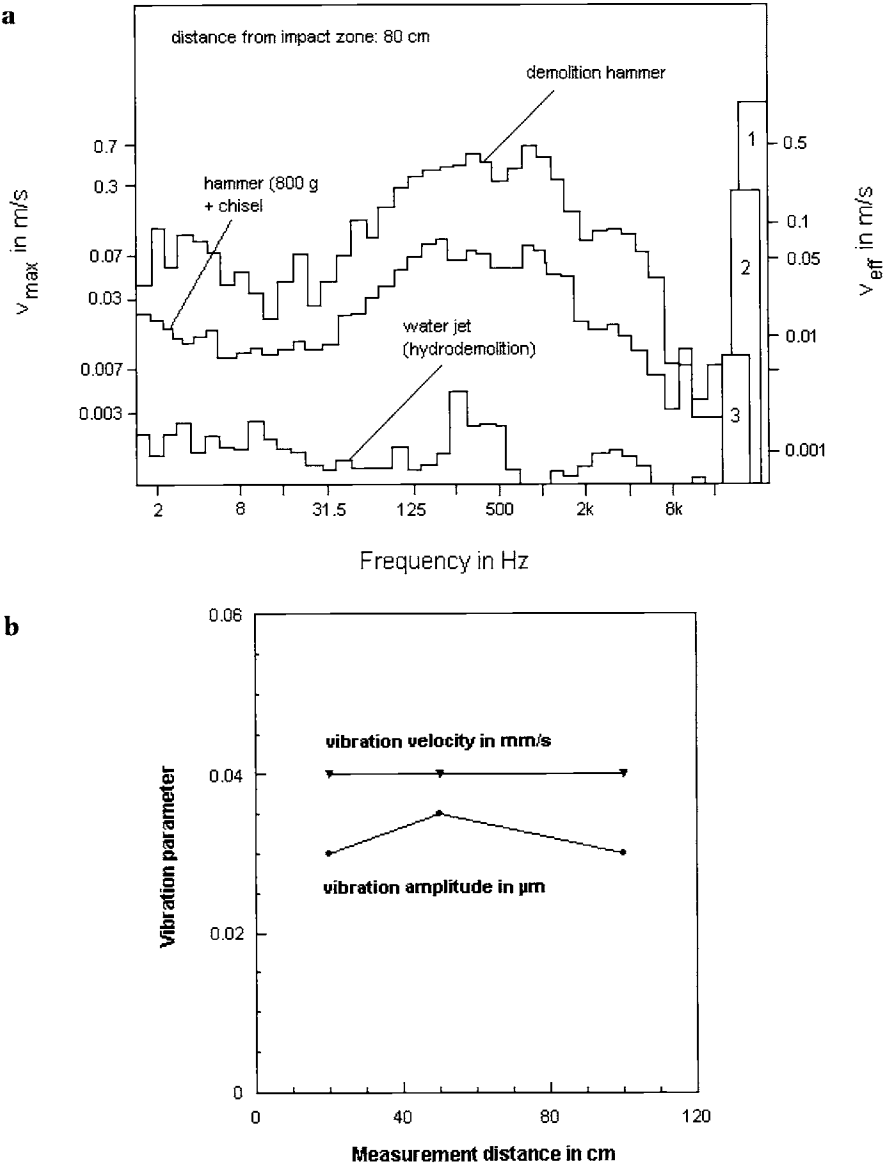

Figure 4.23 Body sound generated on concrete surfaces (Werner and Kauw, 1991, Werner, 1991c)
a – effect of treatment method
b – effect of measurement distance

the extremely low body sound generated if water jets are used. Figure 4.23b shows that frequency and velocity of the vibrations are at a more or less constant level for water jet applications, even if the distance form the vibration source significantly varies. Vibrations generated over a longer period of time in the arms of operators

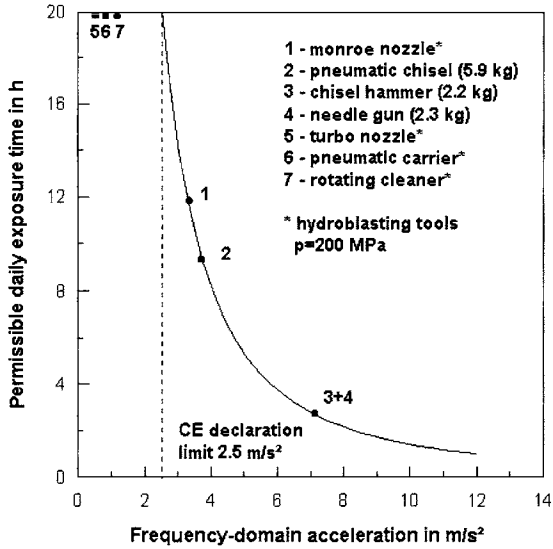

Figure 4.24 Limits for exposure of the hand per day to vibrations (solid line according to Siebel and Mosher (1984); points from different sources)

may cause so called 'white fingers'. The vibration generated by the tool is transmitted through the operator's hand where is does damage to the blood vessels in the fingers (VDI, 1987). Therefore, regulations state minimum working hours depending on the intensity of the vibrations. The intensity is usually given by an acceleration value a_V. Results of measurements obtained from different surface preparation tools (including hydroblasting tools) are show in Fig. 4.24. Note from this figure that any point above the solid line is critical to health. Exposure time is the total time vibrations enter the hand per day, whether continuously or intermittently. Acceleration values for water jet tools are lower than those measured for mechanical tools. However, for hand-arm-vibrations the EC-machine guide requires the following:

- any value in excess of $a_V > 2.5$ m/s^2: the measured acceleration value must be stated in the tool manual (e.g. $a_V = 3.17$ m/s^2 for monroe nozzle);
- any value equal to or lower than $a_V = 2.5$ m/s^2: it must be stated in the tool manual that $a_V \leq 2.5$ m/s^2 (e.g. for the turbo nozzle, pneumatic carrier and rotating cleaner).

Heavy hydrodemolition machines may generate larger vibrations to constructive parts of buildings and constructions. As shown in Fig. 4.25, the velocities of the vibrations generated during hydrodemolition are below the permissible limits.

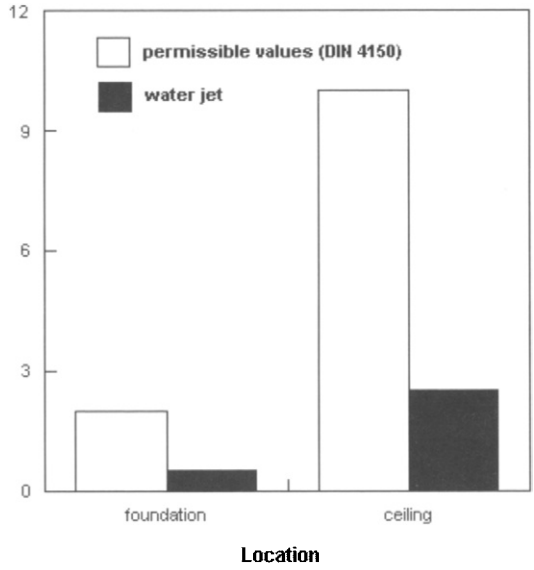

Figure 4.25 Vibrations to concrete structural parts caused by water jets (Temme, 1986)

4.5.4 Emission of aerosols and micro-fibres

A mist of water, vapour and solid particles is generated during hydrodemolition in the immediate environment of the operator. Unfortunately, this mist is difficult to control. The only way to prevent it is the use of shrouded tools (see Table 3.7 and Fig. 4.21). Another way to protect the operator is the application of mechanically guided tools or robotic machinery. A major problem are aerosols that contain microscopically small particles from the removed coating. Many old coatings contain lead; there is a critical situation as the lead may enrich the operator's blood due to breathing the aerosol. There are the following two critical levels:

- Action Level (AL=30 $\mu g/m^3$); if an operator work in an area that at or above that level, the employer must give medical surveillance and training in the hazards of working with lead.
- Permissible Exposure Limit (PEL=50 $\mu g/m^3$); This limit is for the average amount of lead in the air over an 8-hour day.

Extensive studies have shown that airborne lead concentration does not depend on the main lead concentration in coating systems to be removed. The correlation between these parameters was as low as 0.22 (DHHS, 1997). It is, therefore, the surface preparation method that determines airborne lead. Air monitoring tests carried out by the Houston Harbour Authorities (Marshall, 1996) and the US Navy

(Anonymus, 1997) have shown that the lead concentrations in aerosols generated during waterjetting are below the regulatory levels. Some results are displayed in Table 4.19. Note the low levels for the water jet applications. The blood of operators was controlled during several lead paint stripping jobs; some results of pre-job and post-job blood lead level tests are listed in Table 4.20. Although the lead level increased during the blasting job, the regulatory limit was significantly undercut. Systematic lead concentration measurements were performed during the refurbishment of an old power plant for the first ten days (Dupuy, 2001). Fifteen samples were taken with only one above the 'no detection' level. The detected sample was 40 $\mu g/m^3$. Interestingly, the project management decided to remove any respirator requirements initially enforced during the job and to implement a random sampling as necessary to insure personnel safety.

Table 4.19 Measured airborne lead levels for different preparation methods

Object / condition	Lead level in $\mu g/m^3$	Reference
Waterjetting		
Galvanized communication towers	1.5–29	Holle (2000)
Structural steel construction	2–12	Dupuy (2001)
Dock side container crane	2.2*	Marshall (2001)
Dock side container crane	0.79*[1)]	Marshall (1996)
Dock side container crane	< 0.99*[2)]	Marshall (1996)
Slurry blasting		
Highway overpass structure	10.4–34.4	Anonymus (1998)
Steel bridge	45.7–305 [2)]	Frenzel (1997)
Steel bridge	40.1–52.7 [3)]	Frenzel (1997)
Vacuum blasting		
Steel bridge	27–76 [2)]	Mickelsen and Johnston (1995)
Grit blasting		
Blast room	1–100,000	Adley and Trimber (1999)
Steel bridge (blaster)	36–4401	Conroy et al., 1996)
Steel bridge (sweeper)	12–3548	Conroy et al., 1996)
Steel bridge (foreman)	12–3423	Conroy et al., 1996)
Steel bridge (equipment operator)	39–1900	Conroy et al., 1996)
Steel bridge (helper)	22–501	Conroy et al., 1996)
Steel bridge (operator)	50–450*	Randall et al. (1998)
Petrochemical tank	3.31*[2)]	Frenzel (1997)
Ice blasting		
Steel bridge	175	Snyder (1999)

* TWA 8 hours, [1)] downwind, [2)] gun operator, [3)] outside containment

Many old linings contain asbestos. Asbestos fibres are known to be responsible for lung cancer. Results of asbestos emission during the preparation of steel substrates are shown in Fig. 4.26 and listed in Table 4.21. It can be seen that all

preparation methods that contain a liquid phase (wet blasting, waterjetting) generate rather low asbestos concentrations. Tar epoxy coatings contain polycyclic agents, namely polycyclic aromatic hydrocarbons. Results of measurements of hydrocarbon exposure during decoating jobs with different treatment methods are also listed in Table 4.21.

Table 4.20 Results of blood level monitoring during waterjetting (Frenzel, 1997); exposure duration: 892 hours

Condition	Blood lead level in µg/dl
Prejob level	4.77
Post-job level	6.76
Permissible level (OSHA)	40.0

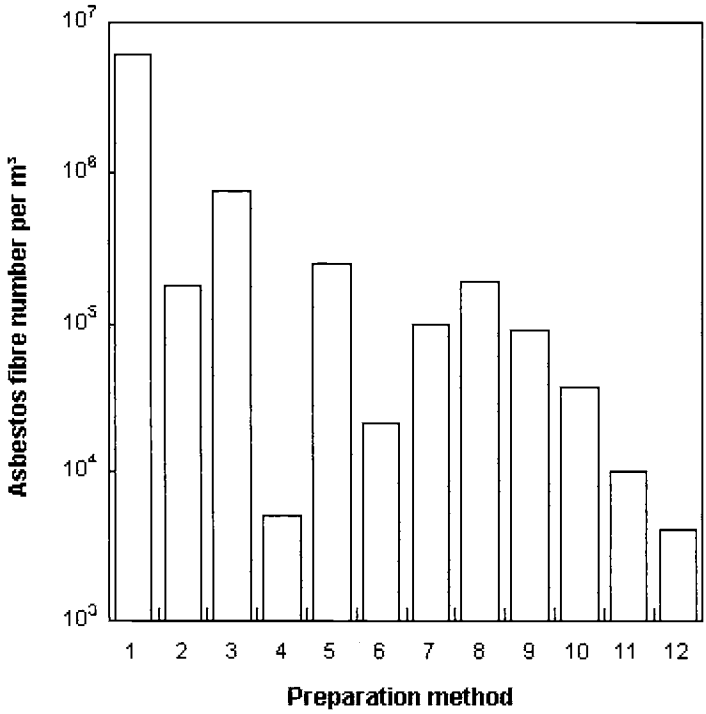

Figure 4.26 Asbestos emissions during coating removal from steel substrates (Schröder, 2000)

1 – dry grit blasting
2 – wet blasting
3 – wet blasting
4 – abrasive water jetting (85 MPa)
5 – water jetting (200 MPa)
6 – abrasive water jetting (120 MPa)
7 – water jetting + dry grit blasting
8 – wet blasting
9 – water jetting (240 MPa)
10 – wet blasting (copper slag)
11 – water jetting (13 MPa)
12 – water jetting (15 MPa)

Table 4.21 Asbestos and PAK emissions during the coating removal from steel substrates (Schröder, 2000)

Method	Number of measurements	Number of fibres per m^3	PAK[1]-value in $\mu g/m^3$
Flame cutter	8	881	Regulatory limit [2] exceeded
Needle hammer	1	< 5,845	–
Needle hammer	1	14,933	–
Needle hammer	1	281,000	80–130
Burner	7	30,000–165,000	14–48
Hand-held grinder	1	25,000	50–152
Water jet (1 3 MPa)	1	5,000–10,000	Regulatory limit undercut
Grinding	2	20,000–45,000	–
Scraping	2	< 5,000	Regulatory limit undercut
Flame cutter	2	Up to 38,000	Regulatory limit exceeded
Flex sawing (1 50 °C)	1	98,074	–
Water jet	1	< 4,045	–
Plane grinding	2	20,000–45,000	Regulatory limit exceeded

[1] Polycyclic Aromatic Hydrocarbons; [2] Limit: 2 $\mu g/m^3$

4.5.5 Risk of explosion

Some source of explosion during water jet application can be electric discharge sparks. Safety hazard analyses identified that static electric charges occur in the following four circumstances (Miller, 1999):

- liquids flowing through piping at rates (velocity) greater than 1 m/s;
- liquids passing through fine filters or orifices;
- liquids being sprayed;
- liquids impacting fixed parts.

These conditions essentially describe the formation and use of high-speed water jets for hydrodemolition. Charge generation is proportional to the square of the jet velocity and inversely proportional to the square of the liquid conductivity. If electric conductivity of a liquid exceeds the value of 10^{-8} S/m, the risk of dangerous electric charges is very low (BGR 132, 2003). From this point of view, water can be considered a low-risk liquid (Table 4.22). However, this criterion cannot be applied to water sprays that are usually formed during hydrodemolition applications. Even if water itself has a rather high electric conductivity, carrier concentrations of droplet clouds can reach critical values. Serious investigations about the explosion risk of water jets included tests with rather low operating pressures up to 50 MPa. It could be shown that density of volume charge of a water droplet cloud increased steeply with rising pressures up to a pressure level of 10 MPa. If this value was

exceeded, density of volume charge remained on a saturation level of about 240 nC/m^3 for pressures up to 50 MPa (Post et al., 1983).

Table 4.22 Physical properties of liquids (BGR 132, 2003)

Liquid	Electric conductivity in S/m	Dielectric constant (20 °C)
Diesel oil	10^{-13}	2
Gasoline	10^{-13}	2
Water (distilled in air)	10^{-3}	2.45
Water (clean)	$5 \cdot 10^{-3}$	2.45

If the following requirements are met for tank cleaning applications, waterjetting is considered uncritical from the point of view of electrostatics (Post et al., 1983):

- metallic tanks; tank volume not larger than 30 m^3 (or tank diameter not higher than 3 m for conventional heights);
- maximum operating pressure of 50 MPa;
- maximum volumetric flow rate of 300 l/min;
- all parts must be connected to ground.

However, these criteria basically apply to low-pressure cleaning jobs and not to the hydrodemolition applications covered by this book.

Results of spark generation tests performed during the cutting with hydro-abrasive water jets are listed in Table 4.23. Xie (1998) found that risk of spark formation during hydro-abrasive cutting of metals depended upon operating pressure and abrasive mass flow rate. No sparking occurred if both parameters were kept at low levels. High volumetric water flow rates reduced the probability of spark formation. Safe mass ratios of abrasive to water were reported to be about 7%. Sparking was more severe if hard materials (stainless steel) were cut, and less severe if soft metals (aluminium) were cut (Xie, 1998).

Table 4.23 Results of spark generation test with hydro-abrasive water jets. Materials being cut: steel and sandstone (Leeming, 1981)

Tests	Gas mixture		
	Hydrogen/air	Methane/air	Total
Total number of tests	46	33	79
Number of tests with ignitable gas left after cutting	41	30	71

4.5.6 Personnel protective equipment

Required personnel protective equipment for hydrodemolition operators includes the following items (AHPWJC, 1995; JISHA, 1992; WJTA, 1999):

- Head protection (helmet): All operators shall be supplied with a safety helmet which shall be worn at all times while at the worksite. Where necessary the helmet should incorporate face protection (see Fig. 4.27b).
- Eye protection (goggles, face shield): Suitable eye protection (adequate for the purpose and, of adequate fit on the person) shall be provided to, and worn by, all operators.
- Hearing protection (foam earplugs, earmuffs, strap with plastic earplugs): Suitable hearing protection shall be worn while in the working area; (see Section 4.5.2).

Figure 4.27 Protective clothing for waterjetting operators (photographs: WOMA GmbH, Duisburg)
a – wet suit, gloves, boots
b – helmet with face and hearing protection

- Body protection (wet suit, reinforced safety suits): All operators shall be supplied with suitable waterproof protective clothing, having regard to the type of hazards in relation to the work being undertaken (see Fig. 4.28). This must be used where there is a risk to health or a risk of injury.
- Hand protection (rubber gloves, reinforced gloves): Hand protection shall be supplied to all team members and shall be worn where there is a risk of injury or contamination to the hands.

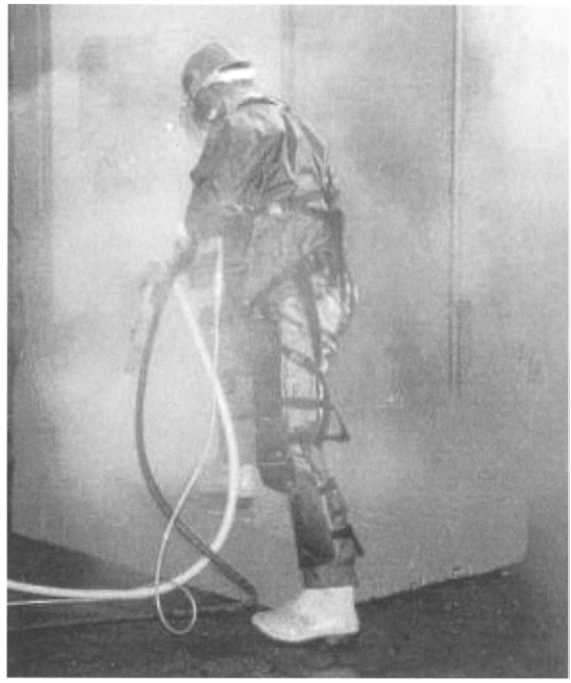

Figure 4.28 Special body protection for waterjetting operators (photograph: WOMA Appatatebau GmbH, Duisburg)

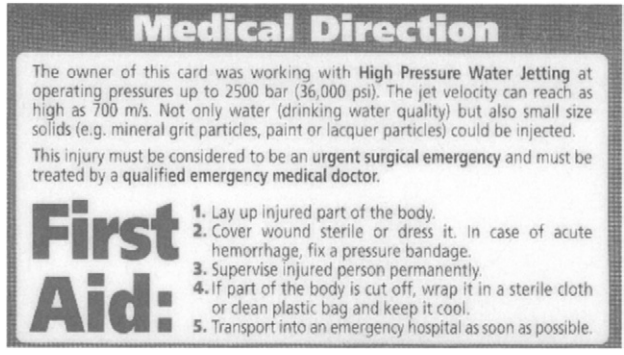

Figure 4.29 First aid card for water jet operators (WOMA Appatatebau GmbH, Duisburg)

- Foot protection (steel-toed boots): All operators shall be supplied with suitable boots or Wellingtons with steel toe caps, and where necessary additional strap-on protective shields. These shall be worn when there is a risk of injury.

- Respiratory protection (sometimes with supplied air. Where necessary suitable respiratory protection, that is either type approved or conform to an approved standard shall be worn.

Operators should carry a First Aid Card as shown in Fig. 4.29 that, in case of an accident, delivers basic information to helpers or medical personnel. Typical personnel protective clothing and equipment for operators are shown in Figs 4.27 and 4.28. Table 4.24 lists results of direct water jet impact tests on the body protection worn by the operator in Fig. 4.28. Further recommendations are given by French (1998), Momber (1993), Smith (2001), and Vijay (1998b).

Table 4.24 Results of resistance tests with body protection (Anonymus, 2002a)

Operating pressure in MPa	Volumetric flow rate in l/min	Nozzle diameter in mm	Distance in m	Traverse speed in m/s	Exposure time* in s	Result
18	13.0	1.2	7.5	0.5	0.0024	no penetration
50	19.7	1.2	7.5	0.5	0.0024	no penetration
100	19.3	1.0	7.5	0.5	0.0020	no penetration
150	15.0	0.8	7.5	0.5	0.0016	no penetration
200	17.0	0.8	7.5	0.5	0.0016	no penetration

* calculated with d_N/v_T

4.6 Cost aspects

A general cost structure may include the following positions:

- investment high-pressure unit;
- investment high-pressure tools;
- investment nozzle carrier heads;
- investment water treatment system;
- nozzle wear;
- fuel (or electricity, respectively);
- fresh water and sewage;
- operators' wages.

Table 4.25 lists costs for different concrete treatment jobs performed with water jets. These costs are, however, valid for hand-held tools only utilised for decontamination and cleaning jobs. Costs for heavy hydrodemolition applications are usually comparatively high for small areas. If larger areas are treated, costs reduce and finally rest at a constant level. This is illustrated in Fig. 4.30. Thus, there may be job size limits for the economic use of hydrodemolition. Wallace (1985) found an lower limit of about 1,000 m^2 which corresponds to the values shown in Fig. 4.30. Andreou (1989) who considered the demolition of reinforced concrete structures found a volumetric limit of about 22 m^3 for a cost-efficient use of a hydrodemolition robot.

Table 4.25 Cost structures of water jet applications (Sindt et al., 1997)

Application	Cost in %					
	Wages[1]	Investments	Water	Diesel + lubrication	Wear[2]	Total
Cleaning of fire damaged concrete	55.8	27.9	1.4	2.8	12.1	100
Removal of glue from concrete floors	55.5	27.8	1.4	2.8	12.4	100
Removal of mineral coating	55.5	27.8	1.8	2.8	12.1	100
Removal of dispersion/latex paint from concrete	55.7	27.9	1.9	2.5	12.0	100
Removal of dispersion/latex paint from lime-sandstone	55.9	27.9	1.7	2.5	12.0	100
Removal of dispersion/latex paint from plaster walls	55.8	27.9	1.5	2.6	12.2	100
Concrete removal (5 mm)	55.9	28.0	1.3	2.7	12.1	100

[1] Two operators

[2] Includes pump and nozzles as well as filters, activated carbon and sand of water treatment system

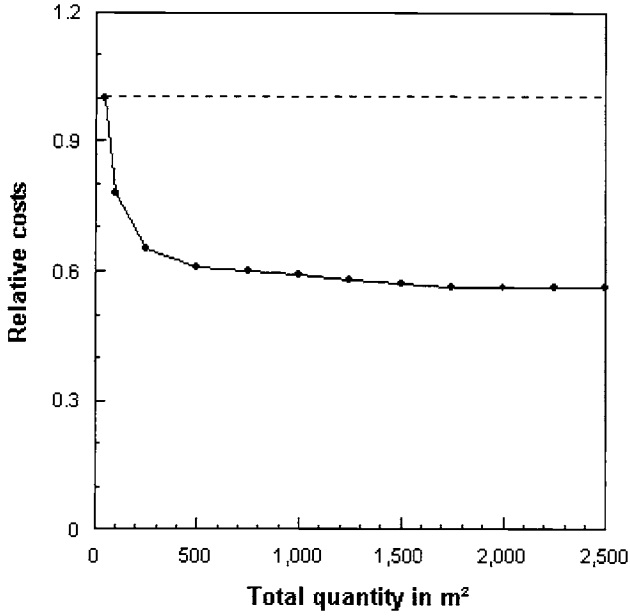

Figure 4.30 Hydrodemolition site size effect on cost (Vorster, 1992)

CHAPTER 5

Surface Quality Aspects

5.1 Surface quality features

Very typical demands on concrete surfaces prepared to carry protective coatings and, respectively, concrete replacement systems are as follows (RILI, 2001):

(i) surface should be free of loose and deteriorated parts (e.g. low-strength crack rims), and free of easy-to-peel layers (e.g. cement lime);
(ii) surface should be free of cracks or detachments running parallel to the surface, and free of cracks or detachments in the near-surface range;
(iii) surface should be free of burrs;
(iv) surface should feature a roughness according to the demands of the overlay materials;
(v) surface should be free of foreign matter (e.g. rubber deposits, separation agents, unsuitable old coatings, oil, growth, etc.).

Numerous standards are issued to define these factors, and testing methods are available to quantify them. Hydrodemolished surfaces show some distinct features, and numerous experimental studies were performed to address this special point, sometimes in direct comparison to other surface preparation methods.

5.2 Surface texture

5.2.1 Role and assessment of concrete substrate texture

Substrate profile parameters are very affective to the bond between substrate and overlay. High roughness, for example, provides a good mechanical bond. But other properties, namely wettability, depend on surface texture as well. Sakoda et al. (1998) and Reinecke (2002) correlated roughness values of profiled concrete substrates to strengths values of concrete joints. Results of these studies are provided in Fig. 5.1. It can be seen that joint shear strength grows as roughness increases.

The macro-topography of the surfaces, defined as 'profile' can be evaluated by mechanical 3D-profilometers. The surface is scanned by a tip. As the tip toughs the surface, a signal is sent to and stored into a signal processing unit. The resulting surface profile is calculated by an appropriate software. Examples, taken from grit blasted concrete surfaces, are shown in Fig. 5.2. Surface profile can also be evaluated with the 'Sand-Section Test' according to Kaufmann (1971) as recommended in RILI (2001). A given volume of finely-grained garnet is applied to the specimen surface and uniformly distributed over the treated surface. The actual evaluation parameter 'roughness depth', R_t, is calculated as follows:

$$R_t = \frac{40 \cdot V}{\pi \cdot D^2} \tag{5.1}$$

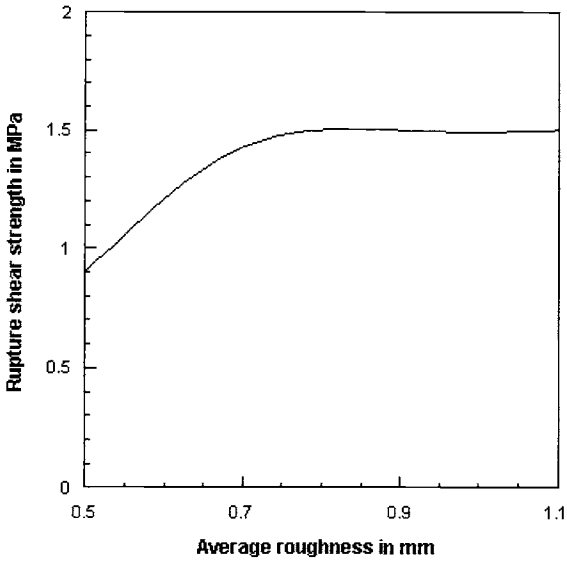

Figure 5.1 Effect of substrate surface roughness on joint shear strength (Reinecke, 2002)

Here, R_t is in mm, V is the garnet volume in cm^3, and D the diameter of the garnet disc formed on the surface in cm. The higher the value for R_t, the higher the surface roughness. A more advanced method is laser profilometry as recently introduced by Maerz et al. (2001). The surface is illuminated with thin slits of a red laser light at an angle of 45°, and the surface is observed at 90°. The projected slit of light appears as a straight line if the surface is flat, and as a progressively more undulating line as the roughness of the surface increases. Examples are shown in Fig. 5.3. This method was used to evaluate concrete substrates after hydro-demolition by Galecki et al. (2001).

Micro-topography and adhesion properties of concrete surfaces can be estimated by contact angle measurements, such as by using the Captive Drop Technique (CDT). The apparatus used for this procedure consists of a modified video microscope with an attachment for mounting a micrometer syringe. The specimen upon a contact angle measurement is made is placed in a thermostatted sample cell on a movable platform at a constant temperature. The cell is then filled with water and a liquid drop is formed at the end of the syringe and allowed to equilibrate. The contact angle is directly calculated from an image of the drop taken with a video camera. Exemplary photographs obtained by this method are shown in Figure 5.4. This method can be used to evaluate the degree of contamination of concrete surfaces with oil, grease, etc. (Gelfant, 1995). The examples listed in Table 5.1 show that contact angle to surfaces increases (wettability decreases, respectively) if degree of contamination rises. Similar results are reported by Fiebrich (1994). Grease, motor oil and silicone deteriorate wettability to a high degree.

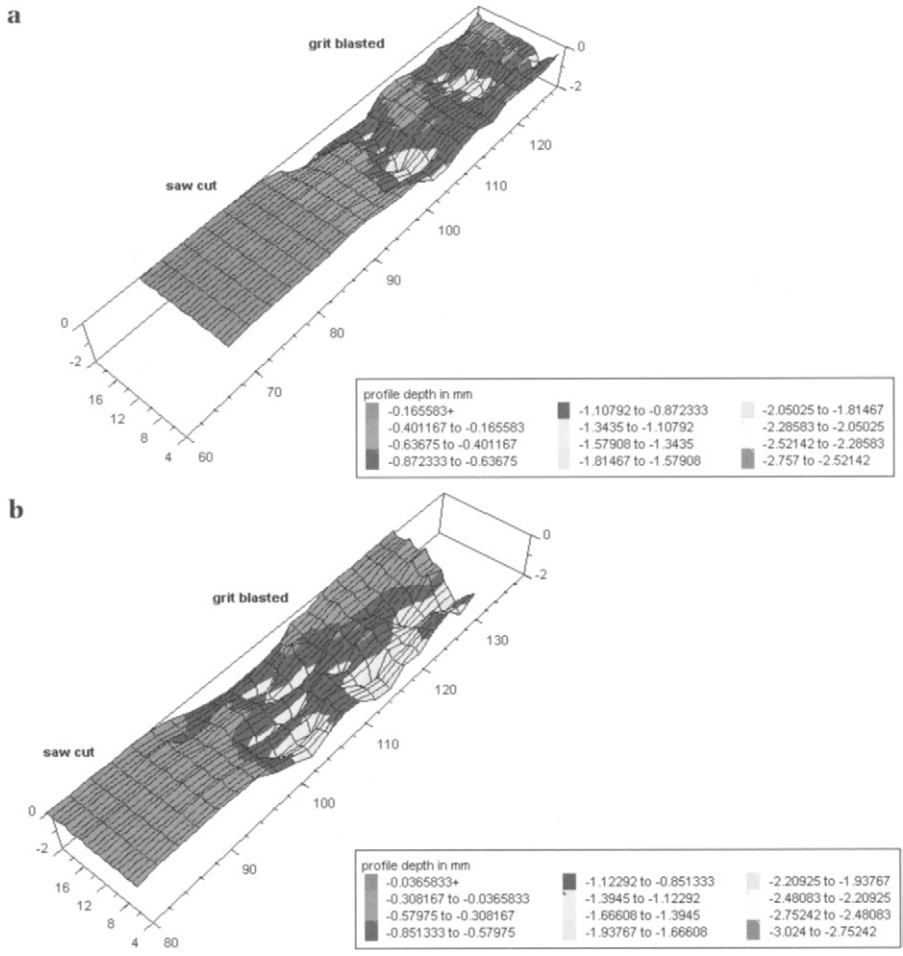

Figure 5.2 Concrete surface topography, estimated with 3D-profilometry (Momber, 2002a)
a – concrete; b – mortar

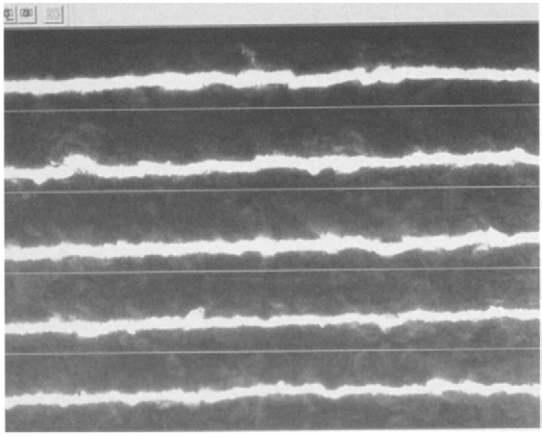

Figure 5.3 Concrete surface profile estimation with laser profilometry (Galecki et al., 2001)

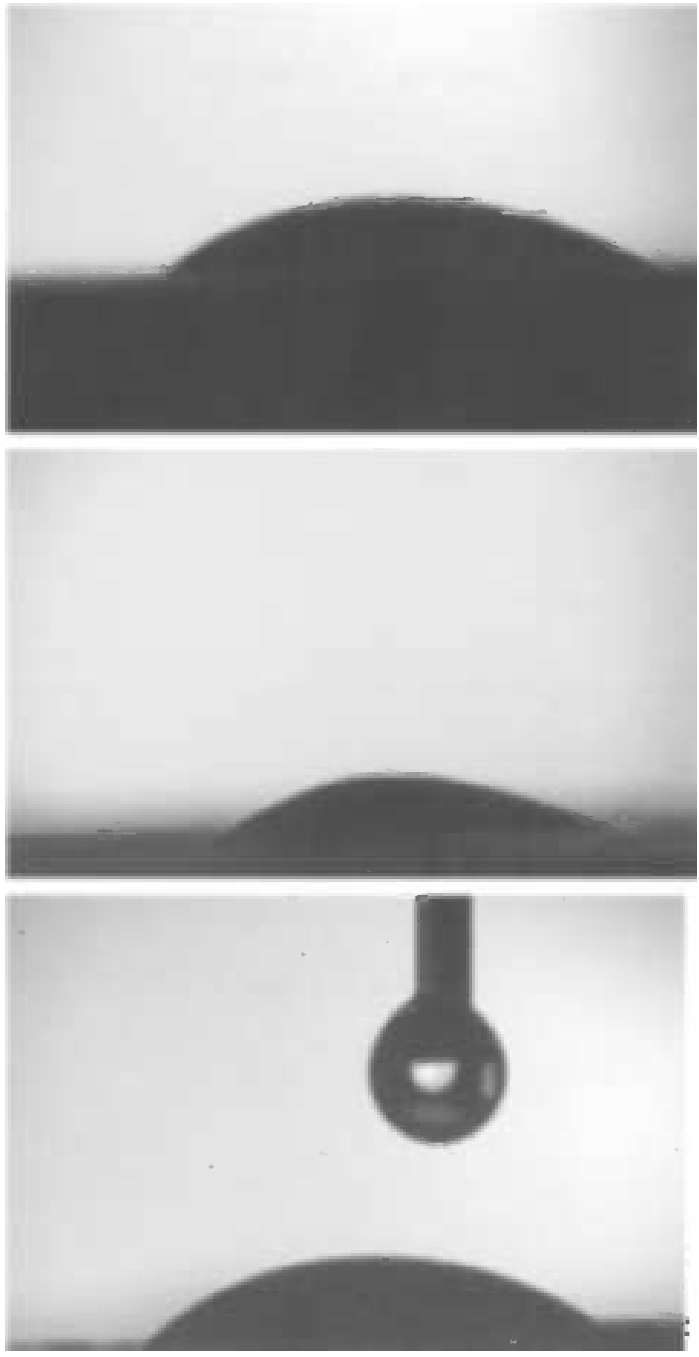

Figure 5.4 Contact angles to profiled concrete substrates (Momber, 2002a)
a – Cement paste; grit blasted
b – Concrete surface; grit blasted;
c – Aggregate in concrete; grit blasted

Table 5.1 Contact angles to concrete surfaces (Gelfant, 1995)

Contaminant	Contact angle in °	
	Contaminated	After waterjetting
Laitance	0–20	0–20
Milk	30–70	0–20
Vegetable oil	30–60	20–40
Oleic acid	30–40	20–30
Silicone	90–100	90–100
Motor oil	60–80	20–30
Grease	40–70	20–30
Hydraulic fluid	20–30	0
Na_2SiO_3	0	0
NaCl	0–20	0
NaOH	0	0
H_2SO_4	0	0

5.2.2 Profile and roughness of hydrodemolished concrete substrates

RILI (2001) states the following: "Substrate roughness must be suitable for the overlay material to be applied." A typical profile of a hydrodemolished substrate is shown in Fig. 5.5. A large variation in the erosion depth can be seen. The extend in profile variation is a function of several process parameters (Ingvarsson and

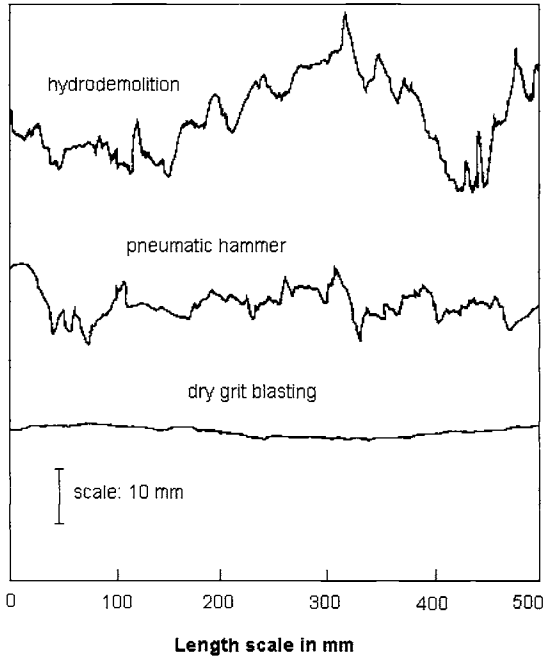

Figure 5.5 Profiles of a concrete substrate prepared with different methods (Silfwerbrand, 1990)

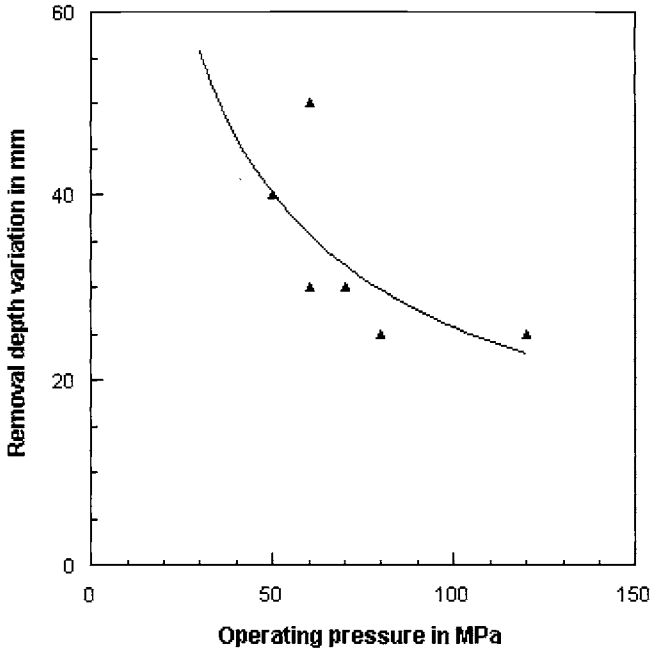

Figure 5.6 Effect of operating pressure on profile depth variation (Ingversson and Eriksson, 1988)

Eriksson, 1988). Figure 5.6 illustrates the effect of operating pressure; high pressure guarantees a more homogeneous texture. This trend is also found by Sakoda et al. (1998). However, a geometrically desired profile cannot be generated with hydrodemolition because of the selective operation mode. Local depth of removal depends on local concrete strength; depth will always be higher in the weaker section. Therefore, a concrete with a homogeneous strength distribution is beneficial to a rather smooth surface profile. If compressive strength increases, roughness values drop (Sakoda et al., 1998). A systematic study about the influence of hydrodemolition parameters on surface roughness, performed by Galecki et al. (2001), showed that roughness increases if rotational speed of the nozzle holder decrease and if operating pressure rises. These relationships are illustrated in Fig. 5.7. Randl and Wicke (2000) applied the Sand Section Test to hydrodemolished substrates and found a value of R_t=2.7 mm. For comparison, grit blasted surfaces have values between 0.2 and 0.8 mm (Momber, 2002a, Randl and Wicke, 2000), and a formworked concrete has a value of 0.1 mm.

Profiling of a surface promotes an increase in the total surface area. This parameter is to some extend more appropriate to describe the capability of substrates to carry overlays. With regard to hydrodemolition, it is proved that this parameter is critically related to operating pressure and nozzle movement (Yasumatsu et al., 1999). Some relationships are shown in Fig. 5.8.

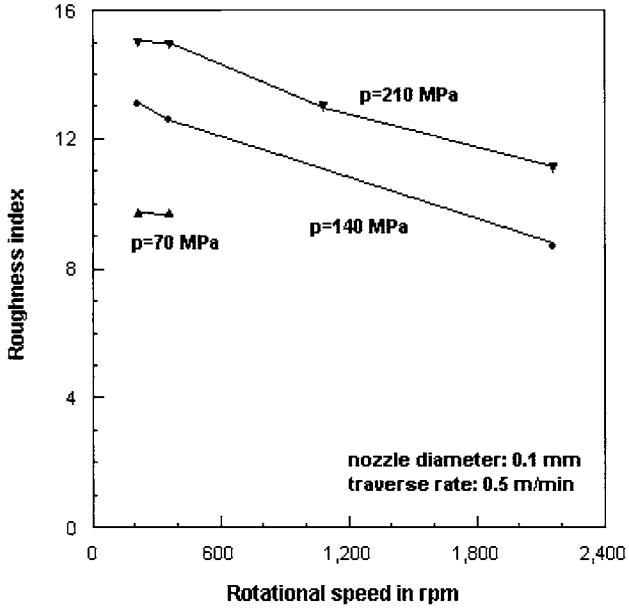

Figure 5.7 Effects of operating pressure and rotational speed on substrate roughness (Galecki et al., 2001)

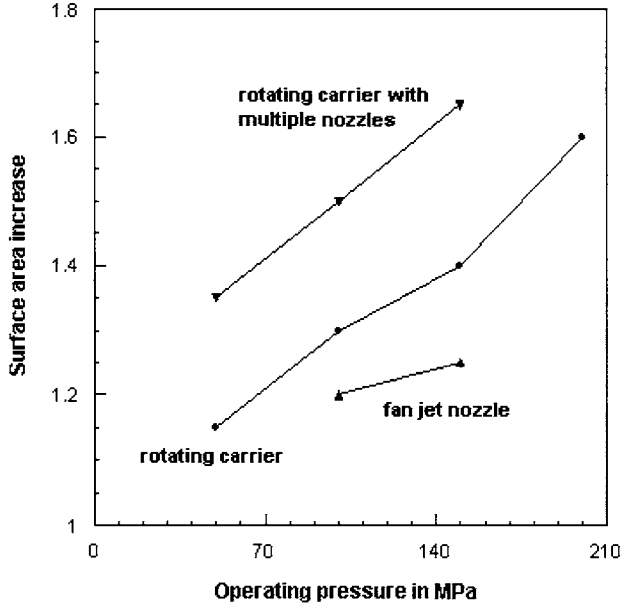

Figure 5.8 Effects of operating pressure and nozzle arrangement on surface area increase (Yasumatsu et al., 1999)

5.3 Adhesion strength

5.3.1 Definitions and assessment of adhesion

The ability to adhere to the substrate throughout the desired life of the coatings is one of the basic requirements of a surface coating or, respectively, a concrete replacement system. Adhesion bases on adhesive forces that operate across the interface between substrate and applied system to hold the systems to the substrate. The magnitude of these forces (thus, the adhesion strength) depends on the nature of the surface and the type of applied system. Factors that affect the bond between concrete substrate and applied overlay system include the following (Silfwerbrand, 1990):

(i) old concrete:
- compressive strength;
- aggregate type and gradation;
- salt content;
- age.

(ii) concrete removal technique:
- interface condition;
- microcracks;
- roughness;
- surface preparation;
- pre-wetting;
- other treatment (bonding agents, etc.);
- surface moisture.

(iii) overlay condition:
- water-cement ratio;
- cement type and content;
- aggregate type and gradation;
- fibre content;
- admixtures;
- slump;
- thickness;
- compaction method and time;
- curing;
- time since placement.

(iv) weather conditions:
- temperature and humidity after concrete removal.

In the mechanical interlocking mechanism, the macroscopic substrate roughness provides mechanical locking and a large surface area for bonding; the overlay is mechanically linked with the substrate. Adhesive bonding forces could be categorised as primary valency forces and secondary valency forces. Adhesion between substrate and coating can be evaluated by different methods, including the pull-off testing. Numerous regulations state minimum requirements for the pull-off strength of concrete substrates. Examples are listed in Table 5.2. The pull-off test

delivers quantitative information about the adhesion (usually given in N/mm^2 or MPa), while the picture of the rupture provides information about the weakest part of the system. Typical failure types to be observed are either adhesion failure (substrate-coating) or cohesion failure (internal coating failure). The percentage of failure type must be estimated with an accuracy of 10% (RILI, 2001).

Table 5.2 Required pull-off strength values for concrete substrates (RILI, 2001)

Overlay type	Minimum required pull-off strength in MPa	
	Average value	Minimum individual value
Mortar and concrete	1.5	1.0
Polymer dispersion / polyurethane	0.8	0.5
Polymer dispersion / polymer-cement-mixture	1.0	0.6
Polymer dispersion / polymer-cement-mixture / polyurethane / epoxy resin	1.3	0.8
Polyurethane / epoxy resin	1.5	1.0

5.3.2 Adhesion to hydrodemolished concrete substrates

Only a few studies were performed to estimate the adhesion of coating systems or, respectively, concrete replacement systems to concrete substrates prepared by hydrodemolition. Kauw (1996) could prove that hyrodemolished substrates provide suitable adhesion to concrete replacement concrete systems. In many cases, pull-off strengths of hydrodemolished substrates exceed those of untreated surfaces. Equal observations are made by Obladen (1987) and by Cleland and Basheer (1999). Results of these studies are shown in Figs. 5.9 and 5.10. Tschegg and Stenzl (1991) measured the fracture energies of joints between old and new concretes as functions of surface quality and found rather high values for concrete substrates prepared with water jets (Fig. 5.11). Similar trends are delivered by a study of Toutan and Ortiz (2001) who measured the forces required to separate fibre-reinforced sheets applied to concrete surfaces. As can be seen in Fig. 5.12, waterjetted surfaces exhibit force values much higher than estimated for grit blasted surfaces. Sakada et al. (1998) found that construction joints profiled with waterjets owned high flexural strength, but the strength values depended upon operating pressure and water-cement ratio of the concrete mixtures. In most cases, flexural strength increased as operating pressure increased; this is illustrated in Fig. 5.13. Randl and Wicke (2000) performed a study into the shear stress transfer capability of reinforced concrete joints. Results of this study are displayed in Fig. 5.14. It can be seen that substrates treated with water jets have a notably higher stress transfer capability. Shear stress transfer capacity of a steel reinforced concrete joint can be approximated as follows (Randl and Wicke, 2000):

$$\tau_S = \underbrace{A_1 \cdot c_S}_{\substack{\text{interlock} \\ \text{cohesion}}} + \underbrace{\mu_S \cdot (A_2 \cdot \kappa_S \cdot A_3)}_{\text{friction}} + \underbrace{\alpha_S \cdot A_4}_{\text{dowel action}} \tag{5.2}$$

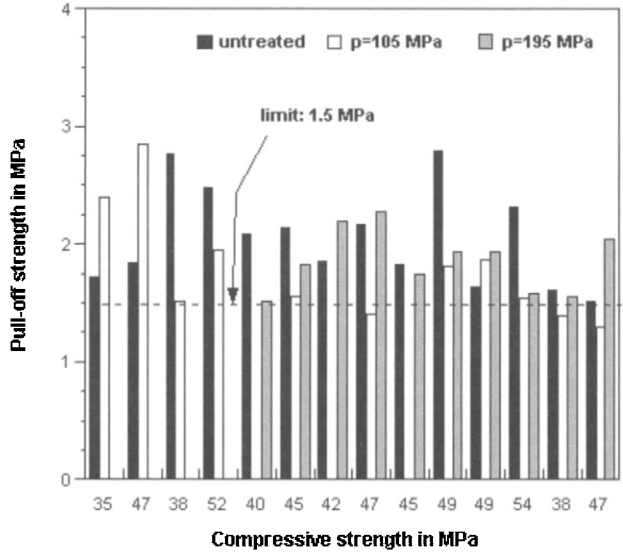

Figure 5.9 Comparative pull-off strengths of concrete substrates (Kauw, 1996)

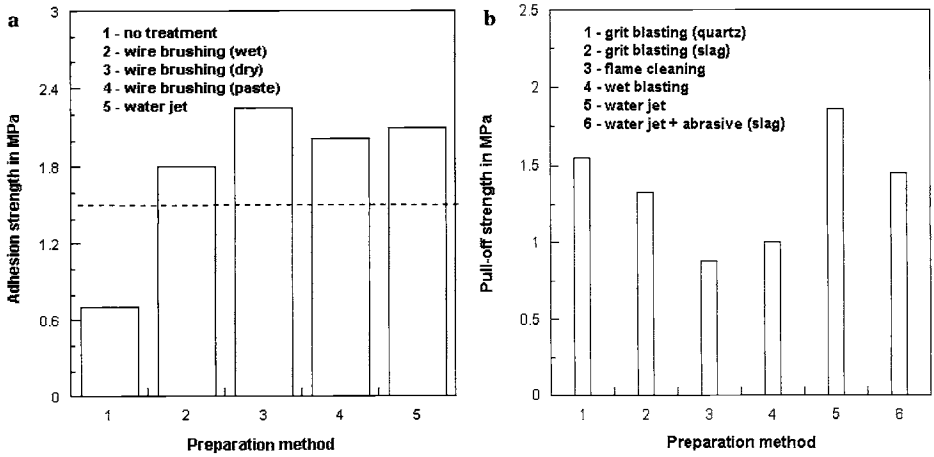

Figure 5.10 Effects of surface preparation methods on adhesion strength
a – Cleland and Basheer (1999)
b – Obladen (1987)

Here, A_1 to A_4 are constants. The dependence of the other parameters on the surface quality or, respectively, surface preparation method, is listed in Table 5.3. From these results, it can be concluded that hydrodemolition contributes mainly to interlock cohesion (c_S) due to the high roughness of the generated profile.

The type of failure occurring during adhesion testing is a further evaluation parameter. The bond between substrate and applied system is usually considered

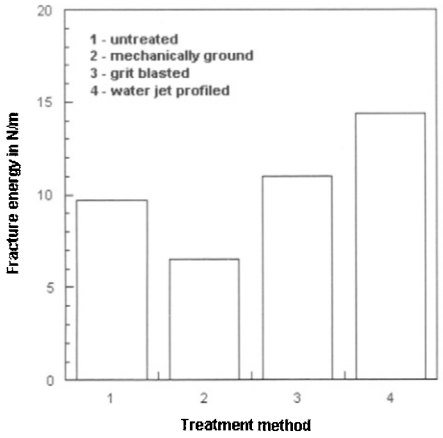

Figure 5.11 Effects of surface preparation methods on interfacial fracture energy (Tschegg and Stenzl, 1991)

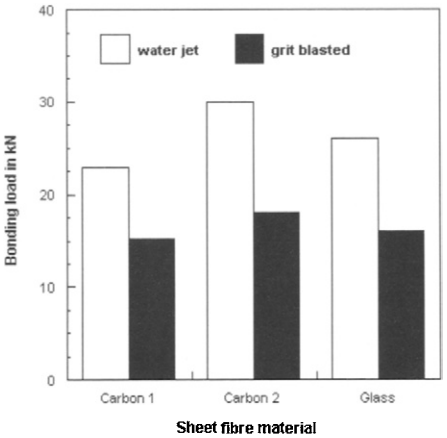

Figure 5.12 Effects of surface preparation methods and sheet fibre material on bonding between concrete substrate and applied sheets (Toutan and Ortiz, 2001)

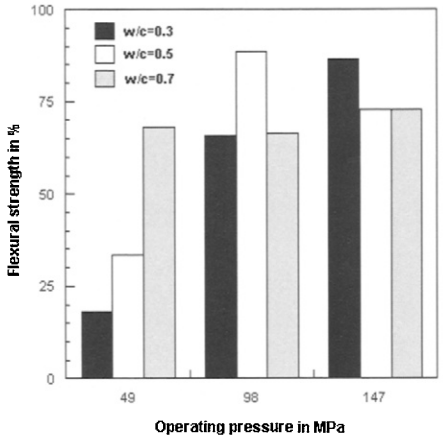

Figure 5.13 Effects of operating pressure and water-cement ratio on flexural strengths of construction joints prepared with water jets (Sakada et al., 1998)

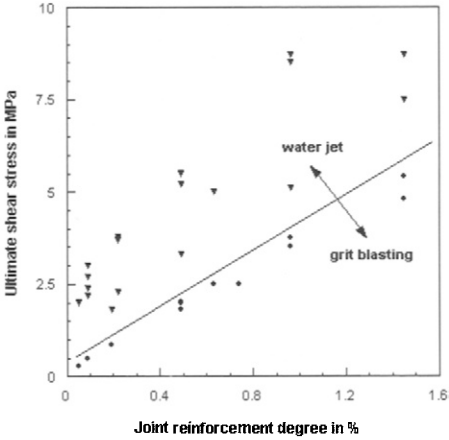

Figure 5.14 Effects of surface preparation methods on ultimate strengths of reinforced concrete joints (Randl and Wicke, 2000)

Table 5.3 Values for the parameters in Eq. (5.2); Randl and Wicke (2000)

Condition	Roughness	c_S	μ_C	κ_S	α_S
Hydrodemolition	3.0 mm	0.4	0.8–1.0	0.5	0.4
Grit blasing	0.5 mm	0	0.7	0.5	0.3
Smooth	–	0	0.5	0	0.2

high if cohesive failure occurs either in the substrate or in the applied system. In contrast, adhesive failure in the intermediate zone between substrate and applied system points to rather bad bond or, respectively, to a damaged substrate surface. Silfwerbrand (1990) compared the pull-off behaviour of concrete overlays applied to concrete substrates prepared with hydrodemolition, jack hammering, and grit blasting. The results of the study proved that water jets generated a surface that forced cohesive failure. Percentage of adhesive (interface) failure was 7% for water jets, 31% for jack hammering, and 38% for grit blasting. Some results are displayed in Fig. 5.15.

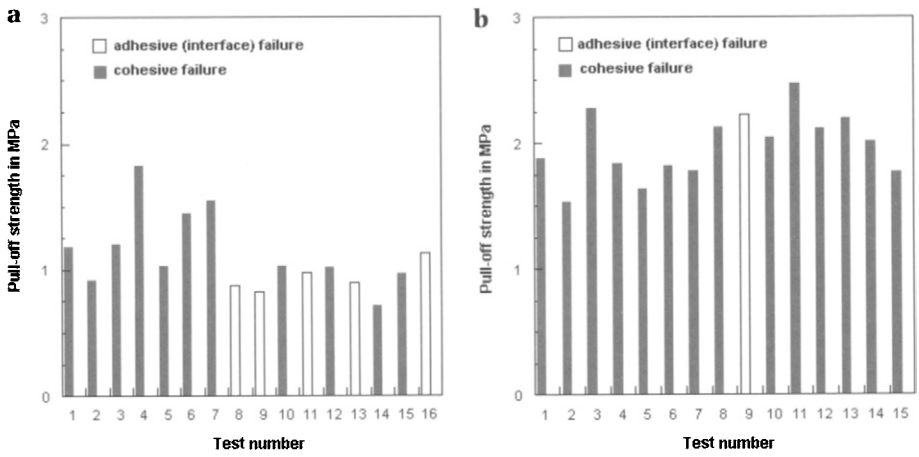

Figure 5.15 Failure type frequency during pull-off strength testing of concrete substrates (Silfwerbrand, 1990)
a – jack hammering; b – hydrodemolition

Talbot et al. (1994) provided a study into the adhesion of shotcrete overlays to concrete substrates. The authors could show that the pull-off strengths exceed the critical value of 1.5 MPa. Some results are listed in Table 5.4.

Table 5.4 Pull-off strengths of shotcrete applied to hydrodemolished concrete substrates (Talbot et al., 1994)

Shotcrete mixture	Pull-off strength in MPa	
	After 2 months	After 6 months
Conventional (dry)	1.57	1.56
With silica fume (dry)	1.49	1.67
With 48 kg/m^3 steel fibres (dry)	2.08	1.86
With 12% latex (dry)	1.50	1.58

5.4 Water content of substrates

Moisture in the near-surface region of concrete substrates affects the adhesion of overlays. If replacement mortars are applied to wet concrete surfaces, adhesive failure occurs with a much higher probability; this is shown in Fig. 5.16. It is frequently argued if the near-surface range of concrete contains critical amounts of moisture after hydrodemolition. Results of a comparative study performed by Werner (1988) are listed in Table 5.5. It must, however, be taken into account that the hydrodemolition unit utilised for the tests was equipped with a suction device in order to remove water and eroded concrete debris from the surface. The amount of water that penetrated the structure during the jetting was comparable to the amount found after a heavy striking rain. Depth of water penetration during hydrodemolition can be approximated as follows (Rehbinder, 1980):

$$h_p = \left(\frac{2 \cdot k_p}{\nu_F} \cdot p \cdot t_E \right)^{1/2} \tag{5.3}$$

Here, p is in Pa, t_E is in s, and k_p is in m^2 (see Table 1.5 for corresponding values). An interpretation of this equation is performed in Fig. 5.17a, and it can be seen that the depth of penetration is just a fraction of a millimetre. The situation becomes critical if the water is not removed from the surface after the jetting and penetrates the structure further. This is illustrated in Fig. 5.18. The reason is infiltration by capillary forces, and this mechanism may apply especially to horizontal surfaces where the water cannot leave the concrete surface. If the operating pressure in Eq. (5.3) is replaced by the capillary pressure (about 1 MPa), the depth of water penetration can be estimated for the period that follows the jetting process (Fig. 5.17b). A much deeper penetration depth can be noted compared to Fig. 5.17a. In case of need, drying is, therefore, required.

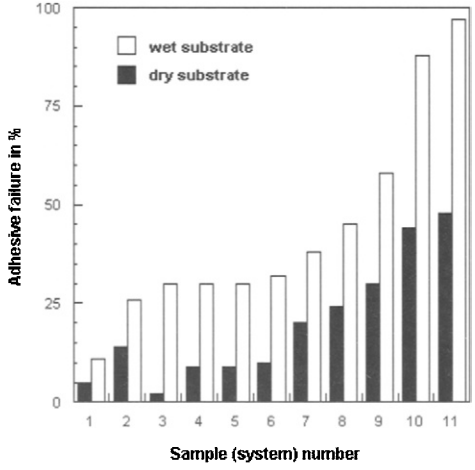

Figure 5.16 Effects of substrate moisture content on failure type during pull-off testing of concrete (Sasse, 1987)

Table 5.5 Water penetration into concrete under different conditions (Werner, 1988) Operating pressure: 200 MPa; volumetric flow rate: 12 l/min; nozzle arrangement: 4 × 0.4 mm

Condition	Water penetration in mass percent	
	Average	Standard deviation
After waterjetting	0.69	0.05
After simulated rainfall (2 minutes)	0.63	0.05
After simulated rainfall (10 minutes)	0.75	0.06
After storage in water (48 hours)	4.08	0.41

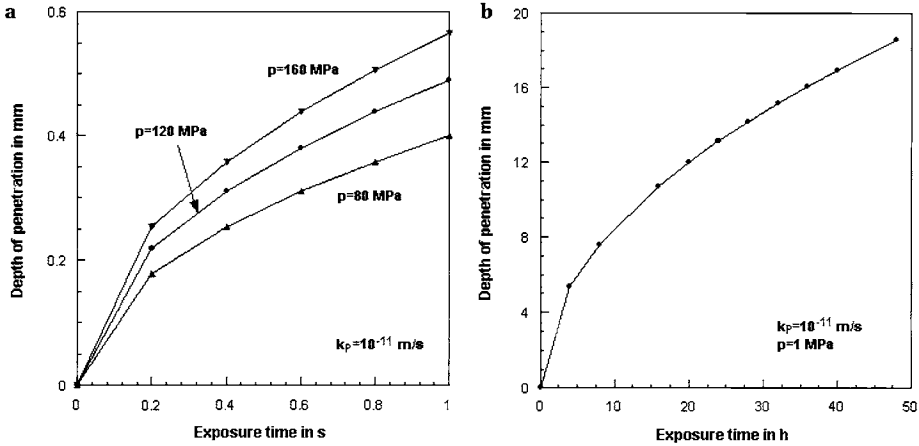

Figure 5.17 Depth of water penetration into concrete structures according to Eq. (5.3)
a – during hydrodemolition (high pressure; short exposure time)
b – after hydrodemolition (capillary pressure, long exposure time)

Figure 5.18 'Standing water' during a hydrodemolition job (Photograph: Aquajet AB, Holsbybrunn)

5.5 Chloride content of substrates

This problem is related to the problems raised in Section 5.4, and the same arguments can, therefore, be applied. It is very unlikely that dissolved chlorides are washed into the concrete structure during hydrodemolition because of the short exposure times. It rather seems that chlorides are removed off the structure and are flushed away with the process water. Again, this issue becomes acute only if water is standing at the concrete surface for a long period of time. Lukas and Kusterle (1991) performed comparative potential measurements on chloride contaminated concrete bridges and found that chloride concentration reduced after water jet erosion. Similar results are reported by Hunkeler (1998); examples are presented in Fig. 5.19. It can be seen that the chloride concentration is highest in the untreated sections (0-10 mm) and reduces if the concrete is removed through hydrodemolition.

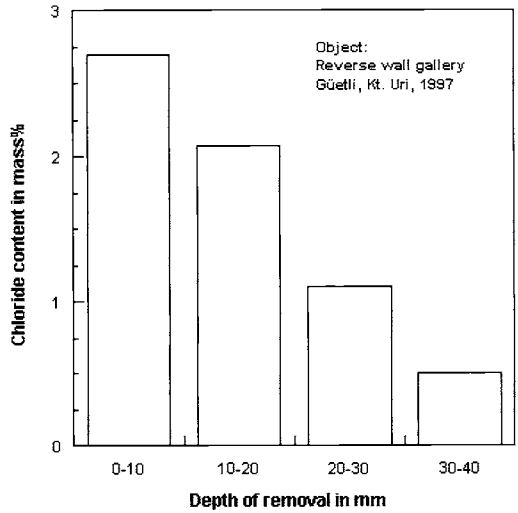

Figure 5.19 Chloride contents in hydrodemolished concrete substrates (Hunkeler, 1998)

5.6 Integrity of (microcracking in) substrates

Although no systematic investigations were available in the early years of hydrodemolition, 'microcrack free' performance was always a rigid argument to use water jets for concrete removal. This argument remained an issue of controversy till today. A totally crack free concrete surface can not be guaranteed due to the fundamental erosion mechanism that bases on the extension and intersection of microcracks. Figure 5.20 illustrates this issue. The question is rather if *additional* cracks are introduced to the surface during the water jet erosion

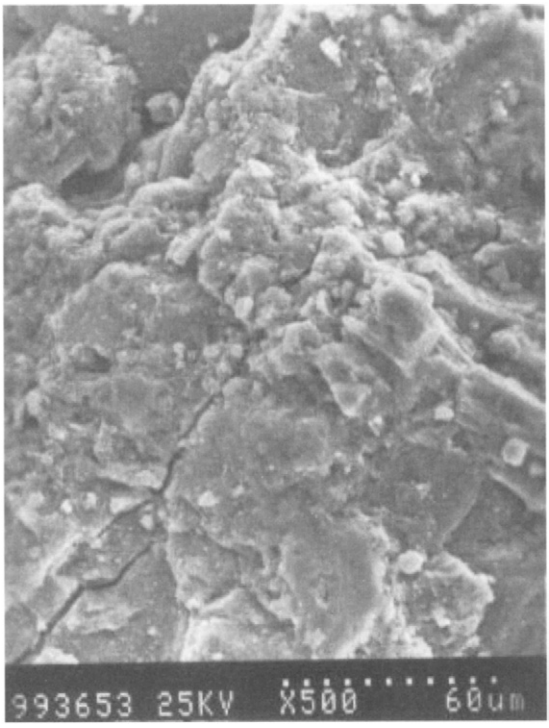

Figure 5.20 Concrete removal by waterjets due to intersecting microcracks (Hu et al., 2004)

process. Hindo (1990) and Werner (1991) who investigated thin-ground sections noted that the number of microcracks in concrete reduced after water jet erosion. A systematic, but restricted, study was performed by Kauw (1996) whose results are summarised in Table 5.6. Typical lengths of cracks were in the range of several millimetres, with a maximum of 20 mm. The widths of cracks were mainly in the range of 0.1 mm. About 70% of all cracks ran partly parallel to the surface. Most of the cracks with rather large widths (> 0.1 mm) could be identified at material projections. Probably, these projections were already damaged but not swept away by the water flow. This situation occurs if operational parameters, namely pressure and traverse rate, are adjusted close to their threshold values (see Section 2.3). Thus, the probability of additional microcracking is high if the jet operates in the threshold range. Evidence to this interpretation is given in Fig. 2.11. Hydrodemolition experience shows that microcracking becomes acute if thick concrete layers are removed with high-energy hydrodemolition machines (Badzong, 1990). This is especially true for concrete construction with low rigidity values (Wolfseher and Hess, 1994). In contrast, if concrete is removed with hand-held tools, the tendency to microcracking is very low (Werner, 1991).

Table 5.6 Results of microcrack testings after hydrodemolition (Kauw, 1996)

Sample	Compressive strength in MPa	Maximum aggregate size in mm	Operating pressure in MPa	Crack number	
				Total	Parallel to surface
1	40	16	0	0	0
2		16	105	1	1
3		16	195	0	0
4	45	16	0	0	0
5		16	105	0	0
6		16	195	1	1
7	42	16	0	0	0
8		16	105	0	0
9		16	195	2	2
10	47	16	0	0	0
11		16	105	4	2
12		16	195	1	1
13	47	32	0	0	0
14		32	105	1	0
15		32	195	1	1
16	49	16	0	0	0
17		16	105	2	2
18		16	195	3	2
19	54	16	0	0	0
20		16	105	1	0
21		16	195	1	1

5.7 Mechanical properties of substrates

To maintain mechanical properties of the substrate material is of primary importance for a reliable function of rehabilitated concrete structures. This aspect was in particular paid attention to during some rehabilitation projects in Switzerland, and the results of corresponding investigations were published by Rechsteiner and Wolfseher (1998) and by Wolfseher and Hess (1994). Figures 5.21 and 5.22 show results of comparative measurements of dynamic Young's modulus and, respectively, tensile strength. These properties were measured prior to any treatment and, respectively, after hydrodemolition. As evidenced in Fig. 5.21, dynamic Young's modulus remains almost unaltered after hydrodemolition, no matter if hand-held tools or mechanical devices are applied. The same conclusion can be drawn for the porosity of the near-surface of the substrate (Wolfseher and Hess, 1994). Figure 5.22 shows that tensile strength is not affected negatively, no matter if manual or mechanical operation is performed. Tensile strength even increases after hydrodemolition. This at the first view surprising result can, however, be explained due to the selective operation mode of water jets. Weak zones

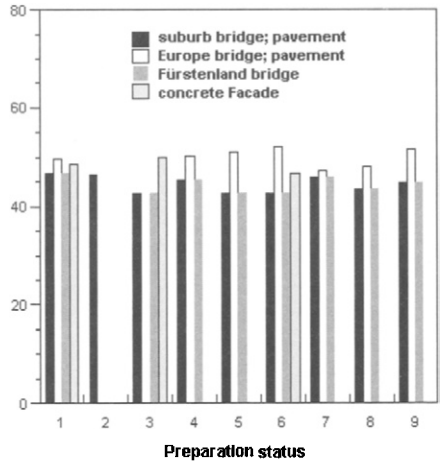

Figure 5.21 Effect of preparation status on dynamic Young's modulus of concrete structures (Wolfseher and Hess, 1994)
1 – untreated; 2 – roughening; hydrodemolition robot; 3 – roughening; robot – followed by hand-held tool; 4 – concrete removal 30 mm; hydrodemolition robot; 5 – concrete removal 30 mm; robot – followed by hand-held tool; 6 – concrete removal 30 mm; hand-held tool; 7 – concrete removal 80 mm; hydrodemolition robot; 8 – concrete removal 80 mm; robot – followed by hand-held tool; 9 – concrete removal 80 mm; hand-held tool

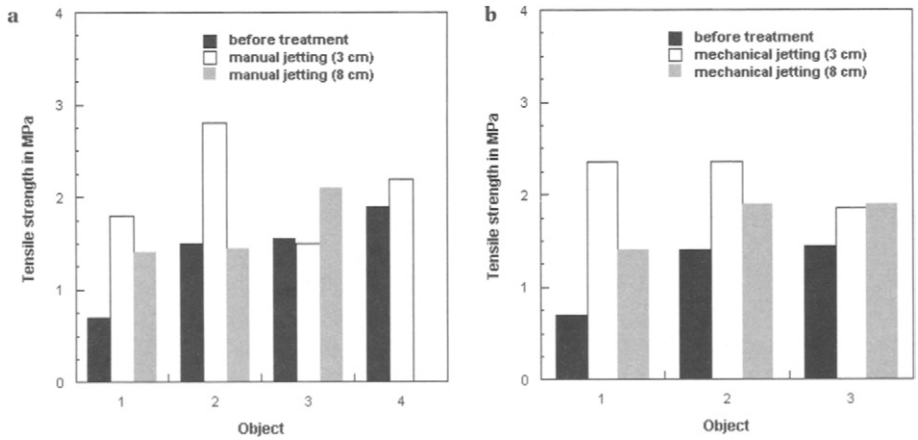

Figure 5.22 Effect of preparation status on tensile strengths of concrete structures (Rechsteiner and Wolfseher, 1998)
a – Utilisation of hand-held waterjetting tools (operating pressure: 150 to 240 MPa; volumetric flow rate: 9 to 48 l/min)
1 – Suburb bridge, Zug; 2– Europa bridge, Zurich; 3 – Fürstenland bridge, St. Gallen; 4 – Concrete façade, Birrfeld
b – Utilisation of hydrodemolition robots (operating pressure: 81 to 100 MPa; volumetric flow rate: 57 to 180 l/min)
1 – Suburb bridge, Zug; 2 – Europa bridge, Zurich; 3 – Fürstenland bridge, St. Gallen

existing in the virgin material were removed during hydrodemolition and regions of a given strength only remain.

5.8 Status of reinforcement in substrates

Status of reinforcement bars includes bar damage, bond to the surrounding matrix, and bar cleanliness. Site experience shows that even fine wires that connect individual reinforcement bars remain undamaged. Examples are shown in Fig. 5.23. It is also reported that tensioning ropes in pre-stressed reinforced concrete

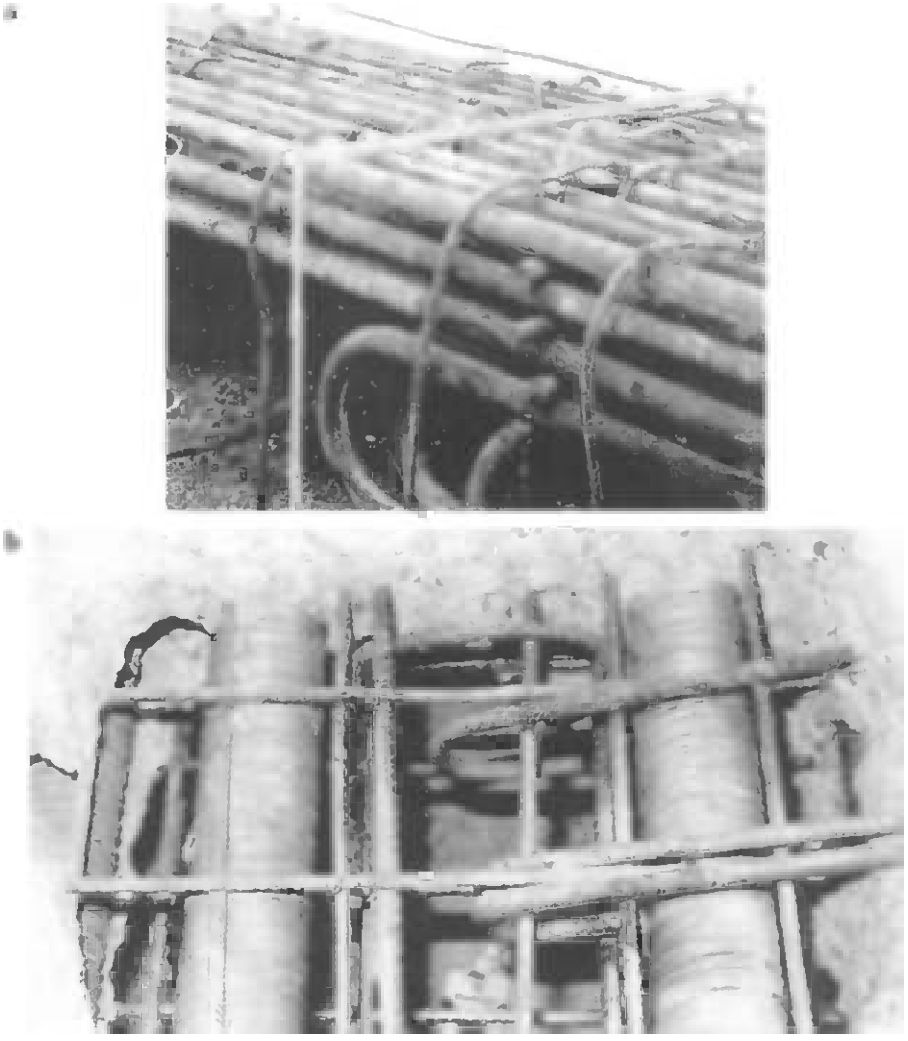

Figure 5.23 Reinforcement status after hydrodemolition (Photographs: Hydrojet AG, Basel)
a – closely spaced reinforcement bars and connecting wires; b – reinforcement bars, hooks and pre-stressing pipes

structures are not affected (Zehr, 1998). Figure 5.24 compares the condition of a reinforcement arrangement after hydrodemolition (Fig. 5.24a) and after mechanical milling (Fig. 5.24b). Severe deformation and dislocation of individual bars can be noted after mechanical milling. Additionally, rather large concrete debris is jammed between the layers of the reinforcing net. Hydrodemolition, in contrast, leaves an almost unaffected reinforcement arrangement.

Microscopic inspections verified that no debonding occurs between reinforcement bars and surrounding concrete matrix due to hydrodemolition (Rechsteiner and Wolfseher, 1998). A respective microphotograph is shown in Fig. 5.25. This is

a

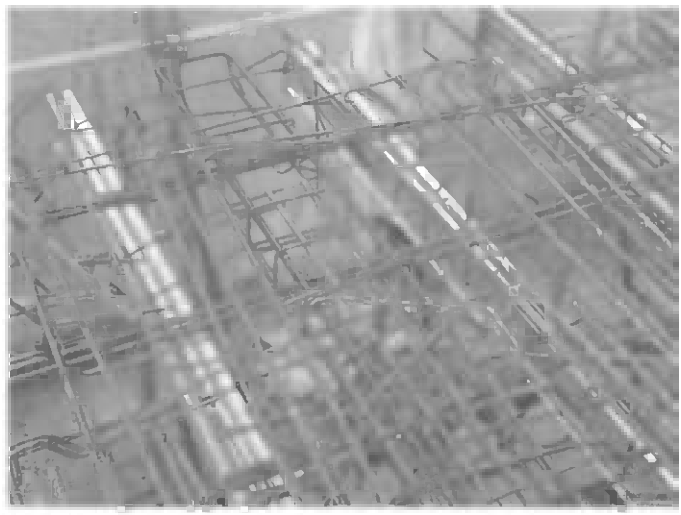

b

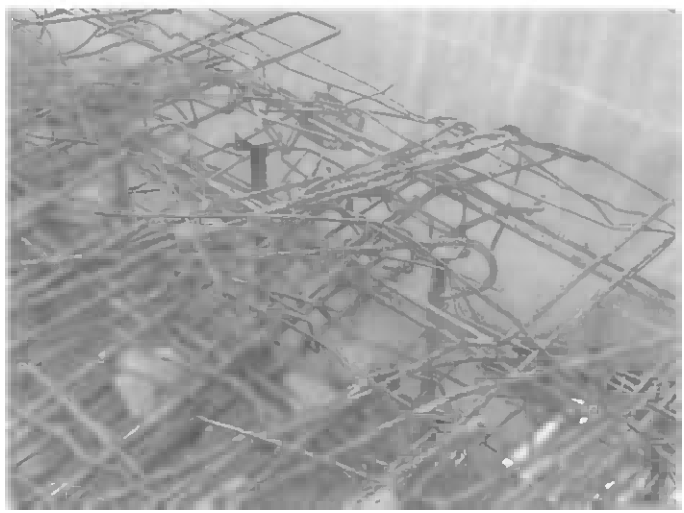

Figure 5.24 Reinforcement condition after concrete demolition
(Photographs: Aquajet AB, Holsbybrunn)
A – After hydrodemolition – unaffected bars
B – after mechanical milling – damaged and deformed bars

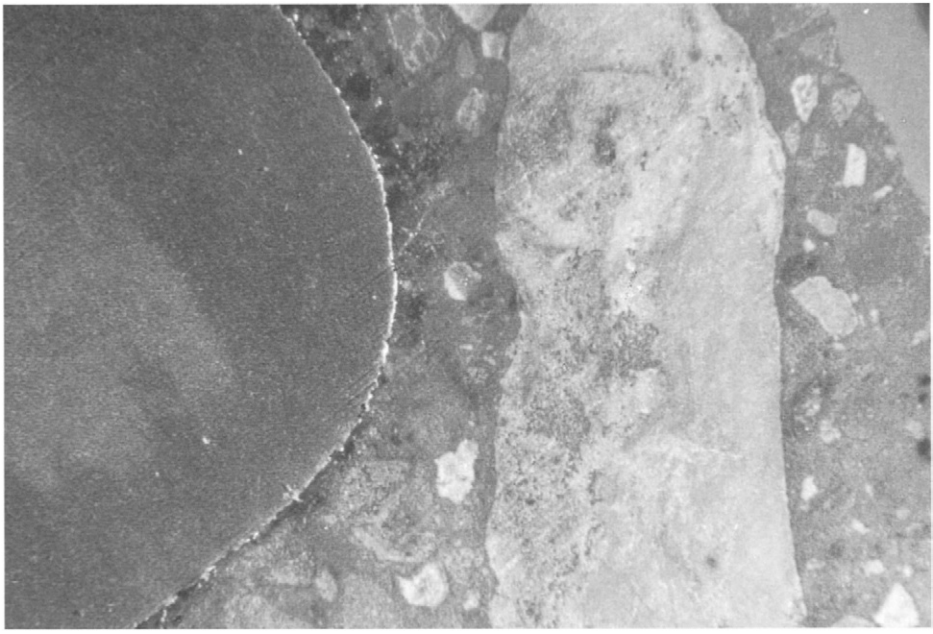

Figure 5.25 Interfacial zone between concrete and reinforcement bar after hydrodemolition (Rechsteiner and Wolfseher, 1998)

mainly due to the gentle, low-vibration performance of hydrodemolition tools. However, some care must be taken if very slim reinforced constructions are going to be treated with heavy hydrodemolition machines. In such cases, a structural engineer should be consulted.

If reinforced concrete is corroded as a result of chloride intrusion, regulations in Germany prescribe the use of high-speed water jets for bar cleaning. The reason is the typical appearance of chloride-corroded bars which show typical 'rust scares'. Mechanical cleaning tools, including grit blasting, can not penetrate these very tiny depressions, but water jets can. The water flow involved in the preparation process enters pores, pits, pockets, etc., and sweeps the salts away. This mechanism is verified by results of SEM-inspections of waterjetted surfaces (Trotter, 2001). From the area of steel corrosion protection is known that water jets remove any type of solved salts from steel substrates with the highest reliability (see Momber, 2003c, for a detailed review). Tables 5.7 and 5.8 list corresponding results. RILI (2001) states that the quality of derusting of steel bars corresponds to the surface standard St 2 according to ISO 8501 even if the appearance of the surface is different from the visual reference photographs (RILI, 2001).

A study that consider other types of salts (sulphates, phosphates, nitrates) was performed by Howlett and Dupuy (1993). This study showed the same trends as for the chlorides (see Table 5.8). It was further found that grit blasting did not remove chlorides to safe levels 50% of the time. Conductivity readings (which characterise not only chloride content, but all dissolved salts) from hydroblasted surfaces were reported by Kuljian and Melhuish (1999). In most cases, conductivity levels

dropped significantly after hydroblasting; 75% of all readings were under 20 μS/cm, and 95% were under 40 μS/cm.

Table 5.7 Chloride levels of steel measured after different pre-treatment methods (Forsgren and Applegren, 2000)

Method	Chloride level in μg/cm²		
	Bresle (10 min)	SSM (10 s)	SSM (10 min)
No pre-treatment	44.8	47.5	61.3
No pre-treatment	54.8	72.8	96.3
No pre-treatment	15.2	*	*
No pre-treatment	24.8	*	*
Wet blasting	1.6	1.4	2.7
Wet blasting	1.6	0.7	2.0
Wet blasting	0	1.7	3.1
Wet blasting	3.2	1.5	4.1
Water jetting	1.6	15.2	–
Water jetting	0.8	1.8	4.2
Water jetting	0	2.4	4.6
Water jetting	1.2	0.1	2.1
Water jetting	2.4	4.8	10.3
Water jetting	1.2	0	1.0
Water jetting	0	0	0.8
Wire brushing	28.8	63.5	–
Wire brushing	16.0	32.6	58.9
Wire brushing	23.2	15.2	25.0
Wire brushing	17.6	18.1	30.3
Needle gunning	27.6	19.9	42.6
Needle gunning	21.2	20.9	35.0
Needle gunning	26.8	41.3	96.1
Needle gunning	29.6	20.6	31.5
Dry grit blasting	4.4	8.3	14.8
Dry grit blasting	6.8	10.8	16.5

* no measurements

Table 5.8 Surface contaminant results from different preparation methods (Howlett and Dupuy, 1993)

Substrate	Contaminant	Salt level in μg/cm²			
		Surface preparation method			
		Uncleaned	Grit blasting	Water jetting	Hydro-abrasive blasting
A-36 steel with mill scale	Sulfates	40	3	0	4
	Phosphates	0	0	0	3
	Chlorides	2	2	1	0
	Nitrates	0	6	0	6
A-285 Grade 3 steel with mill scale	Sulfates	5	5	0	1
	Phosphates	0	1	0	6
	Chlorides	4	3	1	1
	Nitrates	0	11	1	3
Rusted water service pipe	Sulfates	5	2	1	2
	Phosphates	1	2	0	6
	Chlorides	28	32	1	0
	Nitrates	6	1	1	8
Intact coating on water service pipe	Sulfates	8	4	0	0
	Phosphates	0	2	0	3
	Chlorides	6	1	1	0
	Nitrates	4	2	1	5
H_2S scrubber plate	Sulfates	39	7	0	3
	Phosphates	0	0	0	2
	Chlorides	12	8	0	1
	Nitrates	0	1	0	3
Heat exchanger shell	Sulfates	7	4	0	0
	Phosphates	0	0	0	7
	Chlorides	17	31	0	0
	Nitrates	0	3	0	6

CHAPTER 6

Demolition With Hydro-Abrasive Water Jets

6.1 Material loading due to solid particle impingement

6.1.1 Stresses due to particle impingement

Tensile stress generated by an impinging spherical particle are maximum at the surface of the edge of contact according to Hertz's (1882) theory for elastic contact:

$$\sigma_T = \frac{(1 - 2 \cdot \nu_M) \cdot F_C}{2 \cdot \pi \cdot a^2} \tag{6.1}$$

Here, a is the contact radius, and F_C is the contact force. The contact radius is given through:

$$a = \left(\frac{3 \cdot k \cdot F_C \cdot d_S}{8} \right)^{1/3} \tag{6.2}$$

The contact force generated by an impinging spherical solid particle is derived by Knight et al. (1977):

$$F_C = \left(\frac{5}{3} \cdot \pi \cdot \rho_S \right)^{3/5} \cdot \left(\frac{3}{4} \cdot k \right)^{-2/5} \cdot v_S^{6/5} \cdot \left(\frac{d_S}{2} \right)^2 \tag{6.3}$$

The parameter k balances the elastic properties of particle and target material as follows:

$$k = \frac{1 - \nu_P^2}{E_P} + \frac{1 - \nu_M^2}{E_M} \tag{6.4}$$

Eqs. (6.1) to (6.4) deliver the following relationship between maximum tensile stress and particle velocity:

$$\sigma_T \propto v_S^{2/5} \tag{6.5}$$

Figure 6.1 shows tensile stresses, calculated for typical elastic properties of a concrete material.

6.1.2 Material response to particle impingement

Depending on the contact situation, materials respond either elastic or plastic to solid particle impingement. Examples are shown in Fig. 6.2. The critical particle velocity for plastic flow during particle impact is (Johnson, 1985):

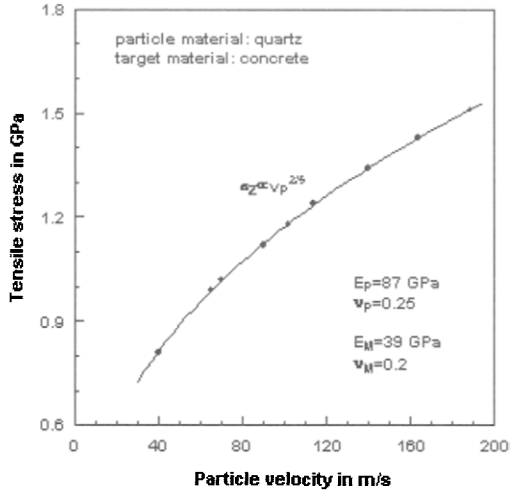

Figure 6.1 Effect of impact velocity on tensile stress (concrete)

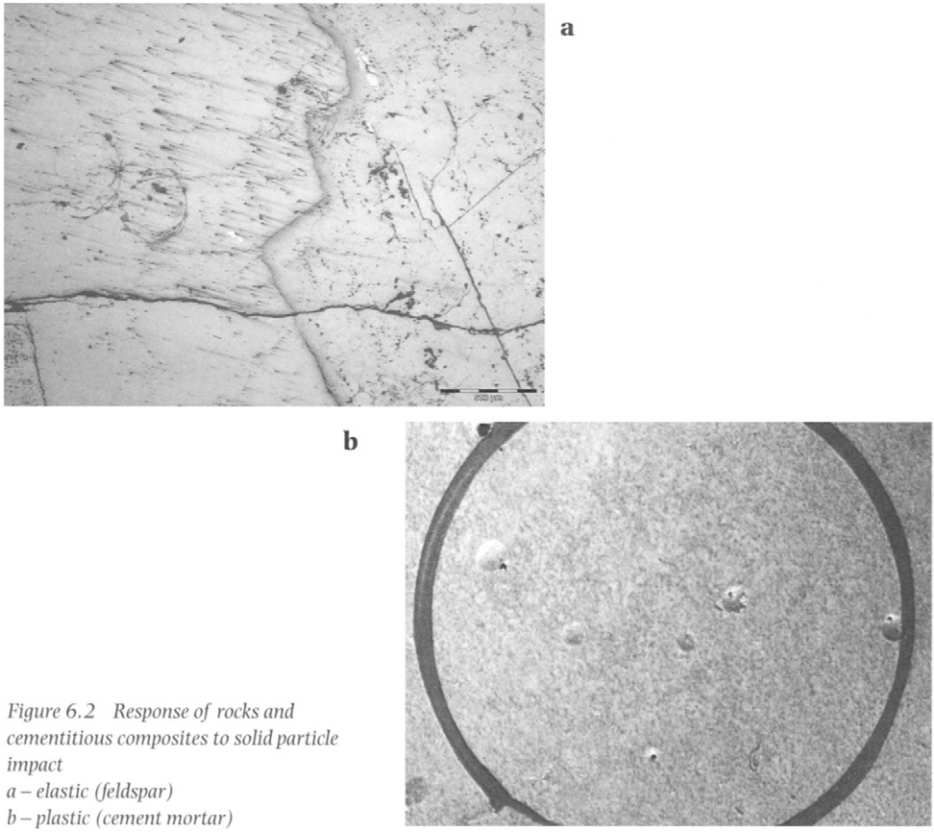

Figure 6.2 Response of rocks and cementitious composites to solid particle impact
a – elastic (feldspar)
b – plastic (cement mortar)

$$v_{PL}^2 = \frac{26 \cdot (\sigma_f / E_M)^4 \cdot \sigma_f}{\rho_S} \tag{6.6}$$

The threshold particle velocity for Hertzian crack formation can be derived from Eq. (6.3) in combination with Auerbach's law ($P_H = A \cdot d_S$). This procedure delivers:

$$v_H = A^{5/6} \cdot \left(\frac{3}{4} \cdot k\right)^{1/3} \cdot \left(\frac{5}{3} \cdot \pi \cdot \rho_S\right)^{-1/2} \cdot r_S^{-5/6} \tag{6.7}$$

Here, A is the Auerbach-constant, and r_S is the radius of the impinging sphere. For $v_H = v_{PL}$ and $\sigma_f = H_M$, Eqs. (6.6) and (6.7) deliver the following condition for elastic-plastic transition:

$$r_{PL} \propto H_M^{-3} \tag{6.8}$$

This relationship is illustrated in Fig. 6.3.

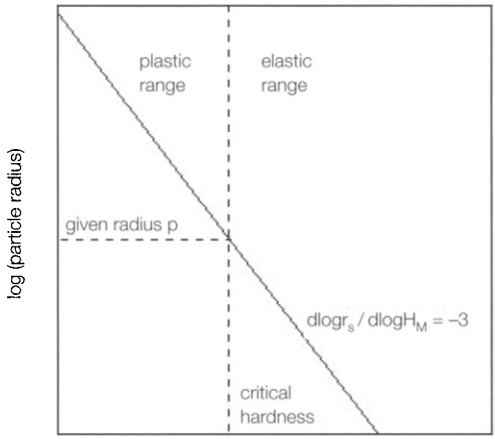

Figure 6.3 Elastic-plastic transition for solid particle impact on rocks and cementitious composites (Momber, 2004f)

6.1.3 Formation of radial and lateral cracks

Radial cracks form in the intermediate surface region of brittle materials if a certain stress level (particle velocity) is exceeded. An example is shown in Fig. 6.4. Radial cracks do not lead to material removal, but they reduce strength in the near-surface region. The length of these cracks depend on process parameters as follows (Anderson et al., 1993):

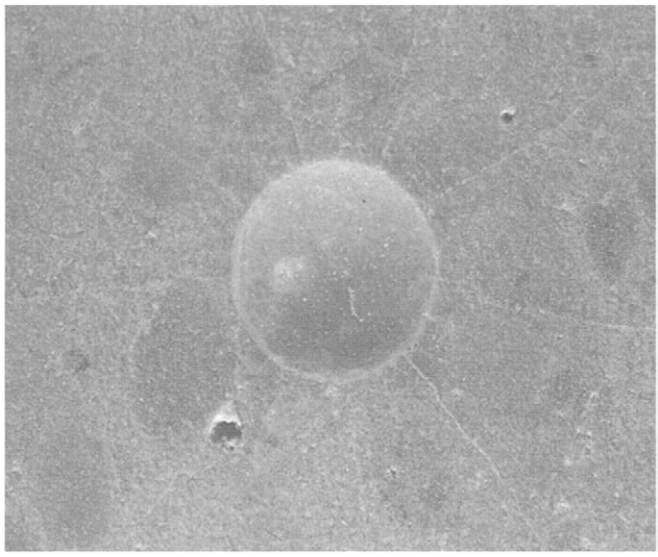

Figure 6.4 Radial cracks in limestone (Momber, 2004g)

$$L_R \propto \frac{d_S^{4/3} \cdot v_S}{K_{Ic}^{2/3}} \tag{6.9}$$

Number and distribution of radial cracks depend upon particle velocity, and the relationship between number of cracks and impact velocity is (Kirchner and Gruver, 1978):

$$N_R \propto v_S^{6/5} \tag{6.10}$$

Lateral cracks are critical to material removal processes. They grow from the bottom of the permanent depression during the unloading phase of the contact. They grow into the direction of the surface, and if they meet the surface, material is removed. This process is shown in Fig. 6.5. The following two threshold criteria for the formation of radial cracks were derived by Hutchings (1992):

$$d_S \propto \left(\frac{K_{Ic}}{H_M}\right)^2 \cdot \frac{E_M^{1/2}}{H_M^{1/4} \cdot \rho_M^{1/3}} \cdot v_S^{-1/2}; \tag{6.11a}$$

this criterion holds for spherical particles.

$$d_S \propto \left(\frac{K_{Ic}}{H_M}\right)^2 \cdot \frac{E_M^{1/2}}{H_M^{1/6} \cdot \rho_M^{1/3}} \cdot v_S^{-2/3}; \tag{6.11b}$$

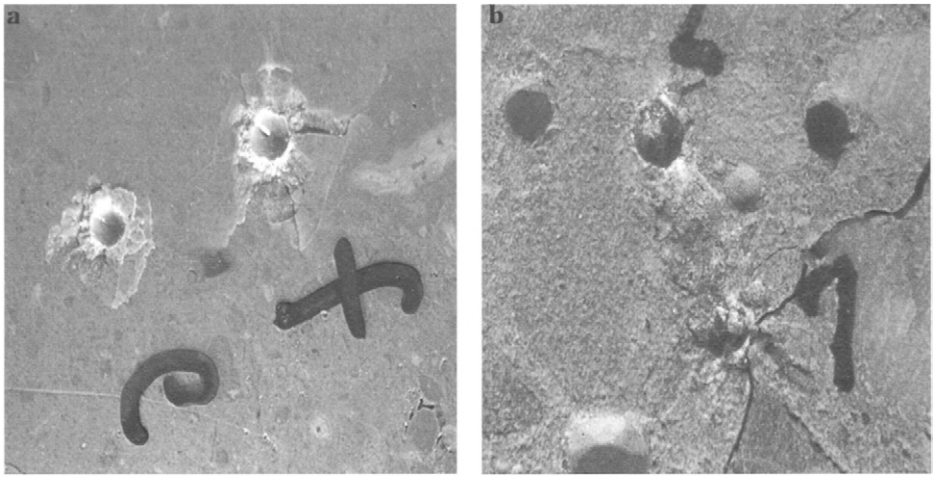

Figure 6.5 Lateral cracks in geomaterials (photographs: Author)
a – limestone b – concrete

this criterion holds for irregular particles. The ratio K_{Ic}/H_M – sometimes referred to as 'brittleness' – plays a dominating role. Graphical solutions to Eqs. (6.11a,b) are provided in Fig. 6.6. If the depth, a lateral crack is formed at, is assumed to be equal to the depth of the permanent depression, it can be approximated as follows (Lange and Evans, 1979; Evans et al., 1978):

$$h_L = \frac{3.5 \cdot d_S}{2} \cdot \left(\frac{\rho_S}{H_M} \right)^{1/4} \cdot v_S^{1/2} \tag{6.12}$$

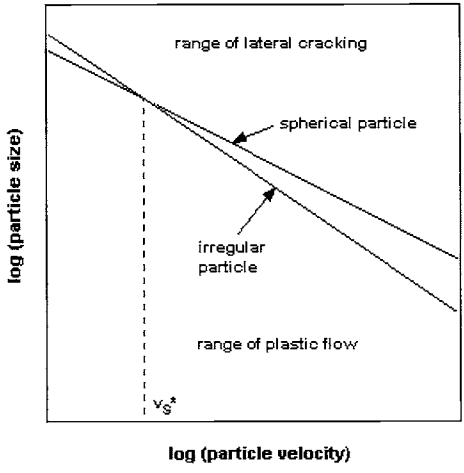

Figure 6.6 Threshold criteria for lateral cracking (Hutchings, 1992); see Eqs. (6.11a,b)

It can be seen from Fig. 6.5a, that length of a radial crack (Eq. 6.9) and depth of a lateral crack (Eq. 6.12) can be used to approximate the volume of the material being removed from the surface:

$$V_M = \alpha_L \cdot \frac{\pi}{4} \cdot L_R^2 \cdot h_L \tag{6.13}$$

The geometry parameter is $0<\alpha_L \leq 1$; in Fig. 6.5a, it is about $\alpha_L=0.5$. Equation (6.13) is the basic approach for the modelling of material removal processes due to solid particle impingement in the elastic-plastic response range. More information is provided by Momber (2004f, 2004g).

6.2 Types and formation of hydro-abrasive water jets

6.2.1 Formation of hydro-abrasive water jets

A comprehensive review about hydro-abrasive jets is given by Momber and Kovacevic (1998). From the point of view of jet generation, the following two types of hydro-abrasive jets can be distinguished:

- injection jets;
- suspension jets.

A hydro-abrasive injection jet is formed by accelerating small solid particles (garnet, aluminium oxide, silica carbide) through contact with one or more high-speed water jets. The high-speed water jets are formed in orifices placed on top of the mixing-and-acceleration head. The solid particles are dragged into the mixing-and-acceleration head through a separate inlet due to the vacuum created by the water jet in the mixing chamber. The mixing between the solid particles, water jet and air takes place in the mixing chamber, and the acceleration process occurs in a focusing tube. A typical design for an on-site mixing-and-acceleration devices is illustrated in Fig. 6.7. After the mixing-and-acceleration process, a high-speed three-phase suspension leaves this tube at velocities of several hundred meters per second. This suspension is the actual tool for hydro-abrasive applications. The entire mixing-and-acceleration process is in detail described by Momber and Kovacevic (1998).

The velocity of the abrasive particles can be approximated by the following equation, based on momentum balance:

$$v_S = \alpha_A \cdot \frac{v_J}{1+(\dot{m}_A/\dot{m}_W)} \tag{6.14}$$

Here, α_A is a momentum transfer parameter; a typical value is $\alpha_A=0.7$ (Momber and Kovacevic, 1998). The mass flow rate ratio is frequently called the mixing ratio:

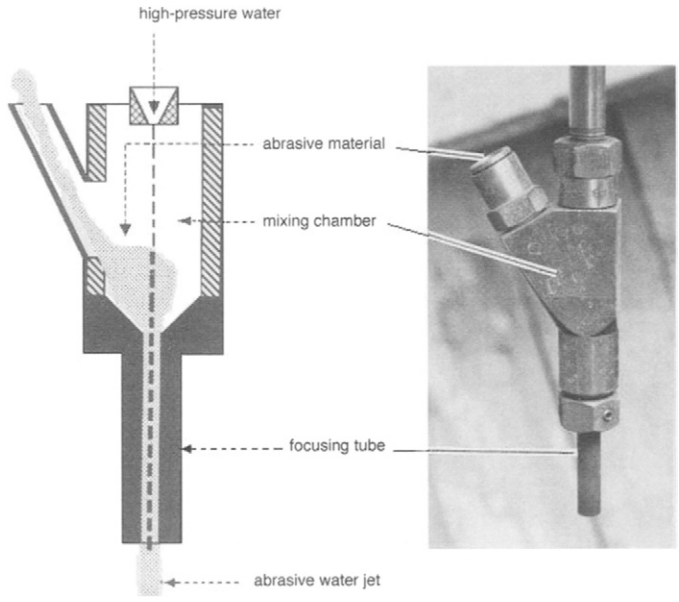

Figure 6.7 Mixing and acceleration head for on-site applications (WOMA Apparatebau GmbH, Duisburg)

$$\dot{m}_A / \dot{m}_W = R_M \tag{6.15}$$

Equation (6.14) is solved for different mixing ratios; the results are shown in Fig. 6.8. For simplicity it is assumed that abrasive particles and water phase in the hydro-abrasive jet have equal velocities (in reality exists a slip of about 10%). The kinetic energy of a hydro-abrasive water jet is:

$$E_A = \underbrace{\sum_{i=1}^{N_S} E_{Si}}_{\text{abrasive particle}} + \underbrace{\frac{m_W}{2} \cdot v_S^2}_{\text{water phase}} \tag{6.16}$$

The number of particles, N_S, depends on abrasive particle size and mass flow rate. The left term of Eq. (6.16) is the energy delivered by the abrasive particles to the erosion site. This portion, denoted 'abrasive particle' is about 10% of the total kinetic energy of a hydro-abrasive jet (Momber, 2001); the remaining 90% are carried by the water phase of the jet (denoted 'water phase'). These relationships are illustrated in Fig. 6.9.

6.2.2 Structure and properties of hydro-abrasive water jets

The structure of a hydro-abrasive jet consisting of solid particles, water, and air is shown in Fig. 6.10. Detailed information about the structure of hydro-abrasive

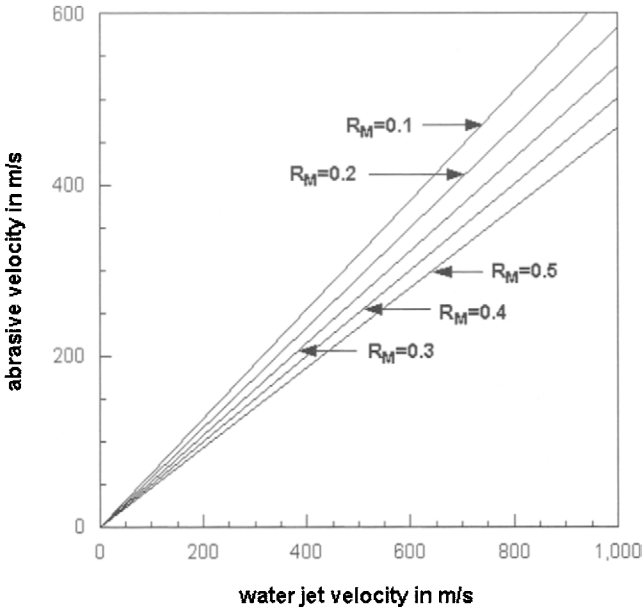

Figure 6.8 Abrasive particle velocities for typical site conditions

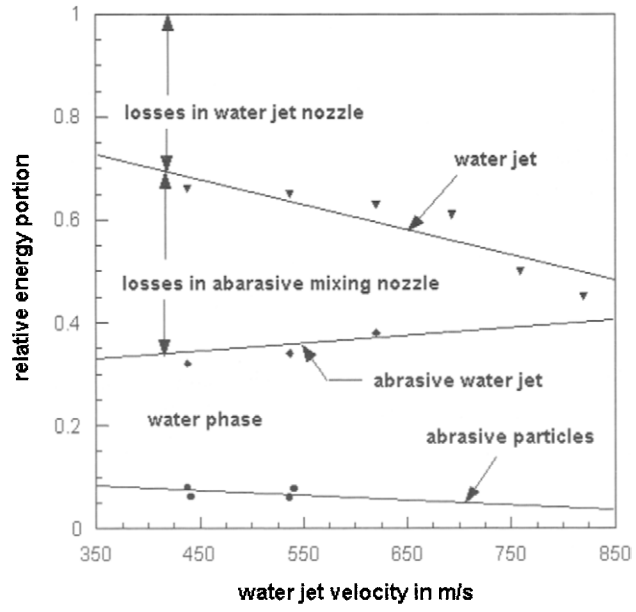

Figure 6.9 Energy history of the abrasive-water jet-mixing process (Momber, 2001)

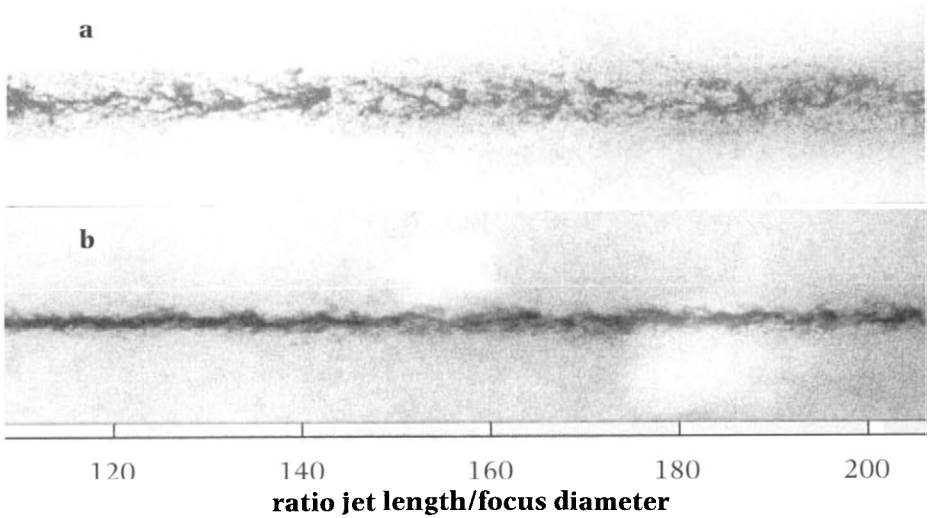

Figure 6.10 Structure of a hydro-abrasive water jet (photograph: Shimizu, Univ. of Hiroshima) a – coarse abrasives, b – fine abrasives

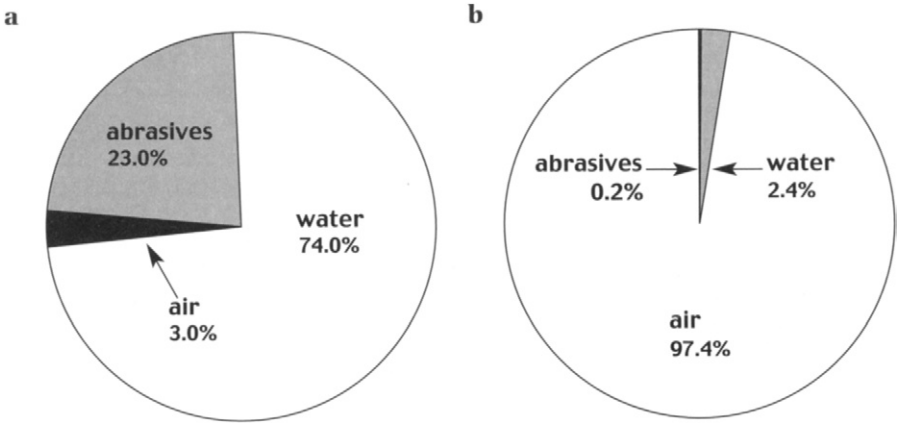

Figure 6.11 Phase distributions in a hydro-abrasive water jet (Momber and Kovacevic, 1998) a – mass related, b – volume related

water jets is provided by Momber and Kovacevic (1998). The portions of the three phases (solid, liquid, gas) in a hydro-abrasive jet are shown in Fig. 6.11. The solid particles occupy about 23% of the mass in the jet, whereas they occupy 0.2% of the jet volume only. If the cross section of a jet is considered, abrasive particles are not distributed evenly. Particle concentration has a maximum outside the core region of the jet, which is a sign of insufficient mixing processes. This is illustrated in Fig.

6.12a. Figure 6.12b shows the velocity distribution in the cross section of a jet. The velocity of the solid particles is at a more or less constant level over the jet radius, whereas the water velocity drops at locations away from the jet centre. This latter behaviour is, however, known from plain water jets.

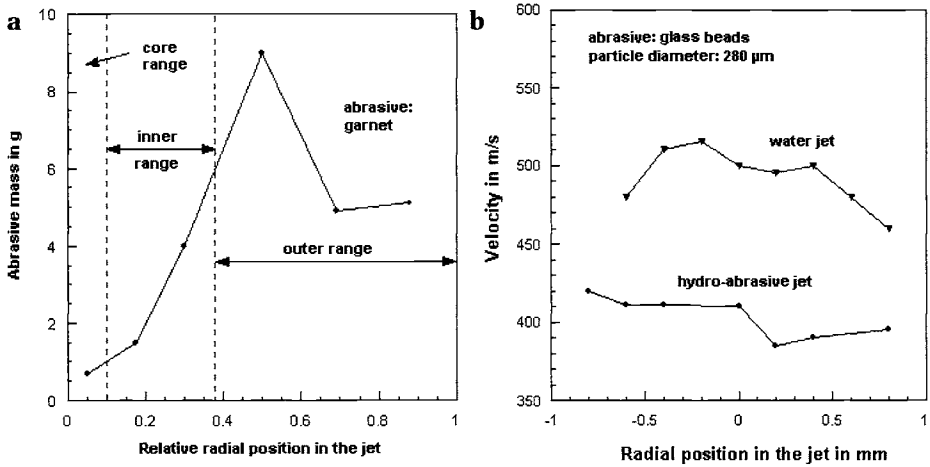

Figure 6.12 Radial mass/velocity distributions in a hydro-abrasive water jet
a – solid particle mass distribution (Simpson, 1990)
b – velocity distributions (Himmelreich, 1992)

6.3 Process optimisation

6.3.1 Process and target parameters

The hydro-abrasive cutting processes are characterised by a large number of process parameters that determine efficiency, economy, and quality of the whole process. Therefore, optimisation of the process is a primary requirement for a successful application. Generally, process parameters in the abrasive water-jet cutting can be subdivided as shown in Fig. 6.13.

6.3.2 Pump pressure effects

Effects of pump pressure on hydraulic and water jet parameters are already mentioned in Section 2.3.2. However, pump pressure (water jet velocity, respectively) also affects the mixing-and-acceleration process during the formation of hydro-abrasive jets. As Eq. (6.14) illustrates, abrasive particle velocity increases linearly with an increase in jet velocity. The momentum transfer parameter depends upon pump pressure as well. These relationships are discussed in more detail by Momber and Kovacevic (1998). Figure 6.14 shows the relationship between depth of cut and pump pressure; a linear relationship can be noted:

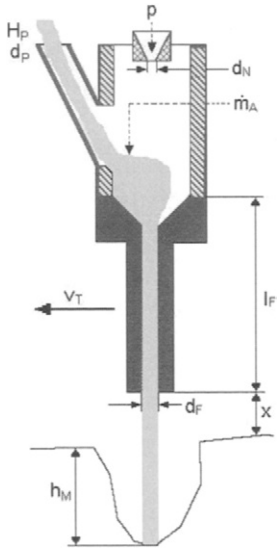

Figure 6.13 Process parameters for hydro-abrasive jet cutting

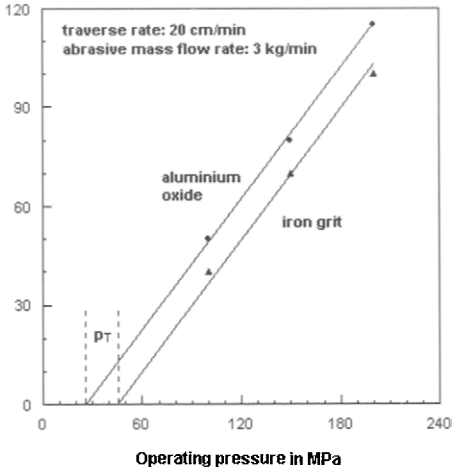

Figue 6.14 Effect of pump pressure on depth of cut in concrete (Nakaya et al., 1984)

$$h_M = A_1 \cdot (p - p_T) \tag{6.17}$$

where p_T is a threshold pump pressure similar to that discussed in Section 2.3.2. From Fig. 6.14, threshold pressure depends on abrasive type, whereas the progress parameter A_1 is independent of the abrasive type. Assuming a purely elastic material response, the threshold pressure can be approximated as follows:

$$p_T \propto K_{Ic}^{10/3} \tag{6.18}$$

From the point of view of energy exploitation, a minimum in the specific cutting energy, $dE_J/dh_M=0$, exists at:

$$p_O = 3 \cdot p_T \tag{6.19}$$

Therefore, energetically optimum cutting can be realised with pump pressures in the range of 150 MPa.

6.3.3 Nozzle diameter effects

There does not exist a serious study about the effect of nozzle diameter variations on the cutting process for concrete. However, Heßling (1988) performed a systematic study into the cutting of rocks. Some results are plotted in Fig. 6.15. The curve can be approximated with the following function:

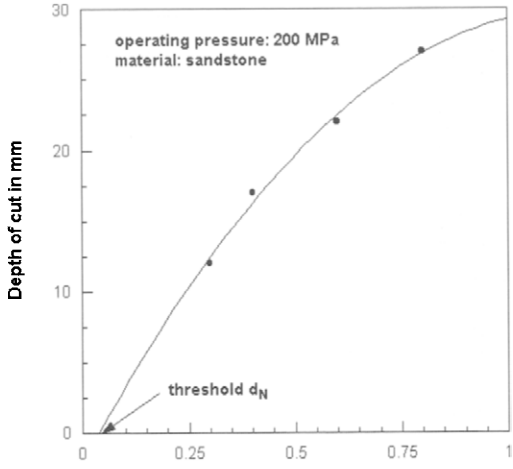

Figure 6.15 Orifice diameter effect on depth of cut (Heßling, 1988)

$$h_M = A_2 \cdot (d_N - d_T)^{B_2} \tag{6.20}$$

with $0<B_2<1$. The threshold diameter can be interpreted in terms of particle acceleration. A certain momentum that is characterised by the volumetric water flow rate is required to accelerate the solid particles to a certain velocity that may be characterised by the particle threshold velocity. As far as this velocity is not reached, no erosion occurs. Similar arguments hold for an upper critical nozzle diameter. The denominator of Eq. (6.14) approaches unity if the water mass flow rate ($\propto d_N^2$) becomes very high. Therefore, if a certain water mass flow rate (nozzle diameter, respectively) is exceeded, a further increase in mass flow rate does not contribute much to the value of the denominator. For this reason, particle velocity rests at a more or less constant level, and depth of cut does not increase notably.

6.3.4 Abrasive mass flow rate effects

A typical relationship between abrasive mass flow rate and depth of cut is shown in Fig. 6.16. After a primarily linear increase in depth of cut, a maximum occurs at an optimum mass flow rate. For given pump pressure and nozzle diameter, this optimum can be interpreted as an optimum mass flow ratio; values for this parameter are listed in Table 6.1. It can be seen that typical values are in the range of $\dot{m}_A/\dot{m}_w=0.3$. If the maximum possible depth of cut is the major target parameter, this value should be kept. To interpret the maximum in the function, mixing-and-acceleration as well as material removal processes must be considered. Firstly, a balance exist between abrasive mass flow rate and water mass flow rate in terms of an optimum acceleration process. This aspect is already discussed in the

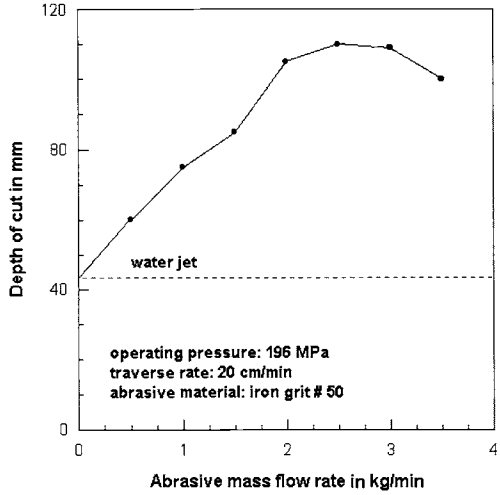

Figure 6.16 Abrasive mass flow rate effect on depth of cut in concrete (Nakaya et al., 1984)

Table 6.1 Typical values for optimum abrasive mass flow rates

Pressure in MPa	Traverse rate in m/s	Abrasive type	Optimum ratio R_O	Target parameter	Reference
241	3.8	garnet	0.25–0.3	depth of cut	Hashish (1982)
196	3.3	steel slag	0.25–0.35	depth of cut	Nakaya et al. (1984)
100	2.7	garnet	0.28	depth of cut	Yie (1984)
241	1.7	garnet	0.16	mass removal	Hashish and Echert (1989)

previous section. If the abrasive mass flow rate is too large, the impulse delivered by the water jet is not sufficient to efficiently accelerate all solid particles. Experimental evidence is delivered by Chen and Geskin (1991), Miller and Archibald (1991), and Rieß and Himmelreich (1991). Secondly, abrasive mass flow rate balances intensity and frequency of material loading. An assumed relationship that illustrates this issue may be the following:

$$v_S \cdot \dot{N}_S \propto C_P \tag{6.21}$$

Here, $\dot{N}_S$ is the number of individual particles per time period, and v_S is the average velocity of an individual particle. Eq. (6.21) is illustrated in Fig. 6.17. If the number of particles (impact frequency) increases because of a higher abrasive mass flow rate, individual particle velocity (impact intensity) drops. Each certain concrete material can be characterised by a fixed point on the curve in Fig. 6.17 for which a decided balance between frequency and intensity of impact exists. Figure 6.16 illustrates a further interesting effect: material is still removed in the case $\dot{m}_A=0$. Thus, concrete can be cut without any abrasive addition, although at low efficiency, and the water phase in the hydro-abrasive jet may contribute actively to

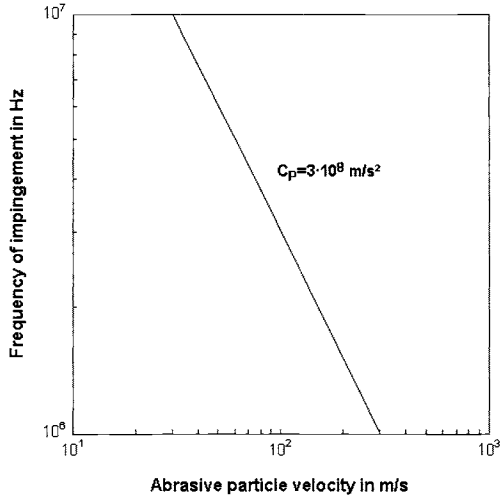

Figure 6.17 Relationships between abrasive particle size and abrasive particle number

the cutting process. More details about this issue are delivered by Momber (2004c). From the point of view of abrasive material exploitation, lower rates are recommended because the function $dh_M/d\dot{m}_A$ has maximum values in the range of low abrasive mass flow rates. A detailed discussion of these aspects in provided by Momber (1995b).

6.3.5 Stand-off distance effects

The influence of stand-off distance on depth of cut is shown in Fig. 6.18. Depth of cut decreases continuously if stand-off distance increases, but the decrease is only marginal. The major reason may be the deceleration of abrasive particles due to air friction, and it was in fact shown by Khan and Geskin (1995) and Neusen et al. (1994) that abrasive and water drop velocity slightly decrease if stand-off distance becomes longer. In order to achieve a maximum depth of cut, stand-off distance should, therefore, be as short as possible.

6.3.6 Traverse rate effects

As illustrated in Fig. 6.19, traverse rate variations affect depth of cut notably. The relationships can be expressed by a formula of the following type (Hashish, 1983):

$$h_M = h_0 \cdot \left[1 - \exp\left(\frac{-A_3}{v_T - v_0}\right)\right] \tag{6.22}$$

where v_0 is the traverse rate below which no increase in depth of cut occurs, and h_0

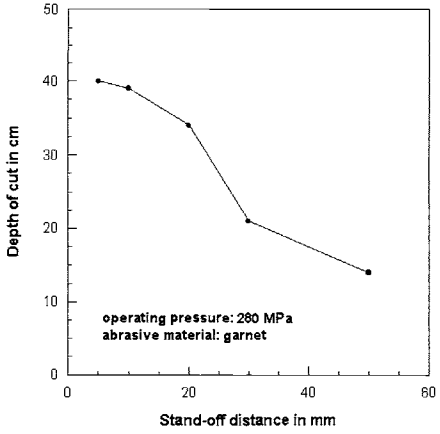

Figure 6.18 Stand-off effect on depth of cut in concrete (Konno, 1988)

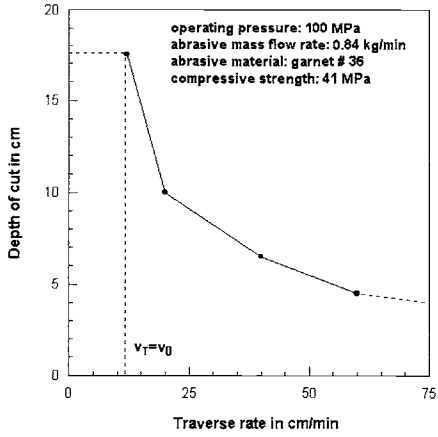

Figure 6.19 Traverse rate effect on depth of cut in concrete (Yie, 1984)

is the maximum possible depth of cut achieved for $v_T=v_0$. Experience shows, however, that a second critical traverse rate, v_G, exists. If this traverse rate is exceeded, no material removal occurs. In the first place this threshold parameter characterises the local exposure time according to Eq. (3.24), whereby the jet diameter may be replaced through the focus diameter:

$$t_E = \frac{d_F}{v_T} \tag{6.23}$$

During the time period t_E a certain number of abrasive particles impinge the concrete surface; this number can be approximated as follows:

$$N_S \propto \frac{\dot{m}_A}{v_T} \tag{6.24}$$

The right term has the unit [kg/m], and it is frequently called particle distribution density (Hu et al., 1991). A critical number of impinging particles is required to introduce measurable removal of material, and this critical number determines the value of the threshold traverse rate. The constant A_3 in Eq. (6.22) covers effects of abrasive mass flow rate. For very high traverse rates, changes in A_3 do not affect the depth of cut significantly which means that the addition of abrasive particles becomes inefficient in case of very high traverse rate. Based on Eq. (6.22), maximum depth of cut is a given parameter in case of cutting the material in one pass. A strategy to form cuts deeper than h_0 is multi-pass cutting as illustrated in Fig. 6.20. In the example shown in Fig. 6.20b, h_M=150 mm is the maximum depth of cut for one cutting pass. However, to achieve a depth of cut of, lets say, 175 mm, several combinations of traverse rate and number of passes can be used. As shown in Fig. 6.20b, multi-pass cutting at high traverse rates becomes inefficient if a

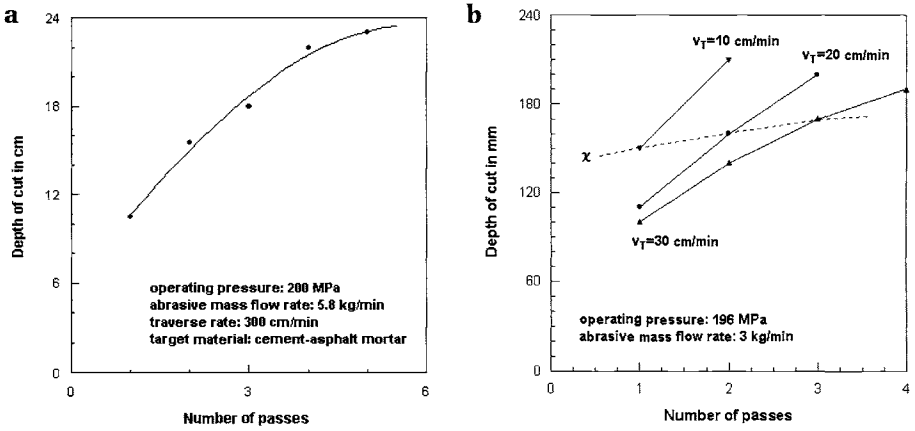

Figure 6.20 Multipass cutting of concrete
a – Effect of number of passes (Yie, 1984)
b – Optimisation strategy (Nakaya et al., 1984)

certain number of passes is exceeded. Reasons are friction between kerf wall and cutting suspension as well as damping of the abrasive particles due to interactions between water, abrasives and concrete debris in deep and narrow kerfs. An evaluation criterion for multi-pass cutting is the ratio between traverse rate and number of passes:

$$\chi = \frac{v_T}{n_S} \tag{6.25}$$

A curve that connects equal χ-values has always a maximum as can be noted from the trend of the lower curve in Fig. 6.20b. This maximum characterises the maximum depth of cut achievable at a given level of jet energy. The lower χ, the higher is the number of passes required to obtain the maximum depth of cut.

Figure 6.21 illustrates the effect of varying traverse rate on cutting rate. In contrast to Fig. 6.19, a maximum exists at high traverse rate values. Therefore, if not maximum depth of cut but maximum length of cut for a desired depth is a primary requirement, rather high traverse rates should be used.

6.3.7 Impact angle effects

It is known from solid particle erosion that variations in impact angle modify the erosion mode. Shallow angles promote micro-machining and chipping, whereas rectangular impacts form microcracks. Cutting tests on concrete could not verify any effect of angle variations for horizontal cutting (Arasawa et al., 1996). If erosion rate is considered, rectangular impact is more efficient, and this advantage articulates at higher pressures (Hu et al., 2002).

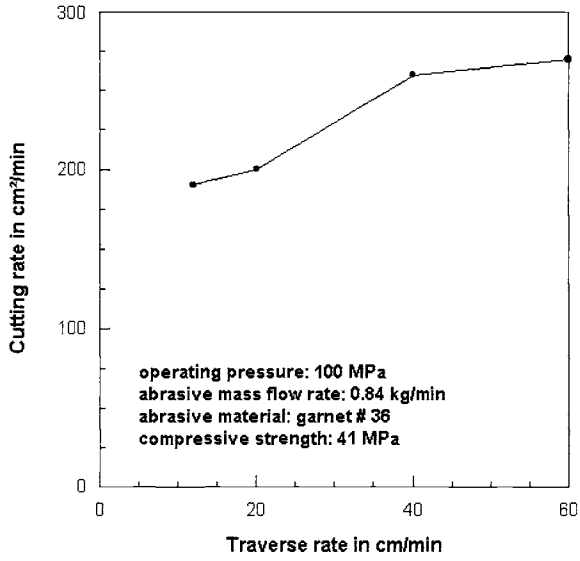

Figure 6.21 Traverse rate effect on cutting rate in concrete (Yie, 1984); values taken from Fig. 6.19

6.3.8 Focus geometry effects

Focus geometry is given through focus length and focus diameter. The effect of focus length is shown in Fig. 6.22; an optimum range, where depth of cut is on its maximum, can be noted. This behaviour is closely related to the acceleration process in the focus. Any solid particle requires a certain distance for an optimum impulse exchange. Below this distance (focus length, respectively) momentum exchange is inefficient and the velocity of the solid particles may be low. If, on the other hand, the focus in too long, friction effects come in front leading to a deceleration of the solid particles. The location of the optimum visible in Fig. 6.22 depends, among others, upon abrasive size, density and shape. These complex relationships are discussed in more detail by Momber and Kovacevic (1998). Results of direct measurements of abrasive particle velocities (Blickwedel, 1990, Himmelreich and Rieß, 1991b) deliver the following relationship:

$$\left(\frac{l_F}{d_F}\right)_{opt} = 25...50 \tag{6.26}$$

Effects of focus diameter variations on depth of cut are displayed in Fig. 6.23. However, target parameter is the removal rate, which increases as focus diameter increases. It can certainly be noted that the progress of the function drops at larger focus diameters. Experimental results obtained on rocks show in fact that an optimum focus diameter exists, which is in the following way linked to the abrasive particle diameter (Heßling, 1988):

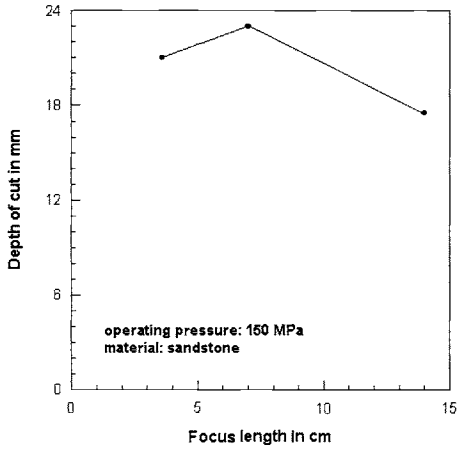

Figure 6.22 Focus length effect on depth of cut in sandstone (Heßling, 1988)

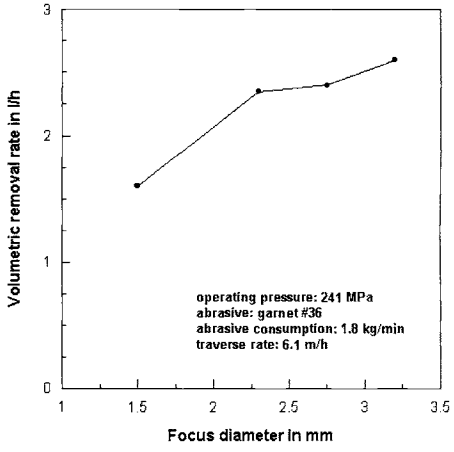

Figure 6.23 Focus diameter effect on material removal rate in concrete (Hashish and Echert, 1989)

$$\left(\frac{d_F}{d_S}\right)_{opt} \cong 3 \tag{6.27}$$

Focus diameter must also be adapted to the water nozzle diameter. An empirical relationship is (Blickwedel, 1990):

$$\left(\frac{d_F}{d_N}\right)_{opt} = 3...4 \tag{6.28}$$

Smaller focus diameters guarantee a denser air-water flow in the focus; thus, increasing the drag force acting on the particles during the acceleration. However, small foci increase the probability of wall-particle and particle-particle contacts.

6.3.9 Abrasive particle size effects

Abrasive particle size is usually evaluated via an average diameter of a particle sample. Some results of particle size effects on depth of cut are shown in Fig. 6.24. Optimum conditions can again be noted. Results obtained by Kokaji et al. (1988) also verify the existence of an optimum particle diameter, especially at rather high traverse rates, in the range of medium particle sizes (about Mesh 40). The corresponding relationships are rather complex and include mixing, acceleration [Eq. (6.14)], breakage behaviour (Matsumoto et al., 1988), and material removal mode. For a given abrasive mass flow rate, larger particles are associated with a decrease in particle number.

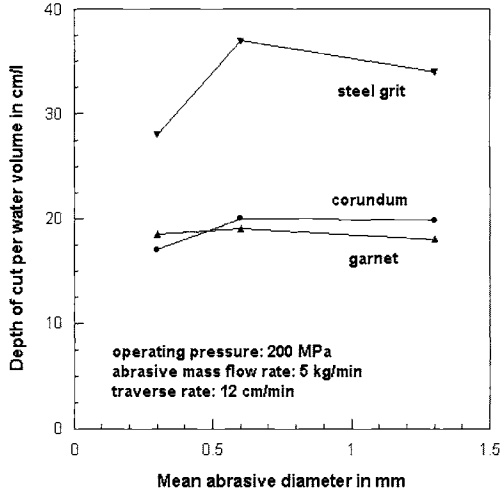

Figure 6.24 Abrasive particle diameter effect on depth of cut in concrete (Nakamura et al., 1989)

$$\dot{m}_A = \frac{\pi \cdot d_S^3 \cdot \rho_S \cdot N_S}{12 \cdot t_E} \quad \rightarrow \quad N_S \propto \frac{1}{d_S^3} \tag{6.29}$$

and the balance between frequency and intensity of particle impact becomes an issue again and determines the location of the optimum. (This argument applies to changes in the abrasive material density as well.) For concrete, a rather intense, but low-frequent loading is useful, and this is one reason for the low depth of cut in the range of small abrasive particles. The decrease in efficiency if large particles are utilised may be caused by the mixing-and acceleration process. Under given physical and geometrical conditions, larger (heavier) particles require a larger acceleration distance for impulse exchange. If this requirement is not met, the particles do not reach their final velocity and travel with a speed lower than those of smaller particles.

6.3.10 Abrasive particle shape and hardness effects

Aspects of abrasive shape are already discussed in Section 6.1, and they apply to this section as well. Unfortunately, no systematic investigation is known that covers shape effects during the cutting of concrete. It could, however, be assumed that because of the small particles and of the high speed of impingement elastic material response does not occur. Another aspect is the fragmentation of the original abrasive grains during the mixing-and-acceleration process, which forms rather irregularly shaped particles.

From traditional tribological arguments, the hardness of the abrasives should at least equal, or better exceeds, the hardness of the target material. Based on Table

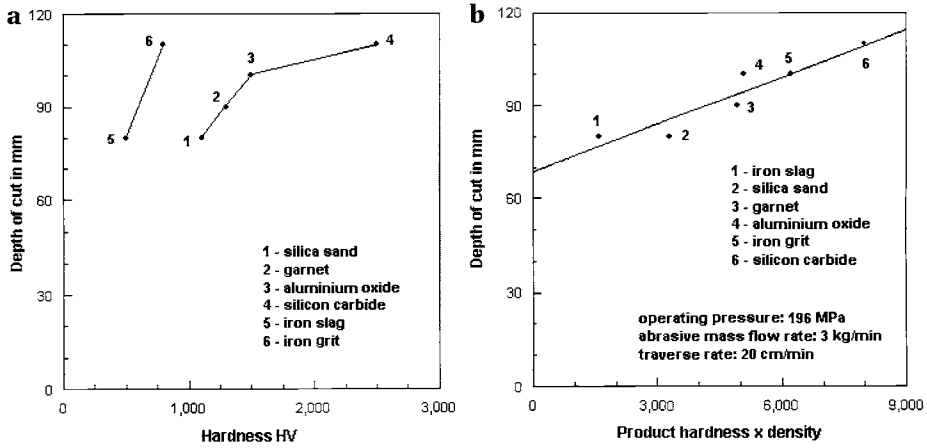

Figure 6.25 Abrasive hardness effect on depth of cut in concrete (Nakaya et al., 1984)
a – Abrasive hardness; b – abrasive hardness and density

1.3, suitable abrasive materials can be selected in dependence of the hardness of the concrete ingredients. Experimental results are plotted in Fig. 6.25a. No general trend can be found if all abrasive materials are considered. However, if steel abrasive and, respectively, mineral abrasives are separated, an almost linear increase in depth of cut with an increase in abrasive material hardness can be noted. Interesting results are displayed in Fig. 6.25b where the depth of cut is plotted against the product of hardness and density. This purely empirical approach delivers a general trend for all abrasive materials used for the experiments.

Abrasive material affects mixing nozzle wear. Very hard abrasives, namely aluminium oxide, are by far more aggressive to nozzle materials than softer abrasives, say steel grit. This relationship is illustrated in Fig. 6.26. Increase in wear

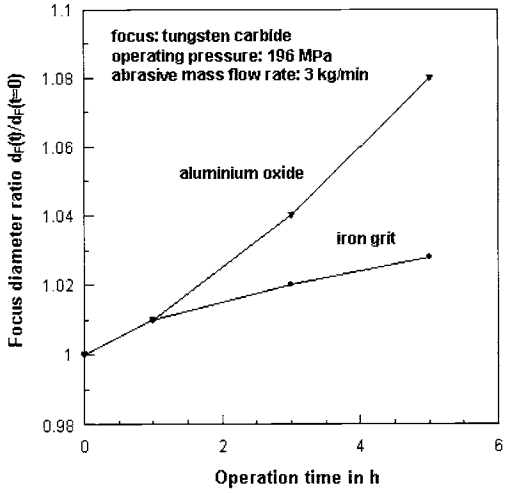

Figure 6.26 Effect of abrasive type on focus wear in hydro-abrasive cutting of reinforced concrete (Nakaya et al., 1984)

a

b

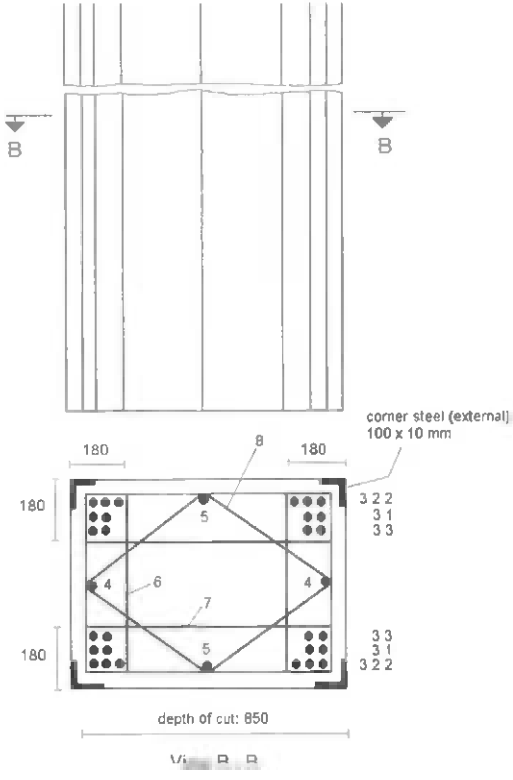

Figure 6.27 Demolition of reinforced concrete with hydro-abrasive jets (WOMA Apparatebau GmbH, Duisburg)
a – Separation of a concrete wall
b – Structure of a heavily reinforced concrete column cut with a hydro-abrasive jet

is progressive in case of aluminium oxide, whereas a slightly decreasing trend can be noted for iron grit. Gain in cutting speed is therefore, to the expenses of nozzle costs. This applied especially to long operation times.

6.4 Demolition of concrete and reinforced concrete structures

6.4.1 General demolition process

Hydro-abrasive cutting offers certain advantages over other demolition tools. An assessment scheme for different demolition methods is provided in Table 6.2. The capability of hydro-abrasive jets to cut heavily reinforced concrete members is illustrated in Fig. 6.27b. The depth of cut is as deep as 850 mm despite the massive steel bar reinforcement. Further examples are listed in Tables 6.3 and 6.4. The fundamental cutting process occurring during the demolition with hydro-abrasive water jets is in great detail discussed by Momber and Kovacevic (1998). From the point of view of surface quality, two cutting regions could be distinguished, as illustrated in Fig. 6.28:

- an upper smooth, striation-free region;
- a lower wavy region, characterised by striation formation.

Table 6.2 Assessment scheme for demolition methods for reinforced concrete (Matsushira, 1988)

Method	Environment			Workability			Effects on concrete	Performance			Global evaluation
	Noise	Vibration	Dust	System size	Reaction force	Safety		Depth of cut	Cutting speed	Working ratio	
Hand breaker	D	D	D	C	C	D	D	C	C	C	D
Cutter drum	D	A	A	C	B	B	A	B	D	D	C
Core-drilling	B	A	A	C	C	B	A	A	D	D	B
Hydro-abrasive jet	B	A	A	B	A	B	A	A	B	C	A
Flame jet	D	A	D	B	A	D	D	B	C	D	D

A – excellent
B – good
C – less desirable
D – undesirable

Table 6.3 Performance parameters for on-site cutting of constructive materials; references: WOMA Apparatebau GmbH, Duisburg

Material (reinforcement)	Pump pressure (MPa)	Power (kW)	Abrasive mass flow rate (kg/min)	Cutting rate (m/h)	Depth / Thickness (mm)
Concrete (heavily reinforced)	130	80	3.6	1.0	40
Concrete (heavily reinforcement)	130	80	3.6	2.4	25
Concrete column * (heavily reinforced)	200	144	2.0	0.5	85
Concrete (steel 6 x ∅6 mm)	200	70	2.6	5.4	14
Concrete (steel 8 x ∅25 mm)	200	70	2.6	1.2	40
Concrete (steel 8 x ∅20 mm)	200	70	2.5	1.3	33
Concrete (steel 2 x ∅6 mm)	125	80	2.2	2.2	33
Concrete (steel 10 x ∅30 mm)	200	75	2.5	1.2	40
Construction steel St 35	200	80	1.5	6.0	1.4

* See Fig. 6.23

Table 6.4 Performance parameters for on-site cutting of reinforced concrete members; abrasive material: quartz sand (Vasek et al., 1991)

Concrete	Reinforcement (diameter / thickness)	Member thickness (cm)	Pump pressure (MPa)	Abrasive mass flow rate (kg/min)	Cutting rate (m^2/h)
Concrete	Bars (28 mm)	30	220	1.59	0.29
Concrete	Bars (14 mm)	15	235	0.54	0.20
Monolithic concrete	No reinforcement	30	220	1.98	1.35
Monolithic concrete	No reinforcement	15	220	1.98	2.34
Shotcrete	Metallic mesh (6 mm)	30	220	1.50	0.59
Shotcrete	Metallic mesh (6 mm)	15	207	1.93	0.84
Shotcrete	No reinforcement	30	220	1.50	0.82
Shotcrete	No reinforcement	15	207	1.93	1.26
Monolithic concrete	Wood boards (20 mm)	30	220	1.50	1.67
Monolithic concrete	Wood boards (20 mm)	15	207	1.93	2.32
Monolithic concrete	Cut wires (0.4 mm)	30	207	1.93	0.78
Monolithic concrete	Cut wires (0.4 mm)	15	207	1.93	0.66

The corresponding erosion mechanisms are described by Momber and Kovacevic (1998); see also Section 6.1. Momber et al. (1999, 2002c) performed acoustic emission studies and found that the erosion modes involved in concrete cutting depended mainly upon aggregate size and distribution. Fine-grained concretes with a high amount of spherical sand particles fail by intergranular erosion as illustrated in Fig. 6.29a, whereas rather coarse concretes with a high

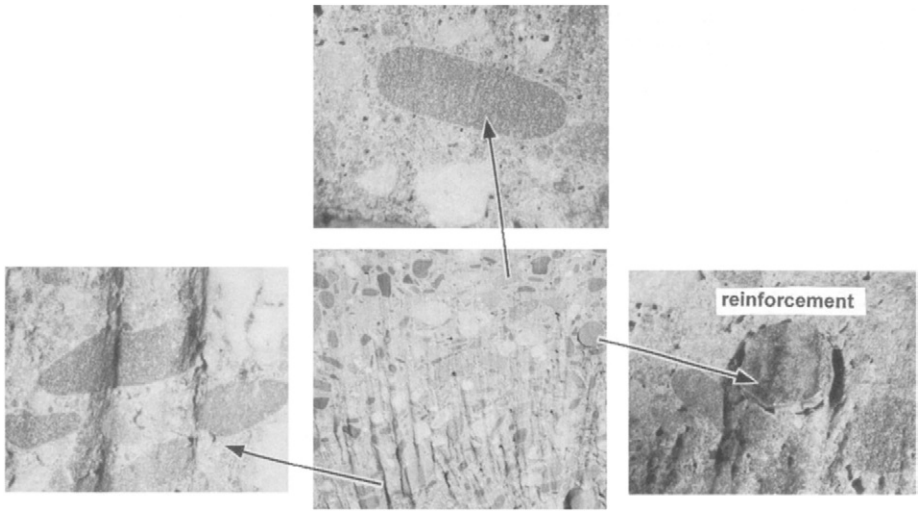

Figure 6.28 Structure of a cut area in reinforced concrete formed during hydro-abrasive cutting (Momber, 1998)

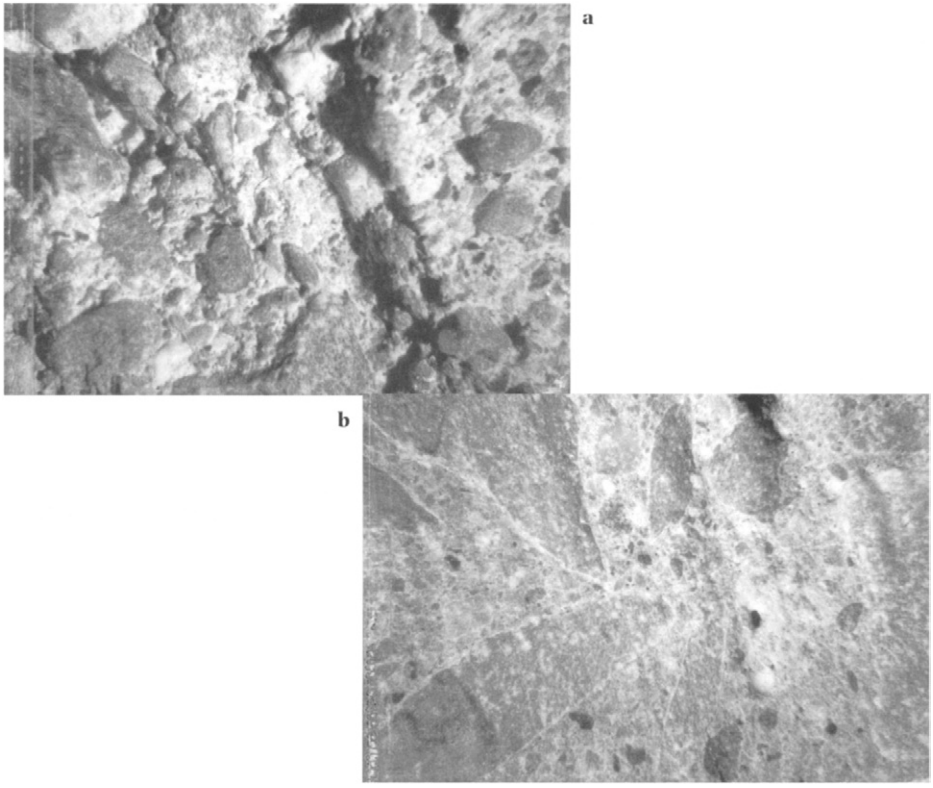

Figure 6.29 Failure modes in concrete samples cut with hydro-abrasive jetting (Momber et al., 2002c) a – intergranular erosion in fine-grained concrete, b – transgranular fracture in coarse-grained concrete

amount of broken coarse aggregates fail in a transgranular mode (Fig. 6.29b). For equal depths of cut, a transgranular mode produces acoustic emission signals with a high amplitude probably caused by the sudden energy release during aggregate fracture. Time domain acoustic emission signals of concrete with larger aggregates is characterised by typical burst emissions; finely grained concrete, in contrast, produces rather homogeneous signals. Examples are provided in Fig. 6.30. A basic property that determined the failure type, is structural homogeneity – very similar to the situation discussed in Section 2.4.1.

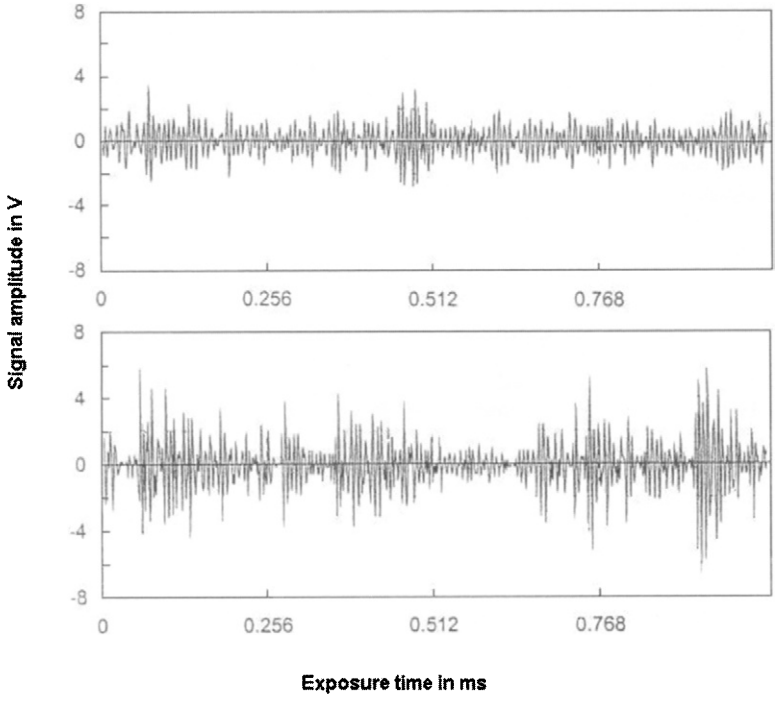

Figure 6.30 Acoustic emission signals acquired during hydro-abrasive cutting of concrete (Momber et al., 1999); upper graph: fine-grained concrete; lower graph: coarse-grained concrete; corresponding failure modes are shown in Fig. 3.29

Effects of concrete material parameters on depth of cut are investigated by Momber and Kovacevic (1997). A statistical analysis of these results showed that crack velocity in the concrete is the governing parameter that determines the resistance against hydro-abrasive cutting. Results of this study are listed in Table 6.5. Specific cutting energy also depends strongly on crack velocity (Agus et al., 1993). A relationship that characterises the resistance of brittle materials against hydro-abrasive cutting is as follows (Matsui et al., 1991):

$$\dot{A} = C \cdot \left(\frac{\sigma_T}{2 \cdot E_M} \right)^{-1.97} \tag{6.30}$$

Table 6.5 Effects of concrete parameters on depth of cut in abrasive water jet cutting (Momber and Kovacevic, 1997)

Material parameter	Correlation regression
Elastic strain energy density	0.939
Young's modulus	0.977
Compressive strength	0.959
Crack velocity	0.078

It is, however, found that rock materials, namely granite and marble, do not fit that relationship (Matsui et al., 1991). An explanation is delivered by Momber (2004a) who argued that the term $(\sigma_T/2{\cdot}E_M)$, which is actually the elastic strain energy density, may be replaced by the true strain energy density for quasi-brittle materials. Zeng et al. (1992) introduced a so called "machinability number" to describe the resistance of materials against hydro-abrasive cutting:

$$N_M = C_1 \cdot \frac{d_M \cdot \sigma_f}{\gamma_M \cdot E_M} + \frac{C_2}{\sigma_f} \tag{6.31}$$

The lower the value for N_M the higher the material resistance. This parameter has to be estimated by reference experiments. Values for concretes and related materials are listed in Table 6.6. Using relationships from linear-elastic fracture mechanics, Eq. (6.31) can be simplified as follows:

$$N_M \propto K_{Ic}^{-2} \tag{6.32}$$

Table 6.6 Machinability numbers of engineering materials (Momber and Kovacevic, 1998)

Material	Machinability number
Alumina Ceramic AD 85	17
Asphalt Concrete	461
Concrete (medium strength)	516
Concrete (high strength)	468
Glass	596
Granite	322
Graphite	875
Mortar	858
PMMA	690
Refractory bauxite	106
Sintered Magnesia	408
White Marble	535

Figure 3.34 shows the drawing of a nozzle type developed to accelerate explosive pellets by high-speed water jets (Becker et al., 1999). The pellets are being accelerated to a high speed and are brought to detonation if they hit the material to

Figure 6.31 Rock sample crushed with the explosive pellet impingement technique (Becker et al., 1999)

be cut. The principle of mixing is comparable to that used for the formation of hydro-abrasive water jets.. Tests on concrete and rocks with pellet speeds between 60 and 80 m/s have shown that effective stand-off distances as high as 6 m can be realised. A rock sample cut with this method is shown in Fig. 6.31. A 10-fold increase in cutting speed compared to conventional techniques is expected (Becker et al., 1999). Further increase in efficiency may be possible if miniaturised shaped charged are used instead of pellets, and if the surface hit by the explosives is pre-cut with water jets.

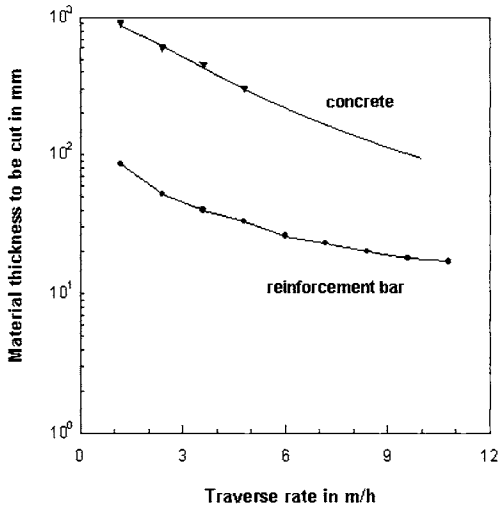

Figure 6.32 Relationships between traverse rate, depth of cut and target material (Momber, 1998)

6.4.2 Effects of reinforcement on cutting performance

Certain investigations have shown that type and density of steel bar reinforcement affect efficiency of cutting as well as the final depth of cut. The simplest way to assess effects of reinforcement is to consider the steel reinforcement as the part of the structure that governs depth of cut. This approach is illustrated in Fig. 6.32. The minimum thickness of the reinforced concrete member than can be cut is assumed to be equal to the diameter of the reinforcement bar. From this assumption, the corresponding traverse rate can be selected. The maximum thickness to be cut depends to a large amount upon number and distribution of reinforcement bars. In Fig. 6.33, the location of the reinforcement bars determines depth of cut. If bars are present, depth of cut decreases. Whereas the first row of reinforcement bars could be cut under the given conditions, the second row could not be cut, and depth of cut varies extremely between 20 cm and 37 cm, which is a deviation of about 80%.

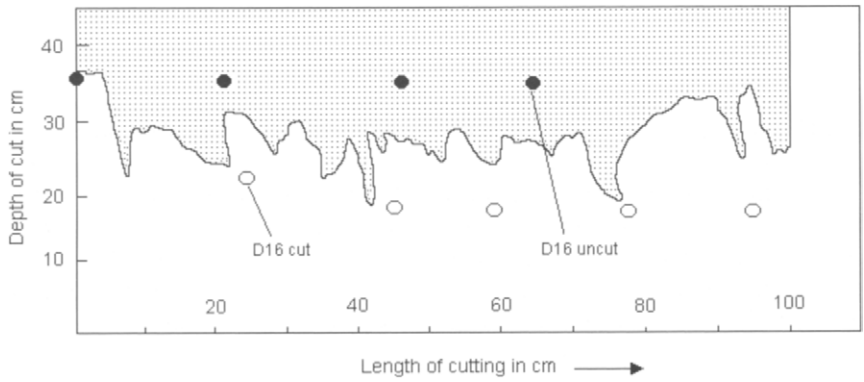

Figure 6.33 Effect of reinforcement bars on cutting depth in reinforced concrete members (Konno, 1988)

In certain cases, damage to any steel inclusion (bars, pipes, tubes) needs to be avoided. An example is shown in Fig. 6.34. Here, all performance parameters are selected in a way that concrete covers are cut, whereas pipes buried in the concrete structure are undamaged. An approximation for the maximum depth of cut in a steel-bar reinforced concrete is as follows (Momber et al., 2004):

$$h_T = -\frac{b_1}{2 \cdot a_1} \pm \sqrt{\frac{b_1^2}{4 \cdot a_1^2} - \left(\frac{c_1 - 1}{a_1} + \frac{E_T}{a_1 \cdot E_A} \right)} \qquad (6.33)$$

The constants a_1 to c_1 must be estimated experimentally. The parameter E_T is a threshold energy level for the steel bar material. As far as this value is reached, no further cutting occurs. An empirical relationship for the reduction in cutting speed due to steel reinforcement is derived by Arasawa et al. (1986):

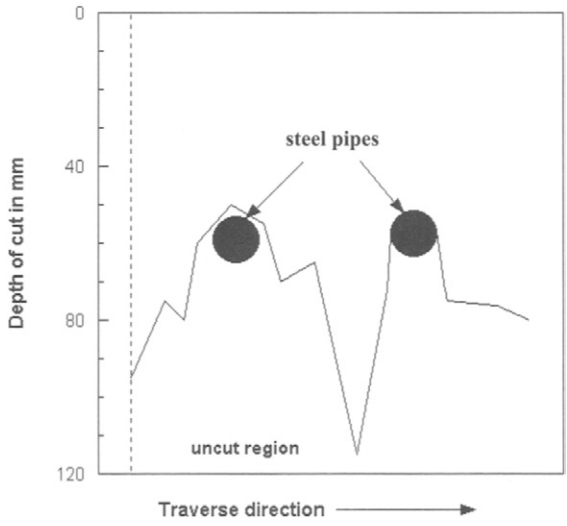

Figure 6.34 Damage-free cutting of concrete with embedded steel pipes (Kokaji et al., 1986)

$$\chi_R = \frac{46.37 - 15.2 \cdot \ln v_T}{78.66 - 20.1 \cdot \ln v_T} \tag{6.34}$$

For a traverse rate of 2 cm/min (1.2 m/h), Eq. (6.34) delivers χ_R=0.55. This result agrees with experience that, for a wall thickness up to 500 mm, reinforcement bars reduce the cutting speed down to about 50% (Sugiyama and Tabata, 1988). Because of the pronounced influence of the reinforcement bars, the on-line monitoring of reinforcement bars during the cutting process is a major problem from the point of view of site applications. This problem applies especially to remotely controlled cutting jobs, such as submerged cutting, cutting in hazardous environment, demolition of nuclear power plants. Methods that can be utilised include noise signals (Hashish and Echert, 1989), vibration acceleration (Sugiyama and Tabara, 1988) and impact voltage signals (Yamada et al., 1988). Results of impact noise measurements are shown Fig. 6.35a. A notable drop in signal amplitude occurs when the hydro-abrasive jet hits and cuts a reinforcement bar. However, due to the curved jet trajectory, the signal is being displayed with a slight delay. Similar is the situation in Fig. 6.35b – a sudden increase in signal amplitude can be seen if a steel bar is cut (note the very similar structure of the acoustic emission signals displayed in Fig. 6.30). Vibration level acquired during cutting can also be used to distinguish between complete cutting and incomplete cutting: if a reinforced concrete member is completely cut through, vibration level increases (Sashida et al., 1988).

The effect of steel-fibre reinforcement on efficiency of hydro-abrasive jet cutting is illustrated in Fig. 6.36. Erosion rate usually decreases if concrete is reinforced

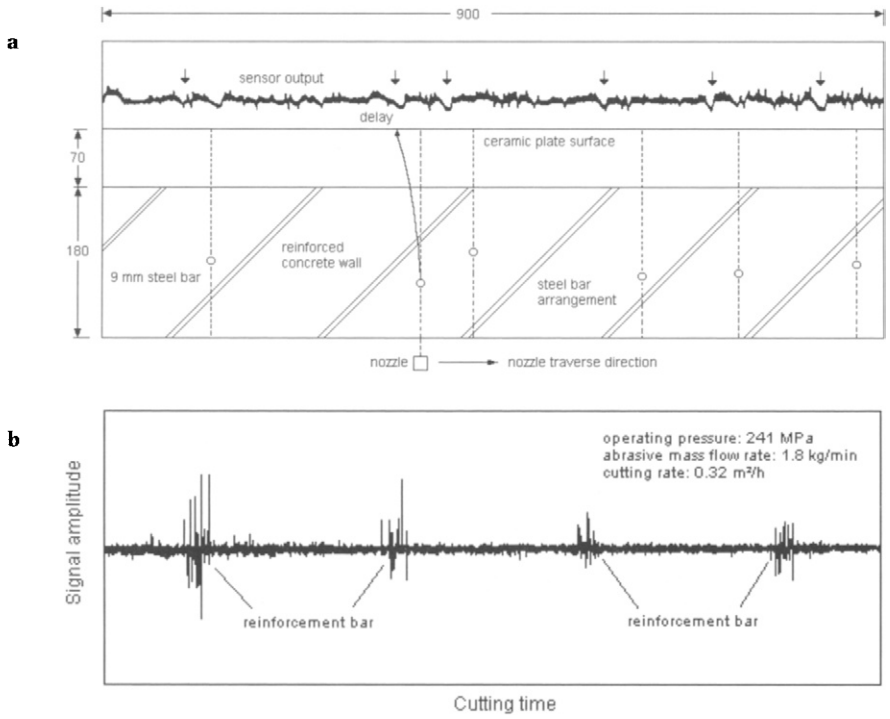

Figure 6.35 On-line monitoring of reinforced bars during hydro-abrasive cutting of reinforced concrete a – impact noise measurements (Yamada et al., 1988); b – filtered noise signals (Hashish and Echert, 1989)

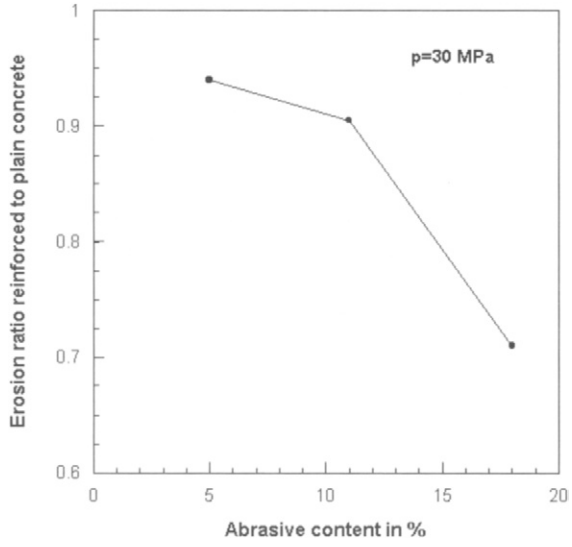

Figure 6.36 Effects of steel-fibre reinforcement on efficiency of hydro-abrasive cutting of concrete (Hu et al., 2002)

with steel fibres. However, the influence of the fibre reinforcement is more pronounced for lower impact angles. This is due the energy absorbed by the fibres while they are cut by the abrasive particles in case of shallow impact angle (Hu et al., 2002). A steel fibre completely cut during hydro-abrasive erosion is shown in Fig. 6.37. In some cases, especially at perpendicular jet impingement, reinforcement can reduce material resistance. This is caused by the additional weak interfaces between matrix and fibres introduced by the fibres. It is, therefore, recommended to incline the nozzle if fibre reinforced concrete is being cut with hydro-abrasive jets.

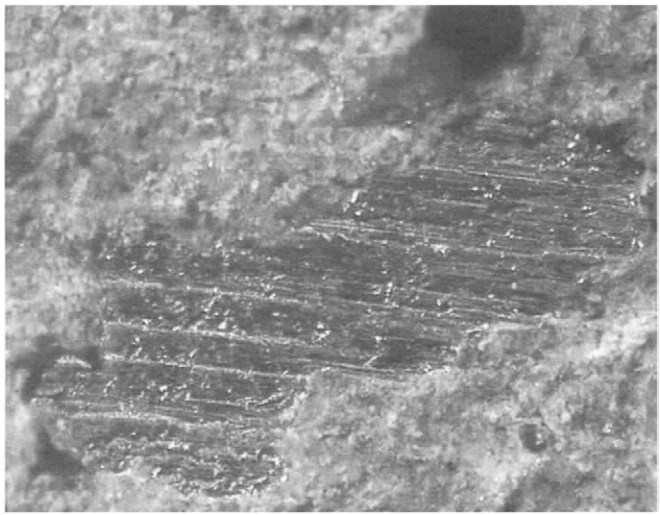

Figure 6.37 Steel-fibre in reinforced concrete cut during hydro-abrasive erosion (Hu et al., 2002)

6.4.3 Vibrations and noise levels

Vibrations to structural elements in the neighbourhood of a demolition site are critical to the acceptance of the method. This applies especially to jobs performed in sensitive areas, say hospitals, hotels, cultural utilities, office buildings. Investigations have shown that hydro-abrasive cutting is a rather smooth demolition method in terms of vibrations. Some results are listed in Table 6.7. The peak vibration acceleration level at a distance of 4 to 5 m from the tool was highest for the air breaker (82 dB) and lowest for a hydro-abrasive jet cutting device (68 dB). The propagation of the vibrations through the walls of a 10-floor reinforced concrete building is shown in Fig. 6.38. The lowest level at all floors is associated with hydro-abrasive cutting. Differences in vibration are low in regions far away from the demolition site (1st and 2nd floor, 10th floor). The relationships between floor number and acceleration level are complex. Acceleration for hydro-abrasive

cutting, for example, first drops for the floors 5 and 4, but it increases for the floors 3 to 1 which are further away from the demolition site.

Table 6.7 Vibration and noise values for different demolition tools (Mugikura et al., 1990)

Tool / method	Vibration level in dB	Noise level in dB(A)
Air breaker	82	94
Air chipper	74	85–86
Electric drill	72	80
Electric hammer	76	85–86
Hand crusher	78	77–78
Hydro-abrasive water jet	68–69	77–78
Wall cutter	68–69	77–78

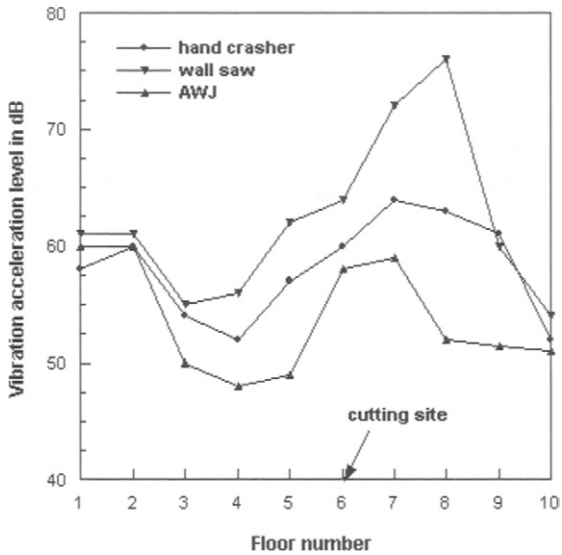

Figure 6.38 Vibration acceleration levels of different demolition tools (Mugikura et al., 1990)

Noise levels are listed in Table 6.7. The peak sound level is maximum for the air breaker, and lowest for wall cutter, hand crusher and hydro-abrasive jet. Notable differences are noted in the frequency ranges of the demolition tools. The main noise components for the air breaker are in the range between 12.5 to 500 Hz, while noise from the hydro-abrasive jet shows a similar tendency than the background noise. Only in the frequency range between 500 Hz and 2 kHz, noise from hydro-abrasive jetting exceeds the background noise (Mugikura et al., 1990).

CHAPTER 7

Pulsed Liquid Jets for Hydrodemolition

7.1 Material loading due to water drop impingement

7.1.1 Stresses due to drop impingement

Liquid drop impingement consists of three predominant stages:

(i) compressible impact stage;
(ii) jetting stage;
(iii) stagnation pressure stage.

Stages (i) and (ii) are illustrated in Figure 7.1. Recent reviews about the phenomena associated with these phases were given by de Botton (1998), Field (1999) and Lesser (1995) who also reported details of loading intensity and duration. As seen in Image 1 of Figure 7.1, the liquid at the edge of the drop is trapped behind a compressive wave that propagates into the drop. The corresponding high stresses can be approximated by the so-called 'water hammer equation':

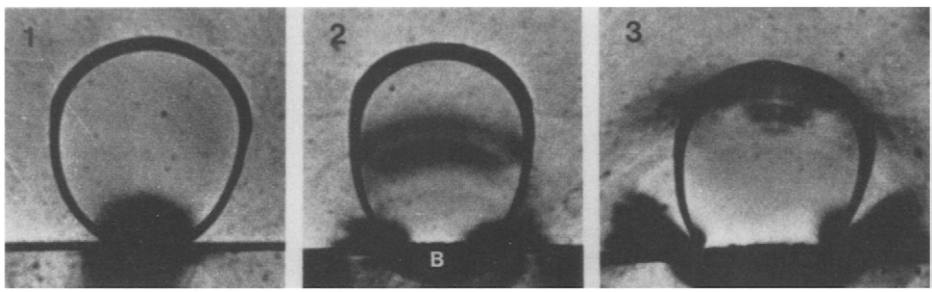

Figure 7.1 Stages of drop impingement on a solid surface (Camus, 1976)

$$\sigma_D = \rho_F \cdot c_F \cdot v_D \tag{7.1}$$

Here, c_F is the speed of sound in the liquid. For water with c_F=1,500 m/s, and v_D=503 m/s from the example in Section 2.1.1, the generated stress is $\sigma_D \cong 7.54 \cdot 10^8$ N/m^2 (754 MPa). A more rigid solution to the stress problem delivers the following equation that considers the properties of the target material:

$$\sigma_D = \frac{\rho_F \cdot c_F \cdot v_D}{1 + (\rho_F \cdot c_F / \rho_M \cdot c_M)} \tag{7.2}$$

The product $\rho \cdot c$ is the acoustic impedance. See Table 7.1 for corresponding values. It can be noted that materials with high acoustic impedance experience lower stresses. Using typical material properties of concrete, Eq. (7.2) delivers a peak stress of $\sigma_D = 8.66 \cdot 10^8$ N/m^2 (866 MPa) for v_D=503 m/s. For target materials with very high acoustic impedance, Eq. (7.2) approximates Eq. (7.1).

Table 7.1 Drop impact parameters for v_D=800 m/s, r_D=1 mm (Momber, 2004b)

Material	v_S in m/s	c in m/s	$c \cdot \rho$ in kg/m^2·s	p_D in MPa	p_B in MPa	r_C in mm	t_P in μs
Water	1,460	3,060	$1.5 \cdot 10^6$	–	–	–	–
Concrete 1	4,311	5,567	$8.6 \cdot 10^6$	1,918	320	0.26	0.13
Concrete 2	4,220	5,484	$9.2 \cdot 10^6$	1,951	320	0.26	0.13
Granite	4,580	5,820	$11.4 \cdot 10^6$	2,021	320	0.26	0.13
Limestone	5,730	6,906	$14.3 \cdot 10^6$	2,083	320	0.26	0.13
Rhyolite	4,082	5,354	$11.0 \cdot 10^6$	2,022	320	0.26	0.13

The duration of the compressible stage can be estimated from geometrical considerations (Erdmann-Jesnitzer and Laschimke, 1966; Lesser and Field, 1983). It is given through the following equation:

$$t_P = \frac{d_D \cdot v_D}{4 \cdot c_F^2} \tag{7.3a}$$

The duration is dependent of impact velocity and drop diameter. This argument applies only to curved liquid slugs. If cylindrical slugs with a plane front are applied, the duration of the compressible stage is given by the following equation:

$$t_P = \frac{d_D}{2 \cdot c_F} \tag{7.3b}$$

and it does not depend upon impact velocity. (d_D is the diameter of the cylinder in that case.) In Eqs. (7.1) to (7.3), c_F is sometimes replaced by the shock wave speed in the liquid given through the following relationship (Heymann, 1968):

$$c_W = c_F + 2 \cdot v_D \tag{7.4}$$

For a drop diameter of 6 μm (for v_D=503 m/s), Eq. (7.3) delivers $t_P = 4.5 \cdot 10^{-10}$ s.

Stresses measured by Daniel (1976) in concrete samples during the impingement of water slugs with velocities of 2,300 m/s were as high as 122 MPa (compressive) and 36 MPa (tensile), whereas strains were estimated to 4,420 με (compressive) and 1,300 με (tensile).

7.1.2 Material response to drop impingement

In brittle materials, high-speed water drop impingement forms an undamaged core zone surrounded by an array of microcracks formed due to propagating Rayleigh surface waves. The corresponding mechanisms are in detail described by Bowden and Field (1964). The diameter of the undamaged core increases linearly with an increase in drop impact speed (Momber, 2004b). Crack nets are very pronounced in hard concrete components (aggregates); this is illustrated in Figure 7.2a for granite and in Figure 7.2b for quartz. In rather soft material components, crack nets become somewhat obliterated; this is shown in Figure 7.3 for a soft and porous limestone and

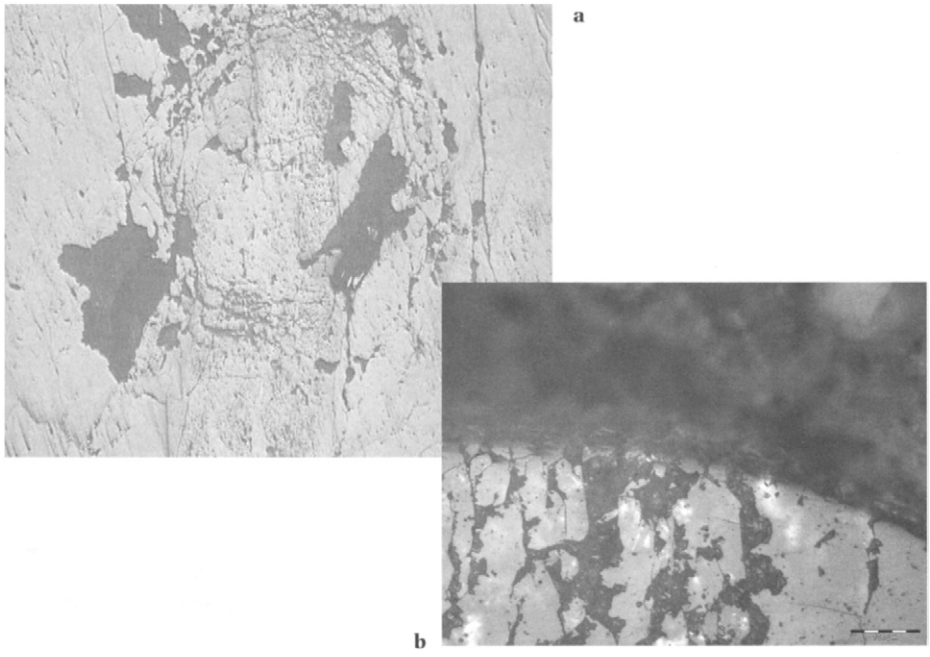

Figure 7.2 Ring of discrete cracks in hard materials formed due to water drop impingement
a – granite b – quartz aggregate in concrete

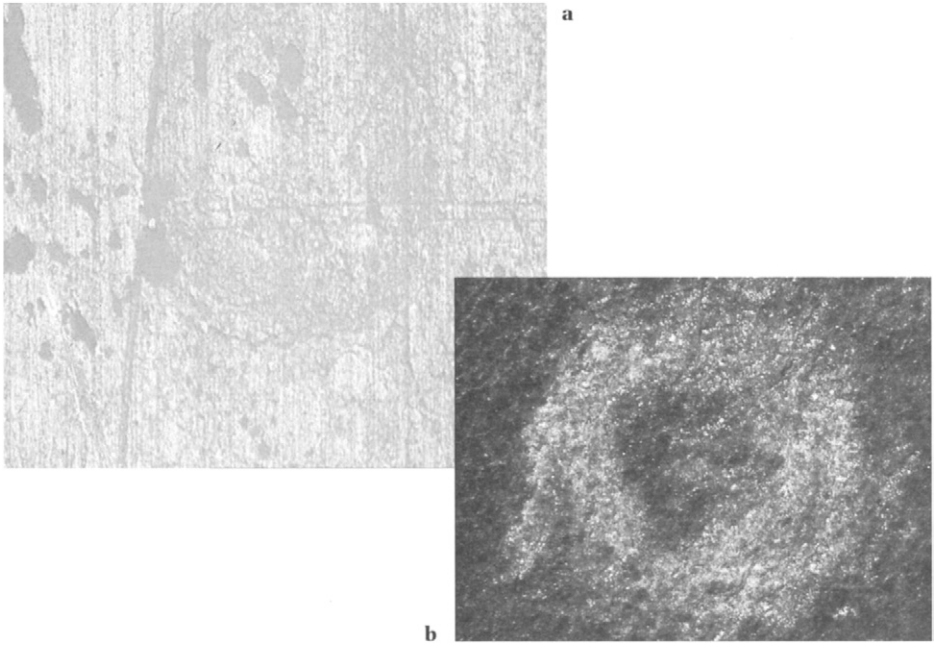

Figure 7.3 Permanent deformations in soft rocks due to water drop impingement
a – limestone b – schist

a very soft schist. In concrete, a mixed mode can be observed. An example is shown in Figure 7.2b. Here, the hard quartz inclusion shows clear features of network cracking, whereas the surrounding matrix is removed to a large extent. Examples of lateral jetting are provided in Figure 7.4a for a granite and in Figure 7.4b for a rhyolite. The severity of this damage increases with an increase in the distance from the impact centre. Cracking is always directed into flow (jetting) direction.

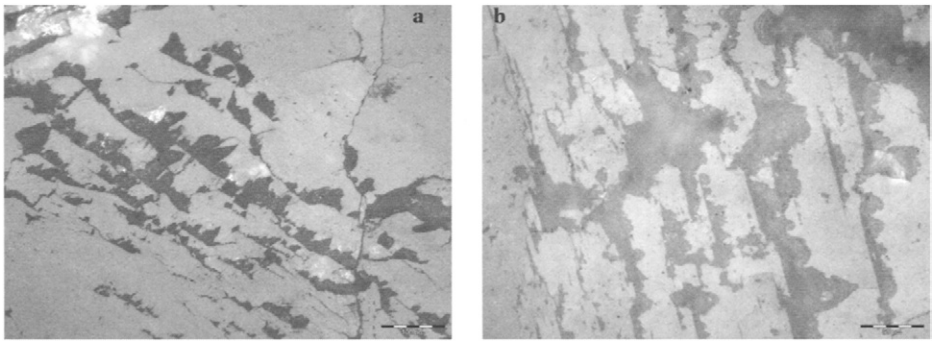

Figure 7.4 Crack extension due to lateral jetting
a – granite b – rhyolite

Drop impact experiments performed by Momber (2004a) delivered evidence that material hardness predominates the failure mode and that a transition stage exists similar to that known for solid impact. The threshold for micro crack extension in rocks due to liquid drop impact can be estimated based on a dynamic failure criterion (Steverding and Lehnigk, 1976):

$$\sigma_P^2 \cdot t_P = \frac{\pi \cdot \gamma_M \cdot E_M}{c_M} \tag{7.5}$$

Combining equations (7.1) and (7.3a) with linear-elastic fracture mechanics, this criterion delivers the following threshold condition for drop impact:

$$v_R^3 = 2.1 \cdot 10^{-6} \cdot \frac{G_{Ic} \cdot E_M}{c_M \cdot d_D} \propto \frac{K_{Ic}^2}{c_M} \tag{7.6}$$

Fracture toughness is the primary material parameter in that case, and the corresponding 2/3-power-relationship between threshold velocity and fracture toughness is verified for brittle materials through experimental results (Coad et al., 1996). A simple yield criterion (Tabor, 1951):

$$\sigma_Y = \frac{H_M}{1.1} \tag{7.7}$$

combined with Eq. (7.1), delivers a threshold impact velocity for the onset of plastic flow:

$$v_{PL} = \frac{H_M}{1.1 \cdot c_W \cdot \rho_W} \tag{7.8}$$

If Eqs. (7.6) and (7.8) are equalised, and the result is solved for d_D, the following transition condition appears:

$$r_C \propto \frac{K_{Ic}^2}{H_M^3} \tag{7.9}$$

Hardness values for some relevant materials are listed in Table 1.3. For many rocks and rocklike materials, hardness and compressive strength show a linear relationship (Szwedzicki, 1998). Therefore:

$$r_C \propto \frac{K_{Ic}^2}{\sigma_C^3} \tag{7.10}$$

This relationship is shown in Figure 7.5 with $K_{Ic}^2/\sigma_C^3=X$. Materials left from the separation line (mainly hard aggregate materials) respond elastic, whereas materials situated right from the separation line (e.g. cement mortar) show features of plastic flow. For a given material, Eq. (7.10) determines that plastic flow is more probable if the material is impinged by drops with rather small diameters.

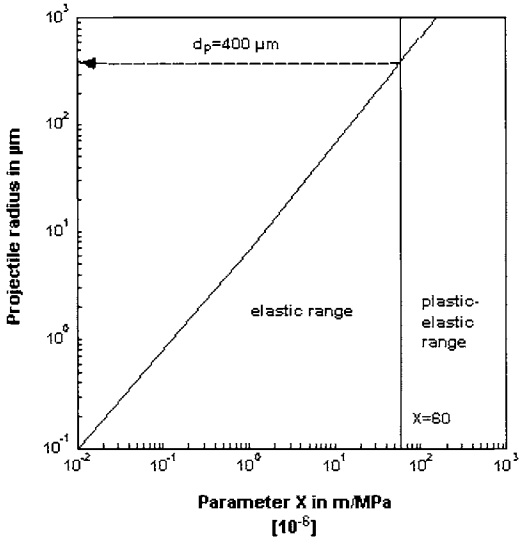

Figure 7.5 Elastic-plastic transition criterion for water drop impact (Momber, 2004b)

Comparative mercury intrusion experiments could verify that failure in concrete starts at the interface between aggregate and matrix. It can be seen in Figure 7.6 that flaws of $l_C<1$ µm in size predominantly grow under water slug loading. In the

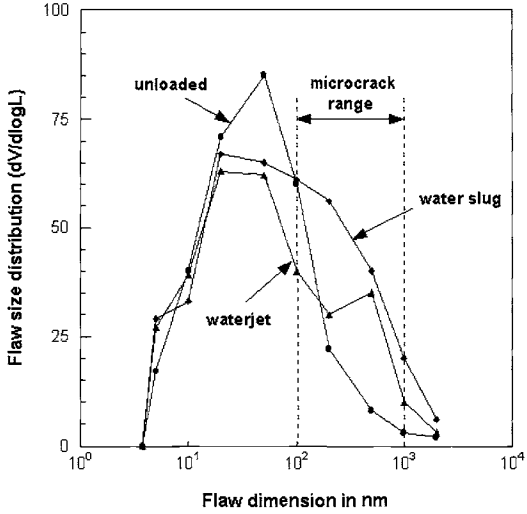

Figure 7.6 Mercury intrusion tests on concrete loaded with continuous water jet and, respectively, pulsating jet (Momber, 2000d)

flaw range l_C>1 μm, however, not much difference exists between stationary water jet and water slug. These results illustrate clearly that a static component is required to widen the cracks activated due to the water slug impact further.

7.1.3 Parameter effects and resistance parameters

The major process parameter is the velocity of the impinging drops. Drop velocity influences the parameters of the microcrack net formed during elastic impact. Erosion rate depends on impact velocity as follows:

$$\dot{V}_M \propto (v_T - v_D)^n \tag{7.11}$$

Here, v_T is the threshold velocity according to Eq. (7.6). The velocity exponent n depends on material type; it is comparative high for porous rocks and lower for rather dense materials. If the erosion process is introduced, two principal erosion modes, a type-I-mode and a type-II-mode, can be distinguished as already known from continuous water jet erosion. These types are illustrated in Figure 7.7. A type-I-mode, comparable to a drilling process, was observed in limestone, sandstone and mortar; the eroded cavities were rather deep, narrow and regular (Momber, 2004a, 2004b). This is illustrated in Figure 7.7a for a fine-grained sandstone. Type-II-mode, found for example in cement matrix, marble or dolomite, corresponded to crushing; the cavities were shallow but wide; erosion debris were large and irregular. This is illustrated in Figure 7.7b for a hardened cement paste. Both modes correspond to those shown in Figure 2.13 for continuous water jet erosion, and

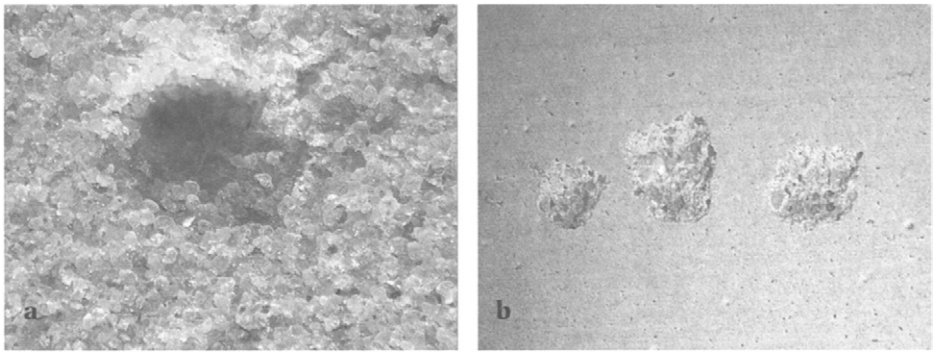

Figure 7.7 Modes of material response (Momber, 2004b)
a – Type-I: fine-grained sandstone b – Type-II: hardened cement paste

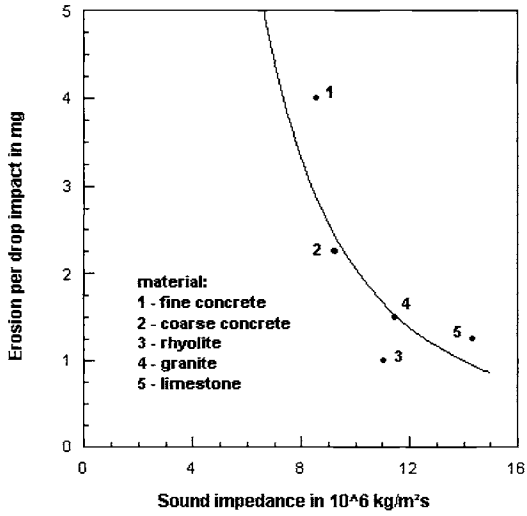

Figure 7.8 Effect of target material sound impedance on mass removal (unpublished results of the author)

they are balanced mainly by exposure time and material structure. Type-I-mode dominates at long exposure time (large drop diameter) and in soft porous materials, whereas type-II-mode is typically found at shorter exposure time (smaller drops) and in rather brittle and dense rocks.

Drop impact is a highly dynamic process and, therefore, acoustic properties can be assumed to be important. Some results are shown in Figure 7.8, illustrating that sound impedance:

$$s_M = c_M \cdot \rho_M \tag{7.12}$$

is a good indication for erosion resistance: materials with a low sound impedance have a lower resistance against drop impact erosion. Fracture parameters do also

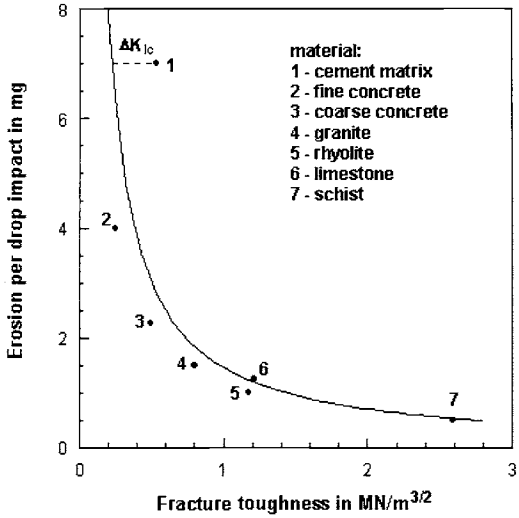

Figure 7.9 Effect of fracture toughness on mass removal (unpublished results of the author)

affect the erosion resistance. The results of the fracture toughness influence are plotted in Figure 7.9 showing a hyperbolic relationship:

$$m_M \propto K_{Ic}^{-m} \tag{7.13}$$

For the conditions in Figure 7.9, m=1.42. An interesting detail is that the experimental point for the hardened cement matrix is located in a notable distance above the regression curve. Compared to the other materials, hardened cement paste can be considered as very brittle. It cannot absorb energy by non-linear fracture processes, and fails in a brittle fashion as shown in Figure 7.7b. This aspect was also observed during other erosion modes (Momber and Kovacevic, 1994). The coarse concrete in Figure 7.9 with a comparative (even lower) fracture toughness shows a higher erosion resistance which may be mainly due to crack-aggregate interactions. Examples for such interactions as well as a preliminary explanation for the exceptional behaviour of the cement paste are presented by Momber (2004e). However, more systematic studies are required to verify this hypothesis.

7.1.4 Multiple drop impingement

The number of impinging water drops is critical to the material removal process. The situation can be generalised by the relationship shown in Figure 7.10. This function can sufficiently be described by:

$$V_M = a_1 \cdot (N_D - N_D^*)^{b_1} \tag{7.14}$$

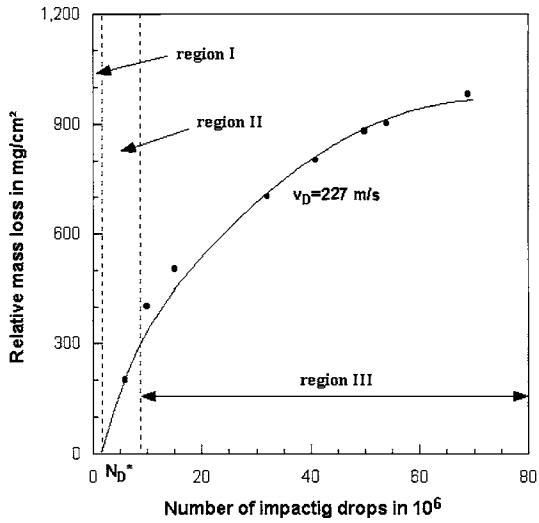

Figure 7.10 Effect on drop number on mass loss (measurements: Baker et al., 1966)

The following three regions can be distinguished in Figure 7.10:

(i) region I ($N_D<N^*_D$): for very small numbers of impinging drops, no material removal occurs; the number of drops is not sufficient to visibly damage the material. The critical drop number N^*_D can be considered to be an incubation number.

(ii) region II ($N_D<N^*_D$, $b_1=1$): a linear relationship with a progress of a_1 exists between drop number and removed material. Any additional drop impact removes an equivalent mass of material.

(iii) region III ($N_D<N^*_D$, $0<b_1<1$): the progress of the function drops, and $a_1=f(N_D)$. The erosion efficiency declines which can be explained by drop break-up due to the roughened surface; also, the impact is no longer normal to the whole of the surface.

7.2 Material loading due to cavitation

7.2.1 Fundamentals of cavitation

Cavitation can be observed during the impact of liquids to solid and liquid surfaces. One example is illustrated in Figure 7.1 where Image 2 shows cavitation occurring in the contact area between drop and target (denoted 'B'). This aspect is in more detail described by Engel (1954). Cavitation erosion may, therefore, play a role during hydrodemolition processes. Cavitation is the growth and implosion of gas-filled bubbles in a liquid. Basically, flow cavitation and acoustically induced cavitation can be distinguished, whereas the first type is more common in practice.

Detailed descriptions of cavitation phenomena are provided in the standard literature (Hammitt, 1980, Brennen, 2000, Lecoffre, 1999). Cavitation can damage and erode materials by the following mechanisms:

(i) generation of shock waves due to symmetric bubble implosion;
(ii) formation of micro-jets due to non-symmetric bubble implosion in the neighbourhood of solid surfaces (Lauterborn and Bolle, 1975, Pilipp and Lauterborn, 1998); see Figure 7.11a;
(iii) formation of micro-jets due to shock-induced bubble collapse (Bourne and Field, 1992);
(iv) collapse of bubble clusters (Dear and Field, 1988); see Figure 7.11b.

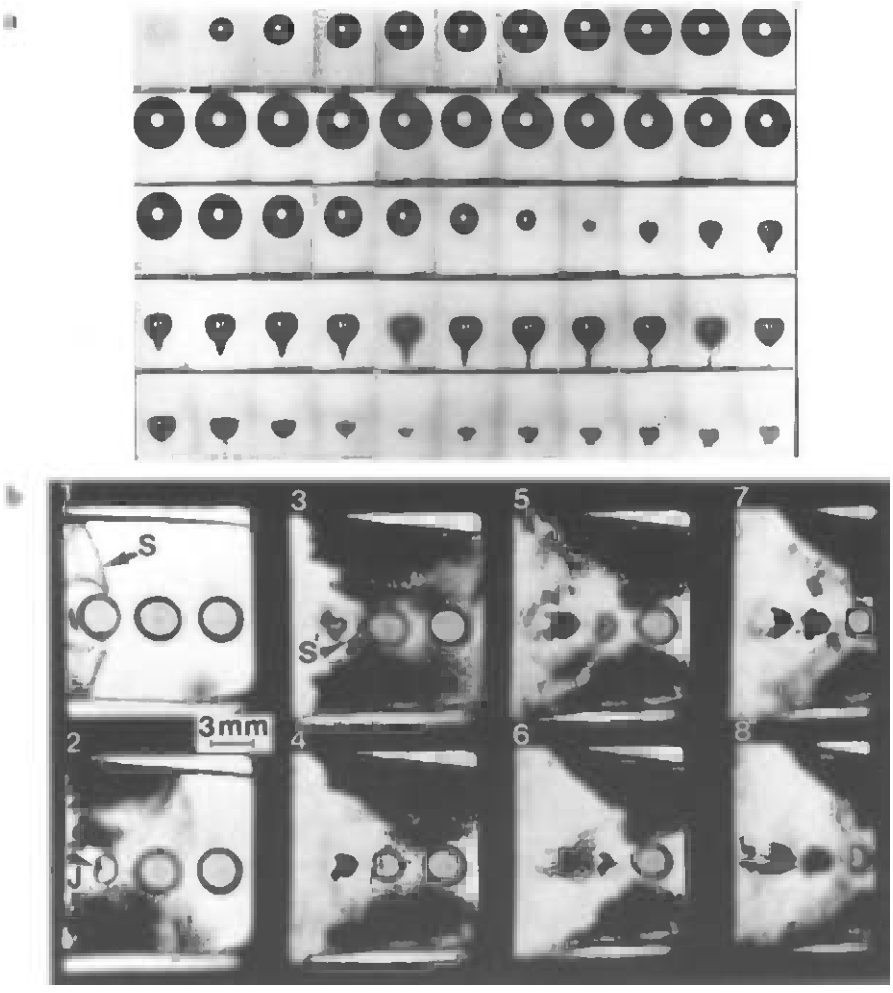

Figure 7.11 Types of loading from cavitation bubble implosion
a – Micro-jet formation during non-symmetric bubble implosion (photograph: Lauterborn, Univ. Göttingen)
b – Shock wave emission (photograph: Fracture Group, Cavendish Laboratory, Cambridge University)

However, a superposition of several individual mechanisms is very likely, and if either mechanism (i) or mechanism (ii) is dominating depends mainly on the distance between bubble wall and solid surface. The pressure generated during the implosion and collapse of cavitation bubbles is typically in the range of several 10^2 MPa. Of particular interest is the formation of micro-jets (ii) which is illustrated in Figure 7.11a. The diameter of a micro-jet formed during the implosion of a gas-filled bubble can be approximated as follows (Plesset and Chapman, 1971):

$$d_J \cong 0.1 \cdot R_O \tag{7.15}$$

where R_0 is the radius of the bubble before the collapse. Assuming a cylindrical geometry of the micro-jet, the duration of the stress pulse can be estimated with Eq. (7.3b). The stress generated at the surface of a rigid material impinged by a micro-jet can be calculated with Eq. (7.1). The velocity of the micro-jet depends on the implosion situation. For shock-induced micro-jet formation during the collapse of 3-mm-bubbles, jet speeds up to 4000 m/s were estimated (Bourne and Field, 1992). Collapse of laser-produced bubbles generated jet velocities of about 150 m/s (Philipp and Lauterborn, 1998). Dear and Field (1988) measured jet velocities of about 400 m/s during the collapse of arrays of cavities. Conn (1972) provided an analysis of the collapse pressure of vapor bubbles cavitating in the region where a liquid jet impacts a material surface. This pressure is given by:

$$p_J = \frac{p_S}{6.35} \cdot \exp(2/3 \cdot \alpha_G) \tag{7.16}$$

The equation illustrates how the gas content in the jet affects the collapse pressure. A graphical solution to Eq. (7.16) for different gas content is provided in Figure 7.12 (the stagnation pressure is replaced by the jet velocity). This graph shows also

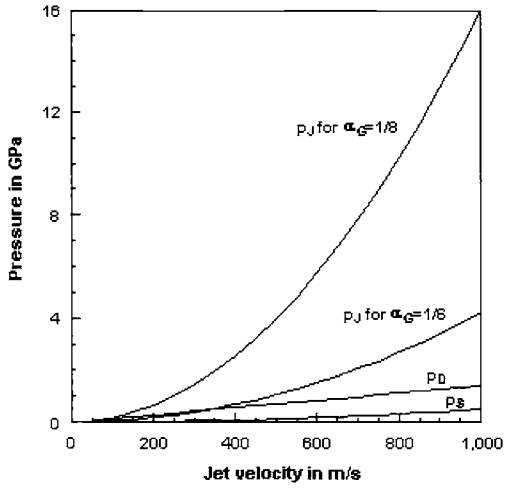

Figure 7.12 Collapse pressures in cavitating water jets

that collapse pressures exceed even the impact pressure developed during the impact of a fluid slug by an order of magnitude. A pressure ratio, R_P^*, can be defined to evaluate the effectiveness of cavitating water jets:

$$R_P^* = \frac{p_J}{p_D} = \frac{v_J}{12.7 \cdot c_F} \cdot \exp(1/\alpha_G) \tag{7.17}$$

Values for the pressure ratio can be as high as $R_P^*=16$ as shown in Figure 7.12. However, exact values depend on gas content and bubble size (Houlston and Vickers, 1978).

7.2.2 Material response to cavitation

The response of relevant materials to cavitation erosion is illustrated in Figure 7.13. The individual pits eroded in the material are usually one order of magnitude larger than the corresponding diameter of the micro-jets formed during bubble implosion. A simple calculation of an expected crack length in rocks showed that the crack length measured in rock and concrete after cavitation erosion is two orders of magnitude smaller than the pit diameter (Momber, 2003a). Therefore, multiplying mechanisms are required to form the pits. In materials with pronounced interfaces between inclusions and matrix, such as concrete, intergranular material removal along the interfaces can be observed in general. Intergranular erosion occurs always if concrete contains rounded aggregate particles; cement matrix is removed, and the aggregates are exposed completely. An example is shown in Figure 7.14. This mechanism can be utilised for selective aggregate liberation from concrete (Momber, 2004d). If concrete aggregate material is considered, mineral content and composition are important parameters. In granite, for example, feldspar is broken into very small pieces, whereas platelets of mica are separated and broken away by basal cleavage (Momber, 2003a).

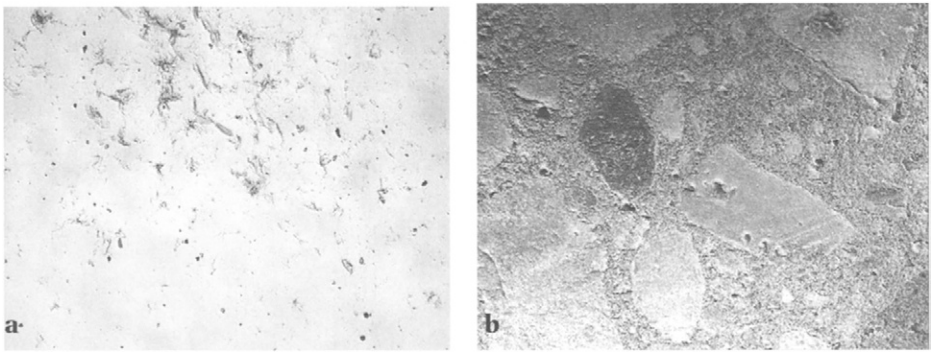

Figure 7.13 Pit formation due to micro-jet impingement (Momber, 2003a)
a – glass b – concrete

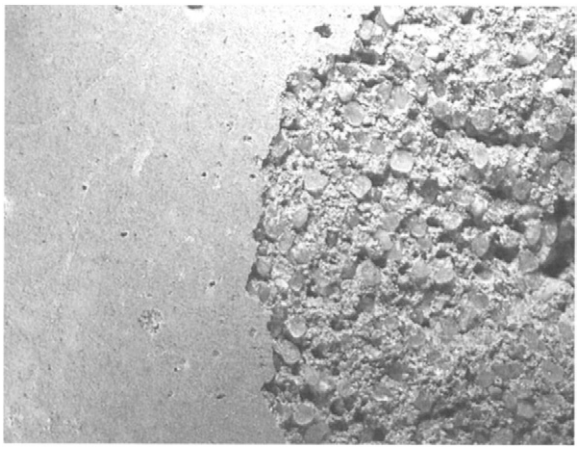

Figure 7.14 Intergranular cavitation erosion of concrete (Momber, 2004d)

7.2.3 Parameter effects and resistance parameters

The most important parameter in cavitation erosion is the exposure time. Microscopic inspections and quantitative surface profiling showed that threshold exposure times were shorter than 30 seconds for numerous rocks, and shorter than 10 seconds for concrete (Momber 2000, 2003a). Figure 7.15 shows a profile plot (3-axis co-ordinate measurement machine) taken from an eroded concrete surface; a notable surface modification can be seen in the right section at an exposure time as low as 5 seconds. Compressive strength and density alone can not determine cavitation erosion resistance of concrete materials and rocks quantitatively. Density influence is illustrated in Figure 7.16, and it can be seen from this figure that

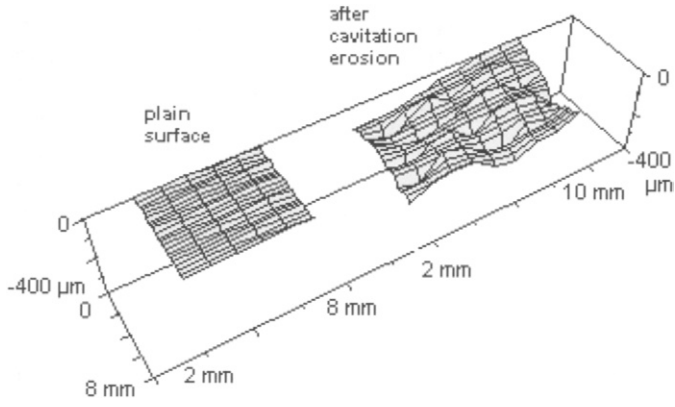

Figure 7.15 Surface plot of a eroded concrete surface; exposure time: 5 seconds (Momber, 2000g)

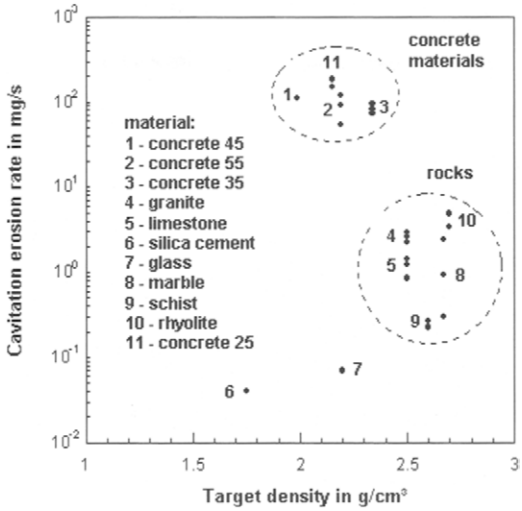

Figure 7.16 Effect of target material density on cavitation erosion (Momber, 2003a)

materials with a low degree of pre-existing flaws, namely high-strength silica mortar and glass, are extremely resistant. This type of relationship was also observed by Lin et al. (1997) and Preece and Hansson (1986). Erosion rates for cementitious composites are notably higher than those for rocks due to the pronounced interfaces formed during aggregate addition.

A preliminary model for the cavitation erosion of rocks and concrete materials delivers the following relationship (Momber, 2003a):

$$m_M \propto \frac{d_M \cdot E_M \cdot \rho_M}{K_{Ic}^m} \tag{7.18}$$

The reverse exponential relationship between erosion rate and fracture toughness is verified in Figure 7.17. The exponent m may depend on the R-curve behaviour of the materials. For materials with a nearly constant fracture toughness (such as brittle ceramics), values of m=1.8 were estimated (Waldherr, 1991), which corresponded to linear elastic fracture behaviour (m=2). For materials with pronounced R-curve behaviour (rocks, concrete, toughened ceramics), however, the exponent is rather high (m=3.4 from Figure 7.17). It can, therefore, be assumed that m is a function of the R-curve behaviour of the materials. The following relationship between m and Φ is assumed (Momber, 2003a, 2004a):

$$m = f(\Phi) = 2 \cdot \Phi^{1/2} + 2 \tag{7.19}$$

For linear-elastic materials with Φ=0, Eq. (7.19) delivers m=2. For materials with pronounced R-curve behaviour with Φ=0.3 to 0.5, Eq. (7.19) delivers m=3.1 to 3.4 which corresponds to Figure 7.17. The influence of the grain size is correctly

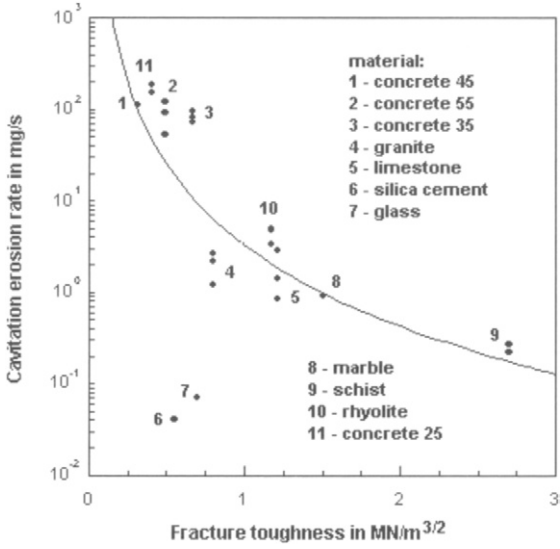

Figure 7.17 Effect of fracture toughness on cavitation erosion (Momber, 2003a)

derived in Eq. (7.18): if other parameters are of comparative order, erosion resistance decreases with grain size. The influence of the density is already mentioned. For materials with comparative fracture toughness (in Figure 7.17: silica mortar and concrete 55; glass and concrete 35) the material with the higher bulk density (lower flaw density) is more resistant.

7.3 Types and formation of pulsed jets

7.3.1 Types of pulsed jets

It has been shown in the previous Section that any impinging water jet exhibits two pressure levels: an impact pressure in the very early stage of jet impact (p_D), and a stagnation pressure (p_{ST}) that is established after the impact period. The impact pressure is given through Eq. (7.1), the stagnation pressure can be estimated based on Bernoulli's law:

$$p_S = (\rho_W / 2) \cdot v_J^2 \tag{7.20}$$

The ratio between these pressure levels depends on the jet velocity and can be estimated from $p_S = p_D$ as follows:

$$R_P = \frac{p_D}{p_S} = \frac{2 \cdot c_F}{v_J} \tag{7.21}$$

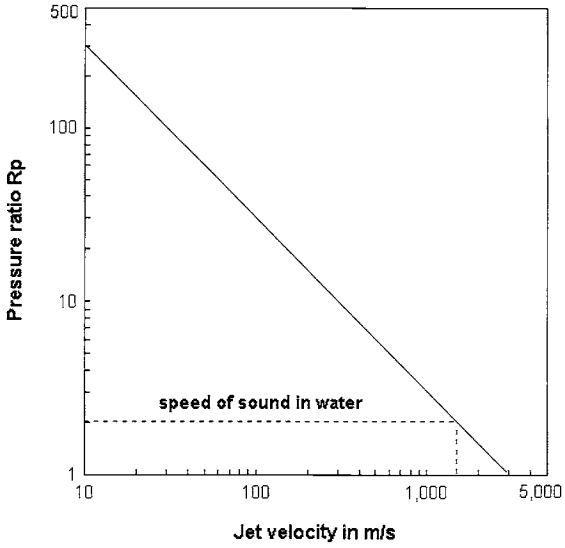

Figure 7.18 Pressure ratio during jet impact

This relationship is illustrated in Figure 7.18 in terms of jet/drop velocity. The pressure ratio equals the value $R_P=1$ for $v_J=2\cdot c_F$. The corresponding operation pressure would be $p\cong 4\cdot 10^3$ MPa. This high value can not be realised by commercial plunger pumps or pressure intensifiers. For a rather low pressure, say 30 MPa, the pressure ratio is about $R_P=11$. This relationship challenges the use of mechanisms able to produce high-speed fluid slugs. Basically, the following two types of pulsed water jets can be distinguished (see Figure 7.19):

- low-frequency water jets;
- high-frequency water jets ($f_P>1$ kHz).

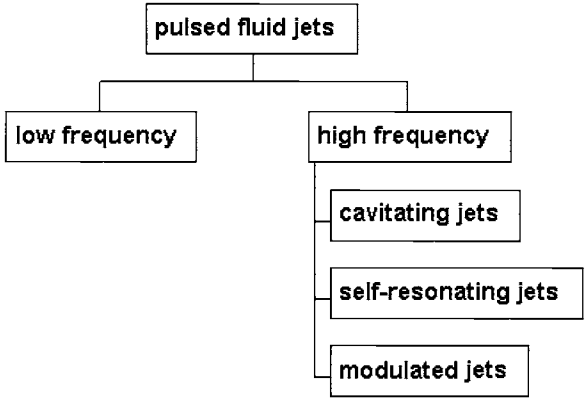

Figure 7.19 Subdivision of pulsating jets

Both techniques involve the modulation of continuous high-speed water jets. The difference to 'naturally pulsed jets' (formed due to aero-dynamic drag, see Figure 2.4) is that the jets are artificially interrupted. Pulsed jets can be produced in several ways using different driving energy sources.

Only a few technical solutions, although much more were successfully applied under laboratory conditions, can currently be used under site conditions; they include the following:

- water cannons;
- ultrasonically modulated jets;
- self-resonating jets;
- pressure and volume modulation;
- cavitating jets.

The two most important parameters of pulsed liquid jets are loading intensity and loading frequency. For some pulsed liquid jet concepts, water jet velocity and pulse frequency can not be varied independently on each other. Both parameters must be selected according to the material to be eroded. Materials usually called ductile may require high-frequency loading, whereas materials usually considered brittle may be more sensitive to a longer loading period. Loading intensity is basically a function of jet velocity. Frequency, however, depends on the mechanism used to form the pulsating jet. The formation of stable, geometrically identical water slugs is a demanding challenge. Figure 7.27 shows two examples of pulsating jets formed during volume modulation in a special nozzle. Whereas the slugs look rather regular in Figure 7.27a, their structure is heavily disturbed in Figure 7.27b (although the same nozzle was utilised in both cases).

7.3.2 Water cannons and impulse cannons

Water cannons have first been utilised as rock fragmentation tools in the mining and quarrying industry. The fundamental principle of water cannons is the rapid acceleration of a given water volume, which is an energy or momentum exchange process. The energy required to accelerate the liquid can be supplied from expanding gases or compressed air. Three basic water cannon designs are known:

- free piston devices;
- pressure extrusion devices;
- hydraulic pulse generators.

Typical performance parameters of these methods are listed in Table 7.2. In free piston devices, a piston is rapidly accelerated by using an external momentum, provided by explosives, bullets, or compressed gases. The nozzle geometry is of primary importance because it determines jet exit velocity and energy, and pulse duration. Information about structure and aerodynamics of jets generated by this method can be found by Pianthong et al. (2002) and Shi and Sato (2003).

Numerous nozzle designs are reported, among them exponential, hyperbolic and parabolic shapes. Maurer (1980) and Summers (1993) provide further information. The design of a free piston water cannon is shown in Figure 7.20a, whereas Figure 7.21 illustrates water slugs produced with the this device. Pressure extrusion devices are essentially snap acting intensifiers which produce a pulsed jet by using compressed air (or other gas) to drive a piston to extrude the liquid through a nozzle. A typical design is illustrated in Figure 7.20b. In hydraulic pulse generators, the energy required to produce the pulse is stored in the liquid itself by compressing it in a vessel to high pressures. Release of a fast acting valve results in the formation of a high-speed slug of water with high energy content. A technical configuration is shown in Figure 7.20c. Pressure history of a hydraulic pulse generator utilised for concrete fragmentation is plotted in Figure 7.22. Pressures as high as 450 MPa can be generated in a time scale of about 0.01 seconds. Parameter studies performed by Vallve et al. (1980) and Yie et al. (1978) clarified the effect of certain design parameters on the fragmentation of concrete: depth of cut increases if liquid volume, water chamber pressure, and nozzle diameter increase. Increase in stand-off distance, however, reduces depth of cut.

Table 7.2 Comparison between culmination and extrusion cannons (DaZong et al., 1985; Puchala and Vijay, 1984; Labus, 1991)

Parameter	Method	
	Culmination	Extrusion
Maximum pressure	high (up to 4,000 MPa)	moderate (ca. 1,200 MPa)
Pressure limit	due to impulse energy	due to material strength
Geometric efficiency	7% of chamber volume	90 to 95% of chamber volume
Pulse duration	short	long (100 to 300 μs)
Efficiency	up to 56%	> 56%
Segment diameter	large	small
Segment length / diameter	low (<1,000)	high (1,000–5,000)
Pulse characteristics	steep	flat

7.3.3 Ultrasonically modulated water jets

Ultrasonic waves generated within a nozzle can be employed to modulate a continuous stream of water to produce either pulsed or cavitating jets (see Vijay et al., 1993; Sitek et al., 2003). The structure of a water jet modulated by this technique is illustrated in Figure 7.23. The vibrations required to modulate the jet are produced by an ultrasonic system consisting of a pulsed electric power supply, a converter, and a horn with replaceable velocity transformers. An on-site device basically consists of a pump, an ultrasonic power generator with a converter, a high-pressure dump gun, a high-pressure hose and numerous accessories. The pump delivers a volumetric flow rate of 22.7 l/min at a maximum operating pressure of 41.4 MPa. The ultrasonic power generator has a capacity of 1.5 kW of output at a resonant frequency of f_p=20 kHz.

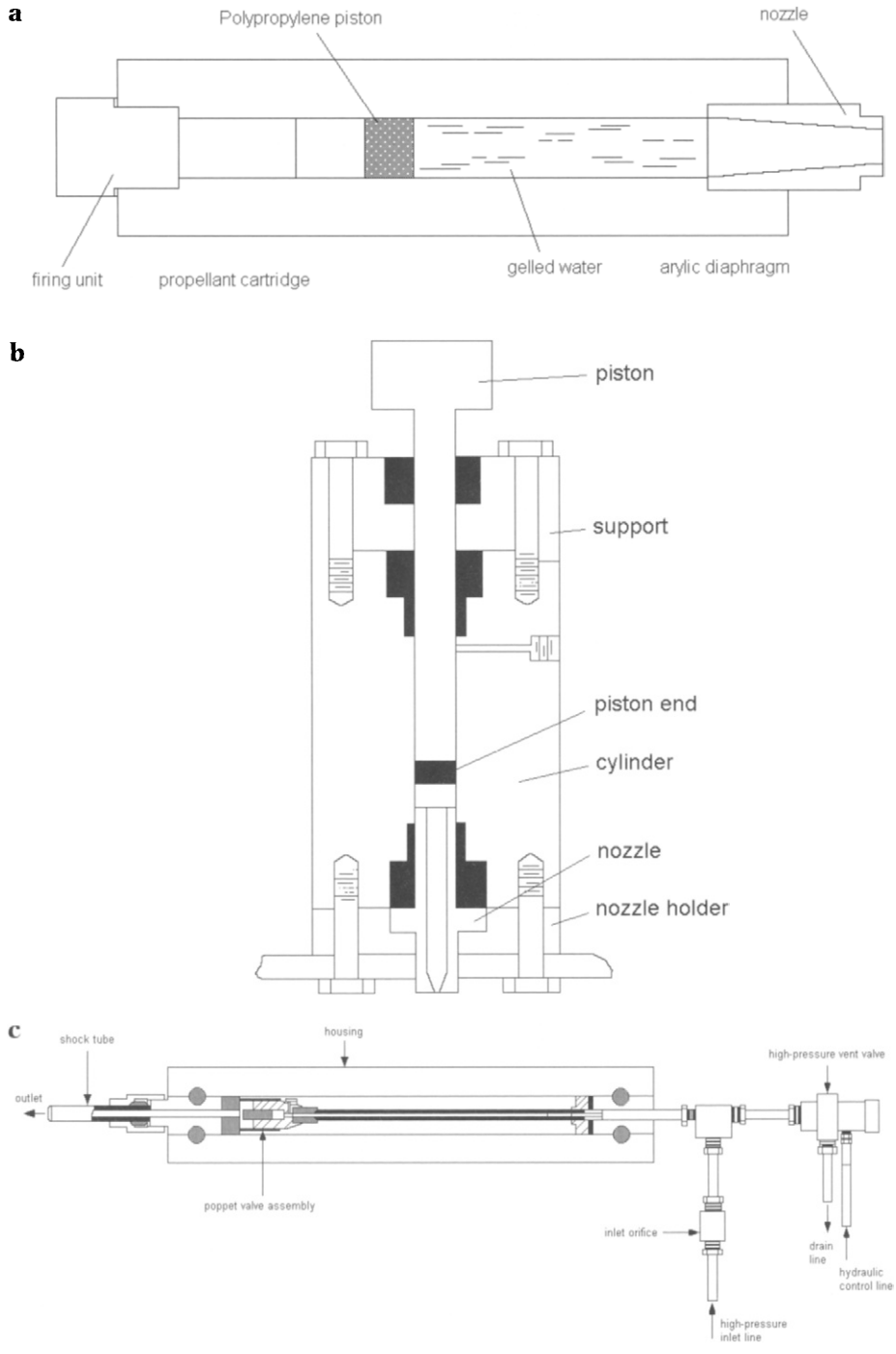

Figure 7.20 Types of water cannons
a – Free-piston device (Watson et al., 1984) b – Pressure extrusion device (Gnirk and Grams, 1972)
c – Hydraulic pulse device (Kolle, 1994)

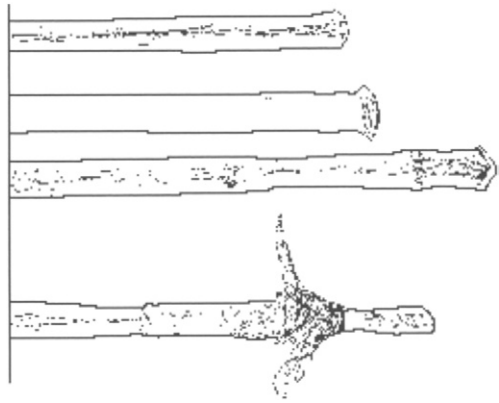

Figure 7.21 Flash-X-ray radiographs of water slugs formed in a free-piston device (Watson et al., 1984)

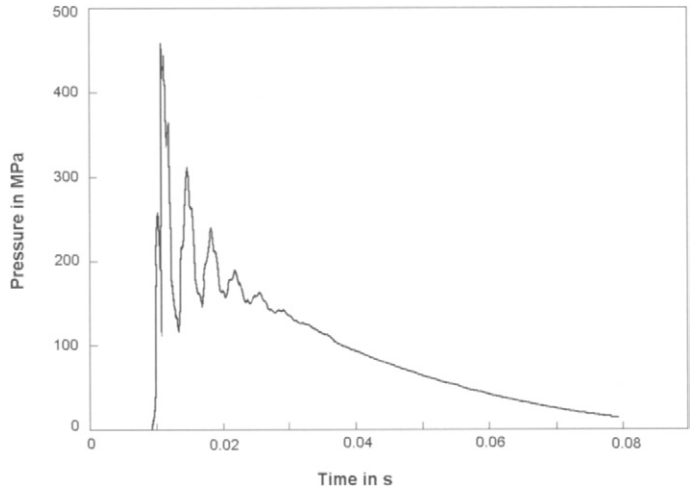

Figure 7.22 Pressure history of a hydraulic pulse device for concrete fragmentation (Kolle and Hashish, 1989

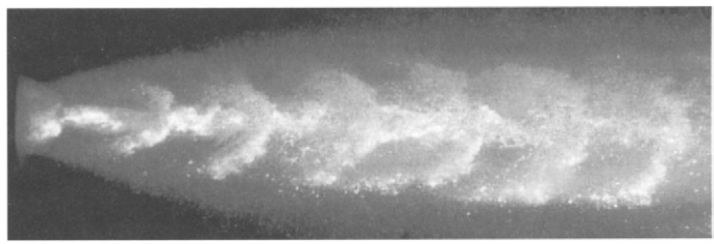

Figure 7.23 Structure of an ultrasonically modulated water jet (photograph: VLN Advanced Technologies Inc.)

7.3.4 Self-resonating water jets

Self-resonating pulsating jets (sometimes referred to as passively modulated jets) are formed by letting a water volume flow through a specially designed nozzle; acoustic resonance effects force the vibration and disintegration of the jet. A boundary shear layer is exited to separate from the nozzle wall, and forms vortex rings. This principle was first noted with air jets (Crow and Champagne, 1971). Several self-resonating nozzle system concepts can be distinguished; see Figure 7.24 for an example. They are in detail described in the original literature (Chahine et al., 1985; Johnson et al., 1984). A non-dimensional parameter which defines the periodic characteristic of self-resonating jets is the Strouhal number, given through:

$$S_d = \frac{f_p \cdot d_J}{v_J} \tag{7.22}$$

This number combines acoustic and aerodynamic parameters. It is known that optimum performance of pulsating water jets occurs for Strouhal numbers between 0.3 and 1.2. However, mechanically interrupted jets usually operate at frequencies which produce Strouhal numbers well below the optimum range. Acoustically resonated jets, however, meet the requirements of optimum Strouhal numbers. The discontinuous appearance of a resonating water jet is illustrated in Figure 7.25. Structural elements of self-resonating water jets, formed in different nozzles, are shown in Figure 7.26.

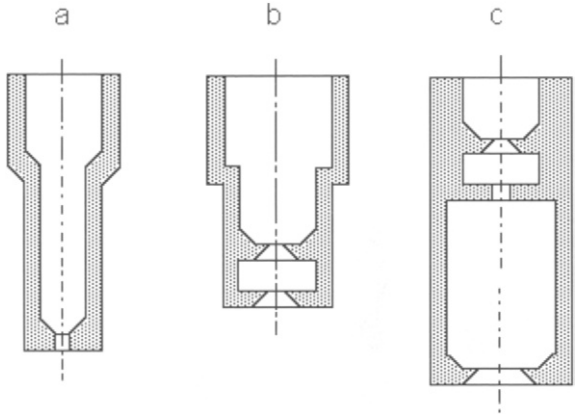

Figure 7.24 Nozzle designs for forming self-resonating jets by acoustic enhancement (Johnson et al., 1984)
a – organ pipe design b – pulser design c – pulser fed design

7.3.5 Percussive water jets

'Percussive jet' is rather a commercial designation and does not tell anything about the basic mechanism of jet formation. A percussive jet consists of a series of large

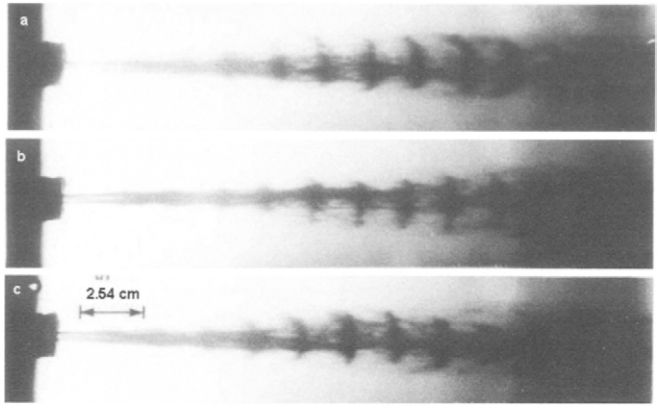

Figure 7.25 Appearance of self-resonating water jets; f_P=4.6 kHz (photograph: Dynaflow®, Inc., Jessup)
a – v_j=94.5 m/s; b – v_j=89.9 m/s; c – v_j=83.8 m/s

Figure 7.26 Structural elements of self-resonating water jets (photographs: Dynaflow®, Inc., Jessup)
a – swirling jet
b – vortex rings

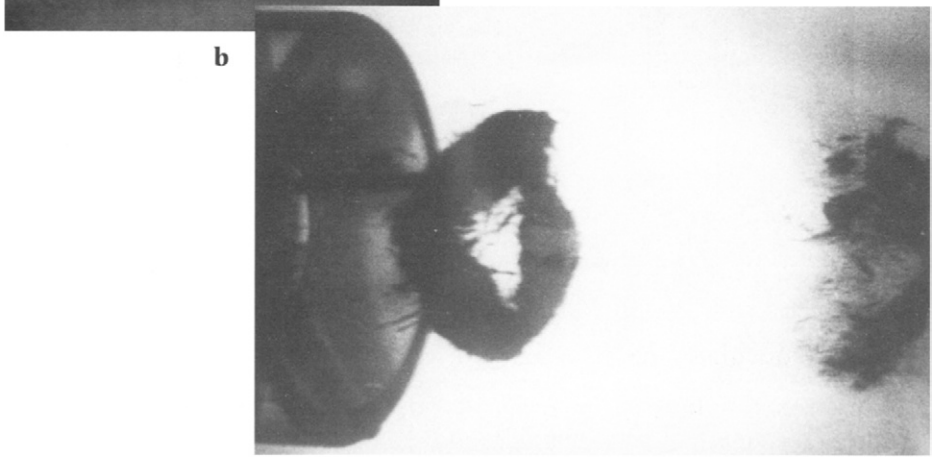

pulses (up to ten times the nozzle diameter) which are obtained by modulating a continuous flow rate of water through the jet discharge nozzle, e.g., by cycling the rate of discharge over and under its average value with some regular amplitude, frequency, and waveform. Modulated jet discharge has the particular property that the slow and fast portions of each discharge cycle tend to flow together or bunch in the free stream. This property is shown in Figure 7.27. Experimental percussive jets were produced at pump pressures up to 57 MPa, nozzle diameter of 1.5 mm, and modulation frequencies between 2 to 5 kHz (Nebeker and Rodriguez, 1976).

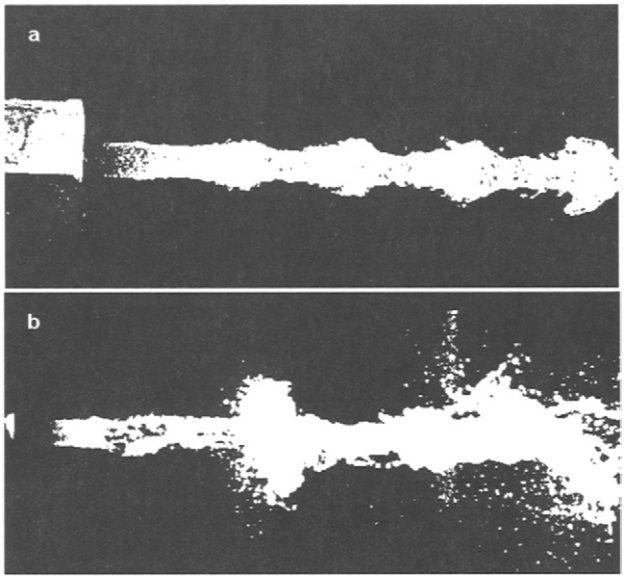

Figure 7.27 Structure of 'percussive jets' (Nebeker, 1984)
a – good-quality jet b – bad-quality jet

Figure 7.28 illustrates another case. Here, the slugs were produced by an ultrasonic horn that vibrated the nozzle in axial direction. Again, the slow (decelerated) and fast (accelerated) portions of the jet tend to meet at a certain distance and bunch. The different appearance of the individual slugs can clearly be seen.

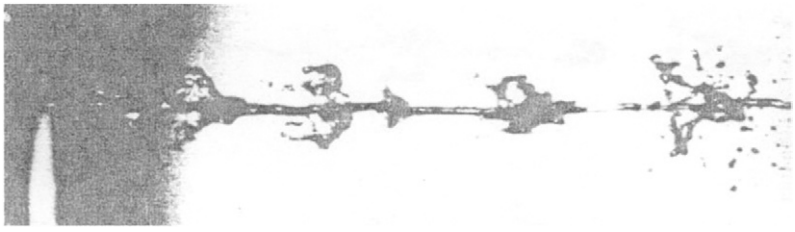

Figure 7.28 Structure of a water jet modulated by ultrasonically induced axial nozzle vibrations (Mazurkiewicz, 1984). Operating pressure: 0.4 MPa

7.3.6 Cavitating water jets

Techniques for producing cavities in liquid jets are shown in Figure 7.29. The first system (Figure 7.29a) uses turning vanes to impart a swirling action to the fluid entering the nozzle, while the second system (Figure 7.29b) uses a cylindrical center body in the nozzle to produce cavitation. Electro-discharge technique is also known to generate cavitation bubbles based on plasma channel formation (Hawrylewicz et al., 1986).

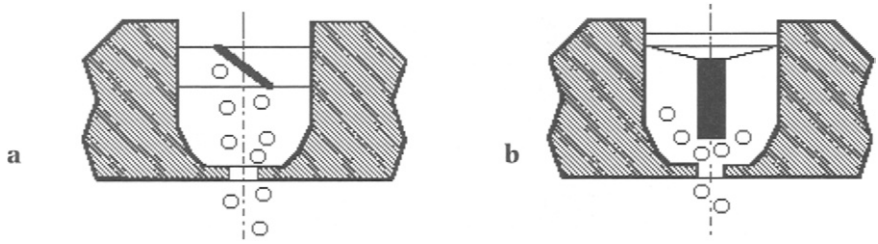

Figure 7.29 Cavitating nozzle designs (Johnson et al., 1972)
a – rotating vane b – center body

7.4 Practical applications

Cavitating water jets are applied to concrete drilling. Figure 7.30 shows some results. Of particular interest is the difference in the drilling rates between conventional jets and cavitating jets. Whereas the specific energy of a cavitating jet is raised up to 160%, its drilling capability increases up to 280%. Cavitating jets are also utilised to

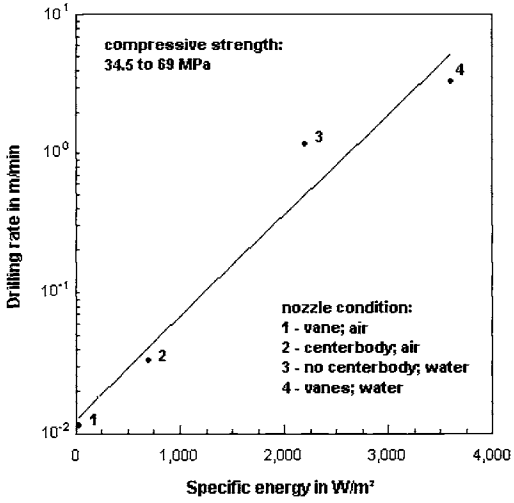

Figure 7.30 Results of concrete drilling with cavitating water jets (Anonymus, 1972)

city street pavements cut open, to allow repairs or maintenance of either the pavement or one of the many services buried below (Conn et al., 1987). The unit performed at an operating pressure of 69 MPa, and it achieved cutting rates between 20 and 23 cm /min in pavement consisting of 5 cm of asphalt over 15 cm concrete. A piece cut off by this method is shown in Figure 7.31. Operating conditions and parameters are listed in Table 7.3. Cutting costs – if compared to mechanical methods – were about one-half with the cavitation method; this is illustrated in Table 7.4. Cavitating jets were also used for the secondary fragmentation of reinforced concrete members from demolition sites, and for the separation of reinforcement bars. Examples are shown in Figure 7.32. The process parameters are listed in Table 7.5. Members with a thickness of 30 cm could be cut through entirely in 48 seconds. In those cases, costs could be reduced down to 50% compared to conventional methods (Conn et al., 1984).

Figure 7.31 Pavement element cut with cavitating water jets (photograph: Dynaflow, Inc., Jessup)

Table 7.3 Summary of Cavijet pavement cutting results Conn et al. (1987)

Parameter	Value
Pavement thickness	
– Asphalt	5.1 cm
– Concrete	15.2 cm
Cut diameter	56 cm
Nozzle diameter	3.6 mm
Pump pressure	69 MPa
Volumetric flow rate	114 l/min
Stand-off distance	15.2 mm
Traverse rate	23 cm/s
Impingement angle	90°
Time to initial cut-through	6 min
Total cutting time	8 min
Cutting rate	22 cm/min

Table 7.4 Cost comparison of pavement cutting techniques (Conn et al., 1987)

Method	Operating pressure	Relative costs (%)
Mechanical tools		190 to 300
Abrasive water jets	241 MPa	188
Cavitating jet	69 MPa	100

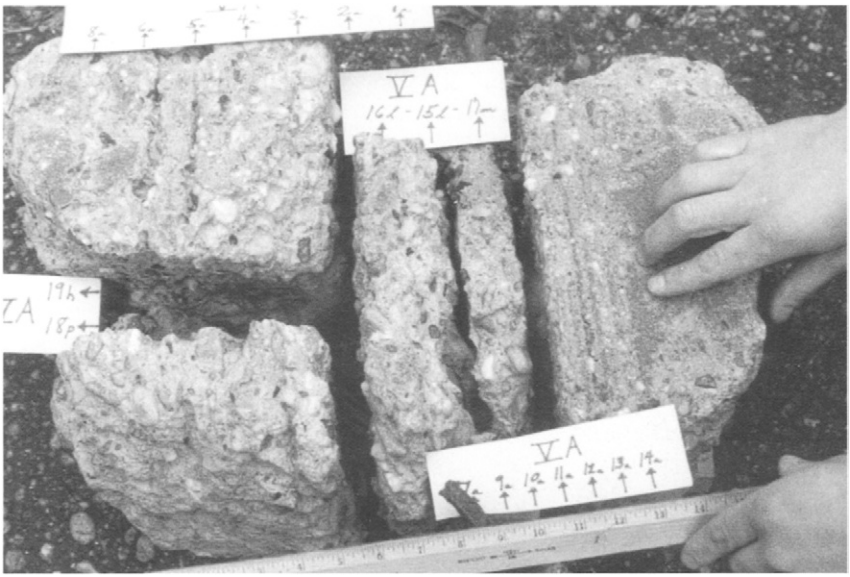

Figure 7.32 37-years old reinforced concrete samples, cut with cavitating water jets (photograph: Dynaflow, Inc., Jessup)

Table 7.5 Parameters for cutting reinforced concrete with cavitating water jets (Conn et al., 1987)

Parameter	Value
Operating pressure	69 MPa
Nozzle diameter	2.7 mm
Nozzle type	Center body
Traverse rate	20 cm/s
Volumetric flow rate	72 l/min
Pump power	79 kW

Self-resonating jets were successfully applied to erode fibre reinforced cement samples in the laboratory stage (Kalumuck et al., 1999). Results are shown in Figure 7.33, and the superiority of discontinuous jets is obvious. At larger stand-off distances, the larger footprint of the self-resonating jets, due to the generation of discrete water slugs, resulted in a volume removal three to five times that of the conventional jets. Promising experience is collected with self-resonating jets during the removal of asbestos with operating pressures up to 69 MPa; the efficiency

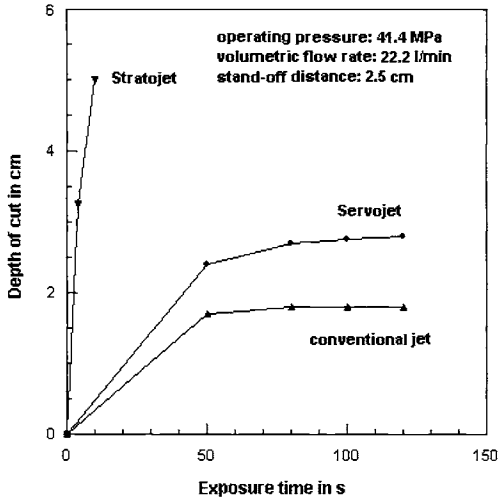

Figure 7.33 Cutting of fibre-reinforced cement samples with self-resonating water jets (Kalumuk et al., 1999)

reported is between 23 and 28 m^2/h (Conn, 1989). Problems of handling, safety and training in relation with the on-site use of self-resonating water jets are discussed by Conn (1991).

Ultrasonically modulated jets and conventional water jets were applied to concrete cutting under laboratory conditions by Sitek et al. (2003), and under site conditions by Yan et al. (2004). Both types of jets formed rather irregular slots. Material was always removed by breaking cement matrix from the interface to the aggregates. However, kerfs formed with modulated jets were more regular, especially at higher traverse rates. In all cases, average depth of cut obtained with modulated jets was about 1.5 times that of conventional jet cutting (see Figure 7.34). The operational conditions are listed in Table 7.6. First experience collected under site conditions show an efficiency of about 11 m^2/h for concrete cleaning, and about 0.14 m^3/h for volumetric concrete removal (Yan et al., 2004). As shown in Table 7.7, ultrasonically modulated jets, although operating at much lower pump pressure, perform more energy efficient than conventional water jets.

Percussive jets and conventional water jets were applied to fragment concrete samples by Nebeker (1984). Whereas conventional jets could not damage aggregate grains and removed the matrix only, percussive jets were able to simultaneously cut aggregate and cement matrix. It was shown that a percussive jet with an operating pressure of 14 MPa could generate cracks in a concrete block, which was located 18 meters away from the nozzle.

The operation of a hydraulic pulse water cannon is shown in Figure 7.35. In that test, a water cannon pulse with an pulse energy of 100 kJ was discharged into a 39 mm bore hole to fragment a 1 tonne basalt boulder. Atanov (1991) reported about the use of a gas-driven impulse cannon to demolish a reinforced concrete wall with a thickness of 600 mm, and to destroy a concrete diversion cut of a

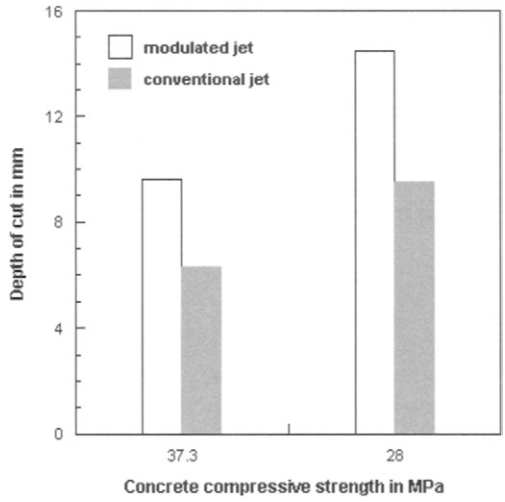

Figure 7.34 Concrete cutting with conventional and ultrasonically modulated water jets (Sitek et al., 2003)

Table 7.6 Parameters for concrete cutting with ultrasonically modulated water jets (Sitek et al., 2003)

Parameter	Value
Pressure in MPa	40
Nozzle diameter in mm	1.98
Stand-off distance in mm	20–140
Traverse rate in m/min	5.0
Ultrasonic power in W	600

Table 7.7 Comparison of concrete removal with regular and pulsed water jets (Yan et al., 2004)

Parameter	Pulsed water jet	Regular water jet
Volumetric removal rate in m^3/h	0.14	0.50
Pump pressure in MPa	69	138
Volumetric water flow rate in l/min	32.6	197
Hydraulic power in kW	37.3	452
Specific energy in kWh/m^3	266	904

power station. Results of these applications are illustrated in Figure 7.36. The unit was loaded 100,000 times without any severe interruptions. Table 7.8 lists the corresponding performance parameters. Figure 7.37 shows further examples for concrete members of 20 cm in thickness fractured by single water pulse impacts.

A very special development is the use of short-term water pulses for directed soft splitting of plain and reinforced concrete. This method is illustrated in Figure 7.38 – it consists of the following steps:

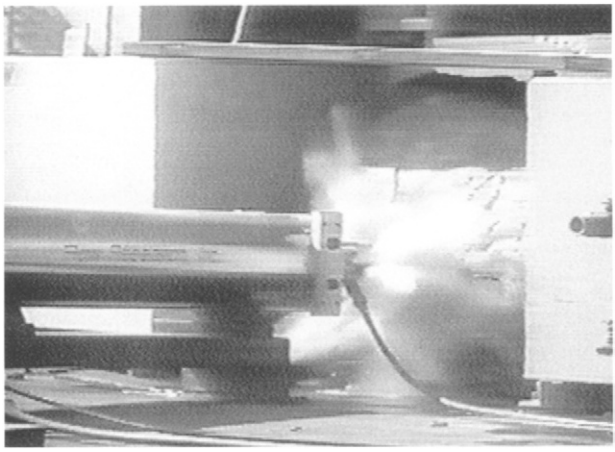

Figure 7.35 Fragmentation of a basalt boulder with a hydraulic pulse water cannon (Kolle, 1998); pulse energy: 100 kJ

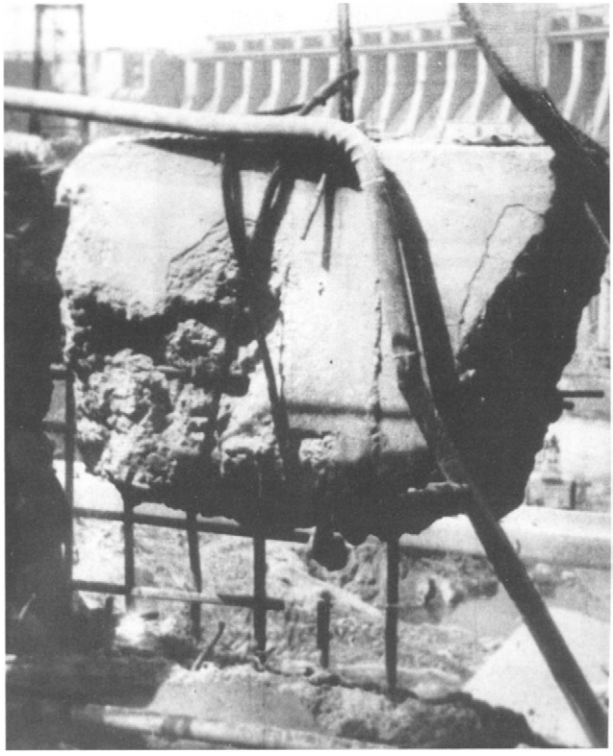

Figure 7.36 Demolition of a steel-reinforced concrete wall with an impulse cannon (Atanov, 1998)

Table 7.8 Concrete demolition with a gas-driven water cannon (Atanov, 1991); see Figure 7.36

Parameter	Value
Total unit mass	20,000 kg
Cannon mass	2,600 kg
Gas pressure	4 MPa
Water pressure	450 MPa
Nozzle diameter	10.5 mm
Water mass flow rate	2 to 3 m^3/h
Frequency	12 shots per min
Power	160 kW
Efficiency	
– Concrete wall	1.5 m^3/h
– Diversion cut	0.5 to 0.6 m^3/h

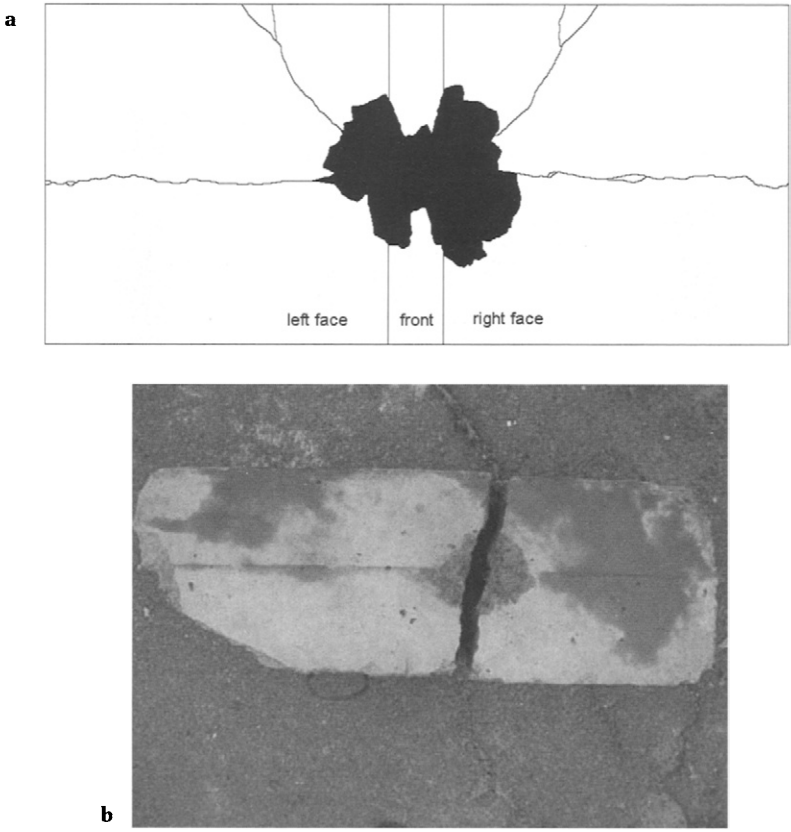

Figure 7.37 Concrete members fractured by a single liquid shot
a – failure structure (Watson et al., 1984) b – fractured concrete sample (photograph: New Jersey Institute of Technology, Newark)

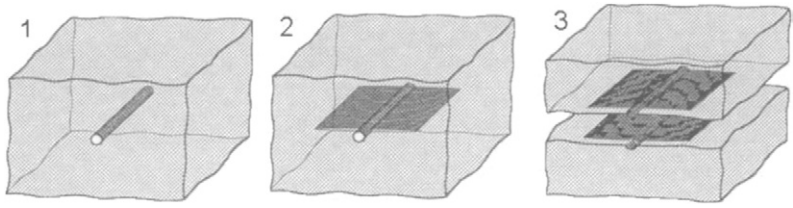

Figure 7.38 Performance steps of directed soft splitting (Witzel, 1998)

- step 1: drilling;
- step 2: directional kerfing;
- step 3: blasting (splitting).

The holes can be drilled with conventional mechanical drills but also with water jets. Directional kerfing occurs with a water jet exiting a nozzle bit in radial direction. The direction of the kerf can be selected; it depends on the desired shape of the fragmentation front (see Figure 7.39). A device for soft splitting basically consists of a high-pressure pump (typical operating pressures are between 100 and 200 MPa), a high-pressure water accumulator and a power breaker. Commercial flexible high-pressure hoses or commercial pressure storage vessels can be used as accumulators. Power breakers can be valves or burst disks, whereby the latter method is more often used. If the breaker is turned off, the water volume, stored in the accumulator, abruptly flows into the hole being drilled into the material. Tests on reinforced concrete members are reported by Witzel (1998). Some results are listed in Table 7.9. Steel bars could be ruptured due to the stresses generated by the

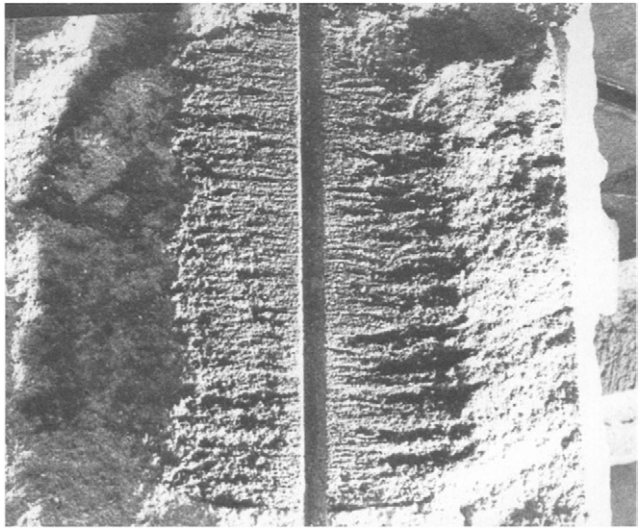

Figure 7.39 Concrete sample separated with the directed soft splitting technique (photograph: BGMR, RWTH Aachen)

accelerated concrete mass. The limit for reinforcement rupture depended upon the capacity of the storage vessel; it was at a total steel bar cross section of about 2 cm^2. Critical was the position of the impulse introduction system in relation to the arrangement of the reinforcement.

Table 7.9 Properties and separation areas of reinforced concrete samples separated with the soft splitting technique (Witzel, 1998)

Separated area (cm^2)	Reinforcement	Number of steel bars	Steel bar diameter (mm)	Total steel cross section (cm^2)
1,600	Steel bar	1	6	0.283
1,600	Steel bar	1	8	0.503
1,600	Steel bar	1	10	0.785
1,600	Steel bar	4	6	1.131
1,600	Steel bar	4	8	2.011
3,600	Steel wire mesh	4	8	2.011
3,600	Steel wire mesh	4	5	0.785
6,000	Steel wire mesh	6	5	1.178
3,600	Steel wire mesh	4	6	1.131
6,000	Steel wire mesh	6	6	1.414

References

Abrams, S., 1999, Handling and disposal of waste. *Protect. Coat. Europe*, Vol. 4, No. 5, 24–29.

Adler, W.F., 1995, Particulate impact damage predictions. *Wear*, Vol. 186, 35–44.

Adley, D., Trimber, K., 1999, Evaluation of substitute materials for silica sand in abrasive blasting. *J. Protect. Coat. & Linings*, Vol. 16, No. 8, 49–71.

Agus, M., Bortolussi, A., Ciccu, R., Kim, W.M., Manca, P.P., 1993, The influence of rock properties on waterjet performance. *Proc. 7th Amer. Water Jet Conf.* (ed. M. Hashish), WJTA, St. Louis, 427–442.

AHPWJC, 1995, *Code of Practice for the Use of High Pressure Water Jetting Equipment*. Association of High Pressure Water Jetting Contractors, London.

Alba, H., Brandt, C., Bremer, H., Eickelpasch, N., Kalwa, H., Louis, H., Reiter, W., 1999, The application of abrasive water suspension jets (AWSJ) for the dismantling of nuclear power plants. *Proc. Int Symp. on New Appl. of Water Jet Technol.* (ed. R. Kobayashi), Ishinomaki, 443–450.

Alitavoli, M.A., McGeough, J.A., 1998, An expert process planning system for meat cutting by high pressure water-jet. *J. Mater. Processing Technol.*, Vol. 84, 130–135.

Anderson, R.M., Adler, T.A., Hawk, J.A., 1993, Scale of microstructure effects on the impact resistance of Al_2O_3. *Wear*, Vol. 162–164, 1073–1080.

Andreou, L., 1989, Optimierung von Betriebsparametern des Hochdruckwasserstrahlens. *Diplomarbeit*, ibb, RWTH Aachen.

Anonymus, 1972, The Cavijet – cavitating water jet. *Technical Memorandum* PMB–16–2, Hydronautics, Inc., Laurel.

Anomymus, 1997, Waterjetting removes lead paint on communication facility. *J. Protect. Coat. & Linings*, Vol. 14, No. 5, 33–36.

Anonymus, 1998, On monitoring airborne lead dust during water jetting. *PMC*, Vol. 2, 8–9.

Anonymus, 2002, New HSE legislation could save lives in UHP water jetting operations. *Int. Ship Repair News*, July/August, 45–47.

Aquino, M.J., Li, Z., Shah, S.P., 1995, Mechanical properties of the aggregate and cement interface. *Adv. Cement Based Mater.*, Vol. 2, 211–223.

Arasawa, H., Matsumoto, K., Yamaguchi, S., Sumita, K., 1986, Controlled cutting of concrete structures with abrasive water-jet. *Proc. 8th Int. Symp. Jet Cutting Technol.* (ed. D. Saunders), BHRA, Cranfield, 211–218.

Atanov, G.A., 1991, The impulsive water jet device: a new machine for breaking rock. *Int. J. Water Jet Techn.*, Vol. 1, 85–91.

Atanov, G.A., 1998, Impulsive hydromechanic method of breaking rocks and concrete. *Water Jet Applications in Construction Engineering* (ed. A.W. Momber), A.A. Balkema, Rotterdam, 73–89.

Atmatzidis, D.K., Ferrin, F.R., 1983, Laboratory investigation of soil cutting with a water jet. *Proc. 2nd U.S. Water Jet Symp.* (eds D.A. Summers, F.F. Haston), Univ. of Missouri-Rolla Press, Rolla, 101–109.

ATV, 2001, Abwässer und Abfälle aus der Reinigung und Entschichtung von Fassaden. *ATV-DVWK-M 370*, Deutsche Vereinigung für Wasserwirtschaft, Abwasser und Abfall e.V., Hennef.

Axmann, H.-D., Laurinat, A., Flügel, M., Louis, H., 1998, Schädigungsmuster von Hochdruck-Wasserstrahlen und Hochdruck-Wasser-Abrasivstrahlen an der Hand. *Handchir. Mikrochir. Plast. Chir.*, Vol. 30, 263–268.

Bache, H.H., 1989, Fracture mechanics in integrated design of new, ultra-strong materials and structures. *Fracture Mechanics of Concrete Structures* (ed. L. Elfgren), Chapman & Hall, London, 382–397.

Badzong, H.J., 1990, Anforderungen an den Betonabtrag mittels hydrodynamischer Abtragverfahren. *Bericht 90–1*, Tiefbauamt des Kantons Solothurn.

Baker, D.W., Jolliffe, K.H., Pearson, D., 1966, The resistance of materials to impact erosion damage. *Phil. Trans. Roy. Soc. London*, Vol. A260, 193–203.

Balaguru, P.N., Shah, S.P., 1992, *Fiber-Reinforced Cement Composites*, McGraw-Hill, New York, 1992.

Bamforth, P.B., 1991, The water permeability of concrete and its relationship with strength. *Magaz. Concrete Res.*, Vol. 43, 233–241.

Barker, C.R., Cummings, A., Andersson, M., 1982, Jet noise measurements on handheld cleaning equipment. *Proc. 6th Int. Symp. Jet Cutting Techn.* (ed. H.S. Stephens), BHRA, Cranfield, 161–178.

Bazant, Z.P., Planas, J., 1998, *Fracture and Size Effect in Concrete and Other Quasibrittle Materials*. CRC Press, Boca Baton.

Becker, C., Schwark-Werwach, B., Uehlin, J., 1999, Hochdruck-Fluidstrahlen unter Zugabe von chemischen Energieträgern (reaktive Stoffe). *18. Sitzung Arbeitskreis Wasserstrahltechnik*, Vortrag, Hannover.

BGR 132, 2003, Vermeidung von Zündgefahren infolge elektrostatischer Aufladungen. Hauptverband der gewerblichen Berufsgenossenschaften, Frankfurt, März 2003.

BGV B3, 2001, Unfallverhütungsvorschrift Lärm. Steinbruchs-Berufsgenossenschaft, Langenhagen.

BGV D15, 1999, Unfallverhütungsvorschrift Arbeiten mit Flüssigkeitsstrahlern. Steinbruchs-Berufsgenossenschaft, Langenhagen.

BIA, 2000, Ermittlung von Grundlagen zur Gefährdungsanalyse und Entwicklung von Präventionsmaßnahmen. Bericht 638.23/077-HAV/AVA, Berufsgenossenschaftliches Institut für Arbeitssicherheit, Sankt Augustin.

Blades, B., 1994, Energy distribution and computer modelled nozzle design in high pressure water jet coating removal. *Proc. 7th National Thermal Spray Conf.*, Boston, 421–424.

Blickwedel, H., 1990, Erzeugung und Wirkung von Hochdruck-Abrasivstrahlen. Dissertation, Institut für Werkstoffkunde, Universität Hannover.

Bond, R.D., Makai, J., 1996, Removal of compensator coating at Paks Nuclear Power Plant, Hungary. *Jetting Technology* (ed. C. Gee), Mechan. Engng. Publ. Ltd., London, 663–675.

Bourne, N.K., Field, J.E., 1992, Shock-induced collapse of single cavities in liquids. *J. Fluid Mech.*, Vol. 244, 225–240.

Bourne, N.K., Obara, T., Field, J.E., 1997, High-speed photography and stress gauge studies of jet impact upon surfaces. *Phil. Trans. Roy. Soc. Lond.*, Vol. A355, 607–623.

Bowden, F.P., Field, J.E., 1964, The brittle fracture of solids by liquid impact, by solid impact, and by shock. *Proc. Roy. Soc. Lond.*, Vol. A282, 331–352.

Brennen, C.E., 1995, *Cavitation and Bubble Dynamics*. Oxford Univ. Press, Oxford.

Brühwiler, E., Saouma, V.E., 1995, Water fracture interaction in concrete – part I: fracture properties. *ACI Mater. J.*, May-June, 296–303.

Calogovic, V., Bjegovic, D., 1996, Specific permeability of near-surface concrete. *4. Int. Koll. Werkstoffwissenschaften und Bauinstandsetzen*, Teil III (Hrg. F.H. Wittmann & A. Gerdes), Aedificatio Publ., Freiburg, 1441–1455.

Camus, J.J., 1971, High-speed flow in impact and its effect on solid surfaces. *Ph.D. Thesis*, University of Cambrigde, Cambridge.

Carlson, J.R., Townsend, T.G., 1998, Management of solid waste from abrasive blasting. *Practice Periodical of Hazardous, Toxic, and Radioactive Waste Management*, April, 72–77.

Carter, E.E., 1998, Containing the cold war's hot waste. *Civil Engng. Magazine*, Nov., 1–7.

Chahine, G.L., Conn, A.F., Johnson, V.E., Frederick, G.S., 1983, Cleaning and cutting with self-resonating pulsed water jets. *Proc. 2nd US Water Jet Conf.* (eds D.A. Summers et al.), Univ. of Rolla Press, Rolla, 195–205.

Chahine, G.L., Johnson, V.E., Conn, A.F., Frederick, G.S., 1985, Passively interrupted impulsive water jets. *Proc. 3rd US Water Jet Symp.* (ed. N. Styler), US Bureau of Mines, WJTA, Paper 34, 1–9.

Chen, W.L., Geskin, E.S., 1991, Measurement of the velocity of abrasive waterjet by the use of laser transit anemometer. *Jet Cutting Techn.* (ed. S. Stephens), Elsevier Sci. Publ. Ltd., Amsterdam, 23–36.

Chermenski, F.P., Davidyants, G.F., 1980, Pulsed water jet pressures in rock breaking. *Proc. 5th Int. Symp. Jet Cutting Techn.* (ed. H.S. Stephens), BHRA, Cranfield, 155–163.

Cheung, J.B., Hurlburt, G.H., 1976, Submerged water-jet cutting on concrete and granite. *Proc. 3rd Int. Symp. Jet Cutting Techn.* (eds H.S. Stephens et al.), BHRA, Cranfield, E5/49–E5/62.

Choo, S., Teck, P.C., 1990a, Study on the standards and criteria for the removal of rubber deposits and effects of cleaning process on Singapore Changi Airport runway. *Proc. 2nd Rim Int. Conf. on Water Jet Cutting*, Singapore, 157–173.

Choo, S., Teck, P.C., 1990b, Removal of rubber deposits from runways using hydro-jetting techniques. *Proc. 2nd Rim Int. Conf. on Water Jet Cutting*, Singapore, 217–227.

Ciccu, R., Bortolussi, A., 1998, Water jet in dimensional quarrying. *Water Jet Applications in Construction Engineering* (ed. A.W. Momber), A.A. Balkema, Rotterdam, 289–305.

Cleland, D.J., Basheer, P.A., 1999, Adhesion and integrity of joints between construction materials. *Proc. 2nd Int. Symp. Adhesion Between Polymers and Concrete* (eds Y. Ohama, M. Puterman), RILIEM Publ. S.A.R.L., 257–265.

Coad, E.J., Pickles, C.S., Seward, C.R., Jilbert, G.H., Field, J.E., 1998, The erosion resistance of infrared transparent materials. *Proc. Roy. Soc. Lond.*, Vol. A454, 213–238.

Conjet, 1999, Pipe cutting and concrete removal at 600 m (see also: Norwegian Offshore Magazine ONS 94).

Conn, A.F., 1972, Recent developments of the cavitating water jet. *Proc. 1st Int. Symp. Jet Cutting Technol.* (eds T.E. Brook, C.A. Richardson), BHRA, Cranfield, A/106–A-110.

Conn, A.F., 1989, Asbestos removal with self-resonating water jets. *Proc. 5th Amer. Water Jet Conf.* (ed. M.M. Vijay & G.A. Savanick), WJTA, St. Louis, 133–139.

Conn, A.F., 1991, A technology transfer case history: introducing water jetting to the asbestos abatement industry. *Jet Cutting Technol.* (ed. E. Saunders), Elsevier, London, 441–447.

Conn, A.F., Rudy, S.L., 1978, Conservation and extraction of energy with the Cavijet™. *Proc. 4th Int. Symp. Jet Cutting Technol.* (eds J. Clarke & H.S. Stephens), BHRA, Cranfield, H2/19-H2/38.

Conn, A.F., Gracey, M.T., Rosenberg, W., 1987, Development of cavitating jet equipment for pavement cutting. *Proc. 4th US Water Jet Conf.* (eds M. Hood, D. Dornfield), ASME, New York, 57–64.

Conn, A.F., Johnson, V.E., Lindenmuth, W.T., Chahine, G.L., Frederick, G.S., 1984, Some unusual applications for cavitating water jets. *Proc. 7th Int. Symp. Water Jet Symp.* (eds I.A. Walls, J.E. Stanbury), 1–12.

Crawford, R., Atkinson, D., 1996, *Liquid Surfaces.* Lecture Reprint, Swinburne University of Technology, Melbourne.

Crine, J.P., 1988, (ed.): *Hazards, Decontamination, and Replacement of PCB.* Plenum Press, New York & London.

Crow, S.C., Champagne, F.H., 1971, Orderly structure in jet turbulence. *J. Fluid Mech.*, Vol. 48, 547–591.

Da Zong, C., Guo, L., Chuo, L., Yung, X., 1985, Relationship between water cannon design, pulsed water jet anatomy and rock breaking effect. *Proc. 3rd US Water Jet Symp.* (ed. N. Styler), WJTA, St. Louis, 309–326.

Daniel, I.M., 1976, Experimental studies of water jet impact on rock and rocklike materials. *Proc. 3rd Int. Symp. Jet Cutting Technol.* (eds H.S. Stephens & N.G. Coles), BHRA, Cranfield, B3/27-B3/46.

De Santis, G.J., 1985, Operational and maintenance misconceptions of high pressure power pumps. *Proc. 3rd U.S. Water Jet Conf.* (ed. N. Styler), US Bureau of Mines, WJTA, 12–19.

Dear, J.P., Field, J.E., 1988, A study of the collapse of arrays of cavities. *J. Fluid Mech.*, Vol. 190, 409–425.

Denier, R., Herrick, T., Mitchell, R.O., Summers, D.A., 1998, The use of waterjets in

the location and exposure of landmines for humanitarian demining. *Jetting Technol.* (ed. H. Louis), BHR Group, Cranfield, 439–452.

DHHS, 1997, Protecting workers exposed to lead-based paint hazards – A report to congress. *DHHS (NIOSH) Publ. No. 98–112*, Jan. 1997.

DIN/EN 1829, 2004, *Hochdruckreiniger, Hochdruckwasserstrahlmaschinen – Sicherheitstechnische Anforderungen.* Teil 1: Allgemeine Fassung, DIN EN 1829–1, Entwurf Juli 2004, Deutsches Institut für Normung e.V., Berlin.

Dinglinger, J., 1998, Operational aspects of water jet application in concrete hydrodemolition. *Water Jet Applications in Construction Engineering* (ed. A.W. Momber), A.A. Balkema, Rotterdam, 189–203.

ISO 11126, 1993, Preparation of steel substrates before application of paints and related products – Specifications for non-metallic blast-cleaning abrasives.

ISO 12944–4, 1998, Paints and varnishes – Corrosion protection of steel structures by protective paint systems. Part 4: Types of surface and surface preparation.

Dorner, W., 1996, Zusammensetzung des Ablaufwassers bei Wasserstrahlverfahren. *Bautenschutz+Bausanierung*, Nr. 4, 47–51.

Dunsky, C.M., Hashish, M., 1995, Feasibility study of the use of ultrahigh-pressure liquefied gas jets for machining of nuclear fuel pins. *Proc. 8th Amer. Water Jet Conf.* (ed. T.J. Labus), WJTA, St. Louis, 505–517.

Dupuy, R., 2001, Ultra-high-pressure waterjetting for maintenance coatings applications. *J. Protect. Coat. & Linings*, Vol. 18, No. 8, 68–75.

Engel, O.G., 1954, Mechanism of rain erosion, part 4: cavitation as a result of waterdrop collision with solid surfaces. *WADC Technical Report 53–192*, Wright Air Development Center, Jan. 1994.

Engel, O.G., 1973, Damage produced by high-speed liquid-drop impacts. *J. Appl. Phys.*, Vol. 44, 692–704.

Engel, P.A., 1978, *Impact Wear of Materials.* Elsevier Sci. Publ. Comp., Amsterdam.

Erdmann-Jesnitzer, F., Laschimke, R., 1966, Untersuchungen zur hydrodynamischen Beanspruchung bei Tropfenschlag. *Archiv f.d. Eisenhüttenwesen*, Jg. 37, 997–1012.

Evans, A.G., Gulden, M.E., Rosenblatt, M., 1978, Impact damage in brittle materials in the elastic-plastic response regime. *Proc. Roy. Soc. of London*, Series A, Vol. 361, 343–356.

Evans, A.G., Ito, Y.M., Rosenblatt, M.E., 1980, Impact damage thresholds in brittle materials impacted by water drops. *J. Appl. Phys.*, Vol. 51, 2473–2482.

Evers, J.L., Eddingfield, D.L., 1984, Liquid phase compressibility in the hydraulic intrusion model. *Proc. 7th Int. Symp. Jet Cutting Technology* (eds I.A. Walls & J.E. Stanbury), BHRA Fluid Engng., Cranfield, 237–248.

Evers, J.L., Eddingfield, D.L., Man, W.S., 1982, Hydraulic intrusion by a traversing water jet. *Proc. 6th Int. Symp. Jet Cutting Technology* (eds H.S. Stephens & E.B. Davies), BHRA Fluid Engng., Cranfield, 199–215.

Fehlemann, G., 1986, Schneiden und Abtragen von Gestein und Beton mit Hochdruckwasser-strahlen. *Diplomarbeit*, Inst. für Baumaschinen und Baubetrieb, RWTH Aachen.

Fiebrich, M., 1990, Kunststoffbeschichtung auf ständig durchfeuchtetem Beton. Deutscher Ausschuß für Stahlbeton, Heft 410, Beuth-Verlag, Berlin.

Fiebrich, M., 1994, Scientific aspects of adhesion phenomena in the interface mineral substrate-polymers. *Proc. 2nd Bolomey Workshop on Adherence of Young and Old Concrete* (ed. F.H. Wittmann), Aedificatio-Verlag, Unterengstringen, 25–58.

Field, J.E., 1999, Liquid impact: theory, experiment, applications. *Wear*, Vol. 233–235, 1–12.

Flack, L., 1992, How well control techniques were refined in Kuwait. *World Oil*, May, 72–77.

Foldyna, J., Hauner, M., Sedlarik, A., 1998, Utilization of waterjets in SS–23 missiles dismantling. *Jetting Technol.* (ed. H. Louis), Prof. Engng. Publ., Bury St. Edmunds, 485–489.

Fosgren, A., Applegren, C., 2000, Comparison of chloride levels remaining on the steel surface after various pretreatments. *Proc. PCE Conf. and Exhibition*, Technol. Publ., Pittsburgh, 271–283.

Fossey, R.D., Blaine, J.G., Tyler, L.J., Sabin, M., Summers, D.A., 1997, Practical problems in the demilitarization of munitions. *Proc. 9th Amer. Water Jet Conf.* (ed. M. Hashish), WJTA, St. Louis, 673–682.

Freitag, A., 1991, Möglichkeiten und Grundsätze der Anwendung der Druckwasserstrahltechnik im Bauwesen. Diplomarbeit, Technische Hochschule Leipzig.

French, M.A., 1998, Safety in high-pressure water jetting. *Water Jet Applications in Construction Engineering* (ed. A.W. Momber), A.A. Balkema, Rotterdam, 387–397.

Frenzel, L., 1997, Continuous improvement initiatives of surface preparation with waterjetting. *Proc. 9th Amer. Waterjet Conf.* (ed. M. Hashish), WJTA, St. Louis, 697–716.

Fritsch, H., 1991, Der volumetrische und energetische Wirkungsgrad von Verdrängerpumpen. *Chemie-Technik*, Jg. 20, Nr. 12, 44–51.

Galecki, G., Mazurkiewicz, M., Summers, D.A., 1991, Preparation of secondary fiber stock by high pressure waterjets. *Proc. 6th Amer. Water Jet Conf.* (ed. T.J. Labus), WJTA, St. Louis, 505–513.

Galecki, G., Maerz, N., Nanni, A., Myers, J., 2001, Limitations to the use of waterjets in concrete substrate preparation. *Proc. 2001 Amer. Waterjet Conf.*, WJTA, St. Louis, 483–493.

Gelfant, F.S., 1995, Contaminated concrete – effect of surface preparation methods on coating performance. *J. Protect. Coat. & Linings*, Vol. 12, 60–72.

Geskin, E.G., 1998, In-situ reactor cleaning by ultra-high pressure water jets. *Water Jet Applications in Construction Engineering* (ed. A.W. Momber), A.A. Balkema, Rotterdam, 339–350.

Glinicki, M.A., Zielinski, M., 2004, Depth-sensing indentation method for evaluation of effectiveness of secondary cementitious materials. *Cement and Concrete Res.*, Vol. 34, 721–724.

Gnirk, P.F., Grams, W.H., 1972, Rock drilling with pulsed high-velocity water jets. *Proc. 14th Symp. Rock Mech.* (eds H. Hardy & R. Stefanko), ASCE, New York, 589–611.

Goldin, J., Nikonow, G., Kusmitsch, I., 1986, *Rasruschenje gornich porod strujamu wodoi wuisokovo dawlenja* (Rock excavation with high-pressure water jets). Publ. Nedra, Moscow.

Grabko, D., Palistrant, M., Shikimaka, R., Zhitaru, R., Rahvalov, V., Zugravescu, D., 2002, Hardness and brittleness of rocks studied by microindentation method in combination with the registration of acoustic emission signals. *Proc. 8th European Conference on Non-Destructive Testing*, Barcelona.

Gross, H.W., Wisinger, F., 1998, High pressure injection technique for soil conditioning. *Water Jet Applications in Construction Engineering* (ed. A.W. Momber), A.A. Balkema, Rotterdam, 231–243.

Halbartschlager, J., 1985, Untersuchung verschiedener Entlackungsverfahren der Automobil-industrie unter besonderer Berücksichtigung umwelttechnischer Belange. *VDI-Fortschritt-Berichte*, Reihe 3, Nr. 109, VDI-Verlag, Düsseldorf.

Hamada, S., Kamiyama, S., Tsubota, M. et al., 1991, The structure of an annular jet and its characteristics (ed. D. Saunders), *Jet Cutting Technol.*, Elsevier Appl. Sci., London, 69–72.

Hammelmann, F., 1997, Die Anwendung der Hochdruckwassertechnik beim Bohren, Kerben und Spalten von Gestein. *Dissertation*, Inst. für Bergbau, RWTH Aachen.

Hammelmann, F., Witzel, J., 1998, Directional hydraulic pulse blasting. *Water Jet Applications in Construction Engineering* (ed. A.W. Momber), A.A. Balkema, Roterdam, 91–103.

Hammitt, F.G., 1980, *Cavitation and Multiphase Flow Phenomena*. McGraw-Hill, New York.

Hand, R.J., Field, J.E., Townsend, D., 1991, The use of liquid jets to simulate angled drop impact. *J. Appl. Phys.*, Vol. 70, 7111–7118.

Hashish, M., 1982, The application of abrasive jets to concrete cutting. *Proc. 6th Int. Symp. Jet Cutting Technol.* (eds H.S. Stephens, E.B. Davies), BHRA, Cranfield, 448–464.

Hashish, M., 1983, Experimental studies of cutting with abrasive water jets. *Proc. 2nd US Water Jet Symp.* (eds D.A. Summers, F.F. Haston), Univ. of Missouri-Rolla Press, Rolla, 379–389.

Hashish, M., Echert, D., 1989, Abrasive-water jet deep kerfing and water jet surface cleaning for nuclear facilities. *ASME J. Engng. for Ind.*, Vol. 111, 269–281.

Hashish, M., Miller, P., 2000, Cutting and washout of chemical weapons with high-pressure ammonia jets. *Jetting Technology* (ed. R. Ciccu), BHR Group, Cranfield, 81–92.

Hawrylewicz, B.M., Puchala, R.J., Vijay, M.M., 1986, Generation of pulsed or cavitating jets by electric discharges in high speed continuous water jets. *Proc. 8th Int. Symp. Jet Cutting Technol.* (ed. D. Saunders), BHRA, Cranfied, 345–352.

Heimhardt, H.J., 1998, Application of the water jet technology for the 'high pressure soil washing process'. *Water Jet Applications in Construction Engineering* (ed. A.W. Momber), A.A. Balkema, Rotterdam, 217–229.

Hennies, W.T., Lauand, C.T., Cortes, G.R., Mazuqui, L.M., 2002, Soil preparation with water jet for geotechnical analysis. *Proc. SWEMP 2002* (ed. R. Ciccu), A.A. Balkema, Rotterdam, 549–552.

Herberholz, J., Schmitz, B., 1999, Flow visualisation and high speed video analysis of water jets in the snapping shrimp. *J. Comp. Physiol. A*, Vol. 185, 41–49.

Hertz, H., 1882, Ueber die Berührung fester elastischer Körper. *Journal für die reine und angewandte Mathematik*, Jg. 92, 156–171.

Heßling, M., 1988, Grundlagenuntersuchungen über das Schneiden von Gesteinen mit abrasiven Höchstdruckwasserstrahlen. *Dissertation*, Institut für Bergbaukunde, RWTH Aachen.

Heymann, F.G., 1968, On the shock wave velocity and impact pressure in high-speed liquid-solid impact. *ASME J. Basic Eng.*, Vol. 90D, 400–402.

Hillerborg, A., Modeer, M., Petersen, P.E., 1976, Analysis of crack formation and crack growth in concrete by means of fracture mechanics and finite elements. *Cement & Concr. Res.*, Vol. 6, 773–781.

Hilmersson, S., 1998, Hydrodemolition of concrete structures – basics and field experience. *Water Jet Applications in Construction Engineering* (ed. A.W. Momber), A.A. Balkema, Rotterdam, 163–175.

Hilsdorf, K.-H., Brameshuber, W., 1991, Code-type formulation of fracture mechanics concepts for concrete. *Int. J. Fracture*, Vol. 51, 61–72.

Hilsdorf, K.-H., Ziegeldorf, S., 1981, Fracture energy of concrete. *Adhesion Problems in the Recycling of Concrete* (ed. P.C. Kreijger), Plenum Press, New York, 101–123.

Himmelreich, U., 1992, Fluiddynamische Modelluntersuchungen an Wasserabrasivstrahlen. *VDI Fortschritt-Berichte*, Reihe 7, Nr. 219.

Himmelreich, U., Rieß, W., 1991a, Laser-velocimetry investigations of the flow in abrasive water jets with varying cutting head geometry. *Proc. 6th Amer. Water Jet Conf.* (ed. T.J. Labus), WJTA, St. Louis, 355–369.

Himmelreich, U., Rieß, W., 1991b, Hydrodynamic investigations on abrasive-water jet cutting tools. *Proc. 3rd Int. Symp. on Underwater Techn.*, Geesthacht, Paper 17, 1–9.

Hindo, K.R., 1990, In-place bond testing and surface preparation of concrete. *Concrete Int.*, Vol. 12, No. 4, 46–48.

Hocheng, H., Weng, C.H., 2002, Hydraulic erosion of concrete by a submerged jet. *J. Mater. Engng. and Perform.*, Vol. 11, 256–261.

Hofacker, S.A., 1993, The large aircraft robotic paint stripping system. *Proc. 7th Amer. Water Jet Conf.* (ed. M. Hashish), WJTA, St. Louis, 613–628.

Horigushi, T., Kajihara, K., 1988, Development of piling system of precast piles by applying rotary jets. *Proc. 9th Int. Symp. Jet Cutting Technol.* (ed. P.A. Woods), BHRA, Cranfield, 591–610.

Howells, W.G., 1998, Enhancing waterjetting by use of water soluble additives. *Water Jet Applications in Construction Engineering* (ed. A.W. Momber), A.A. Balkema, Rotterdam, 41–50.

Howlett, J.J., Dupuy, R., 1993, Ultrahigh-pressure water jetting for deposit removal and surface preparation. *Mater. Performance*, Jan., 38–43.

Hu, F., Yang, Y., Geskin, E.S., Chung, Y., 1991, Characterization of material removal in the course of abrasive waterjet machining. *Proc. 6th Amer. Water Jet Conf.* (ed. T.J. Labus), WJTA, St. Louis, 17–29.

Hu, X.G., Momber, A.W., Yin, Y.G., 2002, Hydro-abrasive erosion of steel-fibre reinforced hydraulic concrete. *Wear*, Vol. 253, 848–854.

Hu, X.G., Momber, A.W., Yin, Y.G., 2003, Flüssigkeitserosion und

Hydroabrasivverschleiß von Stahlfaserbeton. *Beton- und Stahlbetonbau*, Vol. 98, 764–772.

Hu, X.G., Momber, A.W., Yin, Y., Wang, H., Cui, D.M., 2004, High-speed hydrodynamic wear of steel-fibre reinforced hydraulic concrete. *Wear*, Vol. 257, 441–450.

Hull, D., 1999, *Fractography*. Cambridge University Press, Cambridge.

Hunkeler, F., 1998, Anforderungen an den Traggrund: Was verlangt der Korrosionsschutz? *Seminarunterlagen "Der Traggrund"*. Technische Forschung und Beratung für Zement und Beton, Wildegg.

Hutchings, I.M., 1992, Ductile-brittle transitions and wear maps for the erosion and abrasion of brittle materials. *J. Phys. D: Appl. Phys.*, Vol. 25, A212–A221.

Ingvarsson, H., Eriksson, B., 1988, Hydrodemolition for bridge repair. *Nordisk Betong*, No. 2/3, 49–54.

Isobe, T., 2003, High-quality aggregate reproduction method using water jet. *Proc. 7th Pacific Rim Int. Conf. Water Jetting Technol.* (eds T. Le et al.), Korean Soc. Of Water Jet Technol., Taipeh, 2111–218.

Jeremic, M.K., 1981, *Elements of Hydraulic Coal Mine Design*. Gulf Publ. Comp., Houston.

JISHA, 1992, Safety Guidelines for Water Jet Machining. Japan Industrial Safety and Health Association, Tokyo, Japan.

Johnson, K.L., 1985, *Contact Mechanics*. Cambridge University Press, Cambridge.

Johnson, V.E., Kohl, R.A., Thiruvengadam, A, Conn, A.F., 1972, Tunneling, fracturing, drilling and mining with high speed water jets utilizing cavitation damage *Proc. 1st Int. Symp. Water Jet Technol.* (eds T.E. Brook, C.A. Richerdson), BHRA, Cranfield, Paper A3, 37–55.

Johnson, V.E., Conn, A.F., Lindenmuth, W.T., Chahine, G.L., Frederick, G.S., 1984, Self resonating cavitating jets. *Proc. 6th Int. Symp. Water Jet Technol.* (eds H.S. Stephens, E.B. Davies), BHRA, Cranfield, Paper A1, 1–25.

Jung, R.G., Drucks, M., 1996, Optimierung der Reinigung von Filtertüchern bei betrieblich eingesetzten Filtrationsanlagen. *Aufbereitungs-Technik*, 37. Jg., 142–148.

Kalumuck, K.M., Chahine, G.L., Frederick, G.S., Aley, P.D., 1999, Development of high erosivity cavitating and acoustically enhanced water jets for well scale removal. *Proc. 10th Amer. Waterjet Conf.*, Houston, Paper 61.

Karihaloo, B.L., 1995, *Fracture Mechanics and Structural Concrete*. Longman Scientific & Technical, Harlow.

Katakura, H., 2000, Noise of high pressure water jetting operations. *Investigation Report of WJTSJ Safety Committee*, No. 2, Water Jet Technol. Soc. of Japan, Tokyo, 1–20.

Kaufmann, N., 1971, Das Sandflächenverfahren. *Straßenbautechnik*, Vol. 24, No. 3, 131–135.

Kauw, V., 1992, Hochdruckwasserstrahlen in der Baupraxis. Lehrgangsunterlagen, Lehrgang 15178/83.153, TA Esslingen.

Kauw, V., 1996, Optimierung des Einsatzes von Hochdruck-Wasserstrahl-Systemen bei der Betonuntergrundvorbereitung. *Dissertation*, Inst. für Baumaschinen und Baubetrieb, RWTH Aachen.

Kauw, V., 1998, High-speed waterjet: a tool for the removal of jointing mortar. *Water Jet Applications in Construction Engineering* (ed. A.W. Momber), Balkema, Rotterdam, 309–314.

Kennedy, C.F., Field, J.E., 2000, Damage threshold velocities for liquid impact. *J. Mater. Sci.*, Vol. 35, 5331–5340.

Khan, M.E., Geskin, E.S., 1994, Velocity measurements of water jet and abrasive water jet by the use of Laser Transit Anemometer. *FED-Vol. 191*, 59–63.

Kirchner, H.P., Gruver, R.M., 1978a, Localized impact damage in a viscous medium (glass). *Fracture Mechanics of Ceramics* (eds R.C. Bradt et al.), Vol. 3, Plenum Press, New York, 365–377.

Klich, A., Kalukeiwicz, A., 1991, Investigation on water-jet cutting of concrete in water surroundings. *Proc. 6th Amer. Water Jet Conf.* (ed. T.J. Labus), WJTA, St. Louis, 371–380.

Kloner, M., 1987, Häufige Schäden und Instandsetzungsverfahren – Ergebnisse einer Umfrage. *Zement u. Beton*, No. 4, 120–124.

Knapp, R.T., Daily, J.T., Hammitt, F.G., 1970, *Cavitation*. McGraw Hill, New York.

Knight, C.G., Swain, M.V., Chaudri, M.M., 1977, Impact of small steel spheres on glass surfaces. *J. Mater. Sci.*, Vol. 12, 1573–1586.

Knipfer, C., Funke, H.-W., 1997, Lärmbelastung an Baustellenarbeitsplätzen, Teil V. *BIA Report*, Hauptverband der gewerblichen Berufsgenossenschaften, St. Augustin.

Köhler, B., Kiele-Dunsche, M., Berge, G., 2000, Variable Drehzahl senkt die Kosten. *Process*, Nr. 10, 28–30.

Kokaji, C., Sakashita, F., Oura, S., Sato, M., 1988, Effects of abrasives on concrete cutting. *Proc. 9th Int. Symp. Jet Cutting Technol.* (ed. P.A. Woods), BHRA, Cranfield, 571–580.

Kolle, J.J., 1994, Developing a hydraulic pulse generator. *Mechan. Engng.*, No. 3, 81–85.

Kolle, J.J., 1998, Compressed-water cannons for civil engineering. *Water Jet Applications in Construction Engineering* (ed. A.W. Momber), A.A. Balkema, Roterdam, 53–72.

Kolle, J.J., Hashish, M., 1989, Recent developments in high pressure technology for mining and drilling. *Conf. Geomechanics '89*, Ostrava, Supplement Paper.

Kolle, J.J., Marvin, M.H., 2000, Jet assisted drilling with supercritical carbondioxide. *ASME Energy Technol. Conf. & Exhibition*, New Orleans, LO, USA.

Kondo, M., Fujii, K., Syoji, H., 1974, On the destruction of mortar specimens by submerged water jets. *Proc. 2nd Int. Symp. Jet Cutting Technol.* (eds N.G. Coles, S.J. Barrall), BHRA, Cranfield, B5/69–B5/88.

Konno, T., 1988, Abrasive-water jet method for cutting reinforced concrete structures. *Demolition and Reuse of Concrete and Masonry*, Chapman & Hall, London, 177–186.

Krüner, D., Wiedemeier, J., Louis, H., 1982, Safety aspects of jet cutting. *Proc. 6th Int. Symp. Jet Cutting Technol.* (eds H.S. Stephens, E.B. Davies), BHRA, Cranfield, 519–524.

Küfer, K.–H., 1999, Zur Energieverteilung von rotierenden Wasserstrahlwerkzeugen. Inst. f. Techno- und Wirtschaftsmathematik, Kaiserslautern.

Kuljian, G.G., Melhuish, D.C., 1999, Water-jetting productivity study for the marine industry. *Proc. 10th Amer. Waterjet Conf.* (ed. M. Hashish), WJTA, St. Louis, Paper 42.

Labus, T.J., 1984, Material excavation using rotating water jets. *Proc. 7th Int. Symp. Jet Cutting Technol.* (eds I.A. Walls, J.E. Stanbury), BHRA, Cranfield, 503–518.

Labus, T.J., 1991, Pulsed fluid jet technology. *Proc. 1st Asian Conf. on Recent Adv. in Jetting Technol.* (ed. J. S. Tan), CI Prem. Ltd, Singapore, 136–143.

Lange, F.F., Evans, A.G., 1979, Erosive damage depth in ceramics: a study on metastable, tetrogonal zirkonia. *J. Amer. Ceram. Soc.*, Vol. 62, 62–65.

Larbi, J.A., 1993, Microstructure of the interfacial zone around aggregate particles in concrete. *HERON*, Vol. 38, 3–69.

Lauterborn, W., Bolle, H., 1975, Experimental investigations of cavitation bubble collapse in the neighborhood of a solid boundary. *J. Fluid Mech.*, Vol. 72, 391–399.

Leach, S.J., Walker, G.I., 1966, Some aspects of rock cutting by high speed water jets. *Phil. Trans. Roy. Soc. London*, Vol. A260, 295–303.

Lecoffre, Y., 1999, *Cavitation – Bubble Trackers*. Balkema, Rotterdam.

Lee, C.I., Kim, W.M., Kim, H.M., Kim, D.I., 1999, Testing of waterjets for rock surface treatment. *Proc. Int. Symp. New Appl. of Water Jet Techn.* (ed. R. Kobayashi), Ishinomaki, 171–178.

Leeming, A.A., 1981, The potential application of water abrasive cutting in coal-mines. *The Mining Engr.*, June, 871–875.

Lelaidier, M., Spitz, J.A., 1978, Part played by high-pressure water in the nuclear decontamination process. *Proc. 5th Int. Techn. Meeting on Nuclear Industries*, Basel, 1–11.

Lenz, J., Wielenberg, M., 1998, Cleaning of sewage systems by high-pressure water jetting. *Water Jet Applications in Construction Engineering* (ed. A.W. Momber), A.A. Balkema, Rotterdam, 351–363.

Lesser, M., 1981, Analytic solutions of liquid-drop impact problems. *Proc. Roy. Soc. Lond.*, Vol. A377, 289–308.

Lesser, M.B., 1995, Thirty years of liquid impact research: a tutorial review. *Wear*, Vol. 186, 28–34.

Lesser, M.B., Field, J.E., 1983, The impact of compressible liquids. *Ann. Rev. Fluid Mech.*, Vol. 15, 97–122.

Lin, B., Shan, G., Cai, C., 1997, Studies on high-performance concrete and its application. *Proc. 3rd CANMET/ACI Conf. on High-Performance Concrete*, Kuala Lumpur, 485–494.

Lin, B., Watson, J., Gu, D., 1996, Computer modeling of rock cratering by water jets. *Jetting Technol.* (ed. C. Gee), Mechan. Engng. Publ. Ltd., London, 425–440.

Linsbauer, H.N., 1991, Fracture mechanics material parameters of mass concrete based on drilling core testing – review and discussion. *Fracture Processes in Concrete, Rocks and Ceramics.* (ed. J.G. van Mier), F&FN Spon. London, 779–787.

Louis, H., 1982, *Bericht zum Forschungsvorhaben Nr. 4703/78*. FK – FE 100.3. Universität Hannover, Inst. für Werkstoffkunde.

Lukas, W., Kusterle, W., 1991, Großflächige Instandsetzung bei hohen Chloridgehalten im Altbeton. *Int. Fachtagung Konstruktive Instandsetzung,*

großflächige Erneuerung, vorbeugender Schutz und Instandsetzungs-Sonderverfahren von Stahlbetonbauwerken (Hrg. W. Lukas), Innsbruck, 47–54.

Lüling, K.H., 1958, Morphologisch-anatomische und histologische Untersuchungen am Auge des Schützenfisches nebst Bemerkungen zum Spuckgehaben. *Z. Morph. und Ökol. Tiere*, Vol. 47, 529–610.

Lüling, K.H., 1969, Das Beutespucken von Schützenfisch Toxotes jacularix und Zwergfadenfisch Colisa lalia. *Bonner zool. Beiträge*, Vol. 20, 416–422.

Lyubimova, T.Y., Pinus, E.R., 1962, Colloid J. USSR. cited in: Struble, L., Skalny, J., 1980, A review of the cement-aggregate bond. *Cement & Concr. Res.*, Vol. 10, 277–286.

Maerz, N.H., Nanni, A., Myers, J.J., Galecki, G., 2001, Laser profilometry for concrete substrate characterization prior to FRC laminate application. *Concrete Repair Bull.*, May/June, 4–8.

Marshall, A.K., 1996, Lead removal with waterjetting. *J. Protect. Coat. & Linings*, Vol. 13, No. 2, 47–51.

Matsui, S., Matsumura, H., Ikemoto, Y., Kumon, Y., Shimizu, H., 1991, Prediction equations for depth of cut made by abrasive water jet. *Proc. 6th Amer. Water Jet Conf.* (ed. T.J. Labus), WJTA, St. Louis, 31–41.

Matsumoto, K., Arawasa, H., Yamaguchi, S., 1988, A study of the effect of abrasive material on cutting with abrasive water-jet. *Proc. 9th Symp. Jet Cutting Technol.* (ed. P.A. Woods), BHRA, Cranfield, 255–268.

Matsushima, Y., 1988, Partial dismantling of a hospital by water jet system. *Demolition and Reuse of Concrete and Masonry*, Chapmann and Hall, 187–196.

Maurer, W.C., 1980, *Advanced drilling techniques*. Petroleum Publ. Co., Tulsa.

Mazurkiewicz, M., 1984, The analysis of high pressure water jet interruption through ultrasonic nozzle vibrations. *Proc. 7th Int. Symp. Jet Technol.* (eds I.A. Walls & J.E. Stanbury), BHRA, Cranfield, 531–536.

Mazurkiewicz, M., White, J., Galecki, G., 1986, A model study of the water pressure distribution in a crack when impacted by a high pressure water jet. *Proc. 8th Int. Symp. Jet Cutting Techn.* (ed. D. Saunders), BHRA, Cranfield, 189–193.

McCurrich, L.H., Browne, R.D., 1972, Application of water jet cutting technology to cement grouts and concrete. *Proc. 1st Int. Symp. Jet Cutting Technol.* (ed. T.E. Brock, A. Richardson), BHRA, Cranfield, G7/69–G7/91.

Mehta, P.K., 1986, *Concrete: Structure, Properties, and Materials*. Prentice-Hall.

Mehta, P.K., Manmohan, D., 1980, Pore size distribution and permeability of hardened cement paste. *Proc. 7th Int. Cong. Chemistry of Cement*, Paris, Vol. III, VII/1–VII/5.

Meng, P., Geskin, E.S., Leu, C., Tismenetskiy, L., 1996, Waterjet in-situ reactor cleaning. In: *Jetting Technology* (ed. C. Gee), Mechanical Engng. Publ. Ltd., London, 347–358.

Miller, P.I., 1999, Fluid jet ignition hazards safety analysis. *Proc. 10th Amer. Water Jet Conf.* (ed. M. Hashish), WJTA, St. Louis, Paper 70.

Miller, A.L., Archibald, J.H., 1991, Measurement of particle velocities in abrasive jet cutting systems. *Proc. 6th Amer. Water Jet Conf.* (ed. T.J. Labus), WJTA, St. Louis, 291–305.

Mitsui, K., Li, Z., Lange, D.A., Shah, S.P., 1994, Relationship between microstructure and mechanical properties of the paste-aggregate interface. *ACI Mater. J.*, 1–2, 30–39.

Momber, A.W., 1992, Untersuchungen zum Verhalten von Beton unter der Belastung durch Druckwasserstrahlen. *VDI-Fortschrittberichte*, Reihe 4, Nr. 109, VDI-Verlag, Düsseldorf.

Momber, A.W., 1993, *Handbuch Wasserstrahl-Technik*. Beton-Verlag, Düsseldorf.

Momber, A.W., 1995a, Environmental applications of high speed water jet technology – preliminary results. *J. of Jet Flow Engng.*, Vol, 12, 46–53.

Momber, A.W., 1995b, A generalised abrasive water jet cutting model. *Proc. 8th Amer. Water Jet Conf.* (ed. T.J. Labus), WJTA, St. Louis, 359–376.

Momber, A.W., 1997, Investigations into decoating and recycling of pipeline elements using the high-pressure water jet technique. *Inst. Mechan. Engnrs., J. of Mechan. Process Engng.*, Vol. 211, 129–135.

Momber, A.W., 1998a, (ed.) *Water Jet Applications in Construction Engineering*. A.A. Balkema, Rotterdam.

Momber, A.W., 1998b, Pre-evaluation of hydrodemolished concrete surfaces by drilled core testing. *Proc. 8th Int. Symp. on Concrete Roads*, Lisbon, Vol. IV, 7–12.

Momber, A.W., 2000a, A dimensionless number for the control of ultra-high pressure systems. *Inst. Mechan. Engrs., J. of Power and Energy*, Vol. 213, 645-655.

Momber, A.W., 2000b, (ed.) *Materialrecycling mit Hochdruckwasserstrahlen*. Expert-Verlag, Renningen.

Momber, A.W., 2000c, Hydrodynamic cleaning of heat exchangers. *Heat Exchanger Fouling* (ed. H. Müller-Steinhagen), Publico Publ., Essen, 98–107.

Momber, A.W., 2000d, Concrete failure due to air-water jet impingement, *J. Mater. Sci.*, Vol. 35, 2785–2789.

Momber, A.W., 2000e, Short-time cavitation erosion of concrete. *Wear*, Vol. 241, 47–52.

Momber, A.W., 2000f, The fragmentation of standard concrete cylinders under compression: the role of secondary fracture debris. *Engng. Fracture Mech.*, Vol. 67 (2000), 445–459.

Momber, A.W., 2001, Energy transfer during the mixing of air and solid particles into a high-speed waterjet: an impact force study. *Exper. Thermal & Fluid Sci.*, Vol. 25, 31–41.

Momber, A.W., 2002a, Surface issues of profiled cementitious composites. *The Journal of Adhesion*, Vol. 78, 203–221.

Momber, A.W., 2002b, The fragmentation of cementitious composites in a laboratory jaw breaker. *Theoret. Appl. Fracture Mech.*, Vol. 38, 151–164.

Momber, A.W., 2003a, Cavitation damage to geomaterials in a flowing system. *J. Mater. Sci.*, Vol. 38, 747–757.

Momber, A.W., 2003b, An SEM-study of high-speed hydrodynamic erosion of cementitious composites. *Composites Part B: Engng.*, Vol. 34, 135–142.

Momber, A.W., 2003c, *Hydroblasting and Coating of Steel Structures*. Elsevier Appl. Sci., Oxford.

Momber, A.W., 2004a, Wear of rock by water flow. *Int. J. Rock Mech. Min. Sci.*, Vol. 41, 51–68.

Momber, A.W., 2004b, Deformation and fracture of rocks due to liquid impact at high speeds. *Int. J. of Fracture*, Vol. 130, 683–704.

Momber, A.W., 2004c, Synergetic effects of secondary liquid drop impact and solid particle impact during hydro-abrasive erosion of brittle materials. *Wear*, Vol. 256, 1190–1195.

Momber, A.W., 2004d, Aggregate liberation form concrete by flow cavitation. *Int. J. Mineral Proc.*, Vol. 74, 177–187.

Momber, A.W., 2004e, Fragmentation of cementitious composites with high-speed liquid slugs. Unpublished results.

Momber, A.W., 2004f, Damage to rocks and cementitious materials from solid impact. *Rock Mechan. Rock Engng.*, Vol. 37, 57–82.

Momber, A.W., 2004g, Deformation and fracture of rocks loaded with spherical indenters. *Int. J. Fracture*, Vol. 115, 263–279.

Momber, A.W., 2005, A single-stage size-reduction process for the generation of fine-grained concrete. *Mineral Proc. and Extractive Metallurgy*, in print.

Momber, A.W., Kovacevic, R., 1994, Fundamental investigations on concrete wear by high velocity water flow. *Wear*, Vol. 177, 55–62.

Momber, A.W., Kovacevic, R., 1995a, Statistical character of the failure of multiphase materials due to high pressure water jet impingement. *Int. J. Fracture*, Vol. 71, 1–14.

Momber, A.W., Kovacevic, R., 1995b, A fracture model for hydrodemolition. *Proc. 8th Amer. Water Jet Conf.* (ed. T.J. Labus), WJTA, St. Louis, 61–77.

Momber, A.W., Kovacevic, R., 1997, Test parameter analysis in abrasive water jet cutting of rocklike materials. *Int. J. Rock Mech. Min. Sci.*, Vol. 34, 17–25.

Momber, A.W., Kovacevic, R., 1998, *Principles of Abrasive Water Jet Machining*. Springer-Verlag Ltd., London.

Momber, A.W., Nielsen, A.G., 1998, Pipeline rehabilitation by waterjetting. *Mater. Evaluation*, Vol. 37, 97–101.

Momber, A.W., Kovacevic, R., Ye, J., 1995, The fracture of concrete due to erosive wear by high velocity water flow. *Tribol. Trans.*, Vol. 38, 686–692.

Momber, A.W., Mohan, R., Kovacevic, R., 1999, On-line analysis of high-speed erosion of concrete by acoustic emission. *Theoret. Appl. Fracture Mech.*, Vol. 31, 1–17.

Momber, A.W., Wüstenberg, D., Weiß, M., 2000, Entwicklung eines Verfahrens zur werkstofflichen Verwertung von Teppichproduktionsabfällen und Altteppichböden. Abschlußbericht 10831, Deutsche Bundesstiftung Umwelt, Osnabrück.

Momber, A.W., Wong, Y., Budidharma, E., Tjo, R., 2002a, Profiling of low-carbon steel with supersonic water jets. *Wear*, Vol. 249, 853–859.

Momber, A.W., Wong, Y.C., Budidharma, E., Tjo, R., 2002b, Hydrodynamic profiling and grit blasting of low-carbon steel. *Tribology Intern.*, Vol. 35, 271–281.

Momber, A.W., Kovacevic, R., Mohan, R., 2002c, Fracture range detection in the hydro-abrasive erosion of concrete. *Wear*, Vol. 253, 1156–1164.

Momber, A.W., Kovacevic, R., Chen, L., 2004, An energetic model for the separation of reinforced cement composites with a streamline cutting tool. Unpublished results.

Morel, T., 1979, Experimental study of a jet-driven Helmholtz-oscillator. *J. Fluid Engng.*, Vol. 101, 838–890.

Mugikura, K., Andow, K., Ishibashi, J., Yahiro, T., 1990, Noise and vibration propagation in building refreshment and occupant's noise evaluation. *Proc. 2nd Pacific Rim Int. Conf. on Water Jet Cutting*, Singapore, 2–10.

Nakamura, H., Narazaki, T., Yanagihara, S., 1989, Cutting technique and system for biological shield. *Nuclear Technol.*, Vol. 86, 168–178.

Nakaya, M., Kitagawa, T., Satake, S., 1984, Concrete cutting with abrasive-water jet. *Proc. 7th Int. Symp. Jet Cutting Technol.* (eds I.A. Walls, J.E. Stanbury), BHRA, Cranfield, 281–292.

Nakaya, M., Nishida, N., Kitagawa, T., 1983, Development of variable delivery triple reciprocating plunger pump for water jet cutting. *Proc. 2nd U.S. Water Jet Symp.* (eds D.A. Summers, F.F. Haston), Univ. of Missouri-Rolla, 111–118.

Nebeker, E.B., 1984, Potential and problems of rapidly pulsing water jets. *Proc. 7th Int. Symp. Jet Cutting Technol.* (eds I.A. Walls, J.E. Stanbury), BHRA, Cranfield, 51–68.

Nebeker, E.B., Rodriguez, S.E., 1976, Percussive water jets for rock cutting. *Proc. 3rd Int. Symp. Jet Cutting Technol.* (eds H.S. Stephens & N.G. Cole), BHRA, Cranfield, B1/1–B1/9.

Neusen, F.K., Alberts, D.G., Gores, T.J., Labus, T.J., 1991, Distribution of mass in a three-phase abrasive waterjet using X-ray densitometry. *Jet Cutting Technology* (ed. S. Stephens), Elsevier Sci. Publ., Rotterdam.

Neusen, K.F., Gores, T.J., Amano, R.S., 1994, Axial variation of particle and drop velocities downstream from an abrasive water jet mixing tube. *Jet Cutting Technology* (ed. N.G. Allen), Mechanical Engng. Publ. Ltd., London, 93–103.

Neusen, K.F., Gores, T.J., Labus, T.J., 1992, Measurement of particle and drop velocities in a mixed abrasive water jet using forward-scatter LDV system. *Jet Cutting Technology* (ed. A. Lichtarowicz), Kluwer Acad. Publ., Dordrecht, 63–74.

Nikonov, G.P., 1971, Research into the cutting of coal by small diameter, high pressure water jets. *Proc. 12th Symp. Rock Mech.* (ed. G.B. Clark), Soc. of Mining Engrs., New York, 667–680.

Norsworthy, A.G., Mohaupt, U.H., Burns, D.J., 1974, Concrete slotting with continuous water jets at pressures up to 483 MPa (70 ksi). *Proc. 2nd Int. Symp. Jet Cutting Technol.* (eds N.G. Coles, S.J. Barrall), BHRA Fluid Engng., Cranfield, 31–40.

Obladen, J., 1987, Stahlbetoninstandsetzung: Untergrundvorbehandlung, Untergrundhaftfestig-keit, Haftung unterschiedlicher Systeme. *Diplomarbeit*, FHS Münster, FB Bauingenieur-wesen.

Odler, I., Köster, H., 1983, Wassermigration im Porensystem des Zementsteins. *Berichtsband Int. Koll. Werkstoffwissenschaften und Bausanierung* (Hrg. F.H. Wittmann), TA Esslingen, 67–69.

Oertel, M., 2001, *Prandtl-Führer durch die Strömungslehre*. Verlag Viehweg, Braunschweig.

Ohnesorge, W., 1936, Die Bildung von Tropfen an Düsen und die Auflösung flüssiger Strahlen. *Zeitschrift f. angew. Math. und Mechanik*, Jg. 16, 355–358.

Ohta, H., Ouchi, S., Sirai, K., Sibuya, M., 1991, Development of an automatic

laintance cleaning machine. *Proc. 8th Int. Symp. on Automation and Robotics in Construction*, IPA, Stuttgart, 589–598.

Osanai, Y., Matsumura, Y., Murata, M., 1998, High pressure waterjet hydrodemolition robot. *Proc. 5th Pacific Rim Int. Conf. on Water Jet Technol.* (eds M.M. Vijay et al.), Allied Publ. Ltd., New Delhi, 567–573.

Oshina, S., Yamane, R., 1988, Magnetic shape-control of a liquid metal jet. *Proc. 9th Symp. Water Jet Technol.* (ed. P.A. Woods), BHRA, Cranfield.

Philipp, A., Lauterborn, W., 1998, Cavitation erosion by single laser-produced bubbles. *J. Fluid Mech.*, Vol. 361, 75–116.

Pianthong, K., Zakrzewski, S., Behnia, M., Milton, B.E., 2002, Supersonic liquid jets: their generation and shock wave characteristics. *Shock Waves*, Vol. 11, 457–466.

Plesset, M.S., Chapman, R.B., 1971, Collapse of an initially spherical vapor cavity in the neighborhood of a solid boundary. *J. Fluid Mech.*, Vol. 2, 283–286.

Post, L., Lüttgens, G., Maurer, B., Glor, M., 1983, Vermeidung von Zündgefahren infolge elektrostatischer Aufladung beim Versprühen von Flüssigkeiten unter hohem Druck. *Die BG*, Nr. 7, 1–4.

Preece, C.M., Hansson, I.L., 1986, Cavitation erosion of dense silica-cement mortar. *Proc. 6th Int. Conf on Erosion by Liquid and Solid Impact*, Cavendish Lab., Cambridge, 3/1–3/7.

Puchala, R.J., Vijay, M.M., 1984, Study on an ultrasonically generated cavitating or interrupted jet: aspects of jet design. *Proc. 7th Int. Symp. Water Jet Technol.* (eds I.A. Walls, J.E. Stanbury), BHRA, Cranfield, 69–82.

Raghavan, C., Olsen, J., 1989, Development of a 7,000 bar hose. *Proc. 5th Amer. Water Jet Conf.* (ed. T.J. Labus), WJTA, St. Louis, 449–454.

Randl, N., Wicke, M., 2000, Schubübertragung zwischen Alt- und Neubeton. *Beton und Stahlbetonbau*, Vol. 95, 461–473.

Raudensky, M., Horsky, J., Telecky, L., 1999, Thermal and mechanical effect of high-pressure spraying of hot surfaces – descaling. *Proc. 3rd Int. Metallurg. Conf. on Cont. Casting of Dillets*, Trinec, 217–221.

Rechsteiner, A., Wolfseher, R., 1998, Concrete surface quality and structural conditions after hydrodemolition. *Water Jet Applications in Construction Engineering* (ed. A.W. Momber), Balkema, Rotterdam, 177–187.

Rehbinder, G., 1977, The drag force on the grain in a permeable medium subjected to a water jet. *J. Appl. Mathem. and Phys.*, Vol. 28, 1005–1016.

Rehbinder, G., 1978, Erosion resistance of rock. *Proc. 4th Int. Symp. Jet Cutting Techn.* (eds J. Clarke & H.S. Stephens), BHRA, Cranfield, Paper E1/1–E1/10.

Rehbinder, G., 1980, A theory about cutting rock with a water jet. *Rock Mech.*, Vol. 12, 247–257.

Reichman, J.M., Kelley, D.P., Marvin, M., 1983, The further development of an underground cable following tool. *Proc. 2nd U.S. Water Jet Symp.* (eds D.A. Summers, F.F. Haston), Univ. of Missouri-Rolla Press, Rolla, 307–314.

Reinecke, R., 2002, Tragverhalten der Schubfuge zwischen Fertigteilen aus hochfestem Beton und Ortbetonergänzungen aus Normalbeton. *Interner Bericht*, Institut für Massivbau, Universität Leipzig.

Rieß, W., Himmelreich, U., 1991, Geschwindigkeitsmessungen im Wasserabrasivstrahlen. *Seminar zum SFB 264*, Universität Hannover.

RILEM, 1985, Determination of the fracture energy of mortar and concrete by means of three-point bend tests on notched beams. *RILEM Draft Recommendation 50-FMC*. RILEM.

RILI, 2001, *Schutz und Instandsetzung von Betonbauteilen* (Instandsetzungs-Richtlinie), Deutscher Ausschuß für Stahlbeton, Köln.

Rockwell, P.K., 1981, Water jet trenching in submerged clay. *Proc. 1st U.S. Water Jet Symp.* (eds F.D. Wang et al.), Colorado School of Mines Press, Golden, IV/4.1-IV/4.10.

Rodehüser, A., 1930, Kritische Betrachtungen über das Putzen von Gußstücken mittels Wasserstrahl. *Die Gießerei*, Vol. 17, 882–884, 896–903, 926–930.

Rosa, W., 1991, Bearbeiten von Betonflächen mit Hochdruckwasser. *Int. Fachtagung über konstruktive Instandhaltung, großflächige Erneuerung, vorbeugenden Schutz und Instandsetzungs-Sonderverfahren von Stahlbetonbauwerken* (Hrg. R. Kusterle), Innsbruck, 17–25.

Sakada, S., Adachi, I., Yahiro, T., Mitunobu, Y., 1998, Effect of surface treatment on bond strength between new and old concrete using the waterjet method. *Proc. 5th Pacific Rim Int. Conf. on Water Jet Technol.* (eds M.M. Vijay et al.), Allied Publ. Ltd., New Delhi, 561–566.

Sashida, K., Sasaki, K., Kamoshida, B., 1988, Water jets: construction applications (tunnel excavation, cutting of steel pipe, cutting of reinforced concrete wall). *Proc. 9th Int. Symp. Jet Cutting Technol.* (ed. P.A. Woods), BHRA, Cranfield, 561–570.

Sasse, H.R., 1987, Die Adhäsion zwischen Estrich und Beton. *Industriefußböden* (Hrsg. P. Seidler), Ostfildern, 47–56.

Schikorr, W., 1986, Beitrag zum Werkstoffabtrag durch Flüssigkeitsstrahlen hoher Relativgeschwindigkeit. *Dissertation*, Univ. Hannover.

Schlatter, M., 1986, *Entgraten durch Hochdruckwasserstrahlen.* Springer-Verlag, Heidelberg.

Schmidt, P., Walzel, P., 1984, Zerstäuben von Flüssigkeiten. *Physik in unserer Zeit*, Vol. 15, 113–120.

Schneider, U., Herbst, H.J., 1989, Porositätskennwerte von Beton. *TIZ-International*, Vol. 113, 311–321.

Schönert, K., 1974, Über die Eigenschaften von Bruchflächen. *Chemie-Ing.-Technik*, Jg. 49, 711–714.

Schröder, H., 2000, Rechtsgrundlagen bei der Entschichtung von asbesthaltigen Altanstrichen. *Sprechtag der Hafenbautechnischen Gesellschaft e.V.*, Magdeburg, 5. April 2000.

Schulz, R.-R., 1984, Beton als Beschichtungsuntergrund – Über die Prüfung des Festigkeitsverhaltens von Betonoberflächen mit dem Abreißversuch. *Dissertation*, Fakultät Bauingenieur- und Vermessungswesen, RWTH Aachen.

Shah, S.P., Ouyang, C., 1993, Toughening mechanisms in quasi-brittle materials. *ASME J. Engng. Mater. Technol.*, Vol. 115, 300–307.

Shavlovsky, D.S., 1972, Hydrodynamics of high pressure fine continuous jets. *Proc. 1st Int. Symp. Jet Cutting Technol.* (eds N.G. Coles, C.A. Richardson), BHRA, Cranfield, 81–92.

Shi, H.H., Dear, P., 1992, Oblique high-speed liquid-solid impact. *JSME Int. J., Ser. I*, Vol. 35, 285–295.

Shi, H.H., Sato, H., 2003, Comparison-speed liquid jets. *Exper. In Fluids*, Vol. 35, 486492.

Siebel, M.K., Mosher, G.E., 1984, Detecting and controlling vibration. *Modern Casting*, Aug., 34–36.

Siegert, R., Jurk, V., Magritz, R., 2000, *Wasserstrahldissektion in der Medizin*, Books on Demands GmbH.

Silfwerbrand, J., 1990, Improving concrete bond in repaired bridge decks. *Concrete Int.*, Vol. 12, No. 9, 61–66.

Simpson, M., 1990, Abrasive particle study in high pressure water jet cutting. *Int. J. Water Jet Techn.*, Vol. 1, 17–28.

Sindt, V., Ruch, M., Schultmann, F., Funk, W., Rentz, O., 1997, Technisch-wirtschaftliche Bewertung von Verfahren zur Oberflächendekontaminierung. *Bautechnik*, Vol. 74, 127–131.

Sitek, L., Foldyna, J., Scucka, J., Svehla, B., Bodnarova, L., Hela, R., 2003, Concrete and rock cutting using modulated waterjets. *Proc. 7th Pac. Rim Int. Conf. Water Jetting Technol.* (eds K. Lee et al.), Korean Soc. Water Jet Techn., Seoul, 235–244.

Smith, L., 2001, Safe use of ultra-high-pressure waterjetting. *J. of Protect. Coat. and Linings*, Vol. 18, No. 10, 35–40.

Sondermann, W., 1998, Extraction and washing contaminated soils using high pressure jet grouting technique. *Water Jet Applications in Construction Engineering* (ed. A.W. Momber), A.A. Balkema, Rotterdam, 207–216.

Springer, G.S., 1976, *Erosion by Liquid Impact*, Scripta Publishing Co., Washington D.C.

Staskiewicz, L., 1995, Entwicklung eines Modells zur Vorhersage der Kerbtiefe beim Kerben von Bohrlöchern mit Hilfe der Hochdruckwassertechnik. *Diplomarbeit*, Inst. für Bergbaukunde II, RWTH Aachen.

Steverding, B., Lehnigk, S.H., 1976, The fracture pulse penetration depth of stress pulses. *Int. J. Rock Mech. Min. Sci. Geomech. Abstr.*, Vol. 13, 75–80.

Sugawara, K., Obara, Y., Hamaura, T., 1998, Shell-shaped fracture of rocks by water jet impingement. *Rev. High Pressure Sci. Technol.*, Vol. 7, 1466–1468.

Sugiyama, H., Tabata, A., 1988, Abrasive waterjet method for effective cutting of reinforced concrete members (on vibration properties when cutting). *Proc. 9th Int. Symp. Jet Cutting Technol.* (ed. P.A. Woods), BHRA, Cranfield, 581–589.

Summers, D.A., 1991, Historical perspective of fluid jet technology. *Fluid Jet Technology* (ed. T.J. Labus), Water Jet Techn. Ass., St. Louis, 1.1–1.21.

Summers, D.A., 1995, *Waterjetting Technology*. Chapmann & Hall, New York.

Szwedzicki, T., 1998, Indentation hardness testing of rock, *Int. J. Rock Mech. Min. Sci.*, Vol. 35, 825–829.

Tabor, D., 1951, *The Hardness of Metals*. Claredon Press, Oxford University Press, Oxford.

Takagi, K., Satou, M., 1988, Application of abrasive jet to slab track repair. *Proc. 9th Int. Symp. Jet Cutting Technol.* (ed. P.A. Woods), 683–691.

Talbot, C., Pigeon, M., Beaupre, D., Morgan, D.R., 1994, Influence of surface preparation on long-term bonding of shotcrete. *ACI Mater. J.*, Nov./Dec., 560–566.

Taylor, S.A., 2000, Field removal of cold-applied tape systems from large diameter transmission lines using ultra high-pressure water jetting. *Proc. PCE Conf and Exhibition*, Technol. Publ., Pittsburgh, 177–188.

Temme, W., 1986, Wasserhochdruckspülung als Verfahrenshilfe bei der Vibrationsrammtechnik. *Tiefbau-BG*, Nr. 2, 111–117.

Thikomirov, R.A., Babanin, V.B., Pethukov, E.N. et al., 1992, *High Pressure Jet Cutting*. ASME Press, New York.

Thiruvengadam, A., 1967, The concept of erosion strength. *ASTM STP 408*, Amer. Soc. Testing Mater., Philadelphia, 22–41.

Toutan, H., Ortiz, G., 2001, The effect of surface preparation on the bond interface between FRP sheets and concrete members. *Composite Structures*, Vol. 53, 457–462.

Troesch, H.A., 1954, Die Zerstäubung von Flüssigkeiten. *Chemie-Ing.-Techn.*, Jg. 26, 311–320.

Trotter, L.E., 2001, Comparison of surface preparation using different methods. *Proc. 11th Amer. Waterjet Conf.* (ed. M. Hashish), WJTA, St. Louis, 745–763.

Tschegg, E.K., Stanzl, S.E., 1991, Adhesive power of bonded concrete. *Fracture Processes in Concrete and ceramics* (eds J.G.M. van Mier et al.), E.&F.N. Spon, London, 809–818.

Tschegg, E., Kroyer, G., Tan, D.-M., Litzka, J., Tschegg-Stanzl, S., 1995, Charakterisierung der Brucheigenschaften von Asphalt. *Straßenforschung*, Heft 440, Bundesministerium für wirtschaftliche Angelegenheiten, Wien.

Tschegg, E.K., Rotter, H.M., Roelfstra, P.E., Bourgund, U., Jussel, P., 1995, Fracture mechanical behaviour of aggregate-cement matrix interfaces. *ASCE J. Mater. Civil Engng.*, Vol. 7, 199–208.

US Air Force, 1999, *Laser Paint Removal*. Final Report, Joint Depot Maintenance Activities Group, Wright-Patterson-Airbase, Ohio.

Utsumi, H., Sakoda, S., Ying, L., Adachi, I., 1999, Experimental study in the construction joint of concrete structure using WJ technology. *Proc. Int. Symp. New Appl. of Water Jet Techn.* (ed. R. Kobayashi), Ishinomaki, 163–170.

Vallve, F.X., Mohaupt, U.H., Kalbfleisch, J.G., Burns, D.J., 1980, Relationship between jet penetration in concrete and design parameters of a pulsed waterjet machine. *Proc. 5th Int. Symp. Jet Cutting Technol.* (eds H.S. Stephens, B. Jarvis), BHRA, Cranfield, 215–228.

Vasek, J., Foldyna, J., Novak, J., 1991, Test on walls of a railway tunnel and samples of concrete and blocks of rocks with high pressure water jet equipment for outdoor applications in Czechoslovakia. *Proc. 6th Amer. Water Jet Conf.* (ed. T.J. Labus), WJTA, St. Louis, 87–101.

Vauck, W., Müller, H., 1994, *Grundoperationen chemischer Verfahrenstechnik*. Deutscher Verlag für Grundstoffindustrie, 10. Auflage, Leipzig-Stuttgart.

VDI, 1987, Einwirkung mechanischer Schwingungen auf den Menschen – Beurteilung, *VDI-Richtlinie 2057/Blatt 3*, Mai 1987.

Veenhuizen, S.D., 2000, Operating efficiency of crankshaft drive pumps. *Proc. 6th Pacific Rim Conf. Water Jetting Technol.* (eds P.G. Dunn et al.), CMTE, 249–252.

Versluis, M., Schmitz, B., von der Heydt, A., Lohse, D., 2000, How snapping shrimp snap: through cavitating bubbles. *Science*, Vol. 289, 2114–2117.

Vierke, J., 1973, Das Waserspucken der Arten der gattung Colisa. *Bonner zool. Beiträge*, Vol. 24, 62–104.

Vijay, M.M., 1998a, Power of pulsed jets. *Waterjet Applications in Construction Engineering* (ed. A.W. Momber), A.A. Balkema, Rotterdam.

Vijay, M.M., 1998b, Fluidjet technology: safety considerations. *Proc. 5th Pacific Rim Int. Conf. Water Jet Technol.* (eds M.M. Vijay et al.), Allied Publ., Ltd., New Delhi, 309–320.

Vijay, M.M., Foldyna, J., Remisz, J., 1993, Ultrasonic modulation of high-speed water jets. *Proc. Geomechanics '93* (ed. Z. Rakowski), A.A. Balkema, Rotterdam, 327–332.

Vijay, M.M., Yan, W., Tieu, A., Bai, C., Pecman, S., 1999, Removal of hard coatings from the interior of ships using pulsed waterjets: results of field trials. *Proc. 10th Amer. Waterjet Conf.* (ed. M. Hashish), WJTA, St. Louis, Paper 53.

Vorster, M.C., Merrigan, J.P., Lewis, R.W., Weyers, R.E., 1992, Techniques for concrete removal and bar cleaning on bridge rehabilitation projects. *SHRP-S-336*, Strategic Highway Research Program, NRC, Washington.

Waldherr, E.U., 1991, Kavitationserosion keramischer Werkstoffe. *PhD-Dissertation*, Ruhr University Bochum.

Wallace, M., 1985, Waterblasting robot helps complete bridge repair 15 month early. *Concrete Constr.*, Sept., 785–786.

Walser, R., 1999, Instandsetzung der Litti- und Lissibach-Autobahnbrücken in Baar ZG. *Schweizer Baujournal*, Nr. 3, 38–39.

Watson, A.J., Williams, F.T., Brade, R.G., 1984, The relationship between impact pressure and anatomical variations in a water jet. *Proc. 7th Int. Symp. Jet Cutting Technol.* (eds I.A. Walls, J.E. Stanbury), BHRA, Cranfield, 193–209.

Watzl, A., 2001, Spunbonding und Spunlancing. *Technische Textilien*, Vol. 44, 230–233.

Webster, P., Johns, S., 2003, Recommended practices for the use of high pressure hose. *Proc. 2003 American Water jet Conf.*, WJTA, St. Louis, Paper 2-B.

Weiß, M., Momber, A.W., 1998, Carpet recycling with water jets. *Recycling Recovery Reuse '98* (ed. X. Edelmann), Genf, III.123-III.136.

Weiß, M., Momber, A.W., 1999, Selective carpet separation with high-speed waterjets. *Proc. Int. Symp. New Appl. of Water Jet Techn.* (ed. R. Kobayashi), Ishinomaki, 227–231.

Weiß, M., Momber, A.W., 2003, Preliminary investigations into the separation of automotive components by a hydro-erosive method. *Inst. Mechan. Engrs., J. Automobile Engng.*, Vol. 217, 221–228.

Weiß, M., Momber, A.W., 2004, Erosive separation of organic coatings from fibrous substrates. *J. Environ. Management*, Vol. 73, 219–227.

Weiß, M., Wüstenberg, D., Momber, A. W., 2003, Hydro-erosive separation of plastic fibres from textile compounds. *J. of Materials Cycles and Waste Management*, Vol. 5, 84–88.

Werner, M., 1988, Wassereintrag auf Betonflächen bei der Behandlung mit dem Aquablast-Plus Hochdruckwasserstrahlgerät. *Internal Report*, Institut für Baumaschinen und Baubetrieb, RWTH Aachen.

Werner, M., 1991a, Einflußparameter und Wirkmechanismen beim Abtrag von Mörtel und Beton mit dem Hochdruckwasserstrahl. *Dissertation*, Inst. für Baumaschinen und Baubetrieb, RWTH Aachen.

Werner, M., 1991b, Höchstdruckwasserstrahlen in der Bauindustrie – Einsatzmöglichkeiten und Einsatzgrenzen. Lehrgang 13809/83.130, Technische Akademie Esslingen.

Werner, M., 1991c, Ein neues Verfahren zum Ausräumen schadhafter Mörtelfugen in historischem Mauerwerk – Teil 2. *Bautenschutz + Bausanierung*, Vol. 14, 24–26.

Werner, M., Kauw, V., 1991, High pressure water jet system – a new process for cleaning defective mortar joints in historic masonry. *Proc. 9th Int. Brick/Block Masonry Conf.*, Vol. 3, Berlin, 1639–1644.

Werner, M., Kauw, V., Hoffmann, M., 1995, Entsorgung auf Wasserstrahlbaustellen. *Bautenschutz+Bausanierung*, No. 4, 35–40.

Wiedemeier, J., 1981, Flüssigkeitsfreistrahlen hoher Relativgeschwindigkeit und Bruchkinetik spröder Werkstoffe. *PhD Thesis*, Univ. Hannover.

Wilson, D., 2002, Producing the ideal surface for coatings on concrete. *J. Protect. Coat. & Lin.*, Vol. 19, 71–77.

Wilson, E.B., 1918, *Hydraulic and Placer Mining*. John Wiley & Sons, New York.

Witzel, J., 1998a, Anwendungsorientierte Grundlagenuntersuchungen zur Entwicklung eines umweltschonenden hydraulischen Impulsspaltverfahrens. *Dissertation*, RWTH Aachen.

Witzel, J., 1998b, Recycling compact disks using high-pressure waterjets. *Jetting Technol.* (ed. H. Louis), BHR Group, Cranfield, 365–374.

WJTA, 1999, Recommended practices for the use of manually operated high-pressure water jetting equipment. Water Jet Technology Association, St. Louis, MO, USA.

Wolfseher, R., Hess, B., 1994, Traggrundbearbeitung mittels Höchstdruck-Wasserstrahlen. Bericht Nr. 92.152.17, Wolfseher und Partner AG, Baar, 3–21.

Wood, B., 1996, A water-cooled, hydraulically positioned 20,000 psi lance for waterblasting inside a hot kiln. *Jetting Technology* (ed. C. Gee), Mechan. Engng. Publ. Ltd., London, 379–392.

Wright, D., Wolgamott, J., Zink, G., 1997, A study of rotary jets for material removal. *Proc. 9th Amer. Water Jet Conf.* (ed. M. Hashish), WJTA, St. Louis, 525–539.

Wright, D., Wolgamott, J., Zink, G., 1999, Nozzle performance in rotary applications. *Proc. 10th Amer. Waterjet Conf.* (ed. M. Hashish), WJTA, St. Louis, Paper 73.

Wright, D., Wolgamott, J., Zink, G., 2003, Waterjet nozzle material types. *Proc. Amer. Waterjet Conf.* (ed. D.H. Summers), WJTA, St. Louis, Paper 4–B.

Wulf, C., 1986, Geometrie und zeitliche Entwicklung des Schnittspaltes beim Wasserstrahl-schneiden. *Dissertation*, RWTH Aachen, Aachen.

Xie, A., 1998, Engineering feasibility of abrasive water jet cutting in dangerously explosive and inflammable situation. *Proc. 5th Rim Int. Conf. Water Jet Technol.* (eds M.M. Vijay et al.), Alied Publ. Ltd., New Delhi, 266–271.

Xue, S., Fan, Y., Peng, H., Huang, W., Chen, Z., Jiang, T., Wang, L., 2001, Difference and similarity of glue removal for airport concrete runway and bitumen runway. *Proc. WJTA American Waterjet Conf.*, Minneapolis, Paper 43.

Xue, S., Huang, W., Chen, Z., Shi, D., Mi, W., 1996, How to formulate standards of high pressure waterjet units. *Jetting Technol.* (ed. C. Gee), Mechan. Engng. Publ., Bury St. Edmunds, 405–411.

Yamada, B., Yahiro, T., Ishibashi, J., 1988, On the development and application of a method of remodeling utilizing an abrasive jet system. *Proc. 9th Int. Symp. Jet Cutting Technol.* (ed. P.A. Woods), BHRA, Cranfield, 203–215.

Yan, W., Tieu, A., Ren, B., Vijay, M.M., 2004, Removal of delaminated concrete and cleaning the rust off the reinforcing bars using high-freqency forced pulsed waterjet. Proc. *17th Int. Conf. Water Jetting – Advances and Future Needs*, BHR Group, Cranfield.

Yanaida, K., 1974, Flow characteristics of water jets. *Proc. 2nd Int. Symp. Jet Cutting Techn.* (eds N.G. Coles, S.J. Barrall), BHRA Fluid Engng., Cranfield, A2/19-A/2-32.

Yanaida, K., Ohashi, A., 1980, Flow characteristics of water jets. *Proc. 5th Int. Symp. Jet Cutting Techn.* (eds H.S. Stephens, B. Jarvis), BHRA, Cranfield, Paper A3, 33–44.

Yasui, R., Yanari, A., Carletti, F.M., 1993, The removal of excessive resin from semiconductor leadframes with spot-shot waterjets. *Proc. 7th Amer. Water Jet Conf.* (ed. M. Hashish), WJTA, St. Louis, 813–827.

Yasumatsu, T., Kamihigashi, Y., Yoshida, A., Ishida, H., Nakashima, H., 1999, Experimental studies on the application of water-jet technology to rehabilitation of concrete structures. *Proc. Int. Symp. New Appl. Water Jet Technol.* (ed. R. Kobayashi), Water Jet Technol. Soc. Japan, 179–188.

Yie, G., 1984, Cutting hard materials with abrasive entrained water jet. *Proc. 7th Int. Symp. Jet Cutting Technol.* (eds I.A. Walls, J.E. Stanbury), BHRA, Cranfield, 481–491.

Yie, G., Burns, D.J., Mohaupt, U.H., 1978, Performance of a high-pressure pulsed water jet device for fracturing concrete. *Proc. 4th Int. Symp. Jet Cutting Technol.* (eds J. Clarke, H.S. Stephens), BHRA Fluid Engng., 67–86.

Yonekura, R., Terashi, M., Shibazaki, M., 1996, (eds): *Grouting and Deep Mixing.* A.A. Balkema, Rotterdam.

Zehr, R., 1998, Möglichkeiten und Grenzen des Hochdruck-Wasserstrahles. *Seminarunterlagen 'Der Traggrund'.* Technische Forschung und Beratung für Zement und Beton, Wildegg.

Zeng, J., Kim, T.J., Wallace, R.J., 1992, Quantitative evaluation of machinability in abrasive waterjet machining. *ASME Production Engng. Div.*, Vol. 58, 169–179.

Zou, C., Dang, L., Duan, X., Cheng, D., 1985, Investigation on anatomy of continuous waterjet for updating jet performance. *Proc. 3rd US Water Jet Conf.* (ed. N. Styler), WJTA, St. Louis, 160–178.

Index